



HAL
open science

A highly granular semi-digital hadron calorimeter for a future linear $e + e -$ collider and a model independent Higgs boson measurement in the $ZH \rightarrow qq + X$ channel

Yacine Haddad

► **To cite this version:**

Yacine Haddad. A highly granular semi-digital hadron calorimeter for a future linear $e + e -$ collider and a model independent Higgs boson measurement in the $ZH \rightarrow qq + X$ channel. High Energy Physics - Experiment [hep-ex]. Ecole Doctorale Polytechnique; Laboratoire Leprince-Ringuet, 2014. English. NNT: . tel-01191891

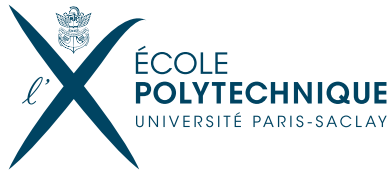
HAL Id: tel-01191891

<https://polytechnique.hal.science/tel-01191891>

Submitted on 2 Sep 2015

HAL is a multi-disciplinary open access archive for the deposit and dissemination of scientific research documents, whether they are published or not. The documents may come from teaching and research institutions in France or abroad, or from public or private research centers.

L'archive ouverte pluridisciplinaire **HAL**, est destinée au dépôt et à la diffusion de documents scientifiques de niveau recherche, publiés ou non, émanant des établissements d'enseignement et de recherche français ou étrangers, des laboratoires publics ou privés.



ÉCOLE POLYTECHNIQUE

THÈSE DE DOCTORAT

Présentée par

Yacine HADDAD

en vue d'obtenir le grade de

**DOCTEUR EN SCIENCES
DE L'ÉCOLE POLYTECHNIQUE**

**A highly granular semi-digital hadron calorimeter for a
future linear e^+e^- collider and a model independent
Higgs boson measurement in the $ZH \rightarrow q\bar{q} + X$ channel**

Soutenue le 14 Octobre 2014 devant la commission d'examen composée de :

Dr.	J.C. Brient	Président du Jury
Dr.	D. Zerwas	Rapporteur
Dr.	M. Titov	Rapporteur
Prof.	J. Repond	Examineur
Dr.	D. Lacour	Examineur
Dr.	V. Boudry	Directeur de thèse

Abstract

The International Linear Collider (ILC) is a concept for a linear electron-positron accelerator with a centre-of-mass energy of up to 1 TeV. Its main purpose is the precise measurement of particles discovered by the LHC such as the Higgs boson particle. The International Large Detector (ILD) is one of its detector concepts, specifically designed for the usage of Particle Flow Algorithms requiring highly granular calorimeters. Within the CALICE collaboration, several prototypes of such calorimeters, exploring different technologies, have been developed and tested. This thesis focuses on one of them: a semi-digital hadron calorimeter (SDHCAL) equipped with Glass Resistive Plate Chambers (GRPC) sensors. It is a sampling calorimeter composed of 48 layers segmented in cells of one square centimetre for a total of half a millions channels. The first part of the present thesis describes the analysis of the data taken during beam tests at CERN, in which the detector was operated in a trigger less mode; saving of all incoming information in local memory. Thus an event-builder was developed and used to extract physics events using new algorithm based on a time clustering methods.

A detailed study of the SDHCAL quality of the detector in term of detection efficiency and pad multiplicity, is performed by a well-reconstructed muons tracks using the imaging capability of the detector. Additionally, a method to measure the induced charge spectrum and the electronic avalanche size in the GRPC sensors is presented, which allows the extraction of the key parameters required to tune an accurate detector simulation. The information acquired by the muons reconstruction was also used to improve the calorimeter response to the pions with a visible impact on its resolution. The sensor's and the electronics's response needs to be modelled for the Monte Carlo simulation (using GEANT-4) in a so-called "digitisation" module; we developed a general digitisation method which can be applied to various high granular gaseous sensors. It has been successfully tested with GRPC and MicroMegas detectors. After this detailed study of the characteristics of our calorimeter, the response to pions is then treated. The test beam at CERN provide a large sample of pions of different energy ranging between 5 to 80 GeV. A detailed selection is applied to choose the hadronic showers, exploring new kind of identification variable such as fractal dimension and hit density. The selected pions are then used for the calibration of the calorimeter in term of linearity and energy resolution.

To assess the performance in the full ILD configuration, the second part of this thesis is devoted to the investigation of the model independent Higgs boson production associated with the ZH process. The final state is characterised by the presence of at least two jets originating from a Z boson beside the Higgs decay products. In order to perform a model independent measurement, the events selection does not constrain Higgs boson decaying modes. The hadronic Z decay is characterised by a high branching ratio with respect to the leptonic one, providing an increase of the statistics of about a factor of ten. In addition, the model-independent context may pinpoint a deviation from the SM expectations of Higgs boson decays. The first analysis demonstrated the feasibility of the model-independent Higgs tagging using the hadronic decay of the Z boson at 250GeV. This was achieved using boosted decision trees implemented in the Toolkit for Multivariate Analysis (TMVA). Further investigation demonstrated the importance of the beam polarisation the sensitivity of this channel and for the background reduction allowing the measurement of the ZH process cross section with 2% of precision.

Résumé

Le collisionneur linéaire international (ILC) est le concept d'un accélérateur d'électrons-positrons linéaire avec une énergie dans le centre de masse allant jusqu'au TeV. Son but est la mesure de haute précision des propriétés des particules découvertes par le LHC, en particulier celles du boson de Higgs. L'ILD est l'un des concepts de détecteurs spécialement conçus pour l'utilisation de l'algorithme de suivis des particules (PFA) nécessitant une calorimétrie très granulaire. Dans le cadre de la collaboration CALICE, quelques prototypes de calorimètres, explorant des technologies différentes, ont été développés et testés en faisceau. Cette thèse se concentre sur l'un d'eux: un calorimètre hadronique semi-digital (SDHCAL) basé sur des chambres à plaques résistives (GRPC). Il est composé de 48 couches segmentée en cellules d'un centimètre carré pour un total de 500 000 canaux, lues de façon sommaire (en 3 seuils).

La première partie de cette thèse se focalise sur l'analyse des données recueillies pendant les tests en faisceau au CERN, dans lequel le détecteur a fonctionné en mode d'auto-déclenchement; enregistrant toutes les informations entrantes dans le détecteur. Une méthode de reconstruction d'évènement a été développée qui permet d'extraire les événements physiques utilisant un nouvel algorithme basé sur une méthode de regroupement temporel. Une étude détaillée de la qualité du SDHCAL en terme d'efficacité de détection et multiplicité des cellules touchées, est effectuée utilisant des traces de muons reconstruits avec le détecteur. Un procédé pour mesurer le spectre de charge induite et la taille de l'avalanche électronique dans les capteurs GRPC est aussi présentée. L'extraction de ces paramètres clés est nécessaire pour une simulation précise du détecteur. La réponse des capteurs et de l'électronique d'acquisition doit être modélisés pour la simulation Monte-Carlo (avec GEANT-4) dans un module dit de *digitisation*; un procédé de digitisation générale a été développé au cours de cette thèse, qui peut être appliquée à divers capteurs gazeux à granularité élevée. Il a été testé avec succès sur les GRPC et les MicroMegas. La réponse aux pions est ensuite traitée. Les tests faisceau au CERN fournissent un grand échantillon de pions d'énergie allant de 5 à 80 GeV. Une sélection fine des gerbes hadroniques est appliquée, à l'aide de nouveaux type de variables d'identification telles que la dimension fractale des gerbes. Les pions ainsi sélectionnés sont ensuite utilisés pour l'étalonnage du calorimètre en terme de linéarité et de résolution en énergie. L'information acquise par la reconstruction des muons a été également utilisée pour améliorer la réponse du calorimètre aux pions avec un impact visible sur sa résolution.

Pour évaluer les performances dans une configuration complète d'un grand détecteur, la deuxième partie de cette thèse est consacrée à l'étude du mode production du boson de Higgs associé au processus ZH avec l'ILD. L'état final recherché est caractérisé par la présence d'au moins deux jets provenant de boson Z à côté des produits de désintégration du Higgs. Pour effectuer mesure indépendante du Higgs, la sélection des événements ne contraint pas les modes de désintégration du Higgs. Le boson Z étant caractérisée par un rapport d'embranchement hadronique plus élevé par rapport à celui leptonique, il offre une meilleure statistique. En outre, le contexte d'indépendance au modèle du boson de Higgs peut identifier des éventuels écarts par rapport aux attentes du modèle standard de la physique des particules. La première analyse consiste à la démonstration de la faisabilité du marquage du boson de Higgs en utilisant la désintégration hadronique du boson Z. Ceci a été réalisé en utilisant des arbres de décision boostés (BDT). Une analyse plus poussée démontre l'importance de la polarisation du faisceau sur sensibilité

de ce canal et pour la réduction du bruit de fond, et ainsi prédire une mesure de la section efficace du processus de ZH avec une précision de 2%.

Remerciement

“Je suis d’une tribu qui nomadise depuis toujours dans un désert aux dimensions du monde. Nos pays sont des oasis que nous quittons quand la source s’assèche, nos maisons sont des tentes en costume de pierre, nos nationalités sont affaires de dates, ou de bateaux. Seul nous relie les uns aux autres, par-delà les générations, par-delà les mers, par-delà le Babel des langues, le bruissement d’un nom.”

— Amine Maalouf, *Origines*.

Mon doctorat peut sans doute être comparé à un bateau qui a navigué en hautes mers. Beau nombre de tempêtes l’on fait basculer à bord et à tribord. Pourtant, ce bateau a fini par atteindre des eaux calmes et ce, grâce aux nombreuses rencontres qui se sont faites et aux liens d’amitié qui se sont tissés durant de nombreuses escales. Ceci a fini par former un équipage composé toutes ces personnes qui ont été présentes et qui m’ont soutenu de loin ou de près durant ce long voyage que fut cette thèse.

Je commence naturellement par toi Vincent. Toi qui as guidé mes premiers instants en tant que chercheur apprenti (d’ailleurs je le suis toujours) et de m’avoir offert ta patience et ton riche d’enseignements. Merci pour toutes ces opportunités et ces nombreuses fois où tu m’avais poussé au-devant de la scène alors que je n’étais qu’un jeune *Padawan*. Merci d’être resté la veille de ma soutenance à une heure aussi tardive (avec Ivo et Claudia), dans un moment de stress ultime.

Henri. Tu as été pour moi une source d’inspiration et bien plus encore. Merci de m’avoir soutenu durant ma dernière ligne droite, d’avoir lu, relu et surtout corrigé ma thèse. Cette thèse aurait pu être la tienne. Merci de tes nombreux conseils et enseignements. J’ai profité avec une très grande joie de ses nombreuses discussions avec toi sur des sujets aussi divers que variés.

J’ai énormément de chance d’avoir fait ma thèse au sein du LLR, un laboratoire qui a fait figure pour moi de famille. Je remercie l’ensemble de ses membres et particulièrement son directeur Jean-Claude Brient, qui a été au aussi d’un grand soutien durant ma thèse et qui m’a conseillé et surtout enseigné l’art de l’analyse e^+e^- . Un grand merci aussi pour m’avoir fait l’honneur de présider mon jury de thèse.

Merci à mes rapporteurs, Dirk Zerwas et Maxim Titov pour leur relecture détaillée, qui m’a permis d’améliorer ce manuscrit. Merci aussi à Didier Lacour d’avoir accepté de faire partie de mon jury de thèse. Je remercie aussi José Répond d’avoir accepté d’être parmi mon jury de thèse, même si les événements qui ont précédés ma date de soutenance l’ont contraint à annuler.

Je remercie également l'ensemble de l'équipe SDHCAL à l'IPN de Lyon. En premier, Imad Laktineh, qui m'a été d'un grand soutien durant ma thèse. J'aimerais te dire merci Imad, pour m'avoir donné ta confiance durant ces tests en faisceau au CERN, de m'avoir permis d'apprendre à tes côtés et surtout de m'avoir soutenu contre vents et marées tout au long de ma thèse. Je n'oublie pas Gérald et Arnaud pour ces heures *shifts* qu'on a partagé ensemble, et qui souvent, se prolongeaient jusqu'au petit matin. J'adresse aussi une pensée à l'équipe de CIEMAT avec Mary-Cruz, Jésus et Gorgé.

Durant ma thèse, j'ai tissé un fort lien d'amitié avec Nadir et Ivo. Nous avons formé, ce qu'on a fini par appeler *le trio*. Merci à vous deux pour ces agréables moments passés ensemble, à trainer sur les quais de Seine, à ces *Jam sessions* et à tout le reste. Vous avez été et vous le serez encore des frères pour moi. Merci Ivo pour ces magnifiques aventures (notamment l'épisode IKEA ... et j'en passe). Merci aussi pour ces heures-là qu'on a passé ressemblant à la BNF à écrire nos thèses respectives durant la dernière ligne droite. Nous avons pu nous soutenir mutuellement malgré le stress et la fatigue. Je te souhaite beaucoup de réussite, à toi, mais aussi à Élodie. Nadir, merci tout d'abord d'avoir fait le déplacement pour assister à ma soutenance. Merci pour ces balades massicoises et ces séances science-fiction chez toi (ou chez moi) et surtout pour ton soutien sur tous les niveaux.

Par la suite notre *trio* s'est agrandi par l'arrivée de Luca au LLR, *l'ultimo crazy Luciano*, armé de sa bonne humeur, dont il avait le secret, il est tout de suite devenu un fidèle ami. Je te souhaite beaucoup de courage pour la fin de thèse.

Un grand merci Alex, de m'avoir offert tout de suite ton amitié et ton soutien. D'avoir partagé avec nous quatre (Ivo, Nadir, Luca est moi) ton ambition, ton énergie et surtout ta bonne humeur. Merci pour ces escapades improvisées en aventuriers quand tu nous rendais visite au LLR.

L'ambiance entre jeunes au laboratoire, est vraiment exceptionnelle. On a comme habitude (ou plutôt tradition) de se retrouver à ces pauses-café chaque après-midi pour partager des idées et des discussions aussi cultivées que drôles et relaxantes. J'ai pu apprécier l'originalité d'Alice, l'humour "spécial" de Hieu, les discussions avec Jon, Ben et Thomas. Sans oublier de mentionner les nombreuses interactions que j'ai eues avec le groupe CMS notamment avec Olivier, Christophe, Pascal et tous les autres. Mais aussi avec l'équipe de l'administration, avec Élodie, Anne-marie, Bambi, Sylvaine et Thu. Sans oublier Nora, Maïté, et Brigitte, qui ont été d'une aide précieuse pour tous mes "nombreux" soucis administratifs.

J'adresse aussi une pensée à mes amis de master Orsay et celui de Paris-Diderot, et en particulier Virginie, Zeynep, Nesrine, Hakim et Damien.

Un tendre merci à mes parents, et à ma famille en Algérie. Tous m'ont constamment encouragé tout au long de ma scolarité, de mes études universitaires et au cours de ma thèse. Au courant de cette thèse, j'ai eu la profonde tristesse de vivre la disparition de mon père. Il m'a toujours encouragé à apprendre, à entretenir ma curiosité et à toujours viser haut. Mon père fut un mécanicien de génie, il m'a appris à utiliser ses outils à chercher à comprendre comment les choses marchent. Nombreuses sont les fois où tu m'as accueilli sous ton aile comme apprenti pour m'apprendre les ficelles du métier. Merci papa, pour tes enseignements, d'avoir cru en moi, de m'avoir soutenu, et appris à devenir l'homme que je suis. Tu es et tu resteras pour moi le premier instituteur, l'exemple qu'il faut suivre et le père que j'aimerais devenir. Merci ma petite maman, de m'avoir couvert de ta tendresse, de m'avoir éduqué et permis de persévérer avec tes encouragements. Je n'oublie pas mon frère Idir et à mes soeurs, Souad, Fariza et Amel.

Et puis il y a toi Claudia, toi qui partages ma vie depuis plus de deux ans maintenant. Toi qui m'a couvert de ton amour. Toi ma petite famille. Toi qui m'as accepté tel que je suis. Toi qui m'a transmis

ta joie de vivre, et a apporter de la couleur à ma vie. Ton soutien indéfectible, m'a donné la force de me lever, quand j'étais à bout de souffle, et a illuminé mon chemin à mes heures les plus sombres. Cette thèse te doit tant ... Mille et une fois merci.

Maintenant, mon bateau quitte les rivages du LLR et s'en va traverser la manche vers d'autres ports. C'est à Londres que mon destin se poursuit. J'avoue que vous me manquez tous déjà, mais je sais fort heureusement qu'on finira par se revoir à un moment ou un autre.

Contents

Remerciement	vii
Abstract	vii
Introduction	1
I Theoretical and experimental background	5
1 The standard model of particle physics	7
1.1 The standard model of particle physics	8
1.1.1 Generalities	8
1.1.2 Electroweak theory	9
1.2 The BEH mechanism: the origin of mass	12
1.2.1 Example of spontaneous $\mathcal{U}(1)$ symmetry breaking	12
1.2.2 The case of $\mathcal{U}(1)$ local symmetry	14
1.2.3 Electroweak symmetry breaking	15
1.2.4 Higgs couplings to gauge bosons	16
1.2.5 Generation of fermions masses	17
1.3 Constraints on the Higgs boson mass	18
1.3.1 Theoretical bounds	18
1.3.2 Experimental bounds	19
1.4 Higgs boson discovery and properties	20
1.5 Higgs production in lepton colliders	22
2 A Linear Lepton Collider For Precise Measurements : Accelerator and Detectors	23
2.1 Why a linear e^+e^- collider ?	24
2.2 The international linear collider project	25
2.2.1 The e^+e^- machine layout	25
2.2.2 The polarised particle sources	26
2.2.3 The damping system	28
2.2.4 The main Linac	29
2.2.5 The beam delivery	29
2.3 The physics potential	30
2.3.1 The implication on the detector design for ILC	32
2.4 Particle flow paradigm	34
2.5 The international large detector concept	36

2.5.1	Tracking system	38
2.5.2	Calorimeter system	40
2.5.3	Magnet Coil and Muon System	42
3	Basics of calorimetry for high energy physics	43
3.1	Energy loss by a charged particle in matter	44
3.1.1	Interaction of electrons and photons: electromagnetic cascades	45
3.1.2	Interaction of hadrons: strong processes and cascade	48
3.2	Sampling calorimeters	51
3.2.1	Energy measurement	52
3.2.2	Energy resolution	53
3.3	CALICE: calorimetry for ILC detectors	55
3.3.1	The electromagnetic calorimeter (ECAL)	56
3.3.2	The analogue hadron calorimeter (AHCAL)	57
3.3.3	The digital hadron calorimeter (DHCAL)	57
3.3.4	Digital versus analogue HCAL and the semi-digital concept	57
II	Characterization of the semi-digital hadron calorimeter	59
4	Construction and commissioning of a highly-granular semi-digital calorimeter	61
4.1	General description	62
4.1.1	Structure and absorber	62
4.1.2	The sensitive detector	63
4.1.3	Very-front-end electronics	65
4.2	The Data Acquisition system	66
4.2.1	The hardware	67
4.2.2	Readout modes	68
4.2.3	Power pulsing	69
4.2.4	The data acquisition software	70
4.3	The CERN/PS-SPS Beam-Test (TB) campaigns	71
4.3.1	SPS north area beam lines	71
4.3.2	Beam configuration	72
4.4	Event building	73
4.5	Data quality control	77
4.5.1	Online monitoring	77
4.5.2	Offline monitoring	77
4.5.3	Gain calibration	79
4.6	Conclusion	79
5	Characterisation of the SDHCAL prototype using muons	81
5.1	The SDHCAL glass resistive plate chambers	82
5.2	Physics of GRPC	83
5.2.1	Gas Ionisation by a charged particle	84
5.2.2	Electron multiplication	87
5.2.3	Induced signal	90
5.3	Study of the GRPC performance using minimum ionising particles	92

5.3.1	Track reconstruction	92
5.3.2	Efficiency and multiplicity	94
5.3.3	Angular dependence	95
5.3.4	Induced signal measurement	96
5.3.5	Chambers uniformity study	100
5.4	Conclusion	101
6	Digitisation procedure for highly granular gaseous detector	103
6.1	Description of the used gaseous detectors	104
6.1.1	Data sample	105
6.2	The determination of induced Charge spectrum	105
6.2.1	Charge sharing	106
6.3	Digitisation procedure	106
6.3.1	Small-cell approach	107
6.4	Results and discussion	108
6.5	Conclusion	110
7	Energy reconstruction in SDHCAL prototype	113
7.1	Particle identification	114
7.1.1	Principal component analysis	114
7.1.2	Fractal dimension	115
7.1.3	Hit density	117
7.1.4	First interaction plate	118
7.1.5	Additional variables	119
7.2	Event selection	119
7.2.1	Beam muon and cosmic rejection	119
7.2.2	Electron rejection	120
7.2.3	Leakage reduction	122
7.3	Reconstructed energy and intrinsic energy resolution	122
7.3.1	Pure digital mode	124
7.3.2	Semi-digital mode	124
7.3.3	Semi-digital mode versus pure-digital mode	128
7.4	Uniformity correction using minimum ionising particle	129
7.4.1	Basic hadronic showers selection	131
7.4.2	First test	132
7.4.3	Energy reconstruction and resolution	134
8	Study of High Rate GRPC for LHC Detectors Upgrade	137
8.1	Experimental setup at DESY test beam	139
8.2	Results and discussion	140
8.3	Conclusion	142
III	Higgs analysis	143
9	Tagging the Higgs boson using $Z \rightarrow q\bar{q}$ at 250 GeV ILC	145
9.1	Introduction	146

9.2	Phenomenological aspects	147
9.2.1	Signal production processes	147
9.2.2	Background processes	148
9.2.2.1	W^\pm pairs production	148
9.2.2.2	Z pairs production	148
9.2.2.3	Production $q\bar{q}$ pairs	149
9.3	Simulation Tools	150
9.3.1	Signal and background processes weighting	150
9.3.2	Simulation of the detector response for particle flow analysis	151
9.4	Analysis Tools	152
9.4.1	Event shape variables	152
9.4.2	Multivariate analysis	153
9.4.2.1	Boosted decision trees	154
9.4.2.2	Toolkit for multivariate analysis (TMVA)	155
9.5	Jet reconstruction	156
9.5.1	QCD phenomena and jet formation	156
9.5.2	Jet clustering algorithms principle	156
9.5.3	Jet energy smearing	158
9.5.4	Z jets identification and optimisation of the jet finder	159
9.6	Fast and full simulations	161
9.7	Visible Higgs boson event selection	163
9.7.1	Rejection of $q\bar{q}(\gamma)$ events	163
9.7.2	WW/ZZ vetoes	163
9.7.3	Boosted decision tree construction	167
9.7.4	Testing the model independence	173
9.8	Total Higgs-strahlung cross section and determination of g_{ZZH} coupling strength	175
9.9	Conclusion	177
	Conclusion	179
	A SDHCAL technical details	181
A.1	Crystal-Ball function	181
A.2	SDHCAL efficiency and multiplicity maps	181
A.3	Observed resolution	190
	B Boosted decision tree training details	191
B.1	Training parameters	191
B.2	Correlation Matrices	191
	Bibliography	193

Introduction

“Begin at the beginning,” the King said gravely, “and go on till you come to the end: then stop.”

— Lewis Carroll, *Alice in Wonderland*

In the last century, physics has made an enormous progress in understanding the fundamental laws of nature. In terms of particle physics, a model has been developed, known as the Standard Model (SM) of particle physics, which describes the fundamental structure of matter and its interactions. It states that all matter surrounding us can be built from twelve particles of spin $1/2$ and their anti-particles. The interactions between these particles can be explained by the existence of four fundamental forces mediated by spin 1 quanta.

Until now almost all the experimental observations are well predicted by the SM. One of the main successes is the discovery at the Large Hadron Collider (LHC) by ATLAS and CMS experiments of the first scalar boson compatible with the Higgs boson. This particle has been hunted during the last 30 years by various experiments. It is believed to be responsible of the mass of the most fundamental particles. Yet it doesn't bring any explanation on the value of the masses, the number of families, neutrinos masses, etc.

A precise measurement of the properties of the newly discovered boson constitutes the main goal of the future experiments in particle physics. Indeed, it is essential to measure its coupling to vector bosons and fermions. These measurements will constitute the validation of the BEH (Brout-Englert-Higgs) mechanism in SM of particle physics, and will open a window to new physics if any deviation is found.

The actual running collider is the LHC. It produces proton-proton collisions and constitutes the most powerful (and complex) machine ever built. However, the protons are composite particles: the type, the energy and the spin state of colliding particles is not well known. This limits the precision capability of the LHC. In addition, the reconstruction of many physics processes suffers from a large QCD background.

While the LHC is an excellent tool for discovering new particles, its final accuracy is limited by the usage of protons as colliding particles. There is a worldwide consensus, that the next machine after the LHC will be a linear electron-positron collider. Since leptons are elementary particles providing an initial state defined in terms of nature, 4-momentum and spin, the environment is much cleaner than in hadron colliders, the conservation of the energy and the momentum leads to a better analysis of decay products and a proper reconstruction of the visible particles.

Today, the most advanced proposal for such an instrument is the International Linear Collider(ILC). It will extend the discoveries made by the LHC and provide a wealth of precise measurements that are essential to deepen our understanding of the infinitesimal world.

The high precision to be reached at ILC imposes stringent requirements on the detector. A typical ILC event will feature a multi-jet final state topology. Many physics channels have to be reconstructed with unconstrained kinematics. In this case a high resolution calorimetric system is required. Thus it is necessary to obtain the complete topology of each event. This requires a new approach which exploits the synergy of hardware and software developments to the level of individual particle reconstruction and identification. The Particle Flow Approach (PFA) is believed to address these requirements. It consists in reconstructing every visible particle in an event, using at best each of the sub-detectors. This new approach requires detectors with high efficiency and reliability, maximum hermiticity, and a highly segmented calorimeter allowing particle shower separation.

CALICE (Calorimetry for Linear Collider with Electrons) is a collaboration formed to take care of the R&D studies needed to build such calorimeters. Several prototypes, using different approaches to calorimetry respecting the constraint imposed by the PFA paradigm in term of the granularity and energy resolution, have been built. One of these concepts is the digital hadron calorimeter, proposed for the TESLA TDR. In such a calorimeter each readout channel delivers only one bit of information. This technique permits to increase the number of channels increasing thereby the granularity. The energy estimation is simply done by counting the number of fired cells. The data volume is reasonable for the electronic readout system. However, the simple counting of hits suffers from a saturation effect at high energy caused by the finite cell size.

To solve this problem the one bit readout can be replaced by a 2-bit readout leading to 3 levels of energy deposits in a cell, the so-called Semi-digital Hadron calorimeter (SDHCAL). In this approach, the additional information permits to use a weighted sum of fired cells to correct the saturation effect at high energy to help compensating the calorimeter and hence to improve the energy resolution. This calorimeter option constitutes the core of the technical part of this thesis.

Different beam test campaigns with different beam conditions at CERN SPS and PS beam facilities were engaged in 2012, in order to measure the response of the SDHCAL to different types of particles. An algorithm of data reconstruction was developed to translate the raw data coming from the acquisition system and then reconstruct the event thanks to a time clustering method, which groups the cells coming from a physical event. This algorithm developed during this thesis, is detailed in the Chapter 4, which introduces also the SDHCAL prototype setup.

In the Chapter 5 the response to muons from either beam or cosmic rays is presented. The physics of the detector is then described, argued with simulation studies. The tracking capability of the SDHCAL was fully exploited to extract the detector performances. The reconstruction of muons allows the determination of a precise model of the detector behaviour. These measurements are key parameters for the tuning of an accurate detector simulation. The latter constitutes the main subject of Chapter 6 where a new digitisation method is presented: a plug-in module that reproduces the detector and the electronic responses, which must be added on top of the shower simulation.

The main purpose of a hadronic calorimeter is the measurement of the hadronic shower energy. The response of SDHCAL prototype to pions is then studied and summarised in the Chapter 7. The high granularity of the SDHCAL allows the use of innovative particle identification techniques such as the fractal dimension. After the selection of the hadronic interaction, the energy response in term of linearity and the energy resolution is studied for the pure digital and semi-digital modes. The information acquired by the muon reconstruction is also used to improve the calorimeter response to

the pions correcting the non-uniform response of the sensors. The linearity as well as the resolution of the calorimeter are derived before and after the correction.

Besides the SDHCAL prototype study, new kind of resistive plate chambers running in high rate conditions is presented in Chapter 8. This device uses a new resistive medium based on semi-conductive glass, which allows a better charge recovery in the gas medium. The high rate resistive plate chambers are proposed for the upgrade of the muon spectrometry in LHC detectors.

One of the important programs at the ILC is the measurement of the Higgs couplings to confirm the BEH mechanism in which the strength of the Higgs coupling has a linear dependence on the particle masses. Thus it is important to provide a model independent tagging of the Higgs boson, without any assumption on its decay process. This will be possible at the ILC where the main Higgs production is through the Higgsstrahlung process. Thanks to the clean environment and the well defined initial state, the Higgs boson can be tagged by reconstructing the decay of the associated Z boson.

Previous studies focuses on the channels where the Z boson decays into leptons, either $Z \rightarrow e^+e^-$ or $Z \rightarrow \mu^+\mu^-$. However, these channels suffer from their low branching ratio, and the main decay mode ($Z \rightarrow q\bar{q}$) has been kept unused until now.

This thesis focuses on the Higgs tagging through the hadronic Z decay as detailed in Chapter 9. First, a jet reconstruction method is given which has been optimised for the Higgsstrahlung process. Then a multivariate technique is applied to reduce the main backgrounds. The model independence is then checked, followed by the measurement of the Higgsstrahlung process cross section and its corresponding errors. The sensitivity of the analysis to the beam polarisations is also explored.

Part I

Theoretical and experimental background

Chapter 1

The standard model of particle physics

It doesn't matter how beautiful your theory is, it doesn't matter how smart you are. If it doesn't agree with experiment, it's wrong.

— Richard P. Feynman

1.1	The standard model of particle physics	8
1.1.1	Generalities	8
1.1.2	Electroweak theory	9
1.2	The BEH mechanism: the origin of mass	12
1.2.1	Example of spontaneous $U(1)$ symmetry breaking	12
1.2.2	The case of $U(1)$ local symmetry	14
1.2.3	Electroweak symmetry breaking	15
1.2.4	Higgs couplings to gauge bosons	16
1.2.5	Generation of fermions masses	17
1.3	Constraints on the Higgs boson mass	18
1.3.1	Theoretical bounds	18
1.3.2	Experimental bounds	19
1.4	Higgs boson discovery and properties	20
1.5	Higgs production in lepton colliders	22

The Standard Model (SM) of particle physics is the theory which successfully describes in a single framework the particles composing the matter and their interactions.

The SM of particle physics was born between 1960 and 1970 in the hands of S. L. Glashow[1], A. Salam [2] and S. Weinberg[3] as a theory of electroweak interactions, which unifies the electromagnetic and weak interactions in a single theory. In 1971 G't Hooft proved its renormalizability [4]. This model was shown to be a viable theory after the discovery of the neutral current in 1973 by *Gargamelle* experiments at CERN[5]. The discovery was then confirmed at Fermilab [6] few years latter. In 1973 the model was extended to the strong interaction and the hadronic sector by H. Frisch, M. Gell-Mann and H. Leutwyler [7] proving its completeness.

Since the rise of the SM, 40 years of experimental evidence has been accumulated becoming the reliable description of the electromagnetic, weak and strong interactions up to the investigated energies. One of its greatest successes was the detection at CERN in 2012 of Higgs boson [8, 9] predicted by the SM.

In this chapter, A brief introduction to the standard model of the strong and electroweak interactions including and mechanism of the electroweak symmetry breaking are presented. More detailed discussions can be found in [10–13].

1.1 The standard model of particle physics

1.1.1 Generalities

The dynamical evolution of particles is well described by the Quantum Field Theory introducing the notion of a field as a function of space-time coordinates x^μ . In this theory, by analogy to the classical mechanics, the dynamics of a given system is described by a scalar function called Lagrangian density \mathcal{L} defined by

$$\mathcal{L}(\phi, \partial_\mu \phi) \quad \text{with} \quad \partial_\mu \phi = \frac{\partial \phi}{\partial x^\mu} \quad (1.1)$$

which is a function depending on the fields ϕ and their first derivatives $\partial_\mu \phi$. The dynamical evolution is obtained by minimising the action $S = \int d^4x \mathcal{L}(\phi, \partial_\mu \phi)$, leading to the equivalent of the classical Euler-Lagrange equation. The appropriate Lagrangian density is an axiomatic statement of the quantum field theory. It is formed in the way that the desired field equations are reproduced.

On the other hand, the Emmy Noether's theorem demonstrates that the invariance of the Lagrangian of a given dynamic system, under a certain transformation, induces the existence of a conserved physical quantity. These transformations global and belong to symmetry groups, such as $\mathcal{U}(1)$ or $\mathcal{SU}(2)$ etc. Another important type of symmetries are the local ones, which introduce the notion of the gauge transformation. The invariance under these gauge symmetries is the origin of the introduction of boson fields associated to the fundamental interactions.

The symmetry group of the standard model is $\mathcal{SU}_L(2) \otimes \mathcal{U}_Y(1) \otimes \mathcal{SU}_C(3)$:

- The group $\mathcal{SU}(2)_L$ is the group under which the charge and the weak isospin are conserved¹. It stems from two observations: the reactions of type $e^- + \bar{\nu}_e \rightarrow e^- + \bar{\nu}_e$ leads to put the electron and its neutrino in doublet

$$L = \begin{pmatrix} \nu_e \\ e^- \end{pmatrix}_L \quad (1.2)$$

The quarks also form a doublets

$$Q = \begin{pmatrix} u \\ d \end{pmatrix}_L \quad (1.3)$$

The right handed leptons (electrons, muons, taus) and quarks are singlets under the group. The leptons do not interact strongly, neutrinos do not interact electromagnetically. Furthermore, they interact only via V-A type coupling[14] which occurs only with the left handed component. Thus, the right handed neutrinos (and the right handed anti-neutrinos) are not introduced in the standard model. The generators of $\mathcal{SU}(2)_L$ are the Pauli matrices associated to the

¹The group $\mathcal{SU}(2)$ is the universal covering group of $\mathcal{SO}(3)$ (the 3D rotations group).

gauge field $\mathbf{W}_\mu = (W_\mu^1, W_\mu^2, W_\mu^3)$. The components *up* and *down* of the fermion doublets are the eigenvectors of the $SU(2)_L$ and their eigenvalues, T^3 are respectively $1/2$ and $-1/2$. The singlets (right fermions) have an eigenvalue equal to zero.

- $U(1)_Y$ is related to the weak hypercharge, it was introduced in order to unify the electromagnetic and weak interactions. The associated charge is the hypercharge (Y). The electric charge has to be expressed by the isospin charge and weak hypercharge. Glashow proposed[1] in 1961 the relation $Q = T^3 + Y/2$ which is a generalisation of the Gell-Mann-Nishijima scheme formulated initially for the strong interaction. The associated quantum numbers, Q , T^3 and Y to each fermion of the standard model is summarized in the 1.1.
- $SU(3)_C$ describes the strong interaction. This group generates 8 bosons, the *gluons*, which mediate the strong interaction. The associated charge of this group is the colour, which can take 3 values *blue green red*. In contrast with the electric charge, the colour charge is not observable. Only the colour singlets (the *baryons* composed of 3 quarks and *mesons* composed by quark and anti-quark) are observables. This fact reflects the quarks confinement.

	I	II	III	T^3	Y	Q
Leptons	$\begin{pmatrix} \nu_e \\ e \end{pmatrix}_L$	$\begin{pmatrix} \nu_\mu \\ \mu \end{pmatrix}_L$	$\begin{pmatrix} \nu_\tau \\ \tau \end{pmatrix}_L$	$\begin{pmatrix} +1/2 \\ -1/2 \end{pmatrix}$	$\begin{pmatrix} -1 \\ -1 \end{pmatrix}$	$\begin{pmatrix} 0 \\ -1 \end{pmatrix}$
	e_R	μ_R	τ_R	0	-2	-1
	Quarks	$\begin{pmatrix} u \\ d \end{pmatrix}_L$	$\begin{pmatrix} c \\ s \end{pmatrix}_L$	$\begin{pmatrix} t \\ b \end{pmatrix}_L$	$\begin{pmatrix} +1/2 \\ -1/2 \end{pmatrix}$	$\begin{pmatrix} +1/3 \\ +1/3 \end{pmatrix}$
	u_R	c_R	t_R	0	+4/3	+2/3
	d_R	s_R	b_R	0	-2/3	-1/3

TABLE 1.1: Classification of fermions in the standard model showing their respective quantum number (weak isospin T^3 , hypercharge Y and electric charge Q).

Interaction	Boson	Charge (e)	Mass (GeV/c^2)
Electromagnetic	γ	0	0
Weak	W^\pm	± 1	80.398 ± 0.025
	Z^0	0	91.1876 ± 0.0021
Strong	8 <i>gluons</i>	0	0

TABLE 1.2: Gauge bosons in standard model

1.1.2 Electroweak theory

The Lagrangian of the electroweak theory (without symmetry breaking) can be decomposed in four terms

$$\mathcal{L}_{EW}^{sym} = \mathcal{L}_{gauge}^{kin} + \mathcal{L}_{fermions}^{kin} + \mathcal{L}_{gauge}^{int} + \mathcal{L}_{fermions}^{int} \quad (1.4)$$

The first term is the kinetic part of the gauge bosons, and has the form

$$\mathcal{L}_{gauge}^{kin} = -\frac{1}{4}F_{\mu\nu}F^{\mu\nu} - \frac{1}{4}B_{\mu\nu}B^{\mu\nu} \quad (1.5)$$

where $F_{\mu\nu}$ and $B_{\mu\nu}$ are respectively the energy-momentum tensors associated to the $SU(2)_L$ and $U(1)_Y$ groups:

$$F_{\mu\nu} = \partial_\mu W_\nu - \partial_\nu W_\mu + gW_\mu W_\nu \quad (1.6)$$

$$B_{\mu\nu} = \partial_\mu B_\nu - \partial_\nu B_\mu \quad (1.7)$$

The second term represents the kinetic part of fermions which can be written as

$$\mathcal{L}_{\text{fermions}}^{\text{kin}} = i\bar{L}\gamma^\mu\partial_\mu L + i\bar{U}_R\gamma^\mu\partial_\mu U_R + i\bar{D}_R\gamma^\mu\partial_\mu D_R \quad (1.8)$$

where $L = \begin{pmatrix} U \\ D \end{pmatrix}_L$, U_R and D_R are the associated field to the doublets and singlets of the weak isospin fermions.

The two last terms, $\mathcal{L}_{\text{gauge}}^{\text{int}}$ and $\mathcal{L}_{\text{fermions}}^{\text{int}}$ describe the interaction occurring between bosons and between bosons and fermions. They emerge naturally when the gauge invariance of the Lagrangian density under local transformation of the electroweak symmetry is imposed. This is done by replacing the partial derivatives by the covariant ones :

$$\partial_\mu \rightarrow D_{\mu,L} = \partial_\mu - ig\frac{1}{2}W_\mu \cdot \vec{\tau} - ig'\frac{Y_L}{2}B_\mu \quad \text{for left-handed fermions} \quad (1.9)$$

$$\partial_\mu \rightarrow D_{\mu,R} = \partial_\mu - ig'\frac{Y_R}{2}B_\mu \quad \text{for right-handed fermions} \quad (1.10)$$

g and g' here are the coupling constants of the $SU(2)_L$ and $U(1)_Y$ groups. The interaction term of fermions with the gauge field can be then written:

$$\begin{aligned} \mathcal{L}_{\text{fermion}}^{\text{int}} = & \bar{L}\gamma^\mu \left(g\frac{\tau_a}{2}W_\mu^a g'\frac{Y_L}{2}B_\mu \right) L + \\ & + \bar{U}_R\gamma^\mu ig'\frac{Y_R}{2}B_\mu U_R \\ & + \bar{D}_R\gamma^\mu ig'\frac{Y_R}{2}B_\mu D_R \end{aligned} \quad (1.11)$$

By decomposing $\tau_a W_\mu^a$ ($a = 1, 2, 3$) as follow

$$\tau_a W_\mu^a = \begin{pmatrix} W^3 & W^1 - iW^2 \\ W^1 + iW^2 & -W^3 \end{pmatrix} = \begin{pmatrix} 0 & \sqrt{2}W^- \\ \sqrt{2}W^+ & 0 \end{pmatrix} + 2I_3 W^3 \quad (1.12)$$

The Lagrangian density then becomes

$$\begin{aligned} \mathcal{L}_{\text{fermion}}^{\text{int}} = & \bar{U}_L\gamma^\mu \frac{g}{\sqrt{2}}W^- D_L + \bar{D}_L\gamma^\mu \frac{g}{\sqrt{2}}W^+ U_L \\ & + \bar{L}\gamma^\mu gI_3 W^3 L + \bar{L}\gamma^\mu g'\frac{Y_L}{2}B_\mu L \\ & + \bar{U}_R\gamma^\mu g'\frac{Y_R}{2}B_\mu U_R + \bar{D}_R\gamma^\mu g'\frac{Y_R}{2}B_\mu D_R \end{aligned} \quad (1.13)$$

The first two terms lead to the creation of charged current which can interact only with left-handed components of fermions. The mediation is done by the W^+ and W^- bosons and describes interactions such as $W \rightarrow e\nu$ or $W \rightarrow ud$. The charged current Lagrangian density, \mathcal{L}_{cc} , can be then written as

$$\mathcal{L}_{cc} = \frac{g}{\sqrt{2}} \left(\bar{U}_L\gamma^\mu W^- D_L + \bar{D}_L\gamma^\mu W^+ U_L \right) \quad (1.14)$$

By introducing the operator $(1 - \gamma^5)$ which makes a projection of fermionic field on its right chirality state. This leads to

$$\mathcal{L}_{cc} = \frac{g}{2\sqrt{2}} \left(\bar{U} \gamma^\mu (1 - \gamma^5) W^- D + \bar{D} \gamma^\mu (1 - \gamma^5) W^+ U \right) \quad (1.15)$$

The left terms in 9.9 describe two neutral currents mediated by B_μ and W_μ^3 fields. The expression of their Lagrangian density is

$$\begin{aligned} \mathcal{L}_{nc} = & \bar{L} \gamma^\mu g I_3 W^3 L + \bar{L} \gamma^\mu g' \frac{Y_L}{2} B_\mu L \\ & + \bar{U}_R \gamma^\mu g' \frac{Y_R}{2} B_\mu U_R + \bar{D}_R \gamma^\mu g' \frac{Y_R}{2} \end{aligned} \quad (1.16)$$

The physical fields of photon and Z boson, respectively denoted by A_μ and Z_μ are obtained by a linear combination of the non charged gauge fields B_μ and W_μ^3 and given by

$$\begin{aligned} A_\mu = & \sin \theta_W W_\mu^3 + \cos \theta_W B_\mu, \\ Z_\mu = & \cos \theta_W W_\mu^3 - \sin \theta_W B_\mu \end{aligned} \quad (1.17)$$

where θ_W is called the Winberg angle.

The part of the Lagrangian density describing the interaction of fermions with electromagnetic field is expressed using the relations $Y_L = 2(Q - I_3)$ and $Y_R = 2Q$:

$$\begin{aligned} \mathcal{L}_{em} = & A_\mu [\bar{L} \gamma^\mu g I_3 \sin \theta_W L + \bar{L} \gamma^\mu g' (Q - I_3) \cos \theta_W L + \\ & \bar{U}_R \gamma^\mu g' Q \cos \theta_W U_R + \bar{D}_R \gamma^\mu g' Q \cos \theta_W D_R] \end{aligned} \quad (1.18)$$

hence

$$\begin{aligned} \mathcal{L}_{em} = & A_\mu [\bar{L} \gamma^\mu (g I_3 \sin \theta_W + g' Q \cos \theta_W + g' I_3 \cos \theta_W) L + \\ & \bar{D}_R (\gamma^\mu g' Q \cos \theta_W) D_R] \end{aligned} \quad (1.19)$$

The electromagnetic field has the same impact on the right and left chirality states of fermion, the previous two terms should then be equals. In addition, the coupling should correspond to the electric charge of electron, e . Then, the relations between the coupling constants are obtained

$$g \sin \theta_W = g' \cos \theta_W = e \quad (1.20)$$

$$\sin \theta_W = \frac{g'}{\sqrt{g'^2 + g^2}} \quad (1.21)$$

$$\cos \theta_W = \frac{g}{\sqrt{g'^2 + g^2}} \quad (1.22)$$

Therefore, the Lagrangian density of the electromagnetic part is expressed noting either left or right fermionic field by f which leads to

$$\mathcal{L}_{em} = \frac{gg'}{\sqrt{g'^2 + g^2}} \bar{f} \gamma^\mu Q f A_\mu \quad (1.23)$$

Using the equations 1.16, 1.17 and the Gell-Mann-Nishijima and taking into account the relations in 1.22 the Z boson contribution to the Lagrangian density \mathcal{L}_{nc} becomes:

$$\mathcal{L}_Z = \frac{\sqrt{g'^2 + g^2}}{2} [\bar{f} \gamma^\mu (C_\nu - C_a \gamma^5) f] Z_\mu \quad (1.24)$$

where $C_\nu = (I_3 - 2Q \sin^2 \theta_W)$ and $C_a = I_3$. The coupling of the Z boson to fermions is a mixing between vector ($C_\nu \gamma^\mu$) and axial ($C_a \gamma^\mu \gamma^5$) couplings. To summarize, the physical fields of the electroweak sector are

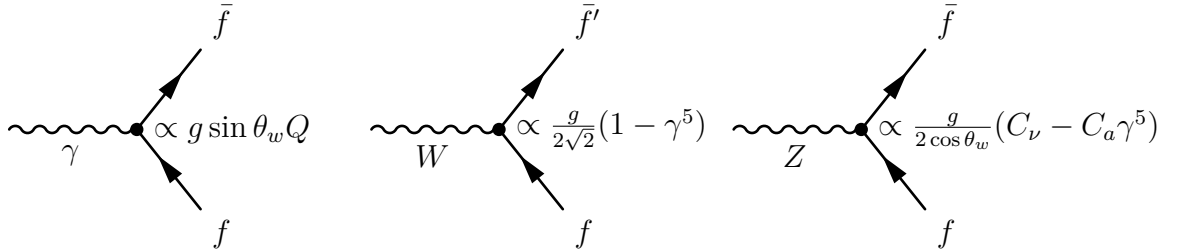
$$W_\mu^+ = \frac{W_\mu^1 + iW_\mu^2}{\sqrt{2}} \quad (1.25)$$

$$W_\mu^- = \frac{W_\mu^1 - iW_\mu^2}{\sqrt{2}} \quad (1.26)$$

$$Z_\mu = W_\mu^3 \cos \theta_W - B_\mu \cos \theta_W \quad (1.27)$$

$$A_\mu = W_\mu^3 \cos \theta_W + B_\mu \cos \theta_W \quad (1.28)$$

they give rise to the interaction between bosons and fermions depicted by the following Feynman diagrams:



1.2 The BEH mechanism: the origin of mass

The electroweak theory, constructed previously, predicts the existence of tree mass-less vector bosons (W^\pm and Z). The experiments have proven that these vector bosons do have masses. The Brout-Englert-Higgs (B.E.H) mechanism [15, 16] was introduced in the early sixties to solve this problem through a spontaneous breaking of the electroweak symmetry.

1.2.1 Example of spontaneous $\mathcal{U}(1)$ symmetry breaking

Even the electroweak symmetry is local, it can be shown, as an example, the consequences of a spontaneous symmetry breaking of the global symmetry of a Lagrangian density, \mathcal{L} , describing the evolution of massive scalar charged boson

$$\mathcal{L} = T(\phi) - V(\phi) = (\partial_\mu \phi)^\dagger (\partial^\mu \phi) - \mu \phi^\dagger \phi - \lambda (\phi^\dagger \phi)^2 \quad (1.29)$$

where

$$\phi = \frac{1}{\sqrt{2}} (\phi_1 + i\phi_2) \quad (1.30)$$

Note that \mathcal{L} is invariant under the *global* $\mathcal{U}(1)$ transformation²:

$$\phi \rightarrow e^{i\alpha} \phi \quad (1.31)$$

The potential $V(\phi)$ expressed in term of the real fields ϕ_1 and ϕ_2 takes the form:

$$V(\phi) = \frac{\mu^2}{2}(\phi_1^2 + \phi_2^2) + \frac{\lambda}{4}(\phi_1^2 + \phi_2^2)^2 \quad (1.32)$$

The terms in ϕ_i^2 represents the self-interaction of the field via the non-null coupling $\lambda > 0$. At this stage, two situations have to be considered:

- Case $\mu^2 \geq 0$, the minimum of the potential $V(\phi)$ is reached by the trivial constant field $\phi = 0$. The ground state is unique and respect the $\mathcal{U}(1)$ symmetry. The corresponding Lagrangian density in QED theory describes a particle spectrum with 2 bosons of spin 0 having the same mass μ .
- Case $\mu^2 < 0$, the potential $V(\phi)$ for $2|\phi|^2 = v^2 = \frac{-\mu^2}{\lambda}$ has an infinite minimums laying in a circle in the imaginary plane of radius $v/\sqrt{2}$ as depicted in Figure 1.1. In that case no direction is preferred, so the symmetry gets spontaneously broken. The perturbative development of ϕ around potential minimum gives rise to a spin 0 massless particle, known as the Goldstone boson[17].

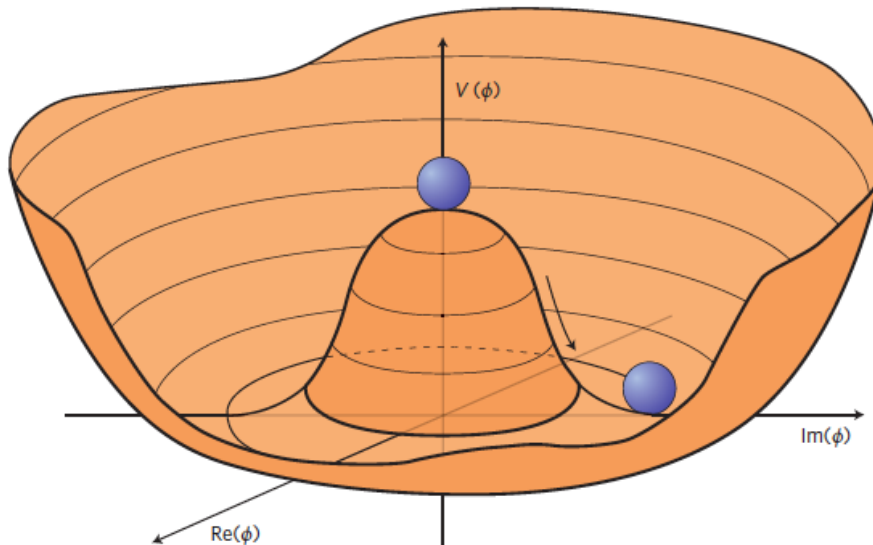


FIGURE 1.1: Illustration of the potential $V(\phi)$ in the case that $\mu^2 < 0$. In this case the minimum is at $|\phi|^2 = -\mu^2/(2\lambda)$. The chose any of the possible point break spontaneously the $\mathcal{U}(1)$ symmetry.

²In the case where $\lambda = 0$ and $\mu^2 > 0$ correspond the Klein-Gordon Lagrangian density, which describes a massive spin 0 particles of mass μ .

1.2.2 The case of $\mathcal{U}(1)$ local symmetry

Let consider the local gauge symmetry $\mathcal{U}(1)$ applied to a scalar field as follows

$$\phi \rightarrow e^{i\alpha(x)}\phi \quad (1.33)$$

The invariance of the Lagrangian density is provided by the covariant derivative defined by

$$D_\mu = \partial_\mu - ieA_\mu \quad (1.34)$$

which introduces the gauge field A_μ . Here the electric charge, e , is conserved. The gauge invariant Lagrangian density is

$$\mathcal{L} = (\partial^\mu - ieA^\mu)\phi^\dagger(\partial_\mu - ieA_\mu)\phi - \mu\phi^\dagger\phi - \lambda(\phi^\dagger\phi)^2 - \frac{1}{4}F^{\mu\nu}F_{\mu\nu} \quad (1.35)$$

The term $F^{\mu\nu}F_{\mu\nu}$ allows the propagation of A_μ . The case of $\mu^2 < 0$ is already described above, except for the term in ϕ_i^4 . By developing the complex field ϕ around a chosen minimum (for example $\phi_1 = v$ and $\phi_2 = 0$) as follows

$$\phi(x) = \frac{1}{\sqrt{2}}[v + h(x) + i\xi(x)], \quad (1.36)$$

where x is the space-time coordinate of the field, the Lagrangian density becomes:

$$\begin{aligned} \mathcal{L}' = & \frac{1}{2}(\partial_\mu\xi)^2 + \frac{1}{2}(\partial_\mu h)^2 - v^2\lambda h^2 + \frac{1}{2}e^2v^2A_\mu A^\mu - \\ & evA_\mu\partial^\mu\xi - \mathcal{F}^{\mu\nu}\mathcal{F}_{\mu\nu} + \mathcal{L}_{\text{interaction}} \end{aligned} \quad (1.37)$$

The corresponding particle spectrum is composed by a Goldstone boson ξ (massless spin 0 particle), a massive vector boson A_μ of mass $m_A = ev$ and a spin 0 massive particle h of mass $m_h = v\sqrt{2\lambda}$. The latter is what we call the *Higgs boson*.

It is possible to eliminate the field ξ from the equations by choosing the unitary gauge transformation $U(x) = e^{-i\xi(x)}$ leading to

$$\begin{aligned} \phi(x) & \rightarrow \frac{v + h(x)}{\sqrt{2}} \\ A_\mu & \rightarrow A_\mu + \frac{1}{ev}\xi(x) \end{aligned} \quad (1.38)$$

$$(1.39)$$

The Lagrangian is then expressed by :

$$\begin{aligned} \mathcal{L}'' = & \frac{1}{2}(\partial_\mu h)^2 - \frac{1}{4}\mathcal{F}^{\mu\nu}\mathcal{F}_{\mu\nu} \\ & - v^2\lambda h^2 + \frac{1}{2}e^2v^2A_\mu A^\mu - \\ & - \lambda v\lambda h^3 - \frac{1}{4}h^4 \\ & + ve^2A_\mu A^\mu h + \frac{1}{2}e^2A_\mu A^\mu h^2 \end{aligned} \quad (1.40)$$

The first line gives the propagation terms of the Higgs boson and the vector field and the second line indicates their respective mass terms. The third line provides the trilinear and quadrilinear self-interaction terms of the Higgs boson. The fourth is related to the interactions between Higgs boson and vector field A_μ .

1.2.3 Electroweak symmetry breaking

The scalar sector of the standard model is composed by a doublet of complex scalar field with weak hypercharge Y equal to $+1$:

$$\phi = \begin{pmatrix} \phi^+ \\ \phi^0 \end{pmatrix} \quad (1.41)$$

and the potential term has the form $V(\phi) = \mu^2 \phi^\dagger \phi + \lambda \phi^\dagger \phi$, which has a minimum for the values defined by

$$(\phi^\dagger \phi)_0 = \frac{v^2}{2} \text{ with } v^2 = -\frac{\mu^2}{\lambda} \quad (1.42)$$

Following the same scheme as in the previous section, the potential $V(\phi)$ is added to the Lagrangian density of the electroweak theory expressed in Equation A.1

$$\mathcal{L}_{EW} = \mathcal{L}_{EW}^{sym} - V(\phi) \quad (1.43)$$

The vacuum choice

$$\phi_0 = \langle 0 | \phi | 0 \rangle = \begin{pmatrix} 0 \\ \frac{v}{\sqrt{2}} \end{pmatrix} \quad (1.44)$$

breaks both $SU(2)_L$ and $U(1)_Y$ symmetries. However, the choice of $Y = 1$ provides a null charge to the complex field ϕ^0 , hence the relation $Q\phi^0 = 0$: the vacuum respects the $U(1)_{em}$ symmetry maintaining a null mass to the photon, while W^\pm and Z bosons gain a mass. The Higgs field, h appears, when ϕ is perturbatively developed around the vacuum value:

$$\phi = \frac{1}{\sqrt{2}} e^{-\frac{i}{2} \tau^i \xi^i} \begin{pmatrix} 0 \\ v + h(x) \end{pmatrix} \quad (1.45)$$

The three Goldstone bosons $\xi^i, i = 1, 2, 3$ disappear from the equations by applying the unitary gauge $U = e^{-\frac{i}{2} \tau^i \xi^i}$ transformation. The massive gauge bosons are then obtained by expanding the kinetic term of the field ϕ evaluated at $\phi = \phi_0$:

$$\begin{aligned} (D_\mu \phi)^\dagger (D^\mu \phi)|_{\phi_0} &= \frac{1}{4} \left| \begin{pmatrix} \partial_\mu + i\frac{g}{2}W_\mu^3 + i\frac{g'}{2}B_\mu & i\frac{g}{2}(W_\mu^1 - iW_\mu^2) \\ i\frac{g}{2}(W_\mu^- + iW_\mu^2) & \partial_\mu - i\frac{g}{2}W_\mu^3 + i\frac{g'}{2}B_\mu \end{pmatrix} \begin{pmatrix} 0 \\ v + h(x) \end{pmatrix} \right|^2 \\ &\vdots \\ &= \frac{g^2}{4} (v+h)^2 W_\mu^- W^{\mu+} + \frac{1}{2} \partial_\mu h \partial^\mu h + \frac{1}{8} + (v+h)^2 \frac{g^2}{\cos^2 \theta_W} Z_\mu Z^\mu \end{aligned} \quad (1.46)$$

Here the definitions of the W^\pm from $W^{1,2}$ and Z_μ as function of W_μ^3 and B_μ are used. Now, using the expression

$$\phi^\dagger \phi = \frac{1}{2} (v+h)^2 \quad (1.47)$$

in the potential $V(\phi)$ introduced previously in Equation 1.32, the Lagrangian density of the introduced field ϕ reduces to:

$$\begin{aligned} \mathcal{L}_\phi = & \frac{g^2 v^2}{4} W_\mu^- W^{\mu+} + \frac{1}{8} \frac{g^2 v^2}{\cos^2 \theta_W} Z_\mu Z^\mu \\ & + \frac{1}{2} (\partial_\mu h \partial^\mu h + 2\mu^2 h^2) \\ & + \frac{g^2 v}{2} h W_\mu^- W^{\mu+} + \frac{g^2}{4} h^2 W_\mu^- W^{\mu+} + \frac{1}{4} \frac{g^2 v}{\cos^2 \theta_W} h Z_\mu Z^\mu + \frac{1}{8} \frac{g^2}{\cos^2 \theta_W} h^2 Z_\mu Z^\mu \\ & + \frac{\mu^2}{v} h^3 + \frac{\mu^2}{4v^2} h^4 \end{aligned} \quad (1.48)$$

The first and the second terms give the mass to the charged W^\pm and Z bosons respectively:

$$\begin{aligned} M_W &= \frac{1}{2} v g \\ M_Z &= \frac{1}{\sqrt{2}} \frac{v g}{\cos \theta_W} \end{aligned} \quad (1.49)$$

As expected, there is no $A_\mu A^\mu$ term, meaning that the photon is indeed massless.

Three degrees of freedom of the Higgs boson doublet are used to give mass to the vector bosons, while the fourth shows up as a new particle with zero charge, zero spin and mass related to the Higgs potential parameters by

$$M_H = \sqrt{2} \mu = \sqrt{2} \lambda v \quad (1.50)$$

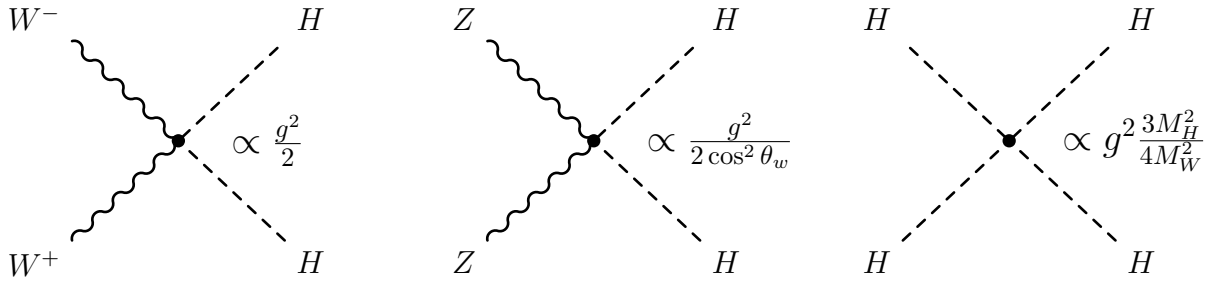
1.2.4 Higgs couplings to gauge bosons

The line 3 of the Lagrangian density in Equation 1.48 shows that the Higgs boson couples to the massive gauge field via trilinear and quadrilinear terms.

The trilinear terms give rise to 3 Feynman diagrams with the following coupling factors:

$$\begin{aligned} & \propto \frac{2M_W^2}{v} \quad \propto \frac{2M_Z^2}{v} \quad \propto g \frac{3M_H^2}{2M_W^2} \end{aligned}$$

The quadrilinear are the remaining terms in Equation 1.48, they represents the coupling of the Higgs boson to gauge boson W and Z , and the self-coupling as well. This can be seen in the following diagrams:



1.2.5 Generation of fermions masses

At the current stage of the theory built previously, only the gauge bosons W and Z have acquired a mass, while the fermions remain massless³. A specific coupling between fermions and Higgs field must be introduced in order to generate the fermion masses. This coupling is known as the *Yukawa* coupling having the $y\bar{\psi}\phi\psi$ form, it is invariant under the local gauge group $SU(2)_L \otimes U(1)_Y$. The Lagrangian density corresponding to this coupling is expressed for leptons as:

$$\mathcal{L}_{\text{Yukawa}}^{\text{lep}} = -y \left((\bar{U}, \bar{D})_L \begin{pmatrix} \phi^+ \\ \phi^0 \end{pmatrix} D_R + h.c \right) \quad (1.51)$$

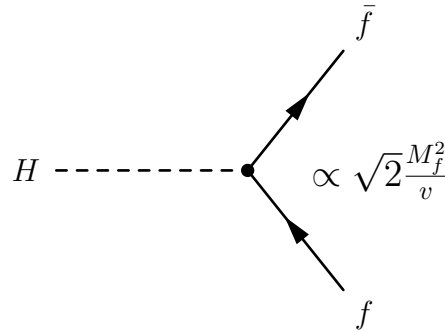
This expression at the minimum of the Higgs potential which is $\phi = \frac{1}{\sqrt{2}} \begin{pmatrix} 0 \\ v+h \end{pmatrix}$ is:

$$\mathcal{L}_{\text{Yukawa}}^{\text{lep}} = -\frac{y}{\sqrt{2}}v(\bar{D}_L D_R + \bar{D}_R D_L) - \frac{y}{\sqrt{2}}v(\bar{D}_L D_R + \bar{D}_R D_L)h, \quad (1.52)$$

which can be written by defining the coupling constant y such as $m_D = yv/\sqrt{2}$

$$\mathcal{L}_{\text{Yukawa}}^{\text{lep}} = -m_D \bar{D}D - \frac{m_D}{v} \bar{D}Dh \text{ with } D = D_R + D_L \quad (1.53)$$

The second term in $\mathcal{L}_{\text{Yukawa}}^{\text{lep}}$ corresponds to the Higgs boson interaction with fermions, with a coupling proportional to the fermion's mass. This can be depicted by the following diagram:



Thereby, the Higgs boson through the Yukawa coupling can generate the same mass for the *down* part of the weak isospin doublet and for its singlets, keeping massless the *up* part.

³The mechanism of gauge boson generation cannot generate mass to the fermions since the fermion fields do not appear in the covariant derivative D_μ .

Keeping in mind the Fermi theory⁴, the coupling constants can be written:

$$\frac{G_F}{\sqrt{2}} = \frac{g^2}{8M_W^2} : \text{ and } M_W = \frac{g}{2} \Rightarrow v = \left(\frac{1}{G_F\sqrt{2}} \right)^{\frac{1}{2}} \simeq 246 \text{ GeV} \quad (1.54)$$

The vacuum expectation of the Higgs field is then:

$$\langle 0|\phi^\dagger\phi|0\rangle = \frac{v^2}{2} \simeq (174 \text{ GeV})^2 \quad (1.55)$$

It sets the scale of the electroweak symmetry breaking.

1.3 Constraints on the Higgs boson mass

1.3.1 Theoretical bounds

Although the standard model does not predict the Higgs boson mass, it is however possible to constrain its value on the bases of some theoretical considerations. Upper bounds on the mass can be derived requiring the theory to be valid up to an energy scale Λ . While a lower bound follows from the requirements of vacuum stability. These bounds are briefly discussed in the following.

The study of the scattering of vector bosons[18] allows to put the upper bounds on the Higgs mass value. In absence of the Higgs, the amplitude of the scattering process, $VV \rightarrow VV$, in the limits where $M_H \gg M_W$ and M_Z , and $\sqrt{s} \gg M_H$ (where \sqrt{s} is the centre of mass energy of VV system) would violate unitarity at some centre-of-mass energy, indicating the limit up to which perturbation theory is applicable at most. Beyond this scale, new physics should appear. In the case of the existence of the Higgs boson, the scattering of vector bosons VV should be corrected in the leading order by the exchange of a Higgs boson restoring the unitarity of the scattering matrix. This leads to a constraint on the Higgs boson mass:

$$\frac{M_H^2}{8\pi v^2} < \frac{1}{2} \Rightarrow M_H \leq \frac{4\pi\sqrt{2}}{3G_F} \simeq (700 \text{ GeV})^2 \quad (1.56)$$

Further upper and lower mass bounds can also be obtained by studying the higher order contribution to the Higgs self-coupling. The quadratic coupling constant λ depends on the energy scale, $t = \ln(\Lambda/\Lambda_0)$ (⁵), and on the Yukawa coupling to the top quark ⁶. For a heavy Higgs mass, the corrections involving top quark loop can be neglected. The $\lambda(t)$ becomes then infinite for finite value of t , which defines a Landau pole. The position of the pole is pushed to high values where λ decreases, and become infinite for the $\lambda = 0$. In this case no interaction with scalar field occurs, defining the *triviality* of the theory[19]. Otherwise, the assumption of non-triviality constraints the theory to be valid in a finite scale Λ . Beyond this scale the new physics should appear to push the Landau pole to higher values. The non-triviality defines then an upper bound on the M_H .

⁴The first version of the weak interaction which interpreted as contact interaction characterized by Fermi coupling constant G_F

⁵Here, Λ is the energy at which λ is defined, and Λ_0 is defined such as $M_H = \sqrt{2\lambda(Q_0)}v$

⁶Only the contribution of top quark is taken into account, since the coupling to other fermions is negligible.

When the mass of Higgs boson is lighter, the contribution of the top quark allows negative values of λ . In this case, the potential is unbounded and shows no minimum. The requirement that λ remains positive such that the vacuum is stable puts a lower limit on λ and therefore on the Higgs boson mass.

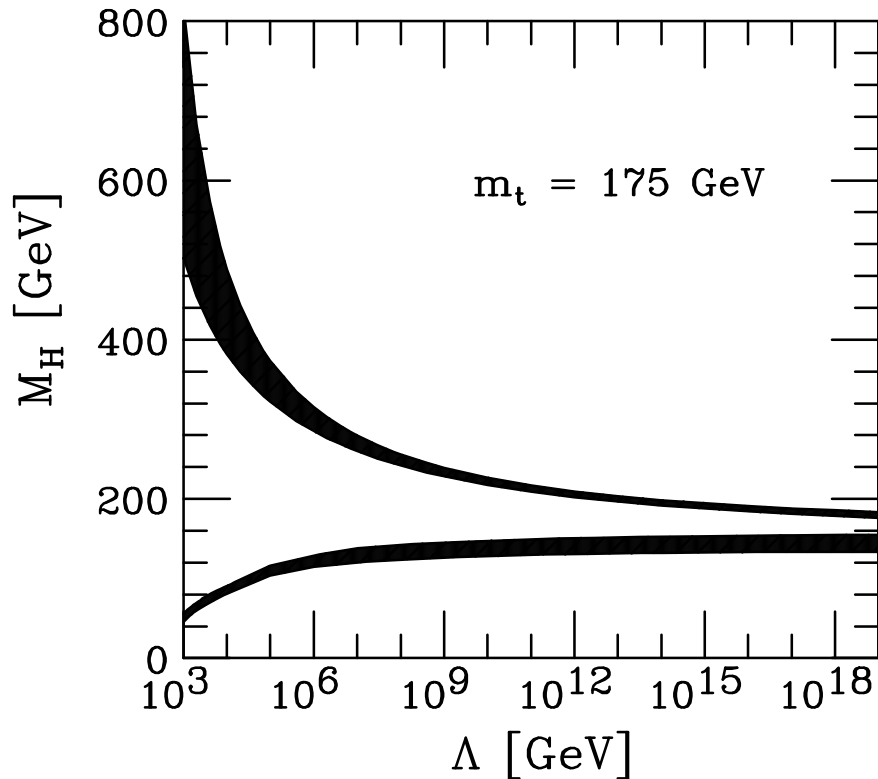


FIGURE 1.2: Upper and lower bounds on the Higgs mass from corrections to the Higgs self-coupling process. The upper bound is given by a small value of the quadratic coupling λ while the lower bound is given by allowing only positive values for λ . Figure from [20].

This is summarised in Figure 1.2 showing the evolution of the upper and lower bounds as a function of the cut-off scale Λ .

1.3.2 Experimental bounds

The direct search at LEP has produced a stringent limit from the combination of the four experiments (ALPEH, DELPHI, L3 and OPAL), they exclude the a SM Higgs boson up to a mass of 114.4 GeV at 95% confidence level[21]. Further limits have been determined indirectly within the framework of the SM[22].

Other observables such as the mass of the quarks and leptons, coupling constants and the Weinberg angle ($M_t, M_W, \sin^2 \theta_W$) have been measured with high precision at LEP, SLD and Tevatron (particularly for the discovery and measurement of the top quark mass [23]). The relation between the observables are subject to high order corrections. Some of these correction involve Higgs boson loops,

and therefore are sensitive to the Higgs boson mass. In order to determine the Higgs boson mass, all the SM parameters are fitted simultaneously to the observables. In other hand, the χ^2 is calculated between the experimental measurements and theoretical predictions of the SM observables. The Higgs mass is left as free parameter. Figure 1.3 shows the deviation of the χ^2 as function of the Higgs boson mass. The M_H fit favours a light Higgs boson.

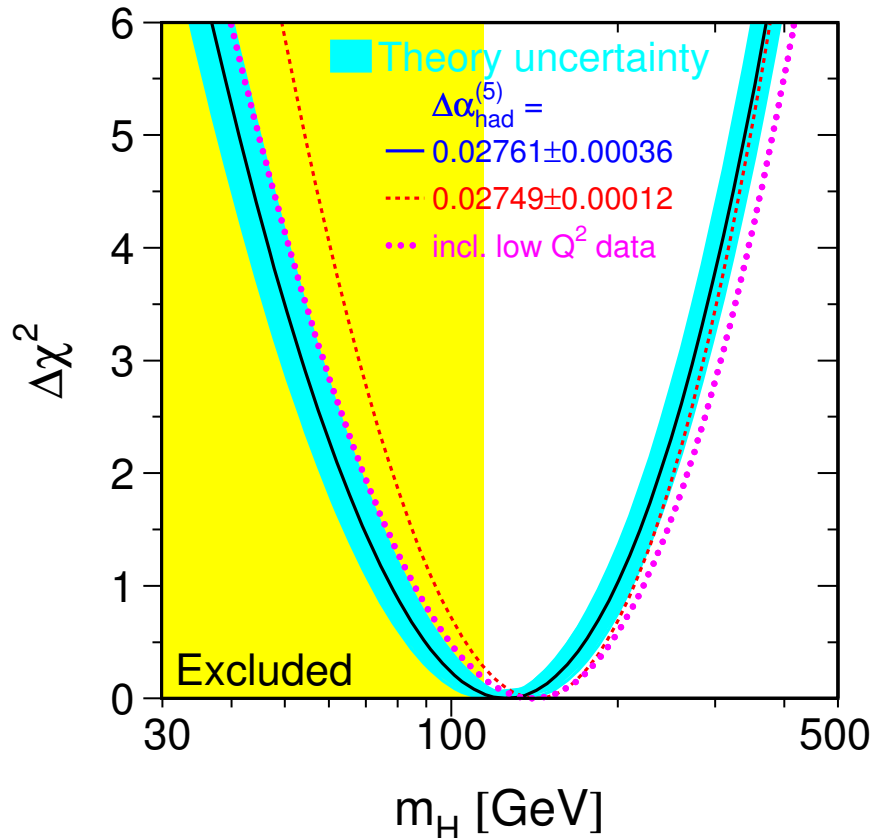


FIGURE 1.3: Deviation from the minimal χ^2 of fit to electroweak precision observables as function of the Higgs boson mass. The yellow area indicates the mass range excluded by direct searches at LEP. Figure from [22]

1.4 Higgs boson discovery and properties

The discovery of a new particle compatible with the SM Higgs boson has been published by both ATLAS and CMS collaborations on July 4th, 2012[8, 9]. The discovery is based on the pp collisions in LHC at CERN. The most sensitive channels in both experiments are the $H \rightarrow 4l$, $H \rightarrow \gamma\gamma$ and $H \rightarrow WW^* \rightarrow e\nu\mu\nu$. The significance of the excess of events observed around $M_H = 125.5$ GeV is above 5σ . The Figures 1.4 show the local probability for a background only hypothesis and the deviation due to the observed resonance. The final results, a milestone in physics history, established

a new benchmark in the understanding of our universe (ATLAS+CMS combined results):

$$M_H = 125 \pm 0.2(\text{stat.}) \pm 0.7(\text{syst.}) \text{ GeV} \quad (1.57)$$

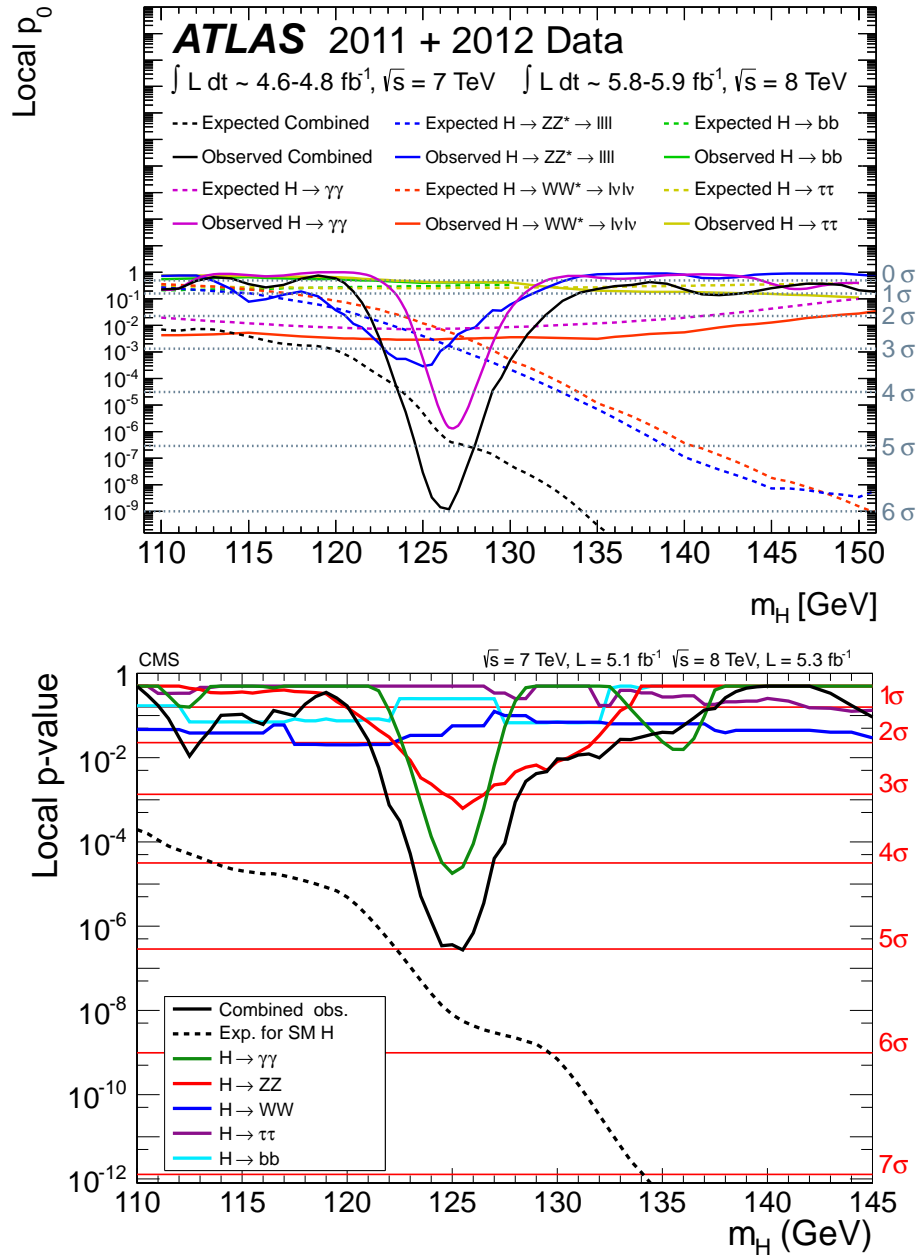


FIGURE 1.4: The observed local p -value in ATLAS(top)[9] and CMS(bottom)[8] experiments for the five decay modes and the overall combination as a function of the SM Higgs boson mass.

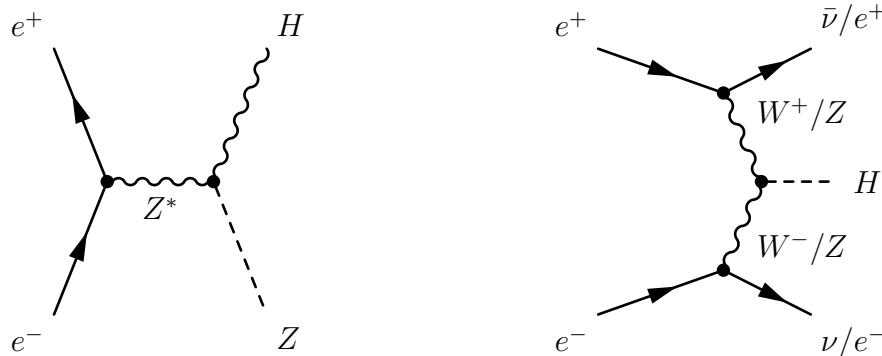
In November 2013, an evidence for Higgs boson decaying into fermions has been reported with more than 3σ significance in $H \rightarrow \tau^+\tau^-$ and $H \rightarrow b\bar{b}$ channels by both experiments[24, 25]. Other results have been performed including the measurement of the spin and CP-parity. The standard model of hypothesis $J^P = 0^+$ has been then compared to the alternative hypotheses $0^-, 1^\pm$ and 2^+ in fits to the

distribution of kinematical variables of the di-boson final states, showing that the SM case is favoured excluding at more than 97% of confidence level the other hypotheses [26, 27].

The measurement of couplings, the spin and the parity of the newly discovered boson still needs to be investigated to show whether the Higgs boson properties exhibit physics beyond the SM.

1.5 Higgs production in lepton colliders

The production of the Higgs boson at the lepton colliders is achieved mainly via *Higgs-Strahlung* process and WW/ZZ fusion. Their respective Feynman diagrams are



For the Higgs boson of mass 125 GeV the production maximum will be reached for a center-of-mass energy around 250 GeV. The main process is then expected to be through the Higgs-Strahlung process. In this process the annihilation of the e^+e^- pair produces an off-shell Z boson which goes on-shell via the radiation of a Higgs boson. The maximum of the cross section of this process is reached at $\sqrt{s} \sim M_Z + \sqrt{2}M_H$ and vanishes according to $1/s$ for higher energies. Further details of this process are discussed in Chapter 9.

For the production via WW/ZZ fusion, the cross section shows an energy dependence $\sigma \sim M_V^2 \ln(s/M_H)$ with $V = Z, W$. These processes become hence important in the limit $M_H/\sqrt{s} \ll 1$. The ZZ fusion is however suppressed since the coupling of leptons to the neutral current is much smaller than the coupling to the charged ones. Thus the WW fusion is the dominant production process of the center-of-mass energies $\sqrt{s} > 500$ GeV.

Chapter 2

A Linear Lepton Collider For Precise Measurements : Accelerator and Detectors

“La situation était très satisfaisante. Les essais de fusée continuaient à très bien rater. [...] Car tel était le premier principe de base de la logique shadok : ce n’est qu’en essayant continuellement que l’on fini par réussir. Ou, en d’autres termes, plus ça rate, plus on a de chances que ça marche.”

— Rouxel, 1994

2.1	Why a linear e^+e^- collider ?	24
2.2	The international linear collider project	25
2.2.1	The e^+e^- machine layout	25
2.2.2	The polarised particle sources	26
2.2.3	The damping system	28
2.2.4	The main Linac	29
2.2.5	The beam delivery	29
2.3	The physics potential	30
2.3.1	The implication on the detector design for ILC	32
2.4	Particle flow paradigm	34
2.5	The international large detector concept	36
2.5.1	Tracking system	38
2.5.2	Calorimeter system	40
2.5.3	Magnet Coil and Muon System	42

	E_{beam} [GeV]	R [m]	$(\Delta E_{rad})_{tour}$ [MeV]
LEP I	45	2785	~ 1303
LEP II	100	2785	~ 3177
LHC	7000	2785	~ 0.007

TABLE 2.1: Energy loss by synchrotron radiation by cycle for few circular accelerators.

2.1 Why a linear e^+e^- collider ?

The most powerful particle collider in the present day collecting data is the Large Hadron Collider (LHC) at CERN ¹. It is designed to collide proton beams with a centre of mass energy of up to 14 TeV ⁽²⁾ and bring to light the physics beyond the standard model. However, the protons are composite particles, the type and energy of the interacting partons is not really known, limiting the precision capability. In addition, the reconstruction of many physics processes suffers from a large QCD backgrounds and from pile-up. A complement to the LHC in terms of precision, will be ideally provided by a high energy lepton collider. Leptons are elementary particles and can collide with well know initial state (energy, polarisation, ...). The environment is much cleaner than in hadron colliders and the conservation of energy and momentum allows for better analysis of the decay products and the reconstruction of the invisible particles.

Circular colliders offer high repetition rate and then luminosity. Their main challenge to reach high energies arises from the synchrotron radiation. Indeed, the energy loss E_{rad} by a particle of mass m and energy E in the circular orbit of radius R is $E_{rad} \sim (E/m)^4/R$. This implies that the radiation losses increase greatly with the particle energy E , whereas increasing the radius has relatively little effect. The Table 2.1 shows a comparison of the energy loss for few circular accelerators. In view of the m^{-4} contribution³, colliders with heavy leptons (muons or taus) would be ideal, but these particles are unstable and there is currently no realistic proposal on how to build such machines. An e^+e^- collider is therefore the only promising option for the near future.

The solution, at high energy, is a linear collider. The most advanced and promising linear e^+e^- collider project is the International Linear Collider (ILC). This machine should reach an energy in centre of mass up to 250 GeV in the first phase and 500 GeV in a second one (upgradable to 1 TeV). Its polarised beams and the tunable beam energy, make it ideal for precise measurements.

The actual design of both accelerator and detectors is the result of many years of R&D and its still subject to modifications and optimisation to reach the best performances reducing in the same occasion the cost of the instruments. These efforts have been summarised in the publication of the Technical Report Design (TDR) [28] in 2013.

¹European Organisation for the Nuclear Research (Centre Européen de Recherche Nucléaire)

²This energy will be reached in 2015 during the second long run of the LHC, in the previous run the collision energy was 7 and 8 GeV

³The total power emitted by synchrotron radiation is proportional to $(1/m^4)$. Since protons are about 2000 times heavier than electrons, the energy loss by synchrotron radiation is weaker by about 10^{-13} and becomes noticeable at extremely high energy, such as those at the LHC.

This chapter proposes a description of the ILC proposal. First the accelerator layout is shown reviewing its main parts, and focusing to its technological challenges and on its possible performances. The main physics goals will be also discussed, focusing on their implication on detector design as well as the reconstruction techniques, specially the one called *Particle Flow*. Finally, the International Large Detector will be introduced describing its main components.

2.2 The international linear collider project

2.2.1 The e^+e^- machine layout

The ILC is high luminosity accelerator colliding polarised electrons and positrons. It is based on 1.3 GHz superconducting radio-frequency accelerating cavities, leading for 200-500 GeV energy collisions (upgradable to 1 TeV) in the centre of mass. A schematic view of the accelerator complex with the position of the main sub-systems is shown in Figure 2.1. The Table 2.2 shows the parameters for several centre-of-mass energies.

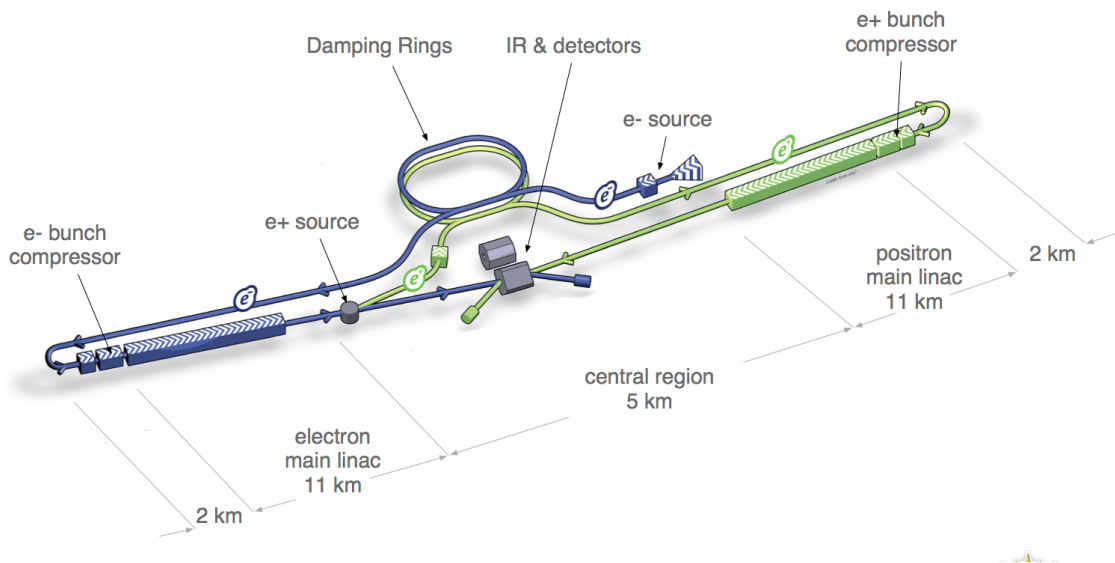


FIGURE 2.1: Schematic layout of the ILC accelerator, showing the main sub-systems.

The main components of the collider are:

- A polarised electron and positron beam sources;
- 5 GeV electron and positron damping rings (DR) with 3.2 km of circumference, housed in the common tunnel;
- Beam transport from damping rings to main linacs, followed by two stages of bunch compressor;
- Two main linacs 11 km long each, using 1.3 GHz superconducting radio-frequency (SCRF) cavities operating with a gradient of 31.5 MV/m, with a pulse length of 1.6 ms;
- Two beam-delivery systems 2.2 km long each, bringing the beams into collision with a 14 mrad crossing angle;

	Baseline 500 GeV Machine		
Center-of-mass energy	250	350	500
Collision rate	5 Hz	5 Hz	5 Hz
Electron linac rate	10 Hz	5 Hz	5 Hz
Bunch population	2.0×10^{10}	2.0×10^{10}	2.0×10^{10}
Bunch interval	554 ns	554 ns	554 ns
Number of bunches	1312	1312	1312
RMS bunch length	0.3 mm	0.3 mm	0.3 mm
Electron $\Delta p/p$	0.190 %	0.158 %	0.124 %
Positron $\Delta p/p$	0.152 %	0.100 %	0.070 %
Electron polarisation	80 %	80 %	80 %
Electron polarisation	30 %	30 %	30 %
Luminosity	$0.75 \times 10^{34} \text{cm}^{-2} \text{s}^{-1}$	$1.0 \times 10^{34} \text{cm}^{-2} \text{s}^{-1}$	$1.8 \times 10^{34} \text{cm}^{-2} \text{s}^{-1}$

TABLE 2.2: Summary of the ILC 250-500 GeV baseline and luminosity parameters.

- Single interaction point leads to a so-called *push-pull* configuration⁴ for two detectors.

The full footprint of the ILC accelerator is ~ 31 km. The electron and the positron sources as well as the damping-rings are located near the central region. The damping-ring installation is shifted laterally to avoid any interference with the detector hall.

The current baseline is to have only one interaction region, where two detectors alternate in the so-called push-pull scheme, for cost reason. While one detector is collecting data, the second one can be maintained or upgraded.

Comparing with the hadron colliders the events rate is much lower, the use of a low-trigger system is not necessary and the detector will be operated in a trigger-less mode. The data will be recorded from every single bunch crossing. The events will be built by collecting the information from different sub-detectors and selected using software triggers, maximising the sensitivity and the efficiency of the detectors.

2.2.2 The polarised particle sources

The electrons are produced by a laser shining a strained Gallium-Arsenic photo-cathode in the DC-gun (Figure 2.2), providing bunches with up to 90 % polarisation [29]. The emitted electrons are extracted in a normal-conducting structure, then accelerated to 76 MeV, then brought to 5 GeV using a superconducting linac. Before injection into the damping rings, superconducting solenoids rotate the spin⁵ into the vertical. The rotation back to the longitudinal direction is performed before the injection into the main linac. A separate superconducting RF cryomodule is used to compress the bunch energy to match the acceptance of the damping rings.

⁴The configuration where the two detectors occupy alternatively the interaction point is called *push-pull* configuration.

⁵The spin of the beam particles need to be parallel to the field of the bending magnet in the damping rings to preserve the polarisation.

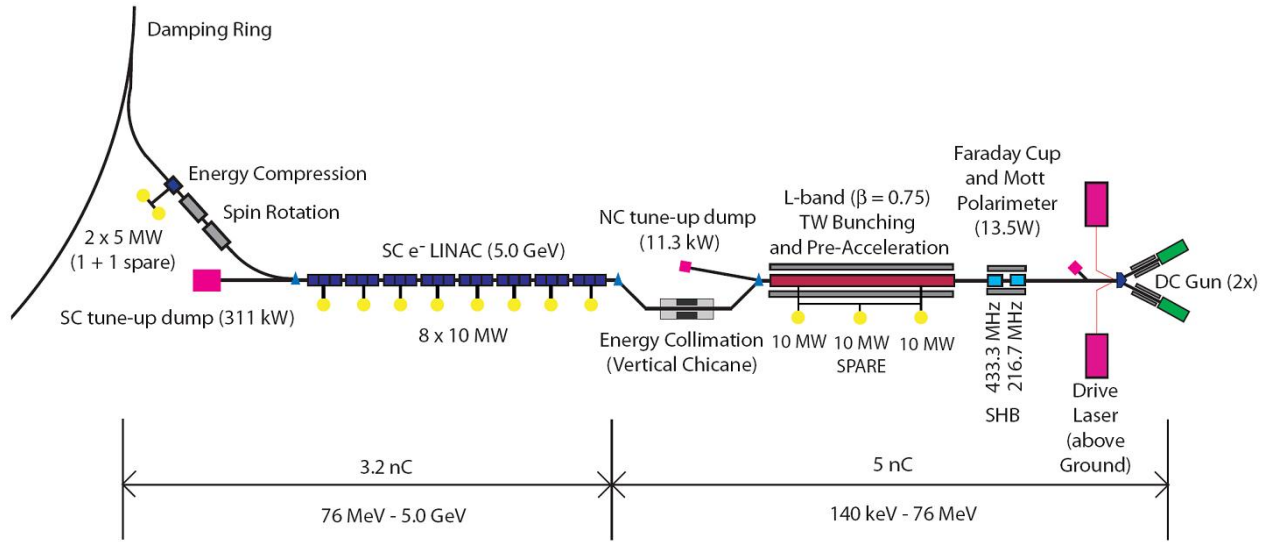


FIGURE 2.2: Electron particle source, as described in the ILC TDR[29].

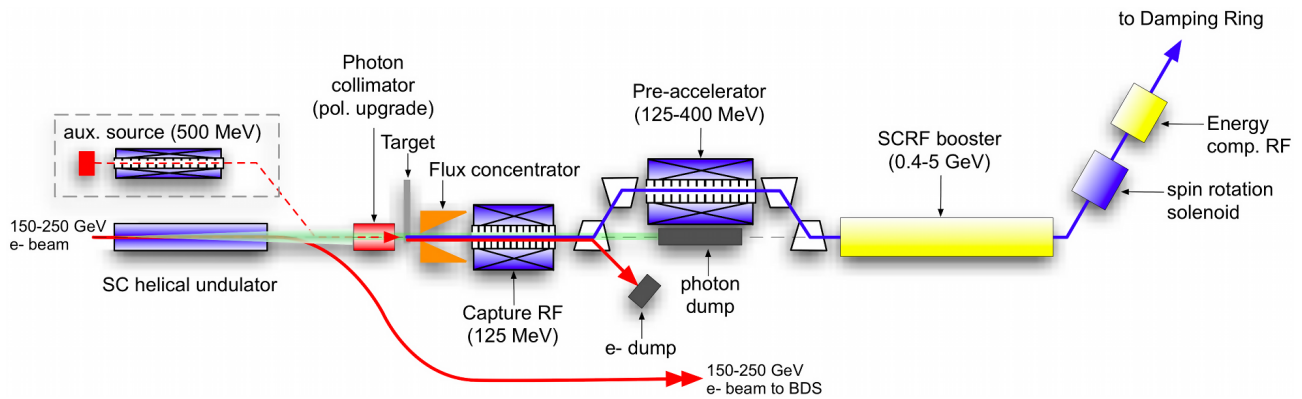


FIGURE 2.3: Positron particle source, ILC TDR[28]

After acceleration in the main linac, the primary electron beam with an energy of about 150 GeV, is transported through superconducting helical undulator⁶ that generates photons with maximum energy up to ~ 30 MeV (Figure 2.3). The emitted photons are directed onto a thin rotated Ti-alloy target, in which there is a good polarisation transfer, producing a beam of electron-positron pairs. The positrons are captured and accelerated to 125 MeV. The electrons and remaining photons are separated from the positrons and dumped. The positrons are accelerated to 400 MeV in a normal conducting linac with solenoidal focusing, and then brought to 5 GeV in a superconducting linac and finally injected into the damping ring after spin rotation and energy compression. The baseline produces positrons with a polarisation of 30 %. More detailed description is given in [28–30].

⁶A helical undulator is a succession of superconducting dipole magnet, which constraints the travelling electrons to emit a synchrotron radiation.

2.2.3 The damping system

Damping rings are necessary to reduce the beam emittance⁷ produced by the particle sources to the small values required for the linear collider. This can be achieved via the radiation damping process, i.e the combination of synchrotron radiation in the bending field with the energy gain in the RF cavities. The design of the damping rings must ensure a large acceptance to e^+ and e^- beams with large transverse and longitudinal emittances and must damp to the low emittance required for the luminosity, within the 200 ms between machine pulses (100 ms for 10 Hz mode). In addition, the injection and the extraction must be done without affecting the emittance of stability or the remaining stored bunches.

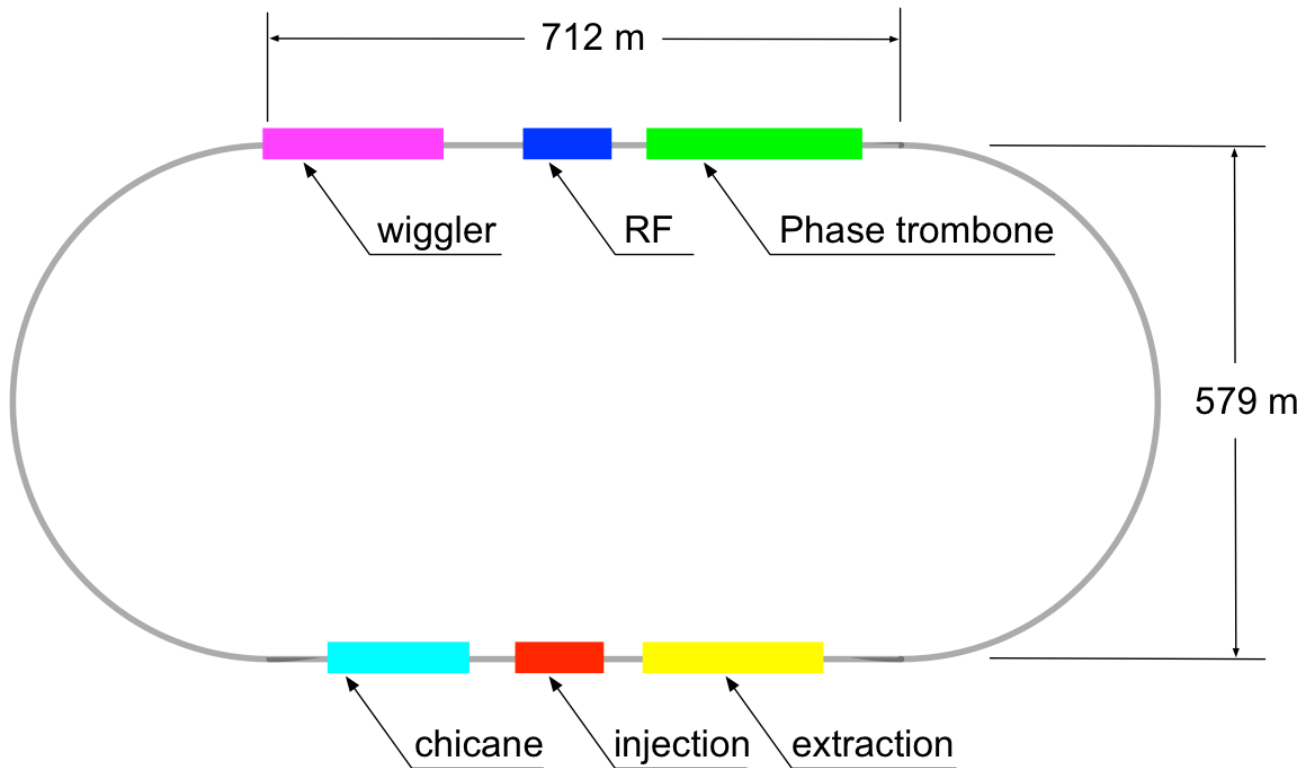


FIGURE 2.4: Schematic of the damping rings layout.

The baseline design consists of one electron and one positron ring operating at 5 GeV. Both rings are installed one above the other and housed in the same tunnel. The damping rings installation is located in the central region, it follows the *race-track* design shown schematically in Figure 2.4. Two arc sections connect 712 m-long straight sections. One of straight sections accommodates RF cavities, damping wigglers, and a variable path length to accommodate changes in beam phase (phase trombone), while the other contains the injection and extraction systems, and circumference-adjustment chicane.

⁷The emittance expresses the average spread of the beam particle coordinates in position and momentum phase space.

2.2.4 The main Linac

After the extraction from the damping rings, both beams are transferred to the Ring To Main Linac (RTML) section, then to the main linacs. The beam reaches the linac with an energy of 15 GeV and has to be accelerated up to 250 GeV.

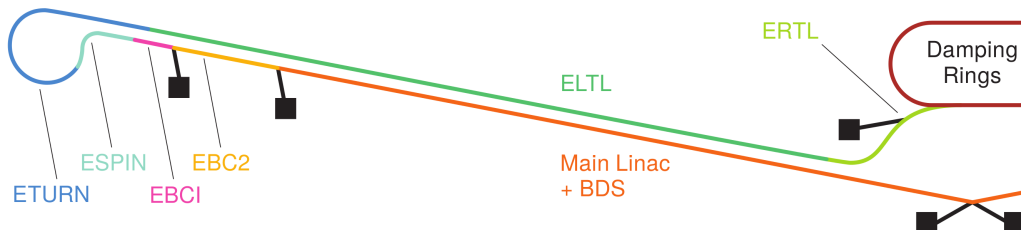


FIGURE 2.5: Schematic of the electron RTML.

The electron and positron RTMLs are the longest continuous beam lines in ILC with identical layout. The RTML consists of a ~ 15 km long 5 GeV transport line (ELTL) connecting to a 180° turn-around ring (ETURN) enabling feed-forward beam stabilisation. A spin rotator ensures the orientation of the beam polarisation before injection in the two-stage bunch compressors which compress the bunch length from several millimetres to few hundred microns, as required at the interaction point.

The main acceleration is done with superconducting niobium cavities (Figure 2.6), each contains 9 accelerating cells, operating at a temperature of 2°K and a frequency of 1.3 GHz. The average accelerating gradient is 31.5 MeV/m . In the present layout as mentioned in the TDR [28], the accelerator tunnel houses also the services as the RF sources and power supply. The total length of the linacs is about 11 km.



FIGURE 2.6: A 1.3 GHz superconducting niobium cavity.

2.2.5 The beam delivery

The last section before the interaction point, about 2 km, accommodates the Beam Delivery System (BDS). The latter is responsible for transporting the beams from the exit of the high energy linacs to the interaction point, focusing them to few hundred nm horizontally and few nm vertically, size required by the ILC design. Then, it transports the spent beam to the main beam dumps. The beams

cross with an angle of 14mrad. The crossing angle simplifies the extraction of the beams after the collisions. The bunches are also rotated in the horizontal plane shortly before the interaction, using crab cavities, in order to increase the overlap between the two beams during the collisions. The BDS must also perform other critical functions like;

- characterisation of the incoming (transverse) beam phase space and match into final focus;
- removal of the beam-halo from the linac to minimise the beam-induced background in the detectors;
- measurement and monitoring of the key physics parameters such as energy, polarisation before and after collisions.

2.3 The physics potential

The TDR [31] sketches in details the physics program of the ILC. It ranges from the precise measurement of the SM physics, the investigation of the Higgs boson sector and the top quark physics up to the hunting of the new physics beyond the SM. This section will give a short overview of the physics goals focusing on the implication on the detector design requirements.

In July, 2012, the ATLAS [9] and CMS [8] experiments at the CERN Large hadron collider announced the discovery of a particle with a mass of 125 GeV. Several investigations, particularly on its spin, confirm the nature of the new particle as the Higgs boson predicted by the SM [26, 32]. The ILC is the ideal machine to study the newly discovered 125 GeV mass particle.

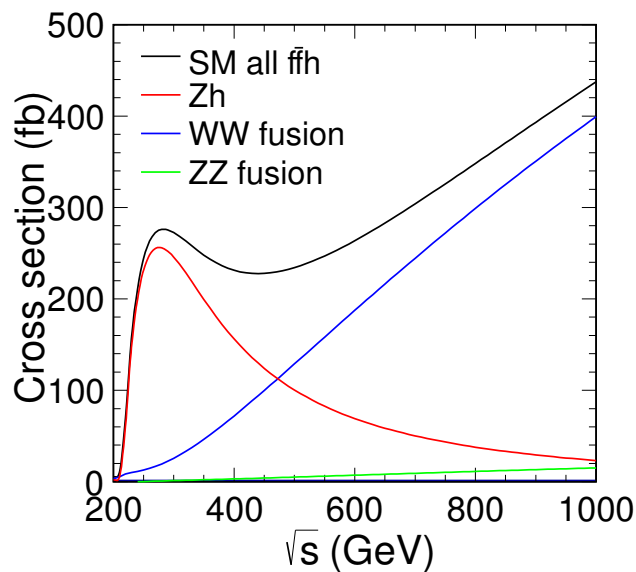


FIGURE 2.7: Higgs production cross section as function of centre of mass energy \sqrt{s} for $M_h = 125$ GeV.

The initial program of the ILC machine for the 125 GeV Higgs boson will be centred at an energy of 250 GeV, which gives the peak cross section for the Higgsstrahlung reaction $e^+e^- \rightarrow ZH$ (Figure 2.7). In this process, the tagging of the Z boson reveals the presence of Higgs (see Chapter 9), even if the H decays invisibly or in unexpected final states. After the Higgs discovery [8, 9] by the LHC, ILC

will provide a precise characterisation. The first stage to be addressed is to check if the Higgs boson follows the SM expectations. ILC can measure the branching ratios to quarks of different flavors, to leptons and to bosons and the self coupling with unprecedented precision. The Figure 2.8 show that the precision with ILC is much higher than with LHC running at high luminosity. It shows also the potential of combining the measurements.

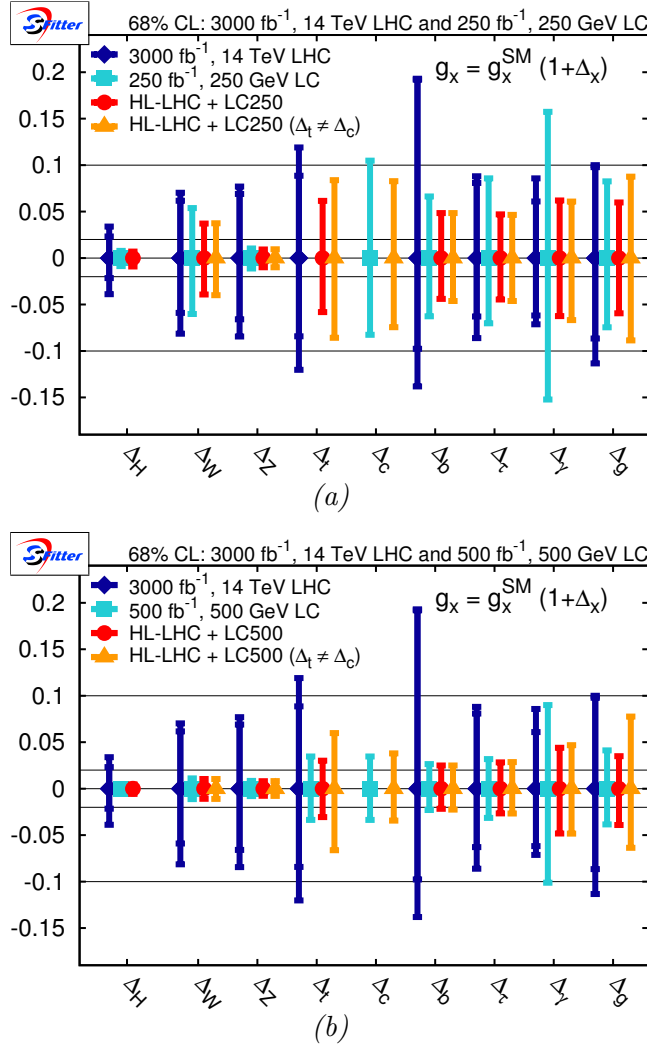


FIGURE 2.8: Expected precision for Higgs coupling measurement at high luminosity LHC and ILC at 250 GeV (a) and 500 GeV (b) and their combination. Figures from [33]

Moreover, ILC machine operating at 350 GeV in centre of mass, can reach the top quark production threshold and then measure its mass and its couplings (Figure 2.9). With LHC the top quark mass was measured with an accuracy of 2 GeV [34], while in ILC a statistical precision of the order of 30 MeV can be obtained[35]. The Yukawa coupling of the top quark with Higgs boson can also be studied in the $t\bar{t}H$ production, reachable by a centre of mass energy higher than 500 GeV.

Other improvements are planned in the ILC road-map coming from the *giga-Z* and *mega-W* options⁸. Indeed, a large production of the Z and W bosons allows to measure in dedicated runs their properties, underlying deviations from the SM.

⁸*giga-Z* and *giga-W* are the massive productions of the corresponding bosons.

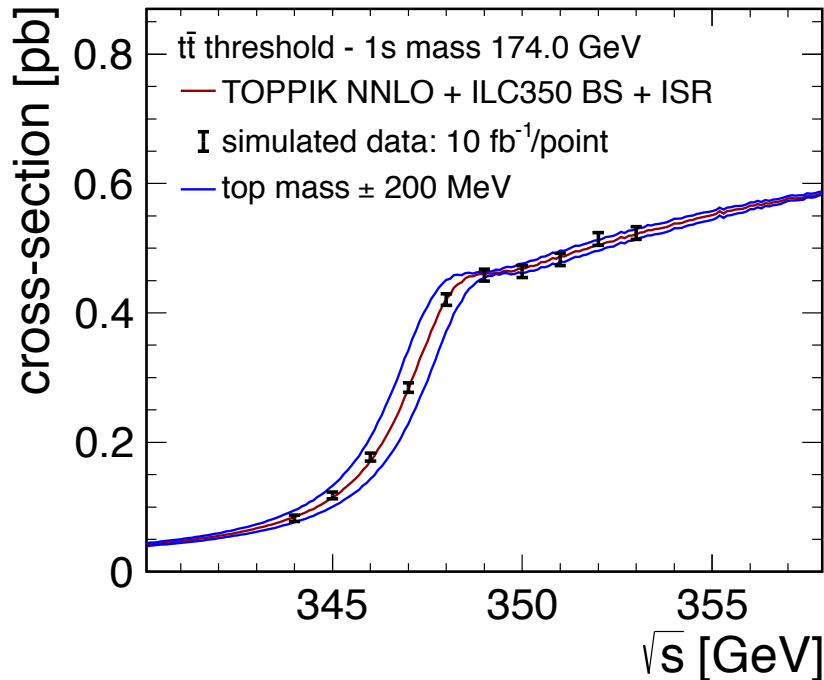


FIGURE 2.9: Top quark threshold measurement at the ILC including initial-state radiation and beamsstrahlung. The mass is chosen to be 147 GeV in the simulation. The blue lines correspond to a variation of ± 200 MeV around the top mass. The Figure from [35]

2.3.1 The implication on the detector design for ILC

The large physics program of the ILC requires multi-purpose detectors with performances significantly superior to the current collider detectors, in particular in terms of precision. With a machine environment much cleaner than LHC standards, advanced designs and technologies can be realised. The experiments will be recording data continuously in order to gather the largest possible amount of information.

Few requirements of the detector for ILC, supported by some selected physics examples, will be summarised in the current section:

Momentum resolution

The momentum resolution precision $\delta p/p^2$ is requested to be about 5×10^{-5} , a factor ten better than what the LEP achieved. This is particularly relevant for the measurement of the Higgs mass from the already mentioned Higgsstrahlung production. The mass of the Higgs boson can be measured with precision from the mass recoiling to the Z , identified as $Z \rightarrow \mu^+ \mu^-$. This measurement is completely model independent and does not need any assumption on the decay mode of the Higgs particle.

Impact parameter resolution

The investigation of the electroweak symmetry breaking requires a detailed study of the decay properties of the Higgs boson. It is important to distinguish between a light Higgs boson decaying into $c\bar{c}$, $b\bar{b}$ and other $q\bar{q}$ pairs. The measurement of the Higgs self-coupling mechanism $e^+e^- \rightarrow HHZ$ predicted by the SM model, has a complicated multi-jet final state. The quark tagging could allow a significant reduction of background. The required resolution is set to:

$$\sigma_{d_0}^2 < (0.5 \text{ } \mu\text{m})^2 + \left(\frac{5.0 \text{ } \mu\text{m}}{p(\text{ GeV}/c) \sin^{3/2} \theta} \right)^2 \quad (2.1)$$

Jet energy resolution

Many interesting physical processes decay in quarks leading to multiple jets final state. The reconstruction of such events requires a good jet energy resolution. The proper reconstruction of two or more jets is essential to distinguish between W , Z and Higgs boson providing an essential tool for discovering new states or decay modes (Figure 2.10). The case of $e^+e^- \rightarrow HHZ$ was mentioned previously. Moreover, in the SUSY scenarios allowing the decays $\chi_2^0 \rightarrow Z^0\chi_1^0$ and $\chi^\mp \rightarrow W^\mp\chi_1^0$, the identification of the Z^0 and W^\pm bosons is crucial to distinguish the two SUSY states.

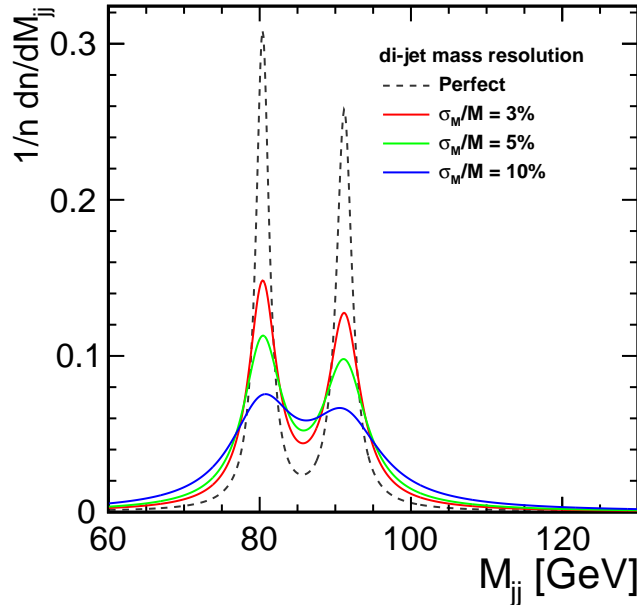


FIGURE 2.10: Illustration of di-jet invariant mass at different resolutions. The Z boson and W boson peaks become confused with the degradation of the jet energy resolution. (Only hadronic decays are considered here with the same number of events for both W and Z)

The performance goal of ILC is to reconstruct the mass of the vector bosons with a precision equivalent to their natural decay width ($\sigma_m/m = \Gamma_{W^\pm}/m_{w^\pm} \sim \Gamma_Z/m_Z \sim 2.7\%$). Under the assumption⁹ of a

⁹It is not clear that this assumption holds under PFA method (see Section 2.4)

jet energy resolution of $\sigma_E/E = \alpha/\sqrt{E[\text{GeV}]}$, a di-jet mass resolution of $\sigma_m/m = \alpha/\sqrt{E_{jj}[\text{GeV}]}$ is obtained, where α is the energy resolution coefficient and E_{jj} the di-jet energy. At di-jet energies in the range of 150 – 350 GeV the resolution rides $\sigma_E/E = 0.3/\sqrt{E[\text{GeV}]}$ which is more than a factor of two better than what the LEP achieved.

Other considerations

The detector performances are not expressed only in terms of energy and momentum resolution. Other relevant properties must be taken into account, such as the hermiticity for better reconstruction of particle in the forward direction which allows the reconstruction of the invisible decays using the momentum conservation¹⁰. In the same way, a good pattern recognition could allow for a better background suppression with an efficient particle identification capability.

2.4 Particle flow paradigm

The actually most promising strategy for achieving a jet energy resolution of $\sigma_E/E = 0.3/\sqrt{E[\text{GeV}]}$ at the ILC detectors is the Particle Flow Analysis (PFA) approach to calorimetry. Unlike a purely calorimetric measurement, the particle flow requires the reconstruction of the momentum and the energy (four-vector) of all visible particles in an event (Figure 2.11). Following the jet fragmentation measurement at LEP, the average energy content of a jet after the decay of the short-lived particle is about 65% charged particles (mainly hadrons), around 27% photons, about 10% long-lived neutral hadrons and 1.5% neutrinos. The momenta of the charged particles are well measured in the tracker, while the calorimetry system is dedicated to measure only neutral hadrons and photons. Consequently, the calorimeters must be able to distinguish the deposit of neutrals from those of charged particles. With this constraint, the particle flow algorithm has to assign the correct calorimeter hits to the reconstructed particles, requiring a good separation of closest showers. A simple example with a tracker of standard momentum resolution of about $\delta_p/p \sim 2 \times 10^{-5}$, a typical calorimeter resolution of about $\sigma_E/E = 0.15/\sqrt{E[\text{GeV}]}$ for photons and $\sigma_E/E = 0.55/\sqrt{E[\text{GeV}]}$ for hadrons, a jet resolution of $0.19/\sqrt{E[\text{GeV}]}$ can be obtained.

In the ideal case the jet energy resolution can be formalized by,

$$\sigma_{jet} = f_{\pm} \cdot \sigma_{\pm} \oplus f_{\gamma} \cdot \sigma_{\gamma} \oplus f_{h^0} \cdot \sigma_{h^0} \quad (2.2)$$

where f is the energy fraction of the particles, the indexes \pm , γ and h^0 indicate the charged particles, photons, and neutral hadrons respectively.

For a real detector some limitations are unavoidable, a possible overlap between the calorimeter hits belonging to charged particle and the ones from the neutral hadrons can happen. Only the energy of the charged particles (measured in the tracker) will be accounted for and the neutral energy will be spoiled. This effect is the so-called *confusion* term, which degrades the jet energy resolution. Another uncertainty comes from the losses, σ_{loss} , in the insensitive regions (cracks, beam pipe, shower leakage ..). The jet energy resolution for a real detector can be written,

¹⁰Indeed, the e^+e^- pairs produced through Bhabha scattering and the Initial State Radiation (ISR) high energetic photons can fake the missing energy signature.

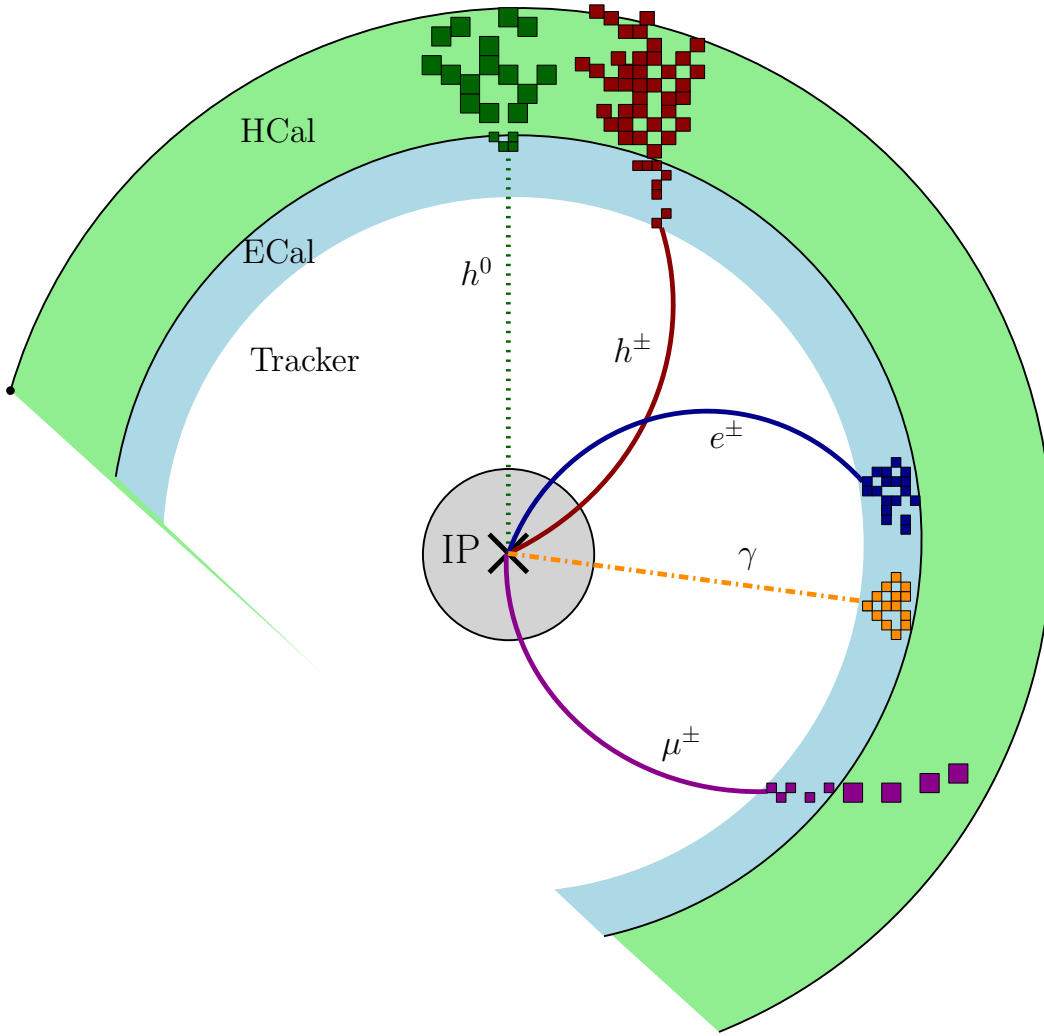


FIGURE 2.11: Representation of the detector response to different type of particle. It includes neutral hadrons (h^0), charged hadrons (h^\pm), electron e^- (positron e^+) photons γ and muons μ^\pm .

$$\sigma_{jet} = f_{\pm} \cdot \sigma_{\pm} \oplus f_{\gamma} \cdot \sigma_{\gamma} \oplus f_{h^0} \cdot \sigma_{h^0} \oplus \sigma_{conf} \oplus \sigma_{loss} \quad (2.3)$$

Usually the *confusion* term σ_{conf} rather than the calorimetric resolution limits the particle flow performance as shown in Figure 2.12

The ability to assign correctly the calorimetric energy deposits becomes the crucial aspect of particle flow. This imposes stringent constraints on the granularity of the electromagnetic and hadron calorimeters. Additionally, the material in front of the calorimeter has to be minimised as much as possible, since it deteriorates the track association to the energy deposit in the calorimeter. A high magnetic field plays also a crucial role in separating close by tracks particularly in boosted jets.

A variable called separability or *figure-of-merit* of the particle flow performance can be defined as:

$$S_{h^\pm/\gamma} \sim BR_{cal}^2 / (R_M \oplus \lambda_{had} \oplus \sigma_p) \quad (2.4)$$

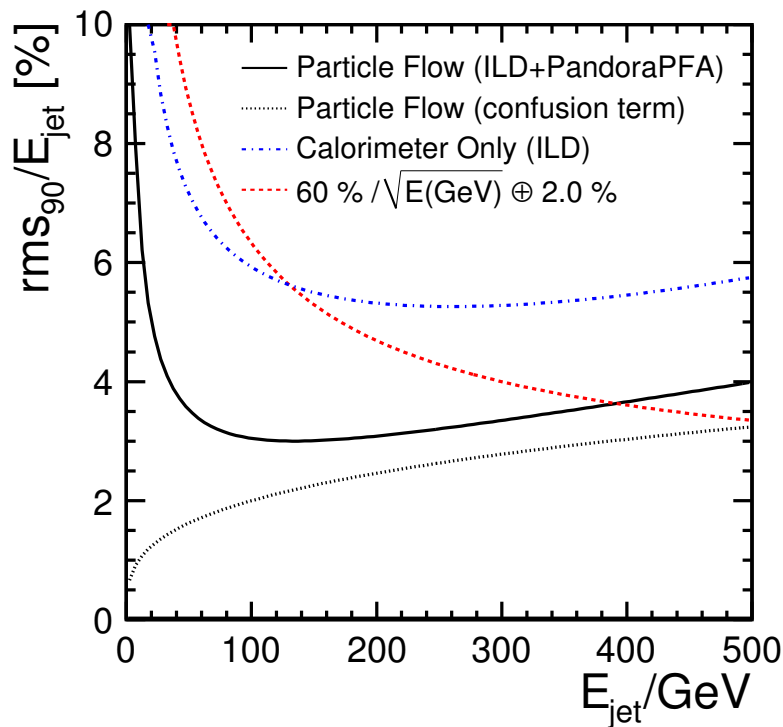


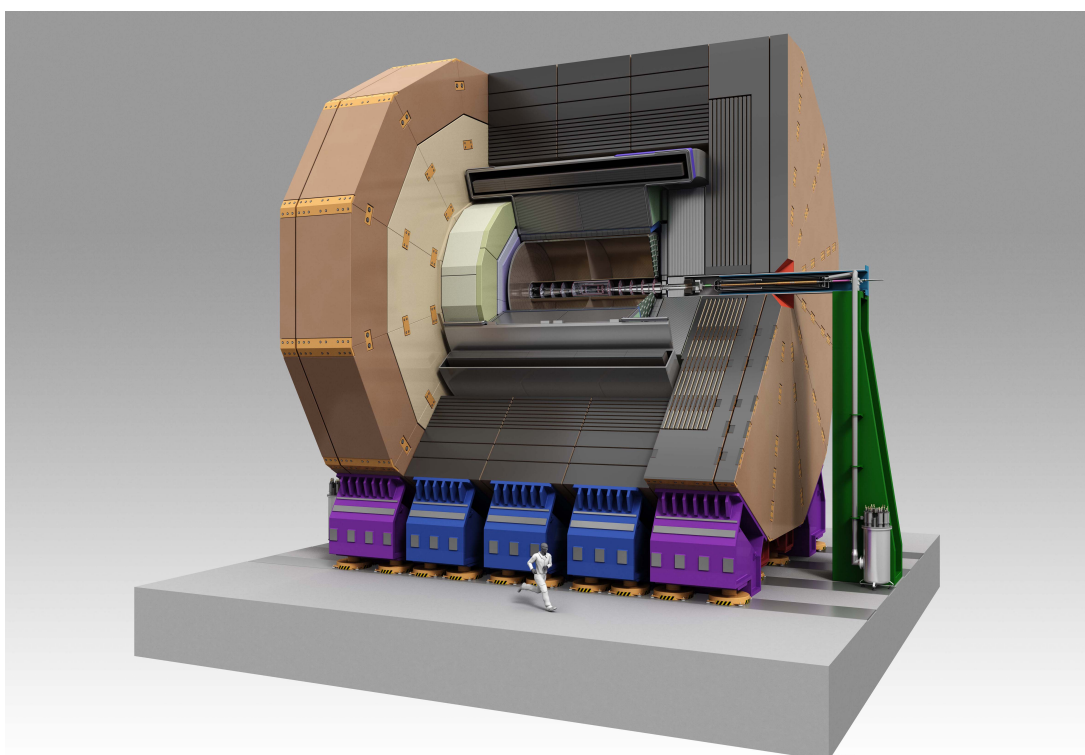
FIGURE 2.12: The empirical functional form of the jet energy resolution obtained from particle flow calorimetry (PandoraPFA and the ILC detector). The estimated contribution from the confusion term is shown with dotted line. From [36].

where B is the magnetic field, R_{cal} is the radius of the calorimetry entrance, R_M is the effective Moliere radius, λ_{had} is the interaction length and σ_p is the size of the readout pads in calorimetry. Larger is $S_{h^\pm/\gamma}$ better is the separation between charged tracks and photons.

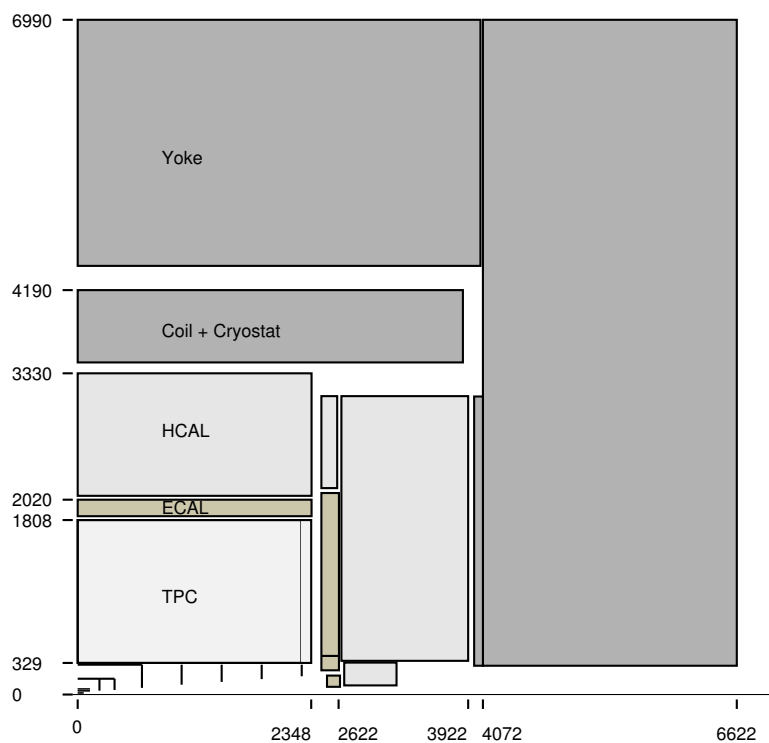
2.5 The international large detector concept

The International Large Detector (ILD) is a detector concept for the ILC collider (see Section 2.2). Its design has been summarised in the TDR[37]. The ILD detector is a multipurpose detector with a standard onion like structure. The ILD has been optimised with a clear emphasis on the precision. The particle flow described in the previous section (see Section 2.4) has a large impact on its design and plays a central role in the optimisation of the system. This emphasises the spacial resolution for all detector systems: a highly granular calorimeter system combined with a Time Projection Chamber (TPC) as central tracker which stresses redundancy and efficiency. Care has also been taken to design a hermetic detector, particularly in terms of solid-angle coverage and in terms of cracks and non-uniformity in response. The Figure 2.13a shows a perspective view of the ILD detector as described in the TDR[37].

In order to take into account the “push-pull” scenario, in which two detectors share the same interaction point and can be moved in and out of the beam position, the full ILD detector is mounted on a movable platform. This ensures the integrity and the stability of the calibration when moving.



(a)



(b)

FIGURE 2.13: Artistic view (a) and cross-section (b) of the ILD detector concept showing its main sub-detectors.

The Figure 2.13b shows a cross section of ILD detector. A brief description of the individual components with some arguments for the respective technological choices are given in the following.

2.5.1 Tracking system

The tracking system enables reconstructing with high efficiency and low fake rate the charged particles, providing their momentum with high precision. The ILD has a large gaseous main tracker, TPC, complemented by silicon tracking, immersed in a 3.5 T magnetic field.

The tracking in ILD is composed of several sub-systems helping for a better charged tracks reconstruction, starting from the interaction point up to the entrance of the calorimetry system.

The main components are described in the following.

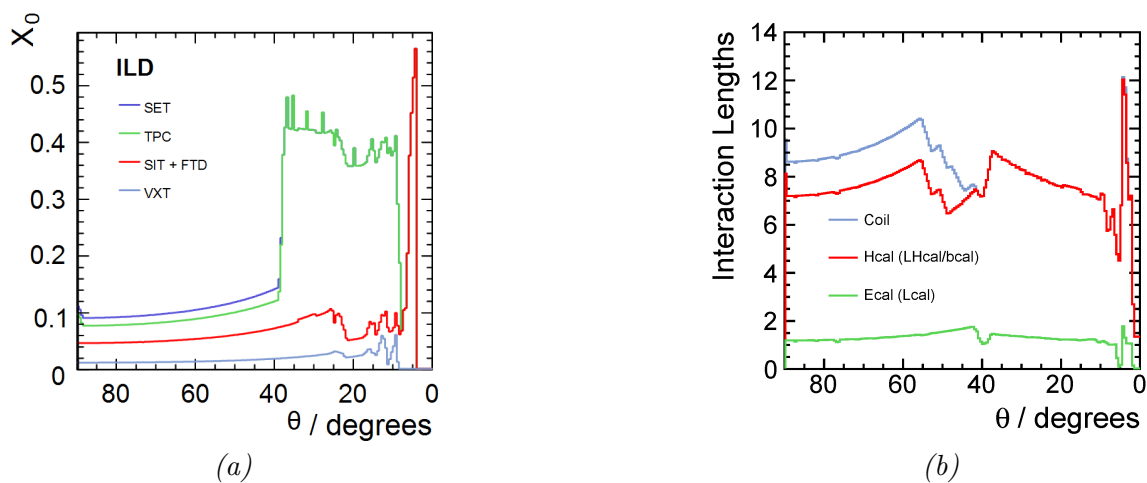


FIGURE 2.14: Average total radiation length (a) and interaction length (b) of the materials in the tracking detectors as function of the polar angle.

Vertex Detector - VTX

The reconstruction of the decay vertices of the short lived particles, such as D and B mesons and tau leptons, requires a transparent and precise vertex detector. The main performance goal of the ILD detector for the vertexing system resumes in a resolution on the track impact parameter¹¹ of

$$\sigma_b < 5 \oplus 10/p \sin^{3/2} \theta \mu\text{m} \quad (2.5)$$

A spacial resolution near the interaction point as low as $3 \mu\text{m}$ while keeping a low material budget, below $0.15\% X_0/\text{layer}$, is the primary design goal. The first layer is very close to the interaction point, located at radius of $\sim 1.6 \text{ cm}$. This imposes to deal with the extreme radiation conditions as well as the strong pair background.

¹¹i.e. the shortest distance from the interaction point to the track.

Silicon Internal Tracker - SIT

A system of two layers of silicon strips provides linking points between the VTX and the TPC detectors. This will not only improve the pattern recognition and the momentum resolution but also time stamps for each bunch crossing.

Time Projection Chamber

A Time Projection Chamber (TPC) is considered as the central tracker in ILD. The advantage of the TPC over a silicon based tracking is the high number of space points per track (up to 224 in ILD), which plays major role to achieve the ILC physics goals, without introducing too much material (Figure 2.14). Indeed, in such a tracker the back-scattering from calorimeters, kinks in tracks and the hadronic interactions in the tracker are easy to identify. The V_0 reconstructions as well as the pair production recovery are naturally feasible. On top of a momentum resolution of $\delta(1/p_t) \sim 2 \cdot 10^{-5} (\text{GeV}/c)^{-1}$, particle identification can be performed by measuring in the gas medium the energy loss per unit of length, dE/dx ¹². This leads, for example, to electron- π separation specially at low energy where the calorimeter based identification is not reliable. Figure 2.15a shows the resolution parameter as function of track momentum in ILD for different track polar angles.

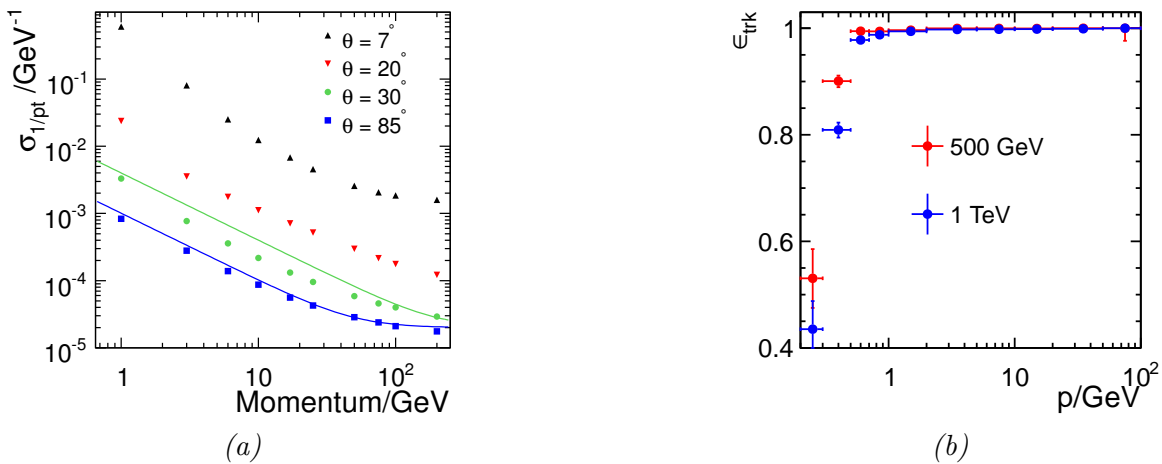


FIGURE 2.15: (a): Momentum resolution as a function of the transverse momentum of particles, for tracks with different polar angles. Tracking efficiency for $t\bar{t} \rightarrow 6$ jets events at 0.5 and 1 TeV as function of the particle momentum.

The combination of the above tracking subsystems yields an efficiency greater than 99% for tracks with $p_t > 1 \text{ GeV}/c$ (Figure 2.15b).

Silicon External Tracker - SET

Another set of two layers of silicon strip detectors, identical to the ones in SIT, surrounds the TPC tracker. This system provides an additional high precision space-points. Furthermore, a measurement close to the calorimeter entry can be used as starting point for the reconstruction of clusters of the deposit energy in the calorimeter system. Together SIT and SET provide three precision space point

¹²The mean rate of energy loss by a charged particle in given medium.

helping to improve the momentum resolution and provide a time-stamping information for bunch separation.

Forward Tracking Detector - FTD

The forward tracking detector covers the very forward region down to 0.15 rad close to the beam pipe. Seven disks are placed on each side of the vertex detector. The first three detectors are equipped with silicon pixel sensors, while the others are made by silicon micro-strips.

Endcap Tracking Detector - ETD

The Endcap Tracking sensor takes place in the gap between the ECAL and TPC end-plates. This single-sided silicon micro-strips detector improves the matching efficiency between tracks and showers in the ECAL. With the FTD it ensures full tracking hermiticity.

2.5.2 Calorimeter system

As shown in the Section 2.4, in order to minimise confusion between neighbour particle showers, the particle flow approach requires a very fine transverse and longitudinal segmentation of the calorimeters. The design of the calorimeters is driven by the requirement of the pattern recognition, instead of single particle resolution. Even more, the high granularity offers the possibility for an efficient software compensation for the difference between the electromagnetic and hadronic response. Both electromagnetic and hadronic calorimeters are planed as sampling calorimeters.

Electromagnetic calorimeter - ECAL

A highly segmented electromagnetic calorimeter provides 30 active layers. Tungsten has been chosen as absorber. For the sensitive medium silicon diodes or scintillator strips are considered. The geometrical design of ECAL is sketched in the Figure 2.16a. An octagon geometry is approximating the cylindrical barrel shape of the TPC. Each octante is subdivided into five modules. The layout of one module is illustrated Figure 2.16b. The first option of the detector, where the sensors are based on pin-diodes $5 \times 5 \text{ mm}^2$, and is considered in this thesis for the later analyses (see Chapter 9).

The choice of tungsten as ECAL absorber allows for a compact design, and provides a good separation of near-by electromagnetic showers due to it small *Moliere* radius (Chapter 3). The high ratio of the interaction length to radiation length one helps for a good separation of electromagnetic and hadronic showers, since hadrons on average penetrate more materials before starting a shower. A depth of roughly $24 X_0$ within 20 cm has been chosen to minimise the leakage, it corresponds to about $1 \lambda_I$. To achieve an adequate energy resolution fixed by the ILC detectors benchmarks, the ECAL is longitudinally segmented into 30 layers, possibly with varying tungsten thickness.

Measurement provided by a physical prototype, using $10 \times 10 \text{ mm}^2$ pixels with 10 layers of $0.4 X_0$, 10 layers of $0.8 X_0$ and 10 layers of $1.2 X_0$ tungsten plates, and silicon wafers $525 \mu\text{m}$ thick, achieved an energy resolution of $\sigma_E/E = (16.6 \pm 0.1)\%/\sqrt{E[\text{GeV}]} \oplus (1.1 \pm 0.1)\%$ [38].

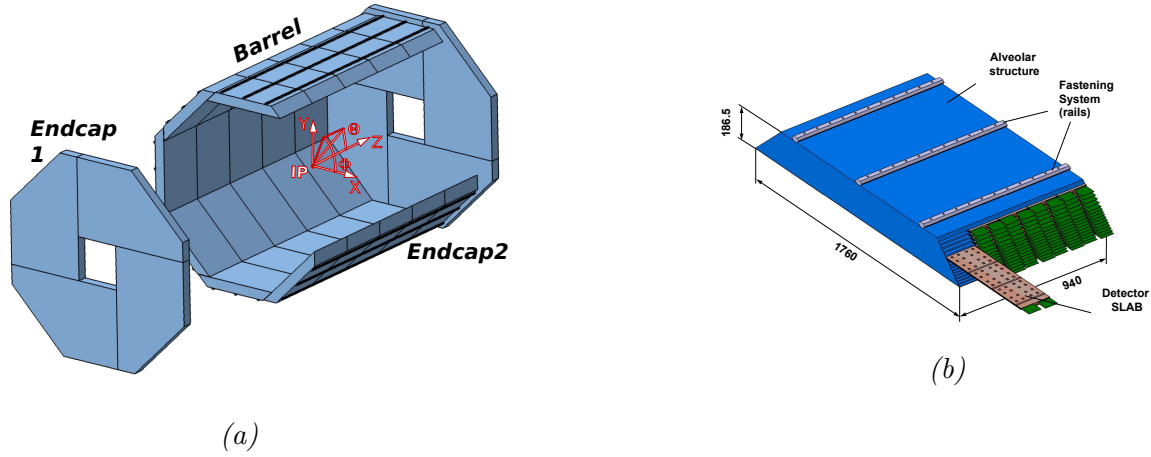


FIGURE 2.16: ECAL barrel and end-cap (a) and one ECAL module (b).

Hadron calorimeter - HCAL

The HCAL geometrical design follows the same octagonal ECAL structure (Figure 2.17a). It provides 48 longitudinal samples, and as small as possible cell size. Currently two technologies are under investigation. A scintillator based calorimeter version with scintillating tiles $3 \times 3 \text{ cm}^2$ and analogue readout, and a gaseous version with only $1 \times 1 \text{ cm}^2$ cell size and semi-digital readout. In this thesis, the HCAL active layers made by Glass Resistive Plate Chambers (GRPC) are assumed to be the active mediums (see Chapter 5).

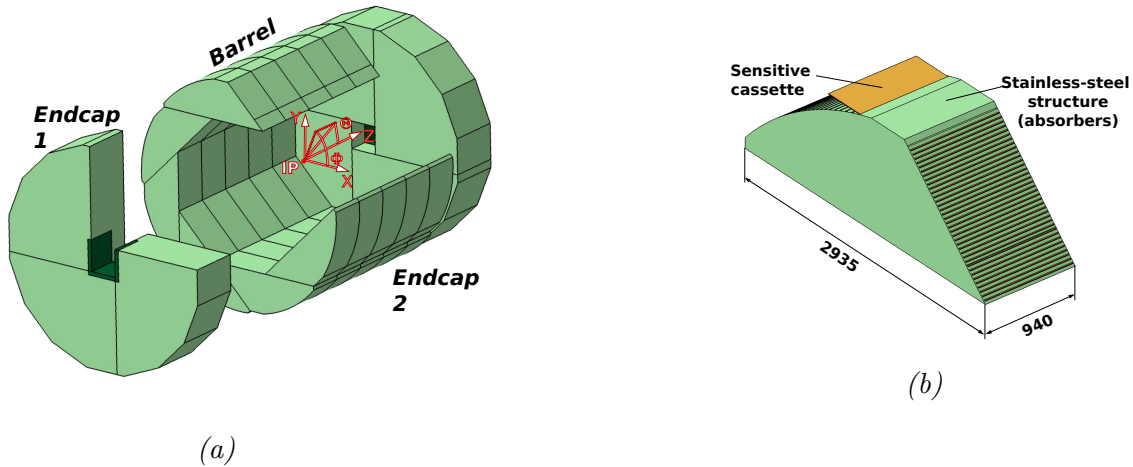


FIGURE 2.17: HCAL barrel and end-cap (a) and one HCAL module (b).

The HCAL as proposed in the ILC TDR [37] is a sampling calorimeter with a stainless steel absorber. A self-supporting structure without auxiliary support is possible thanks to the rigidity of stainless steel. This helps to reduce dead zones and conserves the hermiticity. Furthermore, comparing with other heavier materials, the stainless steel is non-magnetic; its moderate ratio of hadron interaction ($\lambda_I = 17 \text{ cm}$) to electromagnetic radiation length ($X_0 = 1.8 \text{ cm}$) leads to a sampling adequate for the

electromagnetic and hadronic components. Hadron calorimeter barrel and end-caps are composed by 48 absorber plates of 2 cm each leading to $6 \lambda_I$.

Forward calorimeters

A system of high precision calorimeters in the very forward angles, below the calorimeters (ECAL+HCAL) coverage, provides an extension to the angle coverage to almost 4π . These hard calorimetric detectors are listed as follow:

- the **ECAL Ring** fills the space between the ECAL endcap and the beam pipe. It has the same layer-absorber structure as the main part of the ECAL endcap;
- the **LumiCAL** is a cylindrical calorimeter designed to measure the luminosity with a precision better than 10^{-3} at 500 GeV centre of mass energy using Bhabha scattering as gauge process. It is centred in the outgoing beam. The apparatus is placed in a circular hole of the ECAL end-cap, covering an angle between 31 mrad and 77 mrad;
- the **LHCAL** unlike LumiCAL and BeamCAL is a hadron calorimeter located in the region between the LumiCAL and BeamCAL inside the HCAL end-cap. It extends the coverage of the HCAL to small polar angles;
- the **BeamCAL** makes a fast estimation of the luminosity on a bunch-to-bunch basis on beamstrahlung pairs. As the LumiCAL, it is an electromagnetic calorimeter with a cylindrical shape and covers the polar angle range 5 mrad and 40 mrad;
- the **GamCAL** is an electromagnetic calorimeter located 100m downstream of the detector, its purpose is to assist to the beam-tuning using the photons from the beamstrahlung.

2.5.3 Magnet Coil and Muon System

Magnet coil

A superconducting coil surrounds the calorimetric and tracking systems. It creates a solenoidal central field of 3.5 T up to 4 T in a volume of ~ 6.9 m in diameter and 7.35 m in length. The required integral field homogeneity is $|\int_0^{2.25 \text{ m}} \frac{B_x}{B_z} dz| \leq 10 \text{ mm}$ within the TPC volume. An anti-DID (Detector-In) handles the beams inside the detector and reduces the background from the incoherent pairs from the beamstrahlung. The iron return yoke hosts the muon system and serves as the main mechanical supporting structure for the whole ILD detector. In addition, the combination with the calorimeters should make the detectors self-shielding in term of radiation protection.

Muon system

A highly efficient muon identification combined with hadron rejection is an important feature to reach the physics goals of the ILD detector. The Muon System is located outside the magnetic coils and serve also as return yoke for the magnet coil.

Chapter 3

Basics of calorimetry for high energy physics

“ A careful analysis of the process of observation in atomic physics has shown that the subatomic particles have no meaning as isolated entities, but can only be understood as interconnections between the preparation of an experiment and the subsequent measurement.”

— Erwin Schrodinger

3.1	Energy loss by a charged particle in matter	44
3.1.1	Interaction of electrons and photons: electromagnetic cascades	45
3.1.2	Interaction of hadrons: strong processes and cascade	48
3.2	Sampling calorimeters	51
3.2.1	Energy measurement	52
3.2.2	Energy resolution	53
3.3	CALICE: calorimetry for ILC detectors	55
3.3.1	The electromagnetic calorimeter (ECAL)	56
3.3.2	The analogue hadron calorimeter (AHCAL)	57
3.3.3	The digital hadron calorimeter (DHCAL)	57
3.3.4	Digital versus analogue HCAL and the semi-digital concept	57

Introduction

Calorimetry in high energy physics is the measurement of particle energies via the detection of the energy deposited in matter by a total absorption. Originally invented for the study of the cosmic-ray phenomena, this method was developed and adapted for the accelerator-based experiments.

Calorimeters are the devices dedicated for these measurements, composed by an instrumented material in which the particles are fully absorbed and their energy translated into a measurable quantity. The interaction of the incident particle with the detector material (through electromagnetic or strong processes) produces a cascade of secondary particles (shower) with progressively degraded energy.

They can be also further classified according to their construction technique into sampling and homogeneous calorimeters.

The energy deposited in the active part of the detector is detectable as visible signal E_{vis} , which is generally proportional to the energy, E_p , of the incoming particle: $E_{vis} \propto E_p$.

The incident particle interaction depends on the nature of the traversed medium and the type of the incident particles. Charged leptons and photons interact electromagnetically with the atoms of the absorber (the weak force is negligible here). Charged hadrons interact with the absorber's atoms both via electromagnetic and strong processes, while neutral hadron interact strongly with the absorber nuclei. Thus, calorimeters can be broadly divided into electromagnetic and hadronic calorimeters.

Currently, the high energy physics experiments aim at recording complete event information, which places the calorimeters in an attractive position. In contrast with magnetic spectrometers (trackers cf. Chapter 2), in which the momentum resolution deteriorates linearly with the particle momentum, in calorimeters in most cases, the energy resolution improves with $1/\sqrt{E}$, where E is the energy of the incident particle. Moreover, calorimeters are sensitive to all types of particles, charged and neutrals. They even provide an indirect detection of neutrinos and their energy through the measurement of the event missing energy. Additionally, calorimeters can determine position, direction and nature of the absorbed particle.

In this chapter, the interaction of particles with matter is first described, then the principles of calorimetry are explained. Special attention is paid to sampling calorimeters, as they are the calorimeters chosen for ILD detector (Chapter 2). A brief description of the new generation of highly granular calorimeters, developed by CALICE collaboration [39], is also provided.

3.1 Energy loss by a charged particle in matter

A charged particle which passes through matter loses a fraction of its energy through the interactions with the atoms of the medium. With enough energy, it creates secondary particles or eventually a cascade of secondary particles. The mean rate of the energy lost by a heavy charged particle along a path δx with moderate momentum is well-described by the Bethe-Bloch equation

$$\left\langle -\frac{dE}{dx} \right\rangle = K z^2 \frac{Z}{A} \frac{1}{\beta^2} \left[\frac{1}{2} \ln \frac{2m_e c^2 \beta^2 \gamma^2 T_{max}}{I^2} - \beta^2 - \frac{\delta(\beta\gamma)}{2} \right] \quad (3.1)$$

$$K = 4\pi \mathcal{N}_A r_e^2 m_e c^2 \sim 4.92 \times 10^{-18} \text{ m}^4 \text{ s}^{-2} \text{ kg}$$

$$r_e = e^2 / 4\pi \epsilon m_e c^2$$

where m_e is the rest mass of an electron, $\beta = v/c$ is the particle velocity relative to speed of the light in vacuum, γ is the particle Lorentz factor $(1 - \beta^2)^{-1/2}$, Z and A are the atomic number and the atomic mass of the medium respectively. \mathcal{N}_A is the Avogadro constant¹, I denotes the average energy to ionise an atom of medium. The $\langle -dE/dx \rangle$ is usually given in term of $\text{MeV cm}^2/\text{g}$ ². Equation 3.2 describes the mean energy loss per unit of length $\langle -dE/dx \rangle$ in the region $\beta\gamma \in [0.1, 1000]$, with an accuracy of few %. Figure 3.1 shows the energy loss by muons traversing copper absorber. The $\langle dE/dx \rangle$ is high for low energy particles, but fall down to a minimum around $\beta\gamma \sim 3 - 4$. Particles having an energy

¹ $\mathcal{N}_A = 6,022141 \cdot 10^{23} \text{ mol}^{-1}$

²What is the usually provided is $\langle -dE/dx \rangle$ divided by the medium density.

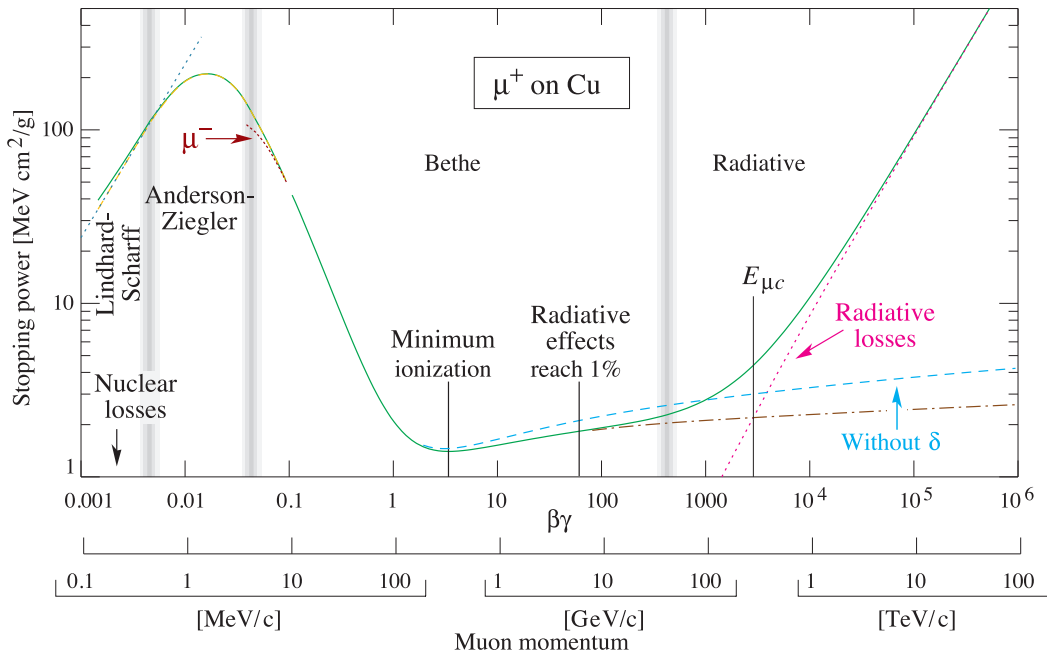


FIGURE 3.1: Stopping power ($\langle -dE/dx \rangle$) for positive muons in copper as function of $\beta\gamma$. From [40].

in this range are called Minimum Ionising Particles (MIPs). Muons with momentum in the GeV/ c range have energy loss comparable to MIPs.

The depth of materials needed to contain muons is therefore very large. Thus calorimeters are not suited for muons ³.

3.1.1 Interaction of electrons and photons: electromagnetic cascades

Electrons (or positrons) and photons interact with matter via a few well-understood QED processes. The average energy lost by electrons (or positrons) in matter (e.g. lead) is shown in Figure 3.2a as function of energy. Two main regimes can be defined. For energies above ~ 10 MeV, the dominant process is the emission via bremsstrahlung. At low energy most of the energy deposited in the absorber is due to collisions with the atoms and molecules of the material thus giving rise to ionization and thermal excitation. Other processes contribute at a minor degree to the deposited energy, such as Møller scattering ($e^-e^- \rightarrow e^-e^-$), Bhabha scattering ($e^+e^- \rightarrow e^+e^-$) and positron annihilation ($e^+e^- \rightarrow \gamma\gamma$).

The energy at which the electrons lose as much energy via bremsstrahlung as via ionization defines the critical energy E_c . It can be approximately given by [41]

$$E_c = \frac{550}{Z} \text{ [MeV]} \quad (3.2)$$

³Mip are often used for detector calibration (cf Chapter 5)

This equation is valid within 10%, for absorbers with $Z \geq 13$. Thus for example the critical energy is ~ 7 MeV for lead and ~ 21 MeV for iron.

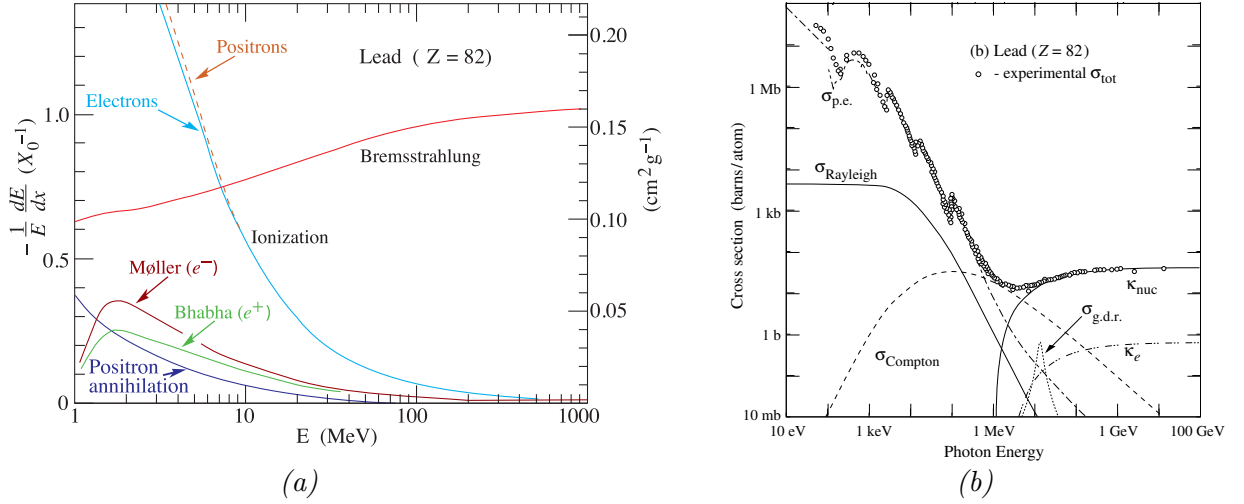


FIGURE 3.2: (a) Fractional energy loss per radiation length in lead as function of electron or positron energy. (b) Photon total interaction cross section in lead as a function of energy, showing the contribution of different processes. From [40]

Photons passing through matter lose energy via different processes in comparison with electrons. Figure 3.2b shows the cross section of these processes and their importance as function of the incident photon energy. At low energies it is seen that the photo-electric effect dominates, but Compton scattering, Rayleigh scattering, and photo-nuclear absorption also contribute. For photon energy above twice the electron mass m_e , the threshold for electron-positron pair production is reached.

Electromagnetic cascade

High energy electrons, positrons and photons, above their critical energy, interact mainly via successive alternation of emission of bremsstrahlung photon (electrons and positrons) and electron-positron pair production (photons). These processes multiply the number of particles and lead to the development of an electromagnetic cascade. The number of produced particles is roughly proportional to the incident particle energy and the length of the charged tracks in the shower.

The electromagnetic shower development in an absorber material depends on the radiation length X_0 , which depends on the atomic number Z and atomic mass A of the absorber [40]

$$X_0[\text{g}/\text{cm}^2] \simeq \frac{716 \text{ g cm}^{-2} A}{Z(Z+1) \ln(287/\sqrt{Z})} \quad (3.3)$$

The radiation length describes the rate at which electrons lose energy dE by bremsstrahlung in the average distance dx

$$-\left\langle \frac{dE}{dx} \right\rangle_{\text{brems}} \simeq \frac{E}{X_0} \quad (3.4)$$

On other hand, the radiation length is the average distance in which the electron has lost $1/e$ of its original energy E_0 . The cross sections in Figure 3.2a and Figure 3.2b show that above a certain energy

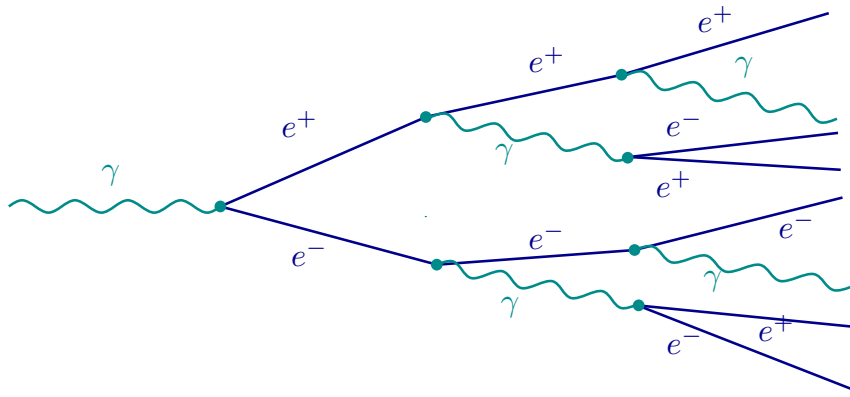


FIGURE 3.3: Example of photon having an electromagnetic cascade.

(roughly $E > 100$ MeV) the cross section is energy independent for both electron and photon. Hence, the radiation length is constant with energy of the incident particle.

Similarly, for a photon at high energy ($E_\gamma \geq 2m_e c^2$), the pair production ($\gamma \rightarrow e^+e^-$) dominates. This process determines the shower development up to the shower maximum. The typical mean free path in which a photon is converted into pair is given as $\lambda_\gamma \approx 9/7X_0$. Whereas the charged particles lose energy in the continuous stream, photons can penetrate the same thickness of matter without interacting.

The electromagnetic cascades can be described in a simplified analytical model using functions of the radiation length.

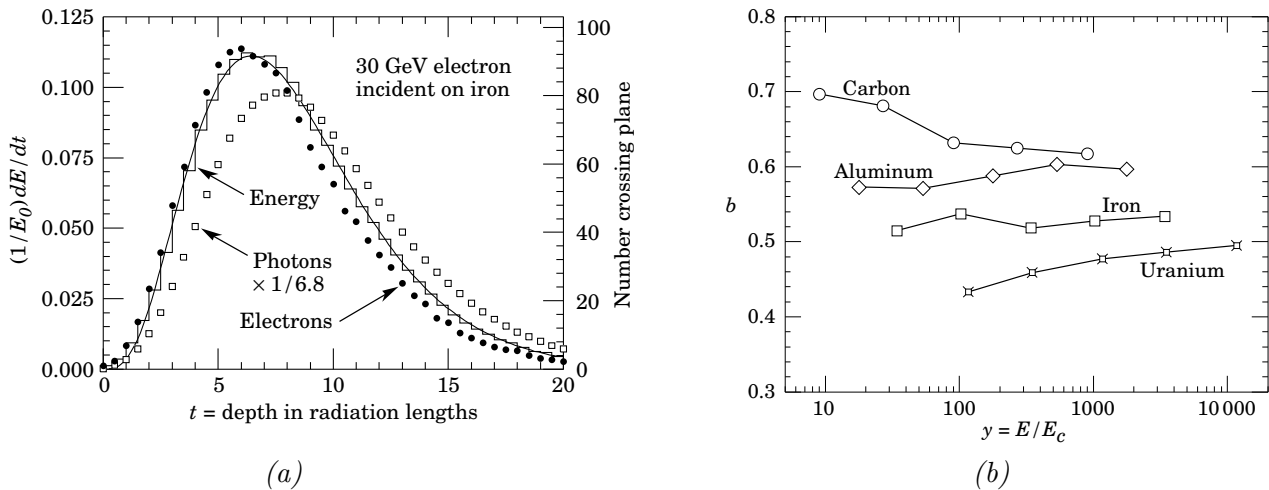


FIGURE 3.4: (a) Simulation of a 30 GeV electron induced cascade in iron. The fractional energy deposition as function of radiation length. The curve represents the best fit using Equation 3.5. (b) Fitted values of the scale factor b (from the Equation 3.5) for energy deposition profiles induced by electron for variety of elements. From [40]

The mean longitudinal profile of an electromagnetic shower induced by a particle with an energy E_0 [GeV] can be described by [42]

$$\frac{dE}{dt} = E_0 b \frac{(bt)^{a-t} e^{-bt}}{\Gamma(a)}, \quad (3.5)$$

where $t = x/X_0$ is the depth inside the material in units of radiation length, $\Gamma(a)$ is the Euler's Γ -function⁴, and a and b are parameters related to the nature of the incident particle (electron or photon). An example of 30 GeV electron longitudinal profile (simulated with EGS4[43]) fitted by Equation 3.5 is shown in Figure 3.4a. Precise values of b , obtained from simulation of incident electrons in the energy range [1, 100] GeV for few absorber materials, are shown in the Figure 3.4b. In this parameterization, the particle multiplication and the energy deposition reach their maximum after a certain depth t_{max} defined by

$$t_{max} = \frac{a-1}{b} = \ln\left(\frac{E_0}{E_c}\right) + C_{(\gamma,e)} \quad (3.6)$$

where $C_\gamma = +0.5$ and $C_e = -0.5$ for photon and electron induced cascades. An example of longitudinal development of 30 GeV electron cascade in iron is illustrated in the Figure 3.4a. The number of electrons and photons as function of the shower depth is compared with the total energy deposition. The electron multiplicity falls slightly more quickly than the energy deposition. This is essentially due to the fact that the fraction of energy carried by photons increases with the depth of the shower. The Equation 3.5 fits with good agreement the deposited energy.

The cascade reaches a maximum of multiplicity and starts vanishing when the electrons and positrons reach the critical energy E_c . The maximum shower depth increases logarithmically with the energy of the particle initiating the cascade. This gives an additional way to estimate the incident particle energy.

The transverse development of the electromagnetic shower, integrated over the full cascade depth, is given by the *Moliere Radius*, R_M defined by

$$R_M = X_0 E_s / E_c \quad (3.7)$$

where $E_s = \sqrt{4\pi/\alpha}(m_e c^2) \approx 21$ MeV (α is the fine structure constant). It represents the lateral deflection of electrons at the critical energy after traversing one radiation length. On average, about 90% of the shower energy is contained in a cylinder of radius R_M independently of incident energy. In most of HEP calorimeter the R_M is of order of few centimeters, since they are made with a dense material.

The transverse shower size is roughly energy independent. So the value R_M helps to design the calorimeters: the detection cells size must be comparable to R_M , if the calorimeter is aimed to be used for precision measurements of the shower position.

3.1.2 Interaction of hadrons: strong processes and cascade

Charged hadrons as well as charged leptons lose energy in matter via the electromagnetic process described in the previous section. However, all hadrons are also subject to elastic, quasi-elastic and inelastic scatterings.

Thus the total hadron-nucleon cross section includes this three main contributions:

$$\sigma_{tot} = \sigma_{elastic} + \sigma_{quasi-elastic} + \sigma_{inelastic}. \quad (3.8)$$

Figure 3.5 shows the total cross section, σ_{tot} , as function of total centre of mass energy, for protons, anti-protons, sigma baryons, pions, kaons and photons colliding with protons.

⁴The Γ -function is defined by $\Gamma(a) = \int_0^\infty e^{-x} x^{a-1} dx$

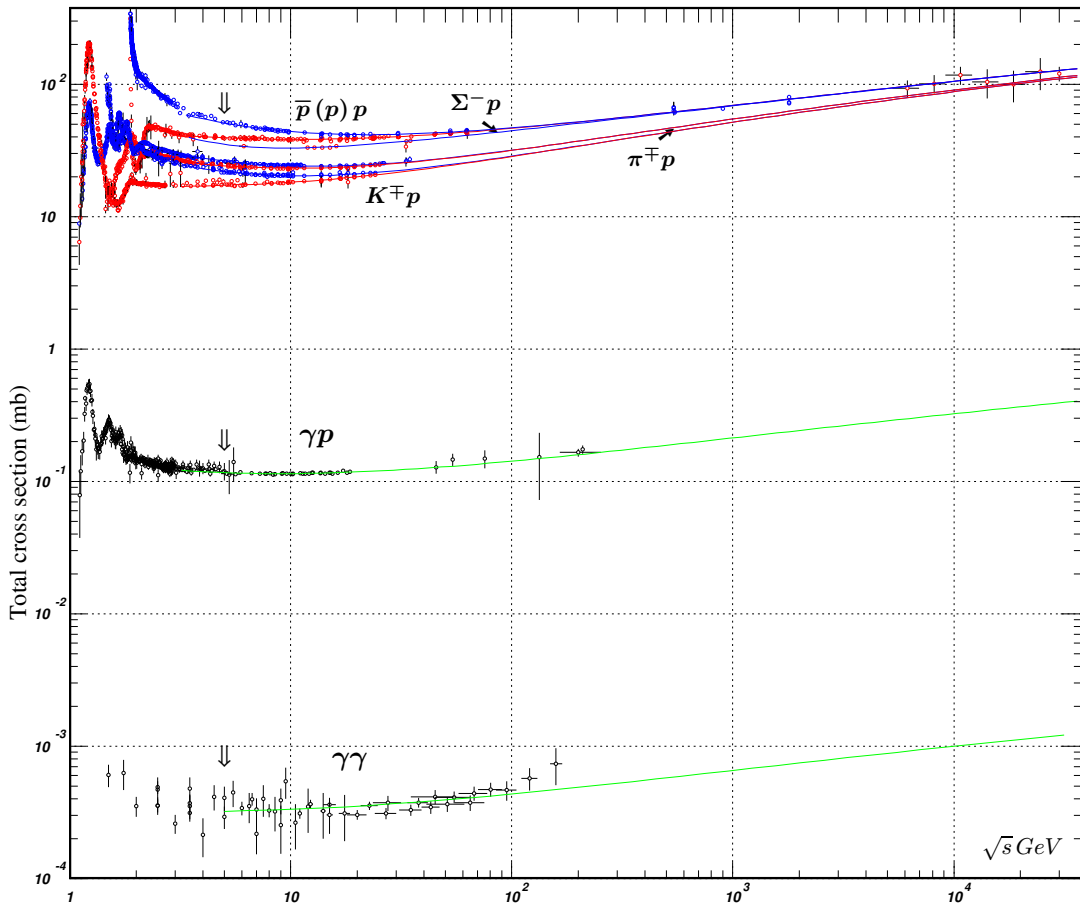


FIGURE 3.5: Summary of total hadronic cross sections as a function of total centre of mass energy, \sqrt{s} . Taken from Figure 46.9 of the Particle data Group 2013.

In the elastic and quasi-elastic collisions, a fraction of the incident particle energy is transferred to the medium nucleus leading to a change in direction, leaving the nucleus otherwise unchanged. In the inelastic interaction or absorption interaction, the nucleus, the incident hadron, or both of them change their identity, and are responsible for the hadron attenuation in the matter. The inelastic cross-section can be parametrised in terms of the atomic mass number, A , and the hadron-proton cross-section, σ_0 , by

$$\sigma_{inel}(A) = \sigma_0 A^{2/3} \quad (3.9)$$

For example for a incident pions, σ_0 represents the pion-proton cross-section.

Phenomenology of hadronic cascade in matter

Hadronic showers are similar to electromagnetic ones but involve more complex processes because of the additional dominant hadronic interactions. Figure 3.6 sketches an example of hadronic shower. On the basis of this picture, the hadronic cascade is propagated through a succession of various inelastic interactions leading to particles production. The multiplicity of produced particles shows a logarithmic dependence with respect to the primary particle energy, as shown in the Figure 3.5. Generally the cascade can be divided in three main parts: the hadronic component, which includes mesons, nuclear fragments and nucleons (protons and neutrons), the electromagnetic component, which is initiated by the neutral meson decay, $\pi^0 \rightarrow 2\gamma$, and neutral component from neutrons and neutrinos.

In hadronic interactions about half of the incoming energy is carried away by leading particles (mainly π^\mp , π^0 or η mesons).

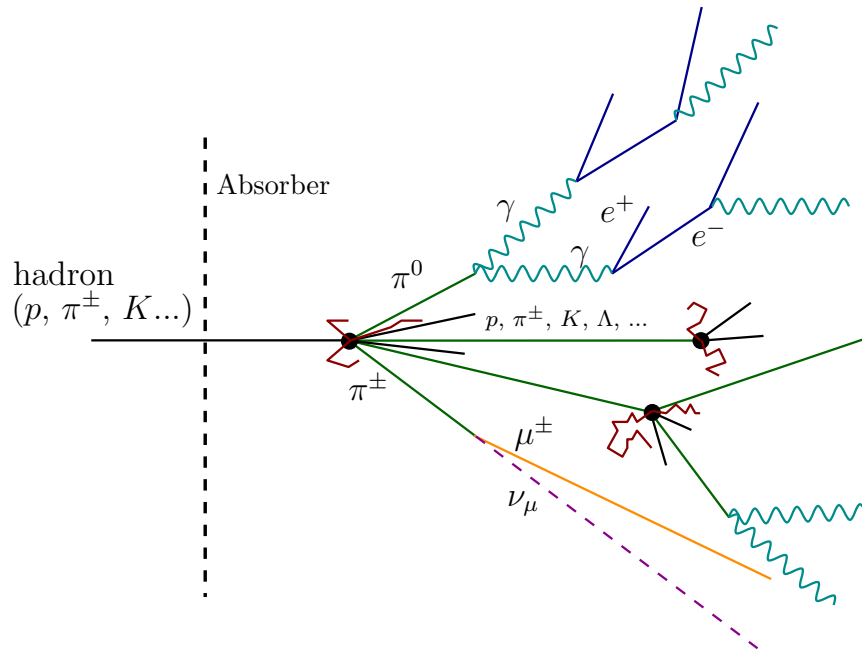


FIGURE 3.6: Example of pion having an hadronic cascade.

The longitudinal development of hadronic cascade is characterized in units of interaction length λ_I . It represents the mean free path before an inelastic hadron-nucleus interaction. The interaction length can be approximated by [41]

$$\lambda_I = \frac{A}{\mathcal{N}_A \rho \sigma_{inel}(A)} \approx 35 \cdot \frac{A^{1/3}}{\rho} \text{ [cm]} \quad (3.10)$$

where A , \mathcal{N}_A , ρ [g cm^{-3}] are the atomic weight, the Avogadro number and the density of the material respectively. $\sigma_{inel}(A)$ is the inelastic cross section on the nucleus of atomic weight A , defined by the Equation 3.10. This quantity as well as the radiation length, X_0 , helps in the design of the hadron calorimeters. Hadron cascades have much larger spacial extension in given absorber than electromagnetic showers. As an example, the ratio between the interaction length and the radiation length λ_I/X_0 for iron is about 9.5 [44].

The shower develops along the incoming particle direction as long as the energy carried by the secondary particles is enough to continue the multiplication process. In first approximation the shower maximum depth, in unit of the interaction length λ_I , is given by [46]

$$t_{max} \approx 0.2 \cdot \ln(E[\text{GeV}]) + 0.7 \quad (3.11)$$

while the longitudinal attenuation length describing the exponential decay beyond the shower maximum t_{max} , varies with energy as

$$\lambda_{att} \approx (E[\text{GeV}])^{0.13} \quad (3.12)$$

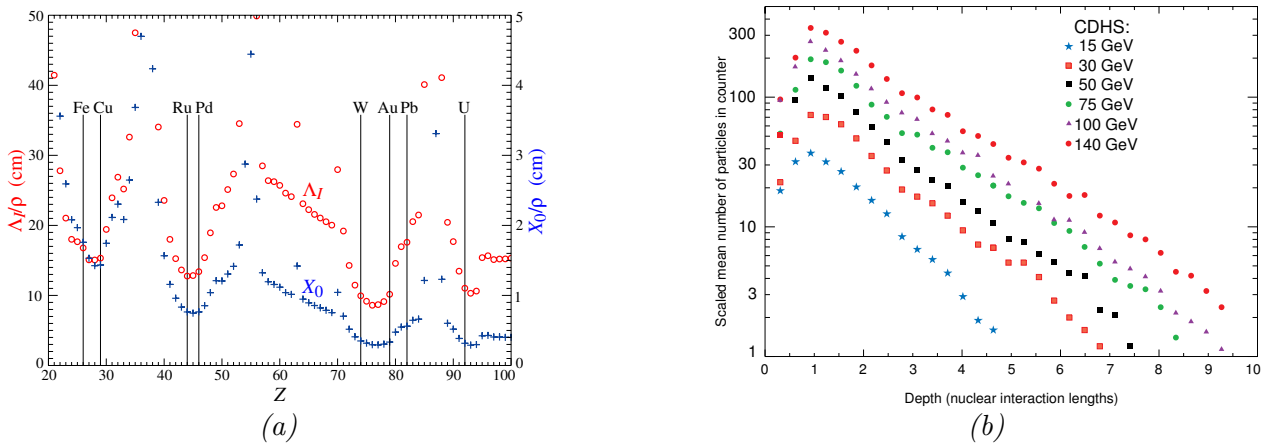


FIGURE 3.7: (a) Nuclear interaction length $\lambda_I/\rho[cm]$ and radiation length $X_0/\rho[cm]$ for few elements (From [40]). (b) Mean profile of π^\pm from CDHS neutrinos experiment [45]

The 95% longitudinal containment of hadronic showers [46] can then be expressed using both Equation 3.11 and Equation 3.13,

$$L_{95\%} \approx t_{max} + 2.5\lambda_{att} \quad (3.13)$$

where $L_{95\%}$ is given in unit of λ_I .

The longitudinal profile of hadronic shower is similar to the profile of the electromagnetic one (see Figure 3.7b) but the scale is different. This is reflected in the difference between the interaction and radiation lengths, λ_I and X_0 respectively. An approximation of the ratio between λ_I and X_0 is given by

$$\left(\frac{\lambda_I}{X_0}\right) = 0.12 Z^{4/3} \quad (3.14)$$

which makes hadronic showers longer and less dense than electromagnetic ones. The containment of hadronic shower is then more demanding in term of the calorimeter depth. Some values of the interaction and radiation lengths are shown in Figure 3.7a for different absorbing mediums.

3.2 Sampling calorimeters

As mentioned above the calorimeters are the device dedicated to the energy measurement of an incoming particle.

There are several ways to categorize calorimeters. They can either be homogeneous or sampling devices. In other hand calorimeters can be classified by the nature of particle which aim to detect. Homogeneous calorimeters have the active and absorber materials are the same. For the sampling calorimeters, layer of absorber samplers are interleaved with active readout planes (active layers). The absorbers are responsible for the shower development, there are usually made by a dense materials with high atomic number and short radiation and interaction lengths. The active layer has usually made with low dense materials having low atomic number, it can be made by scintillating materials, liquid, or gas depending to the technology used. The active layers have thickness much smaller than absorbers.

3.2.1 Energy measurement

The measurement of energy in such devices varies according to the technology used as active medium. Generally, it is based on the principle that the energy released in the detector material by charged particles of the shower, mainly through ionisation and excitation, is proportional to the energy of the incident particle. Only the energy deposited in the active E_{vis} volume can be measured. It is connected to the energy of the deposition in the full calorimeter (active plus absorber mediums) E_{tot} via the sampling fraction defined by

$$E_{vis} = f_{sam} \times E_{tot} \quad (3.15)$$

This equation is the basic principle of calorimetry and translates the linearity dependence between the measured energy and the incoming particle energy. For the electromagnetic shower, the Equation 3.15 works well since almost all the incoming particle energy is dissipated in the visible processes.

For the hadronic showers, as mentioned above (Section 3.1.2), more complex processes are involved including processes which do not produce visible signals.

Response to electromagnetic Showers

The response of the calorimeters depends on the type and the energy of the incident particle. The scale of the electromagnetic signal can be expressed on the unit of the response to the minimum ionising particles (Mip). This assumption is valid only by considering that the secondary particles ionise at the minimum of the dE/dx . The energy deposited by a Mip depends mainly on the thickness of the absorber and the nature of the active medium.

Response to hadronic Showers

Usually in the standard calorimetry, the signal of electron or photon, is larger than a signal of the signal of hadron with same initial energy. This is due to the invisible component of the hadronic showers. As described previously, the decay of π^0 via electromagnetic interaction into two photon or into a photon plus electron-positron pair ($\pi^0 \rightarrow \gamma e^+ e^-$) originates a localised electromagnetic cascade inside the main shower. The amount of the π^0 produced in the hadronic shower varies strongly from event to event and depends on the processes on the early phase of shower development. The photons originating from the π^0 decay can only interact electromagnetically and their energy is no longer sufficient for strong interaction, but enough to produce small electromagnetic showers. The energy carried these cascades (e) is called the electromagnetic fraction f_{em} , and it depends on the primary particle's energy. It can be parametrised [47] by

$$f_{em} = 1 - \left(\frac{E}{E_0} \right)^{m-1} \quad (3.16)$$

E_0 is roughly the energy needed to initiate the inelastic collisions. The exponent $(m - 1)$ is related to the secondary particles' multiplicity and the fraction of produced π^0 per hadronic interaction. E_0 and m must be determined experimentally for each calorimeter device. Their typical values are $m \sim 0.8$ and $E_0 \sim 1$ GeV for pions in iron[47].

Notifying h the response for pure hadronic cascades without the electromagnetic sub-showers ($f_{em} = 0$), the contrast between the electromagnetic and ideal hadronic shower is expressed by the h/e ratio which is equivalent to the ratio of the corresponding visible energy, $E_{vis}(h)$ and $E_{vis}(e)$ respectively.

Usually the ratio h/e is less than one, and does not depend on the incoming particle energy, which makes h/e ratio an intrinsic property of the calorimeters.

The response for an ideal hadron such as pions (π) is usually indicated as the sum of the pure electromagnetic and the ideal hadron signal

$$E_{vis}(\pi) = f_{em}E_{vis}(e) + (1 - f_{em})E_{vis}(h) \quad (3.17)$$

Considering the dependence of the f_{em} on the energy (Equation 3.16), the $E_{vis}(\pi)$ is not linearly dependent on the incoming hadron energy. Thus the ratio π/e , summarising the difference between the response to electromagnetic and real hadronic showers, depends on the incoming energy and the nature of absorber material. This ratio is given by

$$\frac{\pi}{e} \sim \frac{E_{vis}(\pi)}{E_{vis}(e)} = f_{em} + (1 - f_{em})\frac{h}{e} \quad (3.18)$$

Thus the h/e ratio is

$$\frac{h}{e} = \frac{(\pi/e) - f_{em}}{1 - f_{em}} \quad (3.19)$$

When $h/e = \pi/e \sim 1$ is satisfied, the calorimeter gives the same response to hadrons and electron (or photon) of the same incoming energy, this condition is called *compensating condition*. Most of the calorimeters are non-compensating, with a typical $h/e \sim 1.1 - 1.4$. Methods to achieve the compensating condition, or to minimise drawbacks, exist but these will be skipped in the following.

3.2.2 Energy resolution

The measurement of the energy in ideal calorimeters⁵ is a statistical process, subject to many sources of fluctuations. The fluctuation occurs in the active media where the visible energy E_{vis} is deposited. The statistical fluctuation in E_{vis} is determined by the fluctuation of number N of secondary particles contributing to the measured signal. Usually, the number of secondary particles increases with augmenting energy of the incoming particle. The statistical fluctuation of the measured energy can be expressed then by

$$\left(\frac{\sigma_E}{E}\right)_{samp} = \frac{\sigma(E_{vis})}{E_{vis}} \propto \frac{a}{\sqrt{N}} \propto \frac{a}{\sqrt{E}} \quad (3.20)$$

where σ_E is the standard deviation of the measured energy distribution for a detected particle with an energy E . Due to the pure statistic nature of the fluctuation, the resolution improves with increasing energy, which constitutes an important feature for the calorimeters. In addition the fluctuation follows a Gaussian law.

In the real calorimeter, other contribution deteriorate the energy resolution, and can be written in the simplified way by

$$\left(\frac{\sigma_E}{E}\right) = \left(\frac{a}{\sqrt{E}}\right) \oplus \left(\frac{b}{E}\right) \oplus c \quad (3.21)$$

The symbol \oplus indicates the quadratic sum. The first term is called the *stochastic term* which includes the intrinsic fluctuation mentioned above, and it characterized by the coefficient a ; the second term is known as the *noise term*; the third contribution is called *constant term*.

⁵An ideal calorimeter is a calorimeter with infinite size and no response deterioration due to the instrumental effects.

In the particular case of the sampling calorimeter, the energy deposited in the active medium fluctuates event by event due to the alternation of the active and the absorber layers. The resulting fluctuation in the energy measurement, called *sampling fraction*, is due to variation of the number of charged particles $N_{charged}$ that cross the active layer. This number is proportional to $N_{charged} \propto E/\tau$, where τ is the thickness of the absorber in unit of radiation length, the sampling contribution to the energy resolution is given by

$$\left(\frac{\sigma E}{E}\right)_{\text{sampling}} \propto \left(\frac{\tau}{E}\right)^{1/2} \quad (3.22)$$

Smaller is the thickness of the absorber, larger is the number of detected particle, thus better is the energy resolution. The sampling calorimeters can be improved following this principle by reducing the thickness of the absorber layers. The sampling fluctuation represents the most important limitation on the energy resolution in such devices.

The noise contribution to the energy resolution comes mainly from the instrumental effects (from readout electronic). The noise can usually translated into a corresponding amount of measured energy. Although the average contribution of the noise can be subtracted, it underlines fluctuations which are independent from the cascade development and thus contributes to the resolution as

$$\left(\frac{\sigma E}{E}\right)_{\text{noise}} \propto \left(\frac{b}{E}\right) \quad (3.23)$$

This term plays an important role specially at low energy, its contribution vanished at high energy.

The calibration uncertainties, non-uniformity and non-linearity of the detector as well as the readout-out electronics have an energy independent impact to the calorimeter energy resolution degradation. This impact is given then by

$$\left(\frac{\sigma E}{E}\right)_{\text{const}} \propto c \quad (3.24)$$

The performance of the calorimeter depends also on the type of the measured particle. The resolution of the electromagnetic particles is better than the resolution for hadrons. In the first place, in the hadronic shower less particles contribute to the measured signal with respect to electromagnetic one. Additional fluctuation must be also considered such as the fluctuation related the electromagnetic fraction, f_{em} and the invisible energy.

The impact of the fluctuation of f_{em} vanishes only in compensating calorimeters, otherwise it contributes with a term that depends on the energy rather than a constant term. An empirical power law on the form $\sigma_{f_{em}} \propto (E/E_0)^{l-1}$ (with $l < 1$) describes the energy dependence of the electromagnetic fraction, f_{em} . The calorimeter response is then non-Gaussian with a high energy tail. The fractional resolution for hadronic showers can then be expressed by

$$\left(\frac{\sigma E}{E}\right)_{\text{had}} = \left(\frac{a_1}{\sqrt{E}}\right) \oplus a_2 \left(\frac{E}{E_0}\right)^{l-1} \quad (3.25)$$

The value of a_2 depends on the e/h ratio⁶. It varies between ~ 0 for compensating calorimeters and 1 for extremely non compensating calorimeters (equivalent to $e/h \rightarrow \infty$).

Other contributions may have an important impact on the energy resolution. The leakage is one of the most important. The term leakage indicates the non-containment of the showers in the lateral or

⁶A linear relation is assumed for intermediate e/h values ; $a_2 = |1 - (h/e)|$.

longitudinal direction. The loss of part of the showers may also be caused by the presence of cracks and dead area (or cells). A mis-clustering of the calorimeters deposits may also contribute to the leakage as well.

Position measurement

For sampling calorimeters, in addition to their longitudinal segmentation, the active layers are usually segmented along the transverse direction in single readout units, called cells (or pads). The size of the cells is usually chosen to be equal or less than the Moliere radius R_M . The lateral spread of the shower over several cells allows the reconstruction of the impact point of the incident particle with the calorimeter, which is usually measured using the center of gravity of the cell energy, E_i

$$\bar{x} = \frac{\sum_i x_i E_i}{\sum_i E_i} \quad (3.26)$$

The precision obtained on the impact point improves with decreasing cell size as,

$$\sigma_{\bar{x}} \propto \frac{l}{\sqrt{12}} \quad (3.27)$$

It improves also with increasing energy, like

$$\sigma_{\bar{x}} \propto \frac{1}{\sqrt{E}} \quad (3.28)$$

where $\sigma_{\bar{x}}$ represents the resolution on \bar{x} .

3.3 CALICE: calorimetry for ILC detectors

The future linear collider experiment (as discussed in Chapter 2) set constraints on the detector designs to reach the desired physics precision. This is best achieved using the calorimeters with high longitudinal and transverse segmentation allowing to reconstruct the events using the Particle Flow Algorithm (Section 2.4). These constraints give rise to new calorimeters techniques unthinkable in the conventional HEP experiments. The CALICE collaboration was born to study the feasibility to test and to validate few of these concepts. Several physical and technological prototypes were built during the last 5 years, by more than 280 physicists and engineers from various countries.

The calorimeter system in high energy physics experiments normally consists of three main subsystems as shown in Figure 3.8; an electromagnetic calorimeter (ECAL) with the role to detect electromagnetic showers produced by electron (or photon), a hadronic calorimeter (HCAL) to measure the hadron-induced showers (H^\pm and H^0) and a muon spectrometer (or so-called tail catcher) to identify highly penetrating particles such as muons.

CALICE develops several prototypes of these calorimeters with different technologies. Test beam campaigns were engaged since 2006, at different beam facilities such as DESY, CERN and FNAL.

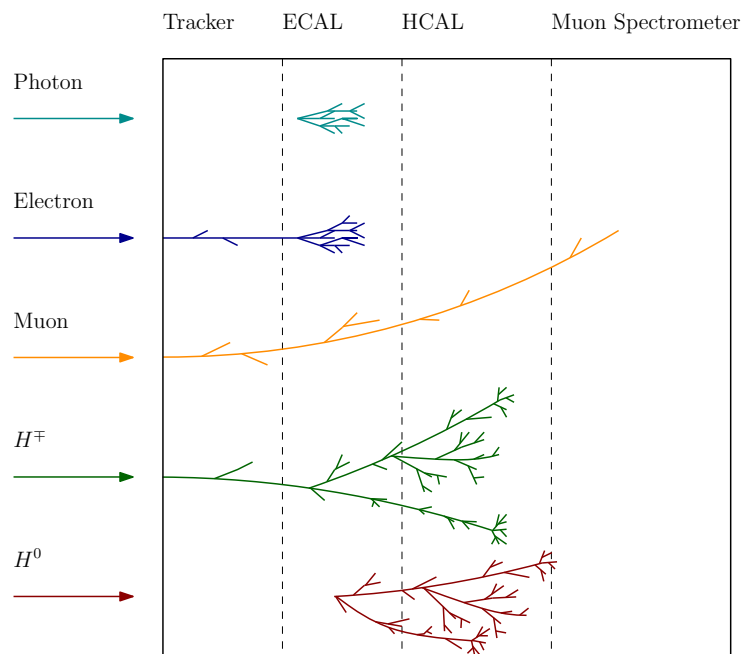


FIGURE 3.8: The main components of a typical particle detector. Different types of particles and their induced interactions.

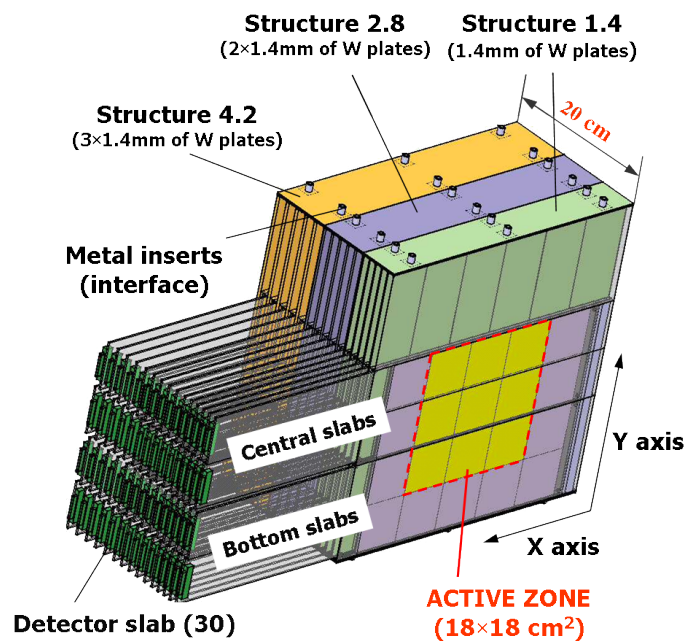


FIGURE 3.9: Schematic view of the SiW prototype.

3.3.1 The electromagnetic calorimeter (ECAL)

As described in Chapter 2, the current ILC and SiD baseline choice of the ECAL is a high granular sampling calorimeter with tungsten absorber and silicon as sensitive medium, so-called SiW-ECAL. As a proof of principle, a physics prototype has been constructed equipped with 30 sensitive layer, and $24X_0$ of absorber. Each sensitive layer has an active area of $18 \times 18 \text{ cm}^2$ and pad size of 1 cm^2 . Other

concepts are under investigation within the CALICE collaboration such as Sc-ECAL using scintillators as active medium, or MAPS-ECAL equipped with silicon detector and digital readout.

3.3.2 The analogue hadron calorimeter (AHCAL)

A first hadronic calorimeter option tested within CALICE collaboration is a steel scintillator *sandwich* calorimeter[48]. Longitudinally segmented in 38 active layers separated by 2 cm of steel absorber. Each active layer is made by 216 scintillator tiles. The central core of the layer of $30 \times 30 \text{ cm}^2$ is covered by a matrix of 100 tiles of $3 \times 3 \text{ cm}^2$ size. The core is surrounded by three rows of $6 \times 6 \text{ cm}^2$ tiles, finally, the outer part is covered by $12 \times 12 \text{ cm}^2$ tiles. The scintillating light produced in the tiles is collected via wavelength shifter fibre and coupled to dedicated silicon-based photo-detector (SiPM). The CALICE-AHCAL prototype consist of ~ 8000 scintillator tiles with an analog readout performed via the SiPM mounted on each tile. A dedicated ASIC ship has been developed to match the requirements of large dynamic range, low noise, high precision and large number of readout channels. A very-front-end (VFE) electronics readout has been designed at DESY.

3.3.3 The digital hadron calorimeter (DHCAL)

An alternative to the scintillator tile readout for the hadronic calorimeters is the digital approach investigated within CALICE. It is based on the recognition, that, if the cells are small enough, the simple counting of the calorimeter hits provides an estimate of the shower energy. This solution was proposed in TESLA TDR[49].

The linearity between the number of hits and the energy of the incident particle is maintained by increasing the transverse segmentation of the readout cells and kept below $1 \times 1 \text{ cm}^2$. For each readout cell (or pad) the information of the hit above a fixed threshold is recorded with no additional amplitude information. Ionisation gas chambers coupled with fine pad readout are best suited to reach this fine granularity. Different gaseous detector technologies are under study: resistive plate chambers (RPC)[50] or gas electron multiplier (GEM)[51]. The RPC has been optimised and the safer avalanche mode has been chosen(Chapter 5). The huge number of channels, more than 40 million, constitutes one of the biggest challenges in term of cost efficient electronics.

3.3.4 Digital versus analogue HCAL and the semi-digital concept

On the basis of simulation studies of the energy resolution of hadronic showers [52], it was shown that with readout pads of 1 cm^2 , the digital approach to calorimetry is expected to be better than the analogue case at low energies, due to the suppression of energy deposit fluctuation (Landau fluctuation). A degradation is however expected at relatively high energy due to an increasing of the probability of multiple hits per readout pad in dense showers. This creates saturation effect in the estimation of the energy and deteriorates the energy resolution. However, the saturation effect can be overcome by reducing the cell size further more or adding coarse amplitude information in form of thresholds. Thus the *semi-digital* option, which consists on a moderate balance between granularity combined with a 2-bit readout ($\equiv 3$ thresholds), constitutes a possible solution.

The hits distribution, ignoring any amplitude information, seen in gaseous based calorimeters, appears more compact than in scintillator, due to different response of low energy neutron and electrons. This

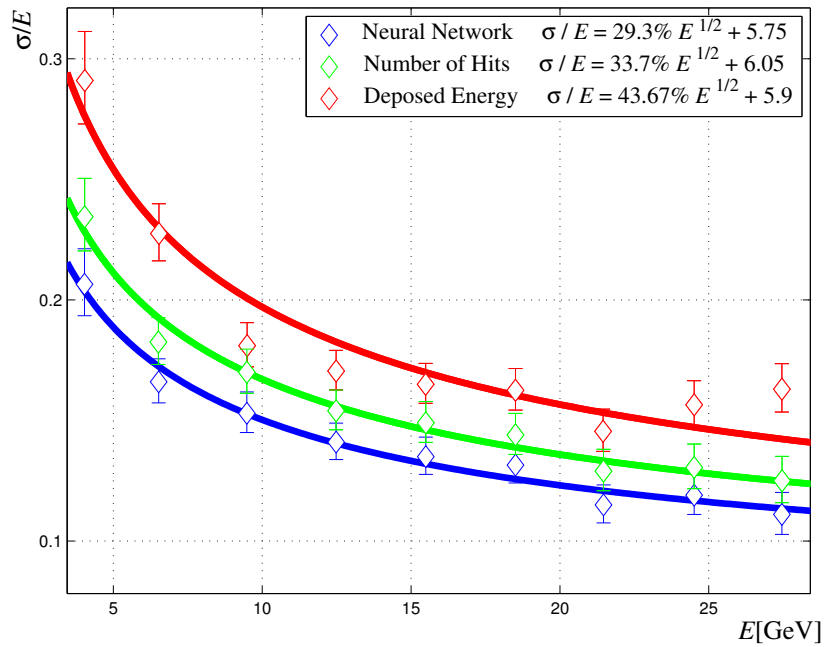


FIGURE 3.10: Comparison of the energy resolution of HCAL option. From[53].

could favour gaseous calorimeter thanks to their imaging performances. However, it was shown, on the simulation basis, that with $3 \times 3 \text{ cm}^2$ tiles with analogue readout, it is possible to reconstruct the internal structure of showers and to separate neighbouring particles even in the case of overlap of hadronic cascades.

An ideal solution is to combine the imaging capability of the gaseous detector and a roughly estimation of the energy with the semi-digital readout (2-bit readout). A such prototype has been build and tested at CERN within the SPS beam lines. A detailed description will be discussed further in this thesis (see Chapter 4).

Part II

Characterization of the semi-digital hadron calorimeter

Chapter 4

Construction and commissioning of a highly-granular semi-digital calorimeter

“My very modest contribution to physics has been in the art of weaving in space thin wires detecting the whisper of nearby flying charged particles produced in high-energy nuclear collisions. It is easy for computers to transform these whispers into a symphony understandable to physicists.”

— George Charpak, Speech at the Nobel Banquet

4.1	General description	62
4.1.1	Structure and absorber	62
4.1.2	The sensitive detector	63
4.1.3	Very-front-end electronics	65
4.2	The Data Acquisition system	66
4.2.1	The hardware	67
4.2.2	Readout modes	68
4.2.3	Power pulsing	69
4.2.4	The data acquisition software	70
4.3	The CERN/PS-SPS Beam-Test (TB) campaigns	71
4.3.1	SPS north area beam lines	71
4.3.2	Beam configuration	72
4.4	Event building	73
4.5	Data quality control	77
4.5.1	Online monitoring	77
4.5.2	Offline monitoring	77
4.5.3	Gain calibration	79
4.6	Conclusion	79

4.1 General description

Most of the studies of ILC and its detectors are based on simulations. However, to prove the validity of such simulations as well as the technical feasibility and the proof of principle, prototypes of the sub-detectors have been built and tested in beam conditions. In CALICE collaboration [39] different types of electromagnetic and hadronic calorimeters have been built and tested so far. This chapter focuses on the description of the semi-digital hadronic calorimeter (SDHCAL) prototype (see Figure 4.1), one of the two calorimeter options considered by the ILD detector and proposed for the future ILC. This calorimeter is designed for the Particle Flow algorithm (Section 2.4) which requires homogeneous and finely segmented calorimeters. The SDHCAL prototype meets these requirements by combining various techniques. Homogeneity is achieved by the use of the large Glass Resistive Plate Chambers (see Chapter 5) as active medium combined with a power-pulsed embedded electronics.

Special care has been taken in the design of the chambers to have a homogeneous sensor: traditional fishing lines (forcing a gas flow) have been replaced by a glued ceramic balls. The gas distribution system has been deported to the sides of the chamber.

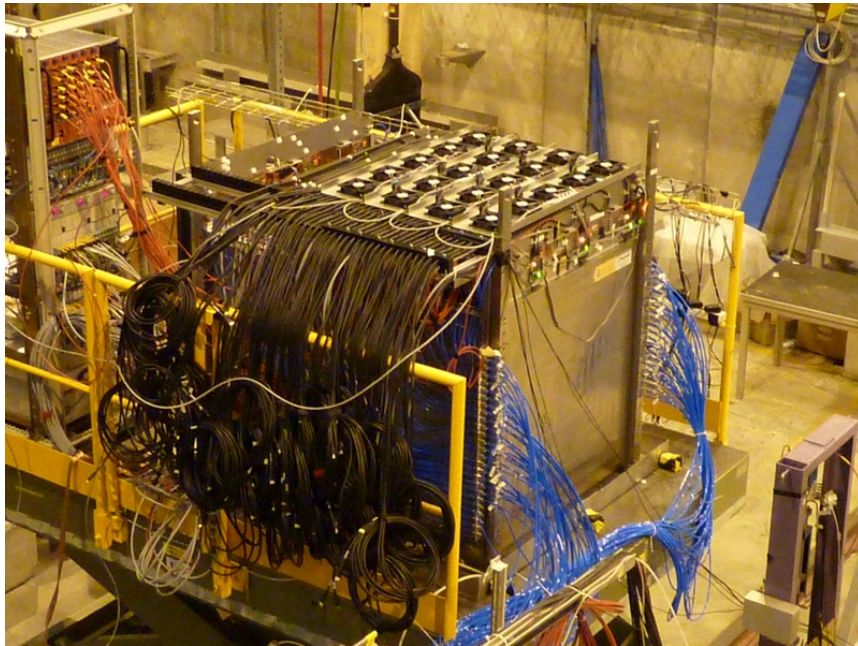


FIGURE 4.1: The SDHCAL prototype in the H2 beam line at SPS/CERN. The black cables insure the readout. The blue tubes bring the gas mixture.

The fine segmentation is achieved transversely by the readout electronic system. An embedded Printed Circuit Board (PCB) with a checked side made of 1 cm^2 cooper pads, reads the signal created the passage of charged particles in the GRPC detector.

4.1.1 Structure and absorber

A cubic meter prototype ($1 \times 1.4\text{m}^3$) of the SDHCAL has been built and tested in 2011 and 2012 (see Figure 4.1).

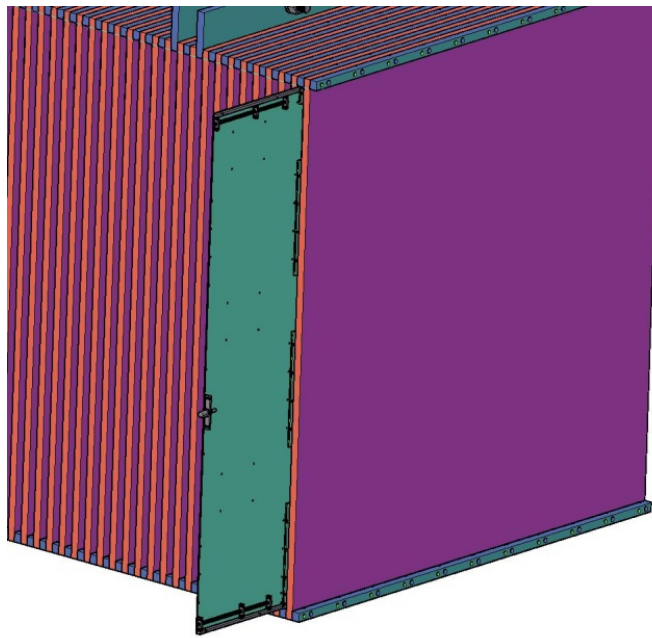


FIGURE 4.2: Three dimensional view of the SDHCAL prototype mechanical structure, showing one cassette inserted.

The prototype calorimeter absorber is stainless steel. The absorber has been manufactured in a self-supporting mechanical structure[54]. It consists of 51 steel squares of $1 \times 1 \text{ m}^2$ and 1.5 cm thick, piled up and separated by 13 mm thick spacers put in along three sides of the squared steel plates. The design allows an easy insertion and extraction of the 11 mm thick cassettes (Figure 4.2). Each cassette contains one GRPC sensor covered by PCB's holding the very-front-end readout electronics. The cassette is a thin box consisting of two 2.5 mm thick stainless steel plates separated by 6 mm wide stainless steel spacers which form the walls of the box. One of the two plates is 20 cm larger than the other to hold the PCBs used for the data acquisition as well as the gas outlets and the high voltage box (Figure 4.3). Both cassette walls and thick stainless steel plates lead for 2 cm absorber which represent roughly $6\lambda_I$ for the whole calorimeter prototype.

4.1.2 The sensitive detector

The 6 mm thick sensitive detectors is made of 3 mm thick GRPC and 3 mm thick PCB. The GRPC is used in saturated avalanche mode: in which the avalanche is initiated by the crossing of the 1.2 mm thick gas gap by one or more charged particles (see Chapter 5). The gap is formed by two electrodes made of borosilicate float glass[55]. The anode and cathode thickness are respectively 0.7 mm and 1.1 mm. The chambers are filled with gas mixture of TFE(93%), CO_2 (5%) and SF_6 (%). This gas mixture has been chosen for its low ionization energy enabling creation of avalanches mainly due to TFE, while the presence of SF_6 and CO_2 plays the role of UV and electron quenchers. (The detail of the role of each gas will be discussed in the next chapter). The high voltage used is typically 7kV. A glass fiber frame with 3 mm width and 1.2 mm height is used to seal the gas volume.

The gas distribution within the chamber is done through an L-shaped channel delimited by the chamber frame and a series of PMMA¹ fibers. Gaps between the fibers allow the gas to leave the channel

¹Poly-Methyl-MethAcrylate, is a transparent thermoplastic

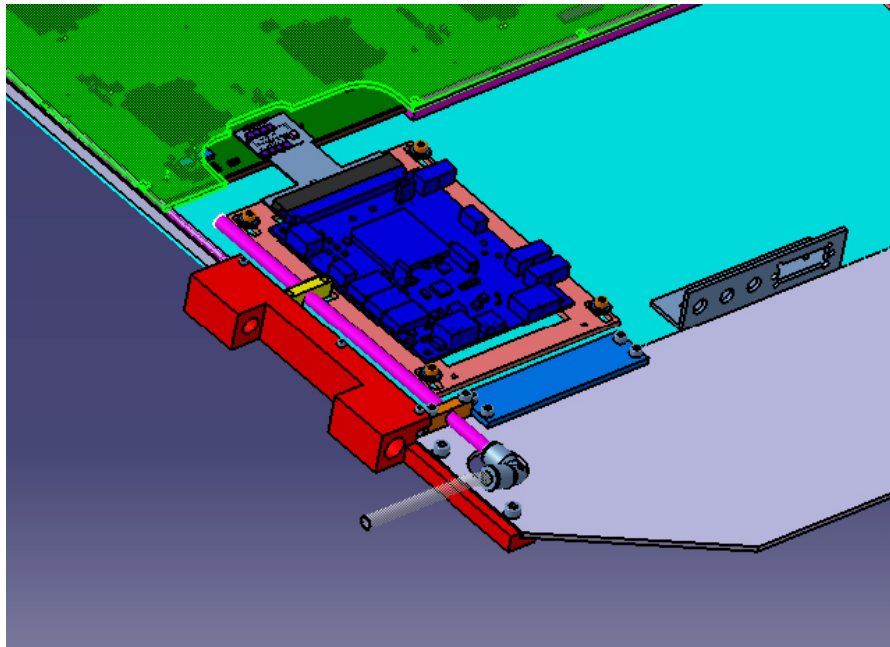


FIGURE 4.3: Assembly details of the cassette's corner showing: the cassette supporting structure (gray), the assertion handlers (red), very-front-end electronic board (green), the detector interface (blue) and gas outlet (pink).

at regular intervals, expanding into the main chamber volume, as shown in Figure 4.4. The usual operating condition is to renew completely the chamber every 20 minutes, which corresponds to a gas flow of 3.61 l/h and over-pressure of 1mbar in the chamber. The over-pressure corresponds to a force per unit of area of 100 N/m^2 , which almost balances the attractive electric field force between the plates.

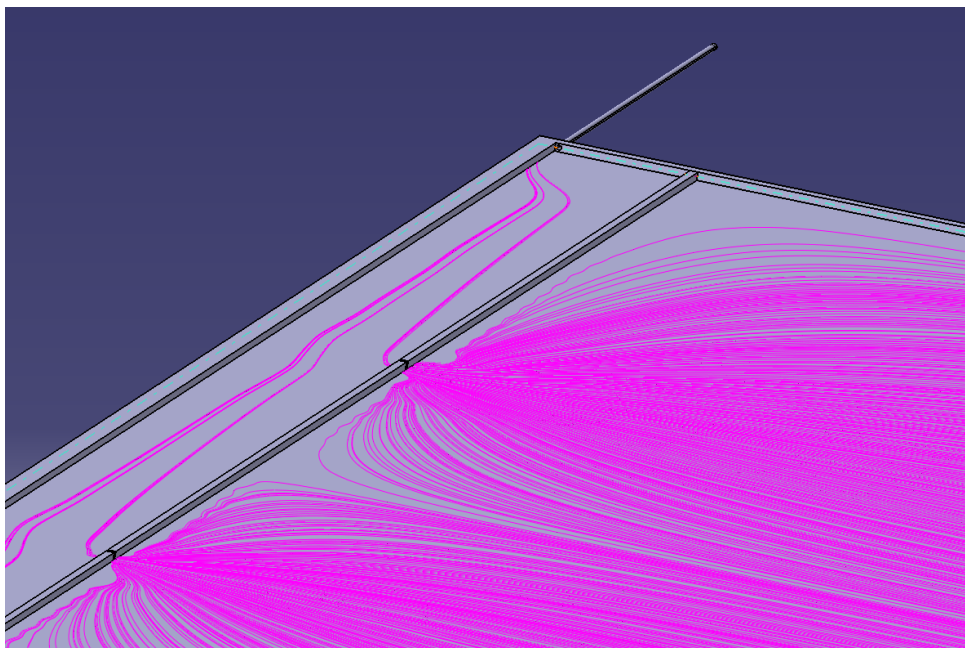


FIGURE 4.4: Detail of internal gas distribution scheme.

The gas gap is maintained by spacers made of precision ceramic (ZrO_2) balls of diameter 1.2 mm. The spacers are glued on the cathode every 10 cm. A finite element analysis [55] taking into account the electric field and the glass plates weight has determined that for this ball distribution, the maximum deflection of the anode glass is of about $44 \mu\text{m}$, while is reduced when the gas circulates. 13 additional balls are added to ensure the physical integrity of the chamber in case of gas circulation but no high voltage. They are placed for each m^2 by cylindrical glass disks glued on both electrodes [55].

The gas tightness is provided by a frame made of robust insulating materials. The frame is 3 mm wide reducing the dead area to less than 1.3%. A gas circulation circuit system was also developed. It allows the renew of the gas content of the chamber taking into account the fact that the gas inlet and outlet are both in one side of the chamber.

4.1.3 Very-front-end electronics

Design

A 1m^2 GRPC sensor is tiled with 6 PCB, $(1/3) \times (1/2)\text{m}^2$. The PCBs have eight layers. One external face presents 1536 copper printed pads of 1cm^2 . The copper pads are separated by $406 \mu\text{m}$ gap. One of the opposite faces, 24 HARDROC ASICs [56] are soldered. Each ASIC is connected to 8×8 pads through the PCB. The electronic channel cross-talk between two adjacent pads is less 2% [57].

Readout chip HARDROC

The very fine granularity of the SDHCAL ($1 \times 1\text{cm}^2$ pads) implies a huge number of electronic channels (over $4 \cdot 10^5$). The HAdronic Rpc Detector ReadOut Chip (HARDROC), is the very front-end chip designed by the *Omega* [58] group for the readout of the RPC's of SDHCAL (Figure 4.5). As the other chips of the ROC family, it implements all the features required by highly granular calorimeters at ILC. It has been designed in SiGe $0.35 \mu\text{m}$ technology. It implements almost all the features required by a highly granular calorimeters at the ILC. HARDROC readout is a semi-digital readout with three thresholds (2 bits readout) and also integrates on chip data storage for delayed readout with a power-pulsing capacity.

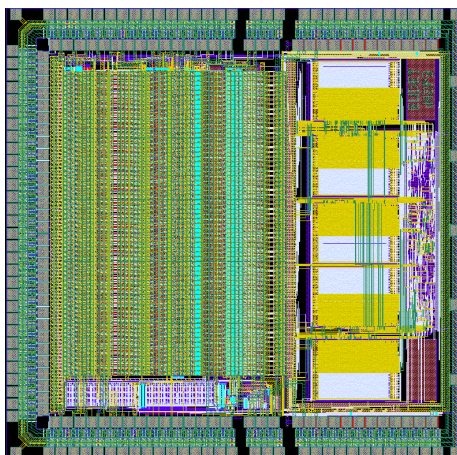


FIGURE 4.5: View of the HARDROC chip. The analogue part is on left, the digital logic and storage are in right part

Each of 64 channels of the chip features:

- a *fast low impedance pre-amplifier* with a variable gain shaped in 8-bit precision;
- a *variable slow shaper* (50 – 150 ns) providing multiplexed analog charge up to 150 pC delivered by pre-amplifier (only used for the diagnostic);
- *3 variable gain fast shapers* followed by low offsets discriminators to auto-trig on signal from 10 fC to 10 pC. The three thresholds are in a ratio 1 – 10 – 100 for better physics performance of the semi-digital and are set by 3 internal 10-bit DACs (Digital to Analog Converter);
- a *128 deep digital memory* to store the 64 encoded discriminator outputs and bunch crossing identification (BCID) coded in 24-bit counter, when one of the channel is triggered the counter is incremented on the 5 MHz clock;
- a *power pulsing*: integration of a Power On Digital module (POD) for the 5 MHz and 40 MHz clocks management during the readout, to reach $10\mu\text{W}/\text{channel}$.

To readout the GRPC detectors of the SDHCAL, ASU of the same size (1m^2) are needed. Feasibility constraints make the tasks of circuit production, components soldering, testing and handling of the assemblies, exceedingly difficult in the case of a single PCB of one square meter. The solution of dividing that circuit in 6 more manageable ASU boards was adopted as shown in Figure 4.6.

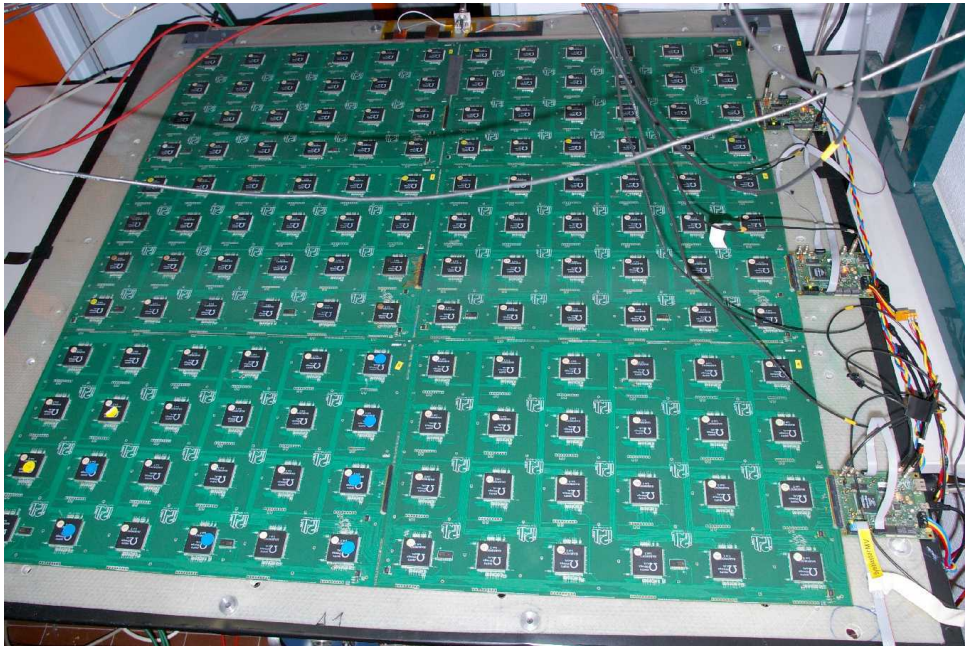


FIGURE 4.6: The electronic of 1m^3 GRPC composed by 6 ASUs connected to 3 DIF.

4.2 The Data Acquisition system

The general architecture of the data acquisition system (DAQ) of the SDHCAL prototype is schematized in the Figure 4.7. The DAQ is connected to the computer network in two main ways: the first one using HDMI transmission protocol responsible of the synchronization of the whole system, second one using the USB transmission protocol which takes care of the data transmission and the register control. A Synchronous Data Concentrator Card (SDCC) manages the synchronization of the system. It receives the commands from the computer network (through USB) and sends them synchronously

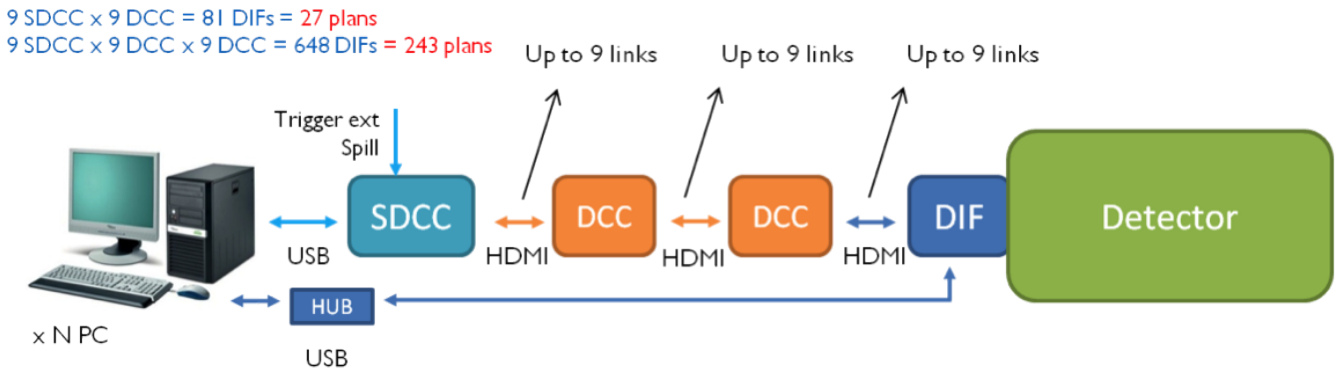


FIGURE 4.7: Scheme of the SDHCAL acquisition system.

through HDMI cables to the different Detector InterFace cards (DIFs), which are the direct link to the active layers. The limited number of the HDMI output ports of the SDCC (9 outputs), additional cards, Data Concentrator Card (DCC), has been added and used as IN/OUT devices to send commands to large amount of DIFs. However, with one level of DCCs (with 9 outputs each) only 81 DIFs can be connected to DAQ. Since each active layer of the prototype is equipped with three DIFs, thus one level of DCCs allows to readout only 27 layers. In order to operate the full prototype's units, a second level of DCCs was added allowing the readout up to 729 DIFs (corresponding to 243 SDHCAL prototype layers).

The operation of the DAQ system needs only one computer, to send the commands to the SDCC card, while several computer units are needed to receive the data. Their number was optimized so it has no incidence on the data flow.

4.2.1 The hardware

In the following, a description of the different components used by the acquisition system.

Detector InterFace (DIF)

The DIF, is sketched in Figure 4.8. The core of DIF is an Altera FPGA Cyclone III[59]. Through USB and HDMI connectors to the DAQ, the data transmission from/to the active layer is digital and goes to the FPGA, which is also connected to two small connectors in case of DIF-to-DIF communication needs. An additional module to monitor the current consumption and the DIF temperature is also present.

The DIF needs 2 different power supplies. One of 6 V which serves to create 5 V for the USB devices using regulators, and another of 5 V serves to distribute the currents for the other devices on the DIF, such as the FPGA which needs 3.3 – 2.5 – 1.2 V, but also to power the active layer electronics (3.3 – 3.5 V).

Each DIF, has an identification number (DIF_{id}), it can be on read the card board or from the network computer by reading the EPROM from USB devices.

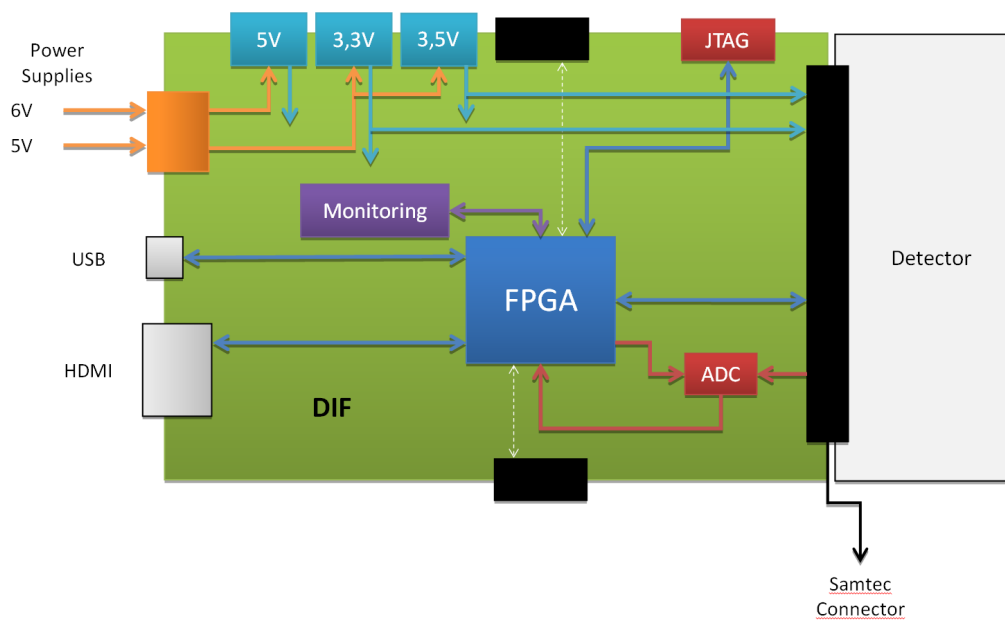


FIGURE 4.8: Scheme of the detector interface representing its main components.

Slow control (ASIC configuration)

The slow control is the configuration of the ASICs on the detector. Each ASIC has its own configuration because of a natural spread in the pedestal, gain and thresholds values. During the slow control, these values are calculated from a scan of the 7200 ASICs in the prototype, allowing the homogenization of the response.

One cassette holds 144 ASICs. Each ASIC needs 872 bits to be configured. When slow control command is sent, more than 6Mbits are sent to the whole detector from the computer network. A 16 bits Cyclic Redundancy Check (CRC) is sent at the end of the transmission to verify the configuration.

4.2.2 Readout modes

After the configuration of the ASICs, the data acquisition can be started following two main modes: the ILC and trigger modes.

- In the ILC mode, or trigger-less mode, the acquisition is started at the beginning of the spill signal. The ASICs are continuously in data taking, until the end of the spill, or until the memory of one of them is full. In latter case a ram-full signal is sent to the SDCC, generating a central stop of the acquisition. Simultaneously, a time-stamp called Bunch Crossing Identifier (BCID) is synchronized with the ASICs one, and is recorded by the DIF and included in the data stream. The readout of ASIC is automatically performed at the end of the acquisition. The DIF's FPGA performs the readout of all ASICs under its control. The data are stored in the FPGA memory and send with other information, specific to the data format, to the computer network through USB link. In addition to the readout function, the FPGA generates also a busy signal which reaches the SDCC in order to avoid starting of new acquisition until all data are read out. When the last ASIC sent its data, the busy signal is released and the DIF can accept again a new

acquisition command from SDCC.

- In the trigger mode, an external signal is used to trigger the readout. The external signal can come from a coincidence with photomultiplier to tag the passage of a particle. It can be also a signal coming from the Cherenkov tubes, which permit to identify the type of incoming particle. The trigger mode is used when the time information of beam particles going through the detector cannot be extracted from the data only. This is typically the case when dealing with small number of sensitive layers².

The raw data format

For every readout operation, the ASIC data are encapsulated by the DIF's FPGA with a header, a trailer and the following information:

- DIF trigger counter (32 bits), counts the number of readout. It is reset at the first acquisition of each run;
- Information counter (32 bits). The bits ranging in $[23 \rightarrow 0]$ counts the dead time corresponding to the time when the ASIC are not acquiring. It is reset in every acquisition. Bits ranging in $[31 \rightarrow 24]$ counts BCID overflow;
- Global trigger counter (32 bits), counts the number of trigger received by the DIF in the case of the trigger mode, or counts the number of readout in the case of ILC mode. It restarts at the first acquisition of each run;
- Absolute BCID (48 bits), increases with the 5 MHz clock coming from the SDCC. It restarts at the first acquisition of each run;
- DIF BCID (12 bits), increases with the 5 MHz clock coming from the SDCC and is synchronized with ASIC's BCID.

4.2.3 Power pulsing

In the ILC operating cycle[60] the active time of collision is expected to occur only during 1 ms every 200 ms. During relatively long inactive period, the ASIC can be turned off in order to reduce the power consumption of the detector and thus reduce the heat dissipation in the calorimeters. This operation is called power pulsing.

With everything on, the power consumption in the SDHCAL prototype is 1.425mW per copper pads. When most of the ASICs are switched off, the consumption is reduced to less than $0.2\mu\text{W}$. By switching on the HARDROC2 only 0.5% of the time, the SDHCAL power consumption is below $10\mu\text{W}$ per channel and sufficiently low to avoid the need of an internal cooling system.

After the switch-on, the ASIC is ready for data taking after a $25\mu\text{s}$ latency [61]. This time is needed to stabilize the digital to analogue converters that set the 192 discriminator thresholds.

During the test beam operations, the power pulsing is synchronized to the accelerator clock by using the particle spill signal delivered by the SPS/PS beam facilities. This signal is required by the DAQ, and should be active during the particles bunches a slightly $100\mu\text{s}$ before. This programmable delay

²Since the ASICs are self-triggered, it can happen that the memory of one of them gets full (ram-full signal) before the external trigger, thus all ASIC memories are reset.

is required before any detector signal can be recorded in the memory, it accounts for the stabilization of the various tensions and currents inside the chip and must be minimum to reduce the power consumption. If the delay is too short, the detector occupancy is dominated by noise until stabilization.

4.2.4 The data acquisition software

The DAQ software is divided in three main parts: the low hardware access that is hiding effective hardware implementation, the configuration data base software handling device description and settings and finally data collection and monitoring. All packages are written in C++ programming language with interactive scripting in `python`. Low level and database C++ libraries are all parsed to `python` object with the SWIG [62] tool.

The low level hardware access

The low hardware access groups are divided in three main parts:

- **USB readout**

DIF and SDCC FPGA's are interfaced with the same USB chip. It is an FTDI³ chip associated to each of the card. The DIF is then uniquely identified by its FTDI device ID stored in an EEPROM and access to a specific device ID is done using either the proprietary library `FTD2XX` or the free version `libFTDI`.

- **Detector readout**

An upper layer software is dedicated to DIF configuration and DIF readout. The class `BasicUsbDataHandl` groups a pointer to a `UsbDeviceDriver` and to configuration buffer handling all DIF and ASIC parameters.

- **DIF manager**

The DIF manager classes present in each computer unit are responsible of the data taking via DIF-USB connection. DIF manager handles the DIFs and chips configuration parameters via a `DIFBDManager` interface. It scans and detects all connected DIF, instantiates one DIF data handler per detected device, distributes configuration parameter and triggers their hardware download. During the data acquisition, it polls thread continuously and reads events on all connected DIFs. Events can be directly dumped to a storage device in LCIO format.

The Figure 4.9 summarises the low level hardware access.

The configuration database

The configuration database (DB) stores and retrieves all parameters needed by the DAQ system. The database itself is hosted on an `Oracle` server at CC-IN2P3 (Villeurbanne, France). A C++ library has been written to interface the SQL database with DAQ software allowing the user to insert and query data without any SQL knowledge.

³Future Technology Devices International, in abbreviation, FTDI, is a Scottish privately held semiconductor device company [63].

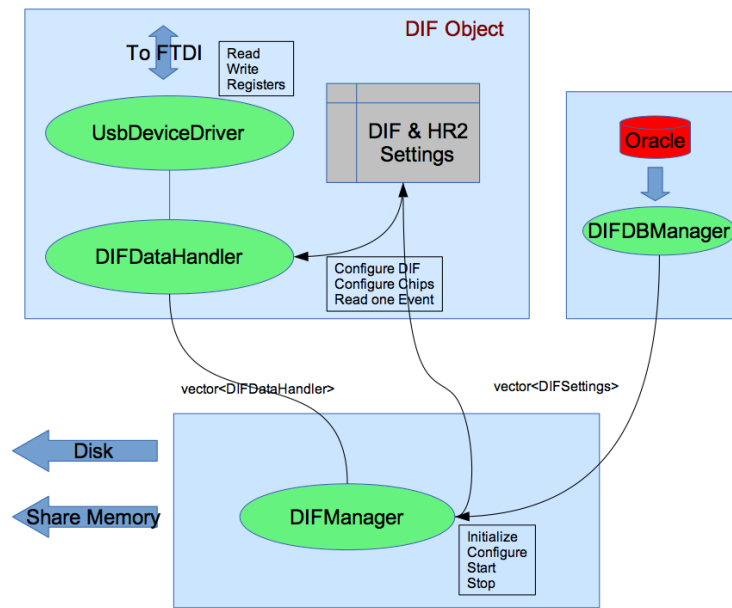


FIGURE 4.9: Low level software architecture

Global data acquisition

During the data taking, several computers are involved, the use of communication framework becomes then necessary. Thus, the CMS data acquisition XDAQ framework has been chosen. It provides:

- a communication with both binary and XML messages;
- a XML description of the computer and software architecture;
- a web-server implementation of all data acquisition application.

Each computer handling DIFs holds a DIF manager XDAQ application obeying to a message driven state machine responsible for initialization (USB scan and DB download), configuration (DIF and chips setting) and running (DIF readout and storage).

4.3 The CERN/PS-SPS Beam-Test (TB) campaigns

In 2011 and 2012, the SDHCAL was exposed to particle beams in the range from 5 GeV to 100 GeV at CERN SPS (Super Proton Synchrotron) beam facilities on main lines: H2, H6 and H8.

Tree main campaigns have been engaged: in May 2012 on beam line H2 (2 weeks), in August and September 2012 on line H6(2 weeks) and finally in November 2012 (2 weeks) H8. More than $4 \cdot 10^5$ of pions and 10^6 of muons has been recorded over these periods.

4.3.1 SPS north area beam lines

The SPS is one of the accelerator complex of CERN, measuring 7 km in circumference. The SPS provides proton beams to the LHC, the COMPASS experiment and test beam experiments. The SPS

is alimeted by a smaller storage ring, the Proton Synchrotron (PS), it can accelerate protons to an energy of up to 450 GeV.

The process of the secondary beam production starts from the steering of 450 GeV/c SPS protons on the Beryllium target (T4 or T2). The protons delivered by the SPS shine on the target of Beryllium leading for strong interactions with the target nuclei and create secondary particles (mainly pions) with a wide momentum spectrum. A complex of magnetic dipoles insures the beam distribution to different experiments.

The momentum of the secondary particles for three lines H6, H8 and P0 are selected with magnets B1T, B2T and B3T. The TAX blocks limit the beam angle and thus can control the particle momentum and serves also as beam dump. The Figure 4.10 resumes the production of secondary beam at SPS.

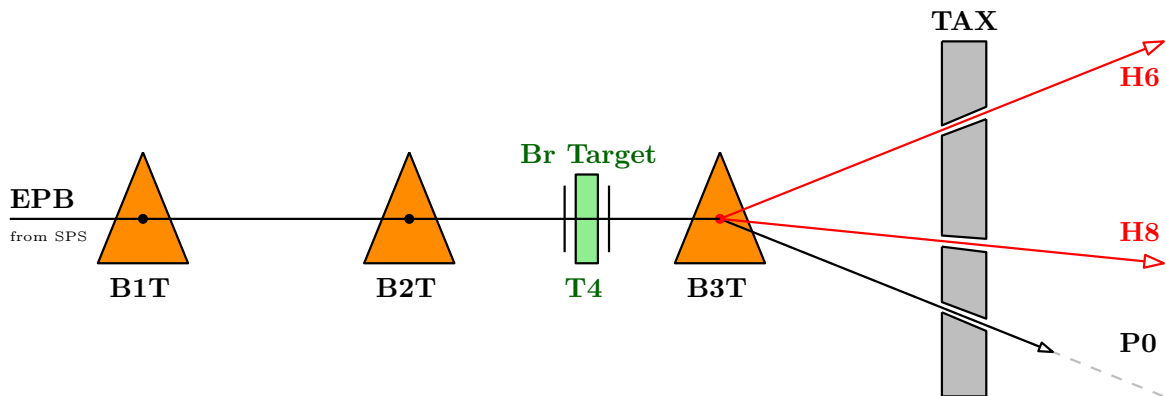


FIGURE 4.10: Secondary beam generation for the beam lines H6, H8 and P0.

For the success of the test-beam experiments, a beam tuning is of great importance. Thus the optimisation of the few beam-line at CERN is under the responsibility of users. This requires the control of several dipoles, quadrupoles and collimators along 500m of beam-lines from the Beryllium target to the detector setup.

4.3.2 Beam configuration

The SDHCAL is composed with GRPC detectors as active medium whose recovery is limited at 200Hz/cm² according to previous studies [64]. The pions beam in both lines H2 and H6/H8 was enlarged to reduce the particle occupancy in the detectors. In addition, several absorbers were moved in the beam line to reduce the beam rate. A particle rate of 10⁵/spill was maintained over the runs and measured with the wire chambers and the scintillators present along the beam line.

Beam time structure

The beam is divided over the experiments present in the North area. Thus the beam time structure depends on number of experiments and on the needs of each one. For the H2/H6/H8 line spill (beam bunch train) length is of about 10 s each 50s.

On the basis of the Figure 4.11, the white and yellow curves, indicating the magnetic pulse high and the instantaneous beam intensity respectively, define four stages:

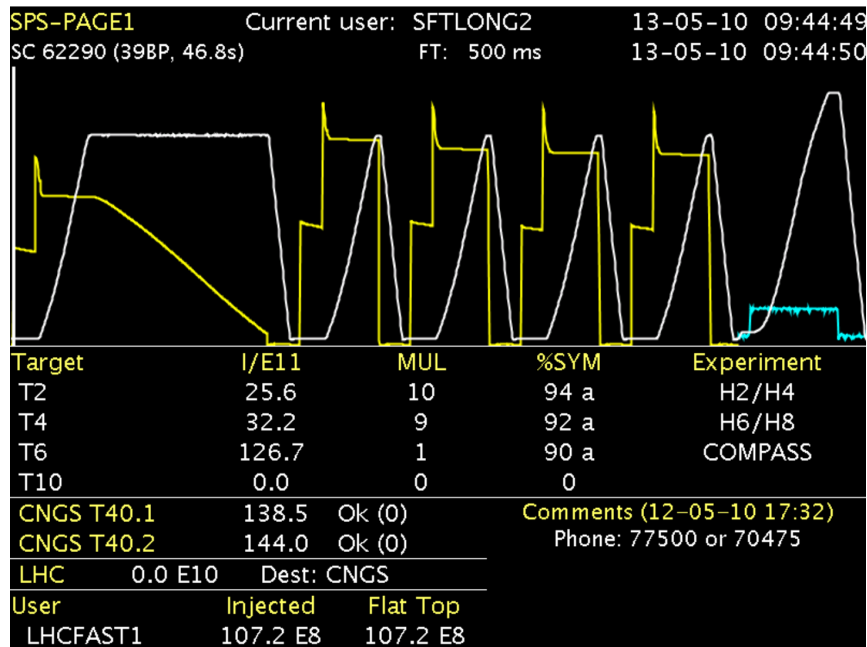


FIGURE 4.11: Example of SPS spill configuration displayed in the control room of the beam line. The white curve indicates the magnetic pulse cycle, the yellow one indicates the instantaneous intensity in the machine.

- **Flat bottom**, in which the particle are injected in the SPS with low momentum. Two injections are visible in the Figure 4.11;
- **Ramp-up**, the intensity of the magnetic filed increase to match the beam acceleration. In this phase, the intensity of the beam is constant;
- **Flat top**, the particle beam is stabilized, then the extraction can begin;
- **Ramp-down**, remaining particle at the end of Flat top are dumped and the SPS magnetic cycle returns to the Flat bottom.

4.4 Event building

The trigger-less mode, described previously, was used of the data acquisition; in this mode, each very-front-end chip auto-triggers and stores the information. The acquisition system reads the full detectors when the memory of at least one chip is full. The collected data thus include not only the information about the incoming particles (pions, muons or cosmons ...) but also the intrinsic noise of the detector. The average duration of one acquisition window is of ~ 30 ms. Within each window, the time of each hit with reference of the start of the acquisition is recorded by a counter (*time-stamp*) or BCID increasing by steps of 200 ns.

Preliminary data format

The raw data are then stored in LCIO format[65] by the acquisition system. Each acquisition window is stored in a preliminary LCIO file as an LCEvent. The LCEvent contains a collection of fired pads including Bunch Crossing ID (BCID), the ChannelID, AsicID and DifID.

The algorithm

The physical event candidate are built from hits collection using a *time clustering method*. In this method, a histogram of hit time occurrence is filled for the full acquisition window with bin-width set to the time clock precision. Only clock tick with a number of hits higher than a certain threshold T_{hit} is used to initiate the time clustering process. Hits belonging to the adjacent clock ticks in a window of $\pm t_{win}$ are combined to build a physical event. Care was taken to ensure that no hit belongs to two different events. The information related to the coordinates of the hits, determined from the location of the fired pad and the related active plate are then saved together with the threshold reached (either 1, 2 or 3).

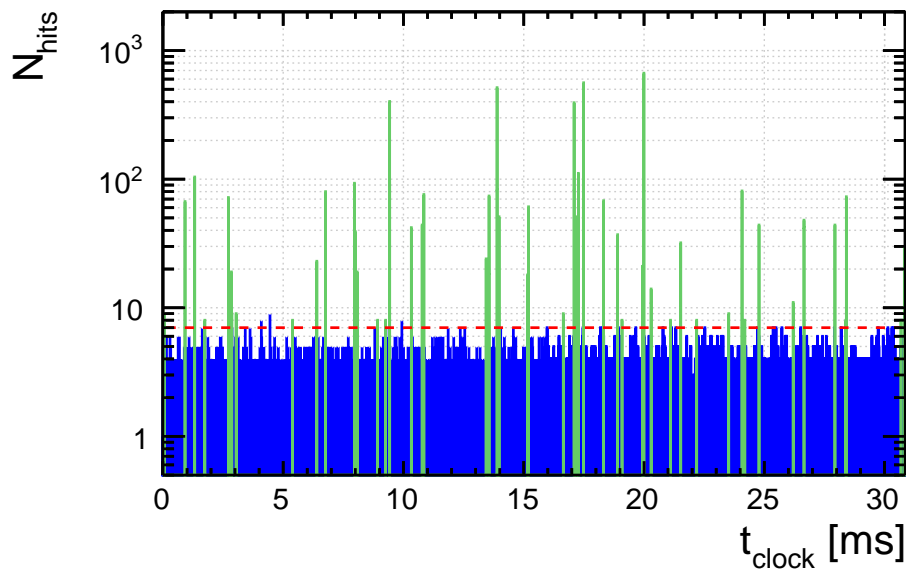


FIGURE 4.12: Time spectrum of an acquisition window with a granularity of 200 ns. The physical event candidates are highlighted (green) over the background noise (in blue). The red line represents the threshold over which the events are considered.

For the SDHCAL prototype the value $T_{hit} = 7$ is chosen as minimum of hits required to build an event. This allows the rejection of intrinsic noise while eliminating a negligible fraction of hadronic showers produced by pions of energy larger than 5 GeV. The width of the time window can be determined from the distribution of the mean distance of found peak time (time bin with $N_{hit} > T_{hit}$) to other bin times, $\delta t = (t - t_{peak})$. The δt distribution is shown in the Figure 4.13. A peak around 0 is observed as expected, where the width of the obtained distribution is of about $\sigma(\delta) 3 \times 200$ ns for pions dedicated runs. Thus taking hits corresponding the peak time within $t_{peak} \pm 200$ ns was enough to build a physical event candidate. The Figure 4.14 shows the distribution of number of hits of the physical events candidates for 80 GeV pion run.

Geometry building

The information provided by the acquisition chain about the hit contains identification numbers (ChannelID, ChannelID, ChannelID) and the position of the DiFID in the layer and the detector. The relative position of pads in the ASIC, and the position of ASICs in the DIF are known from

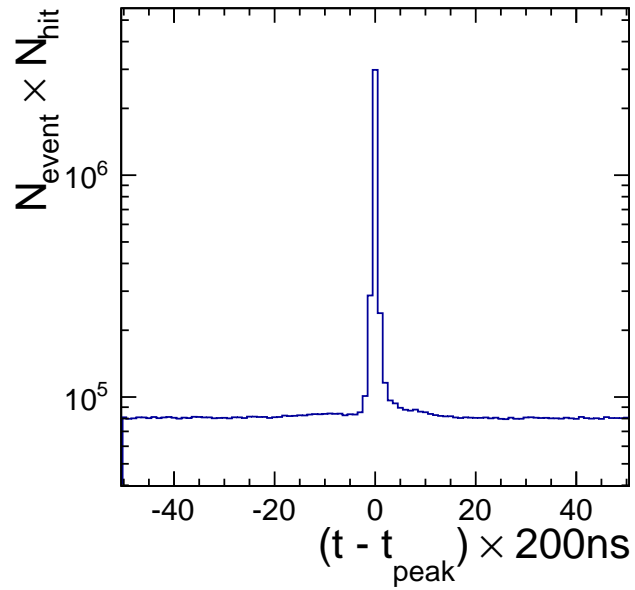


FIGURE 4.13: Difference between the found time peak and the time bins.

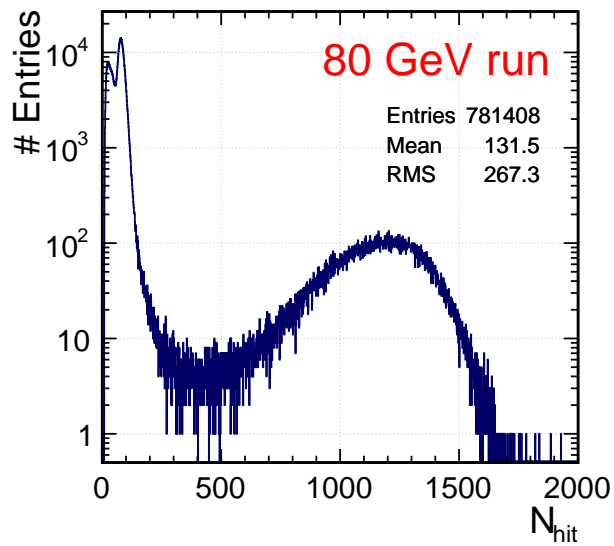


FIGURE 4.14: The distribution of number of hits of the reconstructed events. The first two peaks corresponds to the cosmic and beam muons respectively. The contribution around $N_{hit} = 1200$ corresponds to interaction pions.

the hardware configuration. These information combined with the relative positions of the DIFs and chambers in the calorimeter allow the reconstruction of the hit coordinates.

Fake event removal

An additional selection is applied to the event candidates to remove the noise-induced events, such as the minimum layer fired on each event. The Figure 4.18 shows a typical examples of events produced by electronic grounding problem. These events can easily removed by this selection, since the hits are concentrated in one or two layers. Further selections, based on more sophisticated variables, can be used to avoid the events piled-up with coherent noise.

The C++ package

The introduced event-builder was implemented in a C++ framework called **Trivent** and released in a **ILCSOFT** package. The core algorithm is implemented as a **Marlin** processor. It takes an input a **LCIO** file with a collection of **LCGenericObjects** containing all the information saved by the detector, where a **LCEvent** corresponds to a ram-full. A configuration file in XML format containing the relative position of DIF in the detector is required.

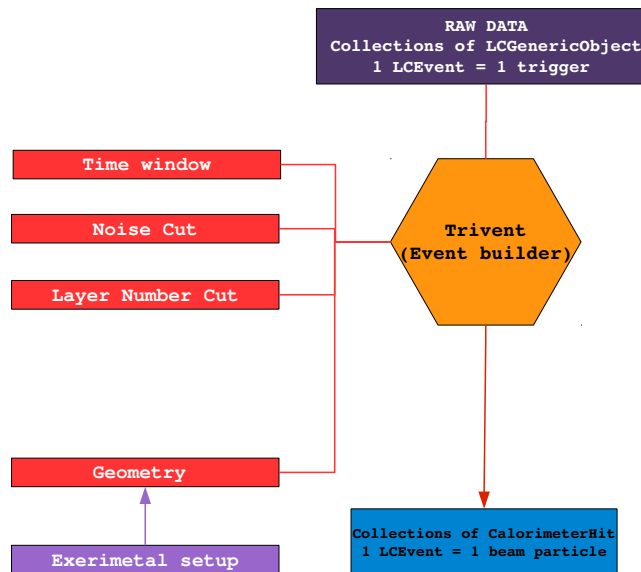


FIGURE 4.15: Trivent event builder diagram.

The running of the program is done by supplying a steering file containing the processor parameters (cut-list, file paths, etc). **Trivent** provides, after running, a **LCIO** file containing **CalorimeterHit** collection, in which each **LCEvent** corresponds to a physical event.

Another module allowing to translate the **LCIO** file to **ROOT** files was also implemented and included in **Trivent** framework. This allows the use of the **ROOT** package for data analysis. The Figure 4.15 summarises the **Trivent** working flow. An example of two reconstructed 90 GeV pion showers is shown in the Figure 4.16.

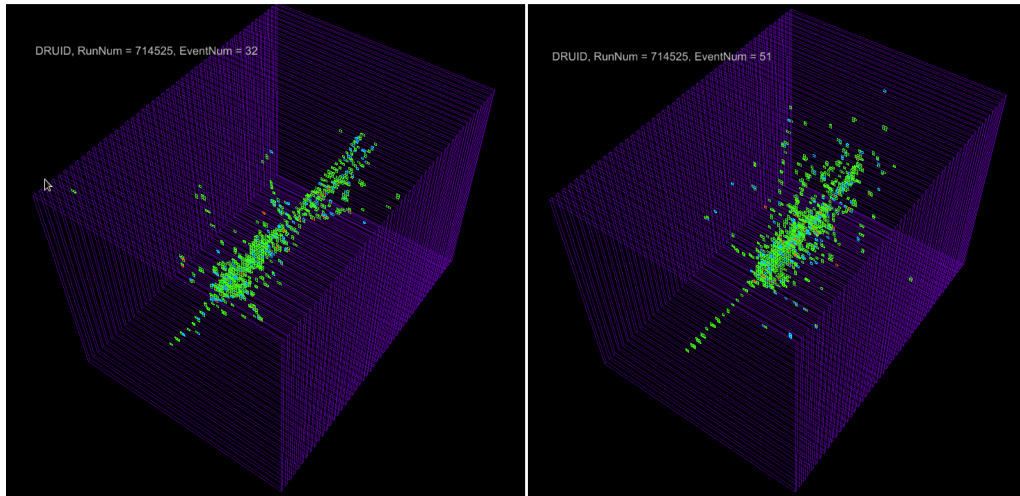


FIGURE 4.16: Examples 90 GeV pion showers in the SDHCAL prototype.

4.5 Data quality control

During the data taking of the beam test periods, several controls have been done to check the validity of the saved data.

4.5.1 Online monitoring

First, an online monitoring reads the data stream from the DAQ and makes a fast analysis in order to estimate the chip occupancy (chip noise) and the detection efficiency of each chamber. The online monitoring constitutes an important step in the data taking, since noisy channels can be isolated and mask them at very-front-end electronic level.

4.5.2 Offline monitoring

Using the event-builder previously introduced, an offline monitoring is performed. It is focused on the measurement of noise, and the performances of chambers and their stability over the time.

Noise estimation

Two kind of noises can be distinguished: intrinsic and coherent noises. Intrinsic noise is defined as the hits outside an event (Figure 4.12), due to the gain fluctuation in GRPC's. Its intensity is a function of temperature and the polarisation high voltage. The Figure 4.17 shows the distribution of the noise in unit of the DAQ time-stamp with an average of $\sim 0.35\text{hit}/200\text{ ns}$. This measurement gives an estimation of the contamination of noisy hits along physics events and shows that the GRPCs are almost noise-free.

Among the reconstructed events some are clearly due to electronic noise. These events are characterised by the recurrence of many hits belonging to the same electronic slab or to the whole electronic layer

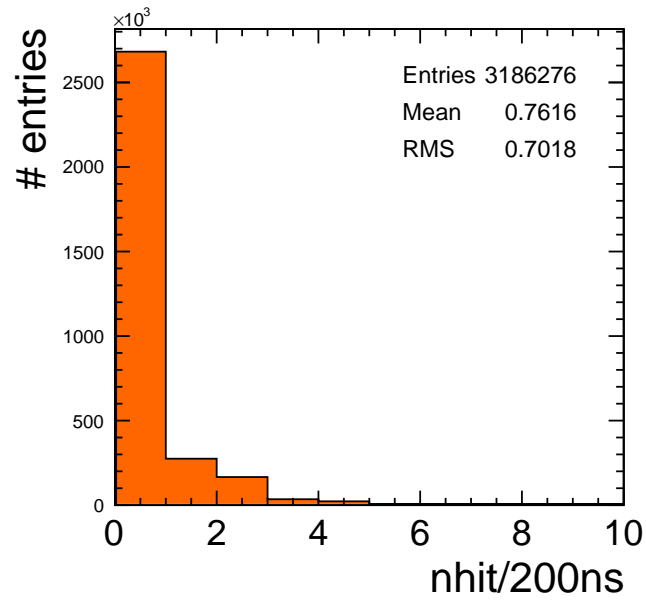


FIGURE 4.17: Intrinsic noise of the GRPC sensors

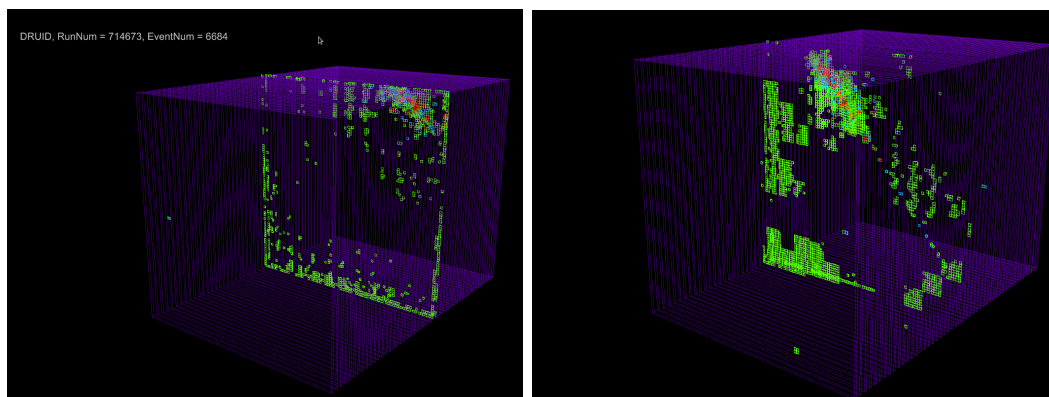


FIGURE 4.18: Example of coherent noise events in the SDHCAL prototype.

(made of three slaps), as shown in the Figure 4.18. They appear with an incidence of $2/10^6$ events and they are easy to identify thanks to their specific topology.

Detection efficiency

The SDHCAL detection efficiency is estimated for each of 48 chambers of the prototype using muon beam tracks. The efficiency is defined as the probability to find at least 1 hits within 3 cm of the reconstructed muon's track. An average efficiency of $\sim 95\%$ is measured over all the chambers as shown in Figure 4.19. A detailed description of the efficiency estimation will be described in the next chapter (cf. Chapter 5).

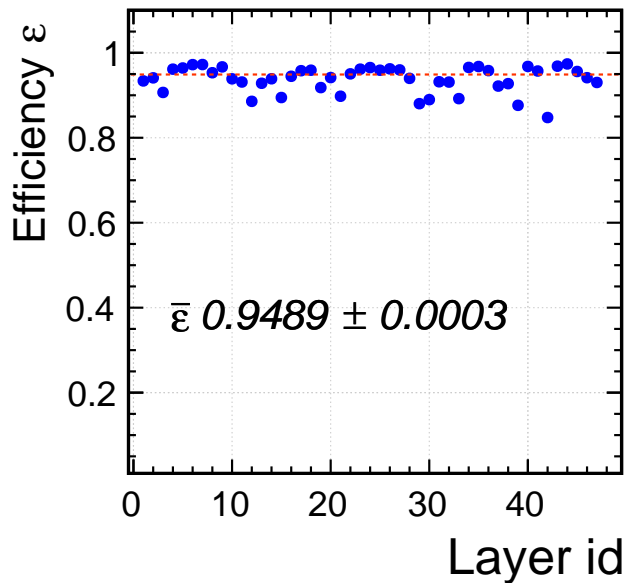


FIGURE 4.19: Detection efficiency of the 48 chambers. The dashed red line is the average efficiency of the prototype.

4.5.3 Gain calibration

During the PS beam test, a preliminary gain calibration method was tested to homogenise the detector response of all the channels and reduce the gain fluctuation. The gain calibration consists on taken a *noise* run (without beam from the accelerator) and calculates the occupancy of each channel over the full calorimeter. Then a correction factor defined by,

$$C_{ch} = \frac{G_{ch}}{\langle G \rangle_{det} \langle G \rangle_{Dif}} \quad (4.1)$$

is applied. Unfortunately, the short time schedule for the beam-test redefined the priorities of the experiment and this method was not longer tested during the test beam. Hopefully, the method will be applied on the future beam-test scheduled on the October 2014.

A software-based method gain correction is however explored in this thesis and fully described in the Chapter 7.

4.6 Conclusion

A technological prototype for a semi-digital hadronic calorimeter has been achieved and successfully operated. The calorimeter is finely segmented as needed for the Particle Flow algorithm. It has an

embedded read-out electronics that has successfully taken data with power-pulsing mode. It has been demonstrated that cost-effective GRPC can operate with high efficiency and uniformity on large area.

Chapter 5

Characterisation of the SDHCAL prototype using muons

“... when you have eliminated the impossible, whatever remains, however improbable, must be the truth.”

— Sir Arthur Conan Doyle

5.1	The SDHCAL glass resistive plate chambers	82
5.2	Physics of GRPC	83
5.2.1	Gas Ionisation by a charged particle	84
5.2.2	Electron multiplication	87
5.2.3	Induced signal	90
5.3	Study of the GRPC performance using minimum ionising particles	92
5.3.1	Track reconstruction	92
5.3.2	Efficiency and multiplicity	94
5.3.3	Angular dependence	95
5.3.4	Induced signal measurement	96
5.3.5	Chambers uniformity study	100
5.4	Conclusion	101

The calibration of a very high granular calorimeter such as the SDHCAL prototype requires a complete characterisation of its sensitive part. This aspect becomes even more important in the case of highly granular gaseous calorimeters. The complete characterisation of the sensitive medium can be then studied by the measurement of two quantities which condense the response information of the device: the detection efficiency and pad multiplicity (the number of fired cells) when a single particle is crossing a sensitive layer.

Muons are considered as minimum ionising particles (MIP) since they have a very little chance of being stopped or deflected in the detector. They lose roughly $1.5 - 2.5 \text{ MeVg}^{-1}\text{cm}^2$ on a wide energy range (from $1 \text{ GeV}/c$ to $100 \text{ GeV}/c$) for various solid mediums, as shown in Figure 5.1¹. This allows

¹Note that over $100 \text{ GeV}/c$ the energy loss by radiation becomes important which may produce a small electromagnetic shower.

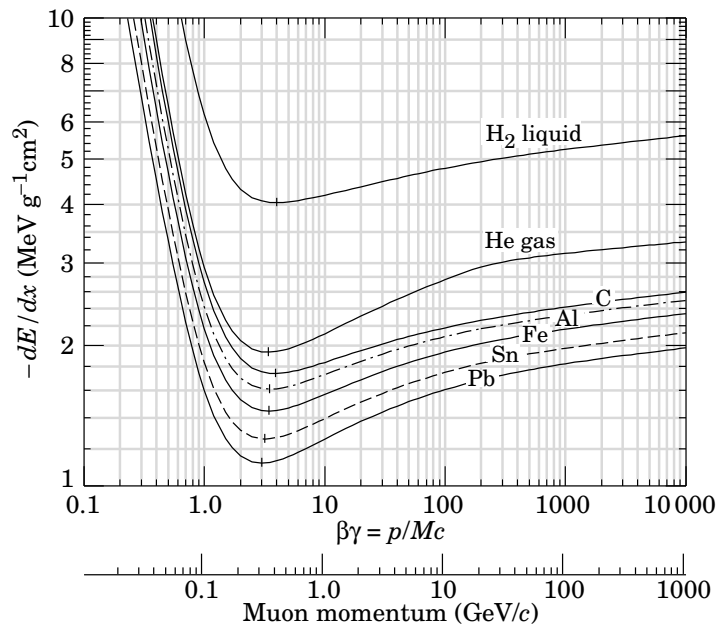


FIGURE 5.1: Mean energy loss in few different mediums as function of the muon momentum.

the measurement of the detection efficiency by reconstructing their passage inside the detector. The intrinsic spacial resolution of the SDHCAL prototype allows then the study of geometrical response which permits a local calibration.

The muons used in the following study have two origins: cosmic rays and accelerators. In both cases, they are produced in the decay of pions produced by nuclear interaction of an incident particle produced either in accelerator facilities or from cosmic origin with a fixed target or on the terrestrial atmosphere respectively. These reactions produce various of secondary particles, in which muons are the main component due to its relatively long life-time. Large number of muon samples are then recorded by the SDHCAL prototype with different energies for beam muons (see Chapter 4), and different incidence angle for cosmic muons.

In this chapter, a description of the physics of the GRPC is first introduced and argued with simulation studies. The muon tracks reconstruction method is then described, followed by characterisation of sensors. A method for the measurement of the induced charge spectrum in the GRPC is presented. The results presented here are based on the data taken during the summer 2012 at SPS beam facilities (see Chapter 4).

5.1 The SDHCAL glass resistive plate chambers

Resistive plate chambers (RPC) were pioneered in 1981 by R. Santonico and R. Cardarelli [66] as a spark counter and as a parallel plate avalanche chamber (PPAC). This apparatus allows to amplify the deposited energy by the ionisation when a charged particle cross the gas mixture. With simple and robust components, this kind of detector was used in many HEP experiments, e.g: ATLAS [67], CMS[68], BaBar[69], BELLE [70] and OPERA [71]. Thereby, many technological solutions were developed over the years to build RPC detectors corresponding to the needs and the context of each experiment.

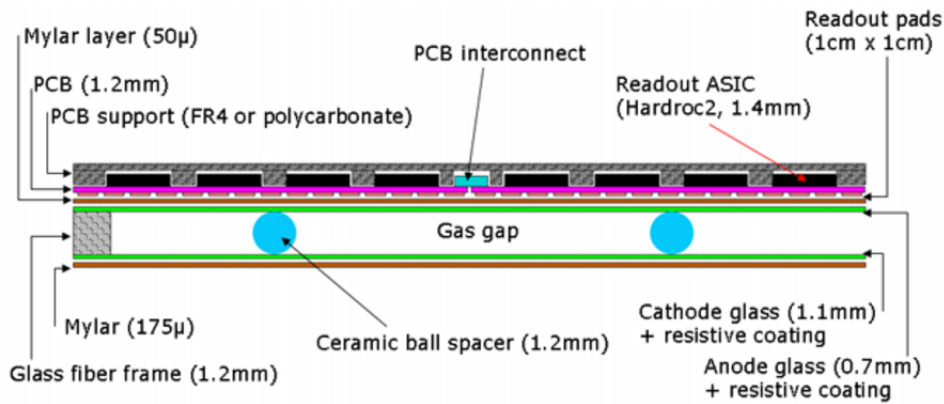


FIGURE 5.2: Schematic view of Glass RPC

Following the actual detector design in the future ILC (Chapter 2), the hadronic calorimeter will be located inside the magnetic field. Cost effectiveness requires a very compact detector, and for sampling calorimeters, a sensitive medium (sensor) as thin as possible having a high efficiency (over 95%) and good homogeneity. The Glass Resistive Plate Chambers (GRPC) satisfy all these requirements (see Chapter 4) in addition to their simple design and cheapness. Unlike Bakelite RPC [66], they do not need surface treatment and thus avoid the related ageing problem [72].

Detector studied and used in this thesis is the GRPC. As shown in the Figure 5.2, it is made of two borosilicate float glass plates. The thinner glass of 0.7 mm is used to build the anode while the thicker of about 1.1 mm forms the cathode. The glass has a resistivity of $10^{11} - 10^{12} \Omega\text{cm}$. They are kept separated by the 1.2 mm gap. A small ceramic ball spacers of 1.2 mm glued on the cathodes every 10 cm, maintain the gas gap over the entire chamber area. The outer side of the glass plates are covered by a thin layer of resistive coating made of silk-printed colloidal carbon paint, connected to the polarisation high voltage. A $50 \mu\text{m}$ Mylar layer separates the anode from the readout pads copper, of the electronic board. The typical high voltage of about 7 kV insures a uniform polarisation electric field in the gas gap.

The operating gas mixture is composed of 93% of $\text{C}_2\text{H}_2\text{F}_4$ TFE, 5% of CO_2 and 2% of SF_6 . The TFE has been chosen for its low minimum ionization energy enabling efficient creation of avalanches, while CO_2 and SF_6 are used as UV and electron quencher respectively. The proportion of SF_6 has been determined after some preliminary studies of small chambers [73].

The development of the GRPC, used for of this study, is the result of many years of R&D (Research and Development) done by the IPNL² group (further details can be found in [73]).

5.2 Physics of GRPC

All the electronically readout gaseous detectors follow the same basic working principle. The electrons from the primary ionization of the gas molecules left by a charged particle crossing the detector, are accelerated by an electric field producing secondary particles. The amplified signal is then detected mostly by the influence of the moving charges.

²IPNL: Institut de Physique Nucleaire de Lyon.

This section will illustrate the principle of GRPC. More detailed discussions can be found in [74, 75]. The theoretical model of the avalanche growing and the induced signal being discussed here is the one proposed in [74–78] which has been validated by many experimental data.

5.2.1 Gas Ionisation by a charged particle

Ionisation process

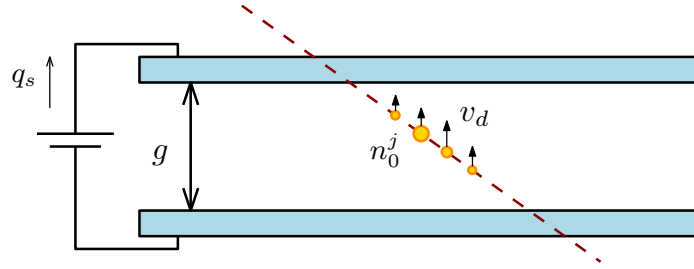


FIGURE 5.3: Schematic view of an RPC with ionisation produced by the passage of charged particle in a gas gap of thickness g . n_0^j is the number of electrons in the cluster j and v_d their velocity.

A charged particle crossing the gas in the resistive plate chamber leaves a track of ionisation (clusters) along its trajectory (Figure 5.3). This is the result of electromagnetic interaction with the medium atoms leading to lose kinetic energy via *excitation*, *ionisation* and *radiative losses*. Excitation and ionisation occur when the charged particle loose energy by interacting with the orbital electrons. In the specific case of excitation, the energy transferred to an electron does not exceed its binding energy and will return to a lower energy level (*de-excitation*). If the transferred energy exceeds the binding energy of the electron, the ionisation occurs, whereby an electron is ejected from the medium atom. Sometimes the ejected electrons hold sufficient energy to produce further ionisation called *secondary ionisation*. These electrons are called *delta rays*.

The collisions with the gas atoms are purely random and characterised by a mean free path λ between the clusters given by the ionisation cross-section $\sigma_{col}(\beta)$ and the gas mixture density ρ by

$$\lambda = \frac{A}{\delta N_A} \frac{1}{\sigma_{col}(\beta)}, \quad (5.1)$$

where A is the average atomic number of the gas mixture and N_A is the Avogadro number. When the energy loss is negligible compared to the particle energy, the probability of an ionisation is independent from the previous collisions, the distance between the ionising collisions is exponentially distributed. The probability to find a cluster between positions z and $z + dz$ on the particle trajectory is then:

$$P(z) = \frac{1}{\lambda} e^{-z/\lambda}. \quad (5.2)$$

Therefore, the number of clusters along any length l follows a *Poisson* distribution with an average of $\bar{n} = l/\lambda$. The probability to get n clusters is given by

$$P(n) = \frac{1}{n!} \left(\frac{l}{\lambda}\right)^n e^{-l/\lambda}. \quad (5.3)$$

The primary charge deposit is then characterised by the number of clusters per unit of length left by the charged particle, and the probability distribution for the number of electrons per cluster for each component of the gas mixture [77].

The numbers can be calculated using HEED[79]: the average number of clusters per millimeter left by a muon with an energy E_μ for GRPC gas mixture, is shown in Figure 5.4a. An average of ~ 9 cluster/mm is obtained for $E_\mu \geq 10$ GeV. The Figure 5.4b shows that small clusters (with 1 electron/cluster) are

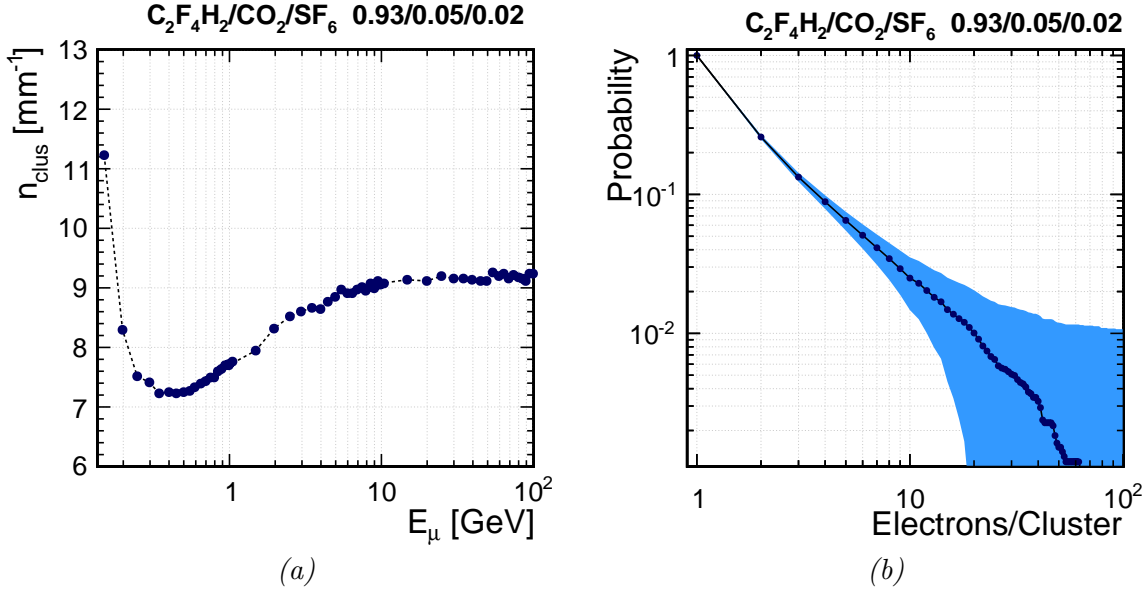


FIGURE 5.4: (a) Average number of clusters per unit of length created by muon as a function of its energy E_μ as predicted by HEED. (b) Cluster size (number of electrons) distribution for muon as simulated by HEED. With a cut-off at 500 electrons, the average number of electrons/cluster is ~ 2.3 for our GRPC gas mixture.

the most probable.

Maximum detection efficiency

From the Equation 5.3, the probability of having zero ionisation along the track length g is given by

$$P(n = 0) = e^{-g/\lambda}. \quad (5.4)$$

This provide a way to measure the inefficiency of the gas sensor. If we assume that all primary clusters in the gas gap are detected, following Equation 5.4 the detection inefficiency is $(1 - \varepsilon_{\text{max}}) = \exp(-g/\lambda)$, where ε_{max} is the maximum detection efficiency.

In the case of incident particle having an angle ϕ with the normal direction of the chamber plates ($0 \leq \phi \leq \pi/2$), the probability 5.3 becomes

$$P(n) = \frac{1}{n!} \left(\frac{g}{\lambda_{\text{eff}}} \right)^n e^{-g/\lambda_{\text{eff}}}, \quad (5.5)$$

where $\lambda_{\text{eff}}(\phi) = \lambda \cos \phi$ ³. The probability to have n cluster in the gap of g width increases with the incident angle ϕ , as well as the maximum detection efficiency. This effect will be demonstrated experimentally in the next section (Section 5.3).

Drift velocity of electrons

In the absence of an external field, the free electrons in a gas have a thermal kinetic energy equal to $(3/2)k_B T$ and a randomly oriented velocity, where T is the temperature of the gas and k_B the Boltzmann constant. Under the influence of an electric field E , an electron of charge e gains the kinetic energy $e|\vec{E}|\delta z$ on the drift distance δz between two collisions with gas molecules. In the next encounter, the electron kinetic energy decreases through recoil or excitation and the electron slow down. Then, under the influence of the electric field, it is again accelerated and again collides, and so on. At the microscopic level, the measured electron drift velocity v_D is an average over large number of collisions. It depends on the electric field sensed by the electron and gas pressure. This dependency can be calculated with the Monte-Carlo simulation program `Magboltz` [80]. The Figure 5.5a shows the evolution of the drift velocity of electron as function of the applied electric field for the GRPC gas mixture.

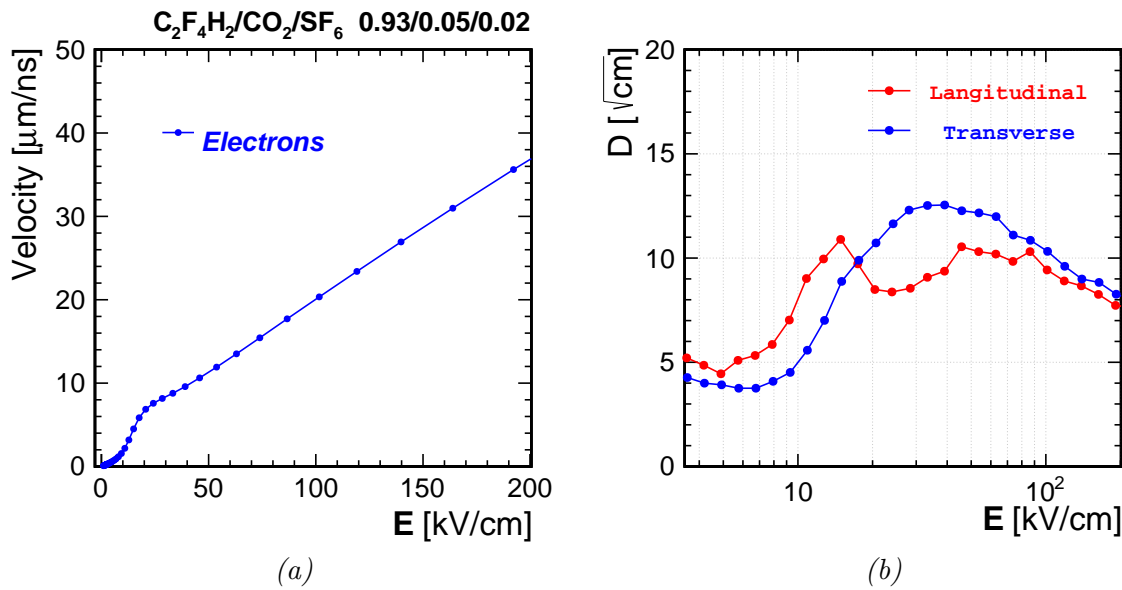


FIGURE 5.5: (a) Drift velocity for the GRPC gas mixture as predicted by `Magboltz`. (b) Diffusion coefficient calculated with `Magboltz` for GRPC gas mixture. All values are for normal conditions ($T = 296.15$ K and $P = 1013$ mbar)

Diffusion of electrons and ions

A charged particle under the influence of an external field collides randomly with the gas molecules. A point-like cloud of such particles spreads out along the field lines. This process is called transverse and longitudinal diffusion. The magnitude of the diffusion differs for the electrons and ions.

³This comes from the distance travelled by the charged particle with an incident angle ϕ in the gas gap g given by $l = g / \cos \phi$

Assuming a point-like cloud of charge in the absence of external electric field, the diffusion is isotropic. It can be shown that after a certain time t from the position \vec{r}_0 , the density distribution is a three-dimensional Gaussian distribution centred at the position \vec{r} . The density $n(\vec{r})$ is then given by

$$n(\vec{r}) = \left(\frac{1}{4\pi\mathcal{D}t}\right)^{3/2} \exp\left(-\frac{(\vec{r}-\vec{r}_0)^2}{4\mathcal{D}t}\right) \quad (5.6)$$

with a mean squared deviation $\sigma_i^2 = 2\mathcal{D}t$ in any direction “ i ” and \mathcal{D} the diffusion constant.

In the presence of an electric field the diffusion becomes anisotropic. The longitudinal and transverse diffusion have to be distinguished. Assuming a cylindrical symmetry along the z -axis the Equation 5.6 becomes

$$n(z, r, t) = \frac{1}{\sqrt{2\pi}} \frac{1}{\sigma_L \sigma_T^2} \exp\left(-\frac{(z-z_0)^2}{2\sigma_L} - \frac{(r-r_0)^2}{2\sigma_T}\right) \quad (5.7)$$

z_0 and r_0 indicate the position of the centre of mass of the distribution⁴. The average time elapsing during the drift of the cloud over a distance l is $t = l/(v_D)$ where v_D is the electron drift velocity. The longitudinal and transverse standard deviations become $\sigma_{L,T} = (2\mathcal{D}_{L,T}t)^{1/2} = (2\mathcal{D}_{L,T}l/v_D)^{1/2} = D_{L,T}\sqrt{l}$, where $D_{L,T}$ is the diffusion coefficient. Thus the Equation 5.7 can be separated to longitudinal and transverse density distribution

$$\begin{aligned} n_L(z, l) &= \frac{1}{\sqrt{2\pi l} D_L} \exp\left(-\frac{(z-z_0)^2}{2D_L^2 l}\right) \\ n_T(r, l) &= \frac{1}{D_T^2 l} \exp\left(-\frac{(r-r_0)^2}{2D_T^2 l}\right) \end{aligned} \quad (5.8)$$

The diffusion coefficients dependency with electric field can be calculated with Magboltz. The Figure 5.5b shows the results using the GRPC gas mixture.

5.2.2 Electron multiplication

A primary electron originated par the ionisation process will be accelerated in the presence of the electric field and will be undergo elastic and inelastic collisions with gas molecules. The secondary electrons newly created take part in the ionisation process and this a so-called *avalanche*.

After a collision leading to an ionisation, the electron usually remains with an energy smaller than the ionisation energy eU_i , where U_i is the minimum ionisation potential for a given gas molecule. The electron has to drift over a distance equivalent to $\xi = U_i/E$ in the direction of the electric field E to reach again enough energy for another ionisation.

To the first order the multiplication of ionisation is described by the first Townsend coefficient α . If the multiplication occurs, the increase of the number of electrons per unit of path ds is given by

$$dN = N\alpha(s)ds \quad (5.9)$$

⁴Note that integration over ϕ was carried out, leading to an additional factor of 2π .

The coefficient α depends on the excitation and ionisation cross-section of the electron and the external applied field.

If the distance s is much lower than the mean free path $1/\lambda$ of electron, the probability for an ionising collision along a distance ds is $p = \alpha ds$ independently from the path the electron travelled since the last ionisation. In this case the multiplication process is known as the Townsend avalanche, characterised by $\alpha = 1/\lambda$. A couple of parametrisation of the dependence of Townsend coefficient on the electric field has been proposed [81], valid in certain range of field. Rose and Kroff [82] proposed a parametrisation valid on an electric field up 50 kV/cm:

$$\alpha/P = \mathcal{A} e^{-\mathcal{B}P/E} \quad (5.10)$$

with P the gas pressure and \mathcal{A} and \mathcal{B} two coefficients which depend on the gas mixture.

Assuming a single electron starting at the position $s = 0$ and moving along the coordinate s , the Equation 9.4 leads to an average

$$\bar{n}(s) = \exp\left(\int_0^s \alpha(s') ds'\right) \quad (5.11)$$

of electrons. Since the multiplication is a stochastic process, the true number of electron fluctuates around this average.

Electronegative gases like $C_2H_2F_4$ and SF_6 in the gas mixture can absorb electrons. This effect introduces fluctuations in the number of primary electrons which initiate the avalanche, and will have an impact on the shape to the induced charge spectrum. It is characterised by the second Townsend coefficient η also called attachment coefficient. As the expression αds represents the probability that an electron makes a ionising collision in the interval ds , the value ηds represents the probability that electron get caught in the interval ds . Using again `Magboltz` program, the Townsend and the attachment coefficients, for our gas mixture, are determined as function of electric field (see Figure 5.6).

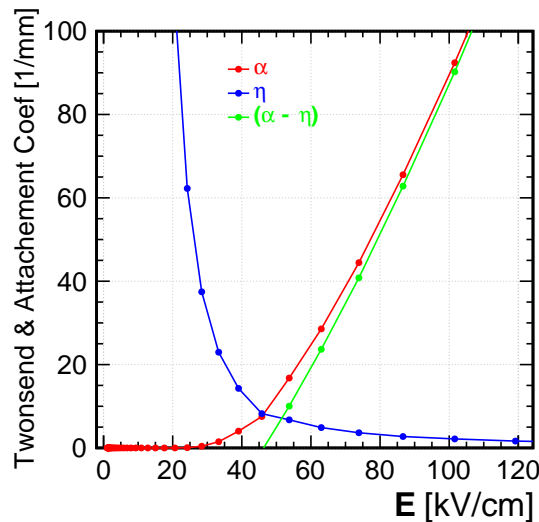


FIGURE 5.6: Townsend and attachment coefficients as function of the electric field for the GRPC gas mixture calculated using `Magboltz`.

The avalanche electron population during the multiplication process can be expressed by

$$\bar{n}(s) = \exp\left(\int_0^s (\alpha(s) - \eta(s)) ds\right) \quad (5.12)$$

The value $\alpha_{\text{eff}} = (\alpha - \eta)$ is called the *effective* Townsend coefficient. The solution for $\bar{n}(0) = n_0$, $\bar{p}(0) = 0$ and the hypothesis of constant coefficients is an exponential growth law

$$\bar{n}(s) = n_0 e^{\alpha_{\text{eff}} s} \quad \bar{p}(s) = \frac{n_0 \alpha}{\alpha_{\text{eff}}} (e^{\alpha_{\text{eff}} s} - 1) \quad (5.13)$$

The average number of negative ions is then $\bar{p} - \bar{n}$. The electron gain can be simply expressed as:

$$G(s) = \bar{n}(s)/n_0 = e^{\alpha_{\text{eff}} s} \quad (5.14)$$

The Reather limit of 10^8 electron for the *streamer* mode transition corresponds to $\alpha_{\text{eff}} s \sim 20$. A streamer is defined as a state in which photons contribute to the multiplication process[83]. Further, streamer can evolve into an electric discharge (or a spark). This effect requires a relatively high current flow in the gap, which is generally suppressed by the high resistivity of the GRPC electrodes.

Gain fluctuation at moderate uniform field

The $\alpha(s)$ and $\eta(s)$ coefficients depend differently on the electric field and thus on s . In the approximation of uniform field, $\alpha(s)$ and $\eta(s)$ are independent on the path s . A detailed development (see [84, 85]) leads to an exponential law for $P(n, s)$: the probability to find n electrons at the position s , called the *Furry's law*

$$P(n, s) = \frac{1}{\bar{n}(s)} \exp\left(-\frac{n}{\bar{n}(s)}\right) \quad (5.15)$$

where \bar{n} is the average avalanche size (of gain) given by the Equation 5.13. In this model small signals are most probable, the pulse-high distribution is purely monotonic and shows no peak. This is actually true under the assumption of weak electric fields as has been observed by [86].

Gain fluctuation at high uniform field

A realistic description of the avalanche grow fluctuations has to take care about the positive ions generated in the same proportion as electrons. Those ions drift slowly to the cathode, and deform the electric field in the gas gap dropping its intensity locally. The mean ionisation coefficient of the avalanche depends on the number of electrons as well as on their positions; at high value of E/P the instantaneous probability of ionisation depends on the previous history of the electron.

A parametrisation of Townsend coefficient $\alpha(n, s)$ was proposed by Curran et al.[87] (and independently Byrne[88] and Lansart and Morucci [89]), in which the probability for an electron to produce an ionisation depends on the total number of electron already produced in the avalanche. The coefficient $\alpha(n, s)$ is assumed to vary with n and s according to

$$\alpha(n, s) = \alpha(s)[1 + (\theta/n)], \quad \text{for } n > 0 \quad (5.16)$$

where θ is an empirically defined parameter. A detailed treatment shows that the probability $P(n, s)$ is distributed according to a *Polya* law, which for large values of n can be simplified to the form

$$p_{\text{polya}}(n, s) \simeq c \left(\frac{n(1+\theta)}{\bar{n}(s)} \right)^\theta \exp \left(-\frac{n(1+\theta)}{\bar{n}(s)} \right) \quad (5.17)$$

Where c is a constant normalising the distribution to 1. Thus the integration lead to the form

$$p_{\text{polya}}(n, s) = \left(\frac{(\theta+1)}{\bar{n}(s)\Gamma(\theta+1)} \right) \left(\frac{n(1+\theta)}{\bar{n}(s)} \right)^\theta \exp \left(-\frac{n(1+\theta)}{\bar{n}(s)} \right) \quad (5.18)$$

The exact physical meaning of parameter θ is not clear, since it includes the space charge effect in an uncorrected way and neglects the attachment ⁵. However, this ad-hoc function parametrises the measured curves in a nice way [90], and has been used further in this thesis work.

5.2.3 Induced signal

Under the influence of the electric field, electrons and ions drift on the opposite towards their respective electrodes. The motion of both electrons and ions in the gas induces charges displacement on the electrodes. The electrons velocities are 2-3 orders of magnitude higher than those of ions. As results, electrons reach the cathode in few ns and the signal is mainly due to their drift. For fast readout electronics, the contribution of positive ions is negligible.

The current $i(t)$ induced by a moving charge $q = en(t)$ onto the readout electrodes (pads) can be calculated by the mean of the Shockley-Ramo theorem [91, 92]:

$$i(t) = \frac{E_w}{V_w} e v_D n(t) \quad (5.19)$$

where e is the electron charge, E_w (weighted field) is the electric field in the gas gap when the electrode is at a potential V_w and all other are grounded, v_D is the electron drift velocity and $n(t)$ is the total number of electrons in the avalanches at time t . The weighting field E_w/V_w for the GRPC geometry is sketched in Figure 5.7 can be calculated for neighbouring layers by the conditions

$$\begin{aligned} \sum_i^{\text{Layers}} E_i d_i &= V_w \\ \varepsilon_i E_i &= \varepsilon_j E_j \end{aligned} \quad (5.20)$$

The weighted field can be then expressed by

$$\frac{E_w}{V_w} = \frac{\varepsilon_r}{d_1 + d_2 + g \varepsilon_r} \quad (5.21)$$

where ε_r is the glass permittivity, g the gas gap and d_1 and d_2 the glass thickness of the electrode and anode respectively. An electrode size much larger than the G thickness is assumed.

⁵More sophisticated and precise model has been reported in [74].

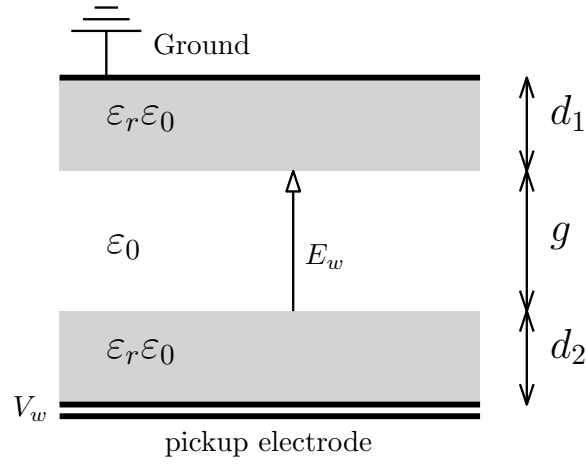


FIGURE 5.7: Schematic view of an RPC representing the weighted electric field E_w , the anode potential V_w and the permittivity of the different layers and their respective widths.

Starting with a single electron at the position x from the cathode producing an ideal exponential Townsend avalanche with a drift path length $(g - x)$, the induced current is

$$i(t, x) = \frac{E_w}{V_w} e v_D e^{(\alpha - \eta) v_D t} \Theta \left(\frac{g - x}{v_D} - t \right) \quad (5.22)$$

where $\Theta(x)$ is the Heaviside function modelling the anode surface. The corresponding induced charge can be obtained by integrating over a relatively large time

$$\begin{aligned} Q_{\text{ind}}(g - x) &= \int_0^\infty i(t, x) dt \\ &= \frac{E_w}{V_w (\alpha - \eta)} e_0 (e^{(\alpha - \eta)(g - x)} - 1) \end{aligned} \quad (5.23)$$

This is to be compared with the total charge Q_{tot} reaches the anode, that is given by

$$Q_{\text{tot}} = e_0 (e^{(\alpha - \eta)(g - x)} - 1) \quad (5.24)$$

The ratio between the total charge in the gas gap and the induced charge onto the readout pads, and substituting the value of E_w/V_w , is given then by

$$Q_{\text{ind}}/Q_{\text{tot}} = \frac{\epsilon_r}{(\alpha - \eta)(d_1 + d_2 + g\epsilon_r)} \quad (5.25)$$

For the GRPC case with the values: $\epsilon_r \sim 7$, $d_1 = 0.7$ mm, $d_2 = 1.1$ mm, $(\alpha - \eta) \sim 20$ mm⁻¹, the Equation 5.25 gives $Q_{\text{ind}}/Q_{\text{total}} \sim 0.03$. Since the avalanche growth is a stochastic process the induced charge Q_{ind} follows also a Polya-like distribution.

5.3 Study of the GRPC performance using minimum ionising particles

As mentioned above, the high granular calorimeters equipped with digital (semi-digital) readout can be characterised by the measurement of the detection efficiency and pad multiplicity. These two quantities condensate the intrinsic properties of the used sensor. They are needed for the monitoring (see Chapter 4) and the calibration of the detector and are indispensable for a proper modelling in the simulation of the prototype (and any large detector).

The reconstruction of the tracks left by the Mips in the calorimeters, thanks to its tracking capability, allows the measurement these quantities.

5.3.1 Track reconstruction

The muons can be saved in the meanwhile of interacting particle (showers). Thus, events with number of hits less than 200 are the only considered for the further study⁶.

Neighbour clustering

All hits in a given layer are clustered using a closest-neighbour clustering algorithm. It consists in merging in each GRPC plate the hits sharing a common edge (Figure 5.8). The position of the cluster is determined as the unweighted average in the two directions x_c and y_c . The errors on the position σ_{x_c} and σ_{y_c} are calculated as X and Y spread divided by $\sqrt{12}$ (assuming a uniform distribution ranges in $x \in [0, 1]$).

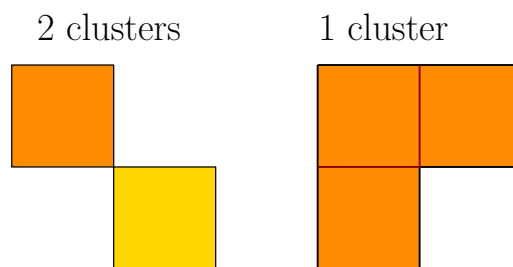


FIGURE 5.8: Example of two cluster configurations. In the left the hits are joined by a vertex, yielding two clusters. In the right configuration, all hits are sharing edges two by two, forming an unique cluster.

Hits cleaning

A removal of the farther hits using a distance between a cluster (c) and the event cluster set (E) is applied to the cluster set. This distance is defined by

$$\delta(c, \mathbb{E}) = \min\{\forall c' \in \mathbb{E} - \{c\} \mid d(c, c')\} \quad (5.26)$$

⁶This number is chosen from the assumption that in the extreme case, a muons track can induce 4 fired pads in each of the 48 pates, which corresponds to ~ 200 hits in total.

were $d(c, c')$ is the euclidean distance between two clusters in the GRPC plan. The cluster farther than 12 cm are then dropped. Event having cluster with $N_{hit} > 5$ are skipped, to exclude any possible hard muon interaction in the calorimeter.

Track reconstruction

Tracks are reconstructed by performing χ^2 minimisation. The reduced χ^2/ndf of the fits is calculated⁷ as

$$\chi^2/\text{ndf} = \sum_i^{N_{plate}} \left(\frac{x(z_i) - x_{c,i}}{\sigma_{x_c,i}} \right)^2 + \left(\frac{y(z_i) - y_{c,i}}{\sigma_{y_c,i}} \right)^2 \quad (5.27)$$

where the sums run over all tracking clusters and

$$\begin{cases} x(z_i) = p_0 + p_1 z_i \\ y(z_i) = p_2 + p_3 z_i \end{cases} \quad (5.28)$$

define a parametric equation of the straight line in the space with four parameters ($p_{i \in \{0,1,2,3\}}$). The errors $\sigma_{x_c,i}$ and $\sigma_{y_c,i}$ refer to the standard spread of the each cluster defined previously.

The minimisation is performed using the MINUIT package [93] implemented in ROOT framework [94]. Two examples of muon events are shown in the Figures 5.9a and 5.9b representing a beam muon and cosmic ray muon respectively.

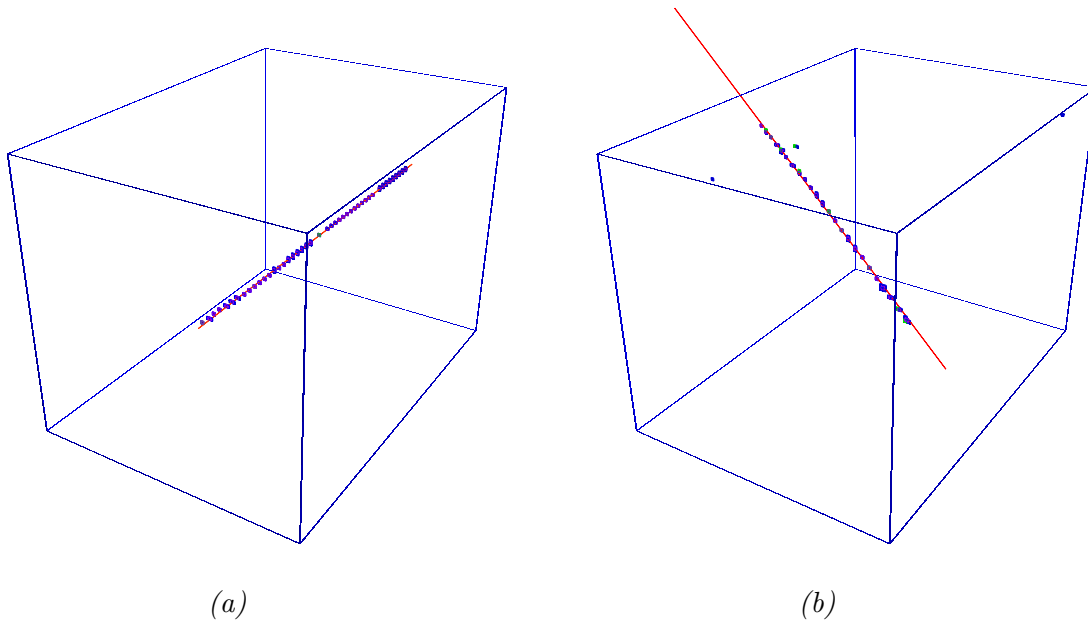


FIGURE 5.9: Example of Mip events in the SDHCAL prototype (beam muon (a), cosmic muon (b))

In order to estimate the performances of the GRPC, only tracks satisfying $\chi^2 < 20$ are considered for the further studies.

⁷z-axis is perpendicular to the plates, x-axis and y-axis are respectively horizontal and vertical.

5.3.2 Efficiency and multiplicity

The efficiency ϵ_i of given layer i is defined as the probability to find at least 1 hit within 3 cm of the reconstructed track. The considered layer “ i ” is removed from the track reconstruction to prevent any bias on the efficiency calculation. The multiplicity μ_i is defined as the number of hits matched on layer i within 3 cm of the track intercept. The Figure 5.10a and Figure 5.10b shows the efficiency and multiplicity on each layer.

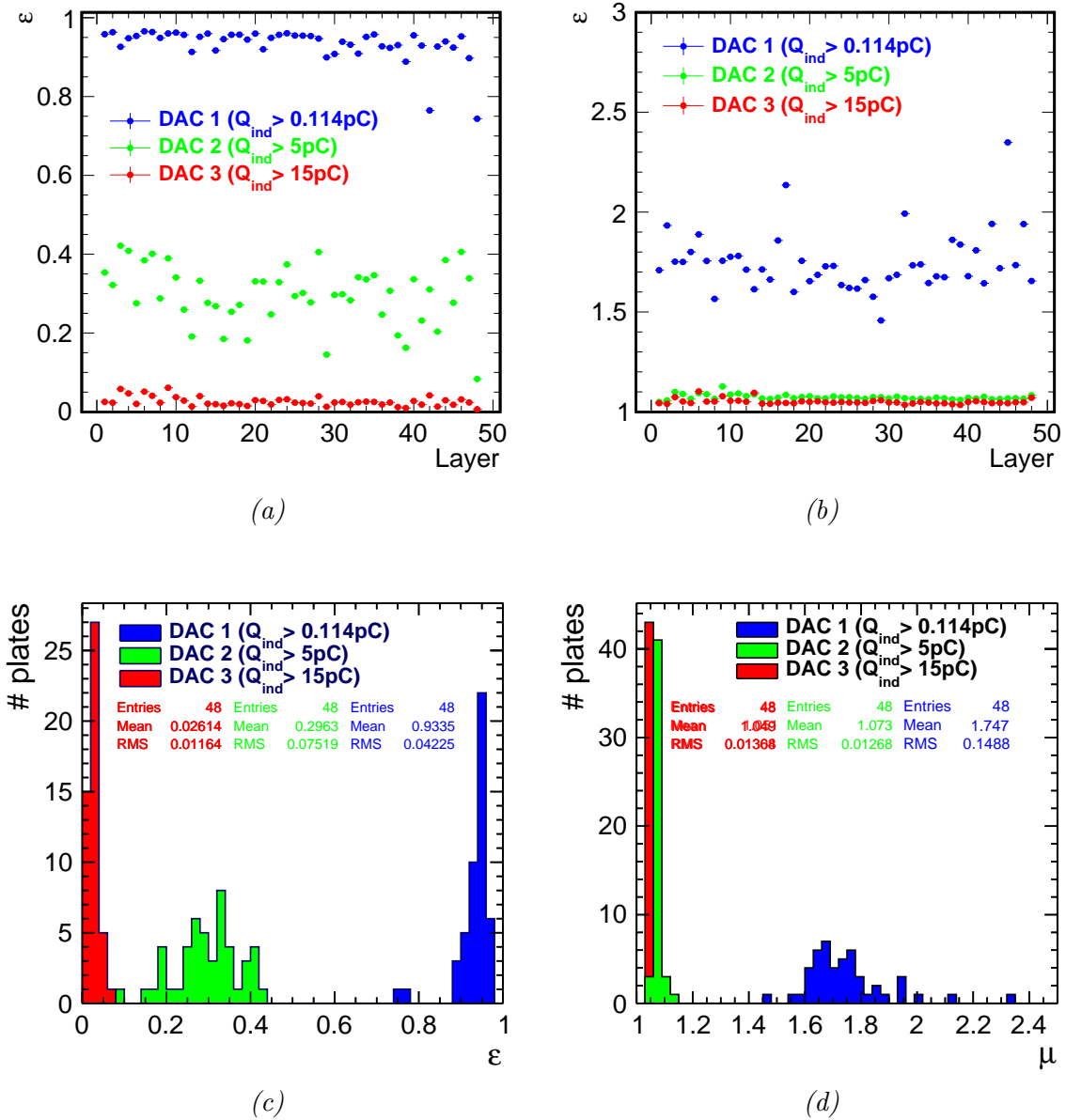


FIGURE 5.10: The efficiency (a) and the average multiplicity (b) for each chamber (layer) and for the three standard thresholds. (c) and (d) represent respectively the distributions of multiplicity and efficiency of the chambers and for the three thresholds.

An efficiency of $\sim 96\%$ is observed over most of the chambers with an average multiplicity for the lowest threshold of about 1.7. The large dispersion is essentially due to the uniformity response of the GRPC sensors, as shown in the next section.

5.3.3 Angular dependence

The reconstruction of the track allows to measure the muon angles. From the Equation 5.28 two incident angles can be determined, $\Phi = \tan^{-1}(p_1)$ (with $\Phi \in [-\pi/2, \pi/2]$) represents the azimuthal angle and $\Theta = \tan^{-1}(p_3)$ (with $\Theta \in [0, \pi]$) represents the altitude.

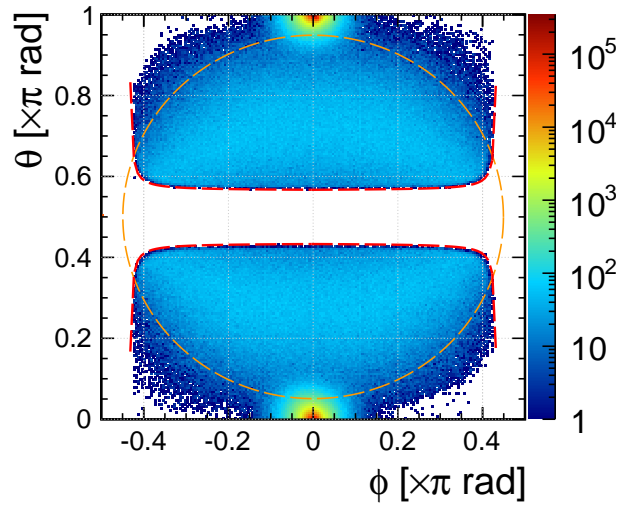


FIGURE 5.11: incidence angles of the cosmic rays including muon beam. The red lines represents the geometrical limits of the detector.

The Figure 5.11 shows the angles of the incident cosmic rays as well as the muon beam (located at $(\Phi, \Theta) = (0, 0)$ and $(\Phi, \Theta) = (0, \pi)$). The red line represents the limit of the detector acceptance, related to the condition to fire at least 7 layers in the event-building as mentioned in Chapter 4. The cosmic rays are delimited by the orange circle and shows that they are uniformly distributed in the region $(\Phi^2 + \Theta^2)^{1/2} < 9\pi/20$ rad.

The first impact on the incoming particle angle is visible on the multiplicity. Indeed, the multiplicity should increase for the large incident angles as shown in the Figure 5.12a. If we consider that the multiplicity is proportional to the crossing length $\mu \propto l$ in the gas gap, then we can easily assume the following relation:

$$\mu(\eta) = \mu_0 + a_\mu g(1/\cos \eta - 1), \quad (5.29)$$

where a_μ is an arbitrary factor and $\mu_0 = \mu(\eta = 0)$. This assumption can be justified by considering that at large incidence angle the number of primary cluster increase by a factor $1/\cos(\eta)$ and that the multiplicity is more or less linearly related to the induced charge. The Figure 5.12a represent the evolution of the multiplicity with respect to the incidence angle η . The multiplicity parametrisation fit well the data with good accuracy (less than few %).

The efficiency presents also a dependence with the incidence angle as shown in the Figure 5.12b. This effect can be justified using the same assumption as for multiplicity. The number of primary clusters

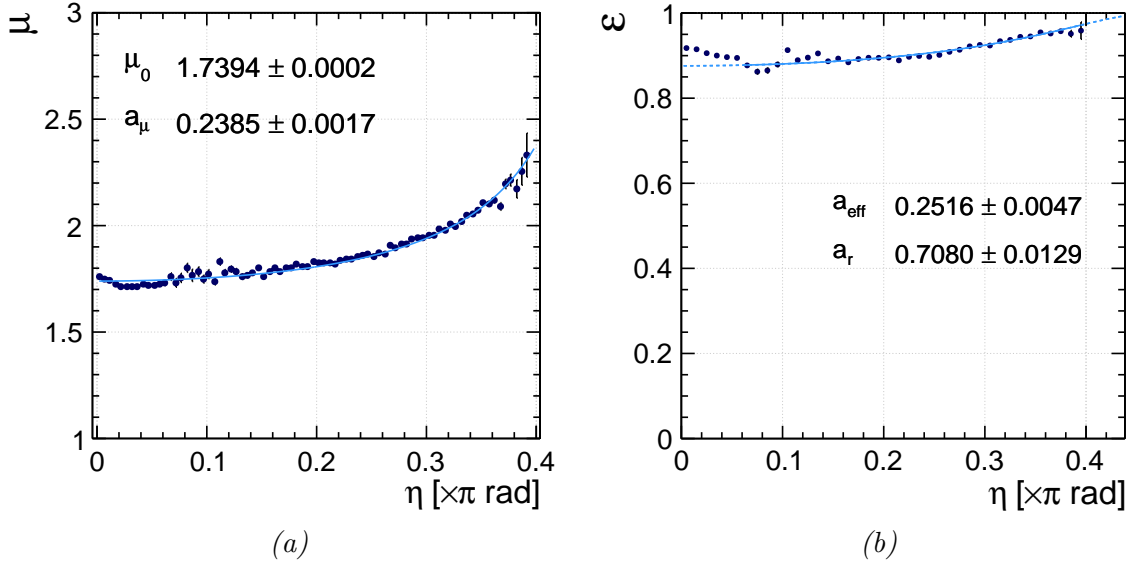


FIGURE 5.12: Evolution of multiplicity (a) and efficiency (b) as function of the muon incident angle η . The blue lines represent the best fits (see the text).

increase with the track length in the gas gap improving the chance to produce a detectable electronic avalanche. In the theoretical case of $Q_{thr} = 0$, the sensor will be sensitive to any event happening in the gas gap. The detector shows then a maximum detection efficiency (limited by the statistic) expressed by

$$\varepsilon_{max} = 1 - \exp\left(-\frac{g}{\lambda \cos \eta}\right) \quad (5.30)$$

where g , η and λ are respectively, the gas gap, the incident angle and the mean free path. On the basis of this equation, the experimental-like expression can deduced by:

$$\varepsilon(\eta) = 1 - a_{eff} \exp\left(-\frac{a_r}{\cos \eta}\right) \quad (5.31)$$

where a_{eff} and a_r are arbitrary parameters introduced to accounts the detection threshold and the rate of the primary ionizations respectively. The Figure 5.12b shows that this parametrisation fits with good agreement the data.

5.3.4 Induced signal measurement

Threshold scan

During the 2012 SPS beam test at CERN, a threshold scan was performed on the 3 DAC commending the 3 SDHCAL thresholds. The efficiency and multiplicity have been measured using the same procedure as previously. They are shown in Figure 5.13a and Figure 5.13b respectively. The measurement were done for threshold values in the range of [0.1, 25] pC. The efficiency drops from 97% for threshold of 0.1 pC to less then 1% at highest thresholds, the multiplicity varies from 1.85 to ~ 1 over the same range.

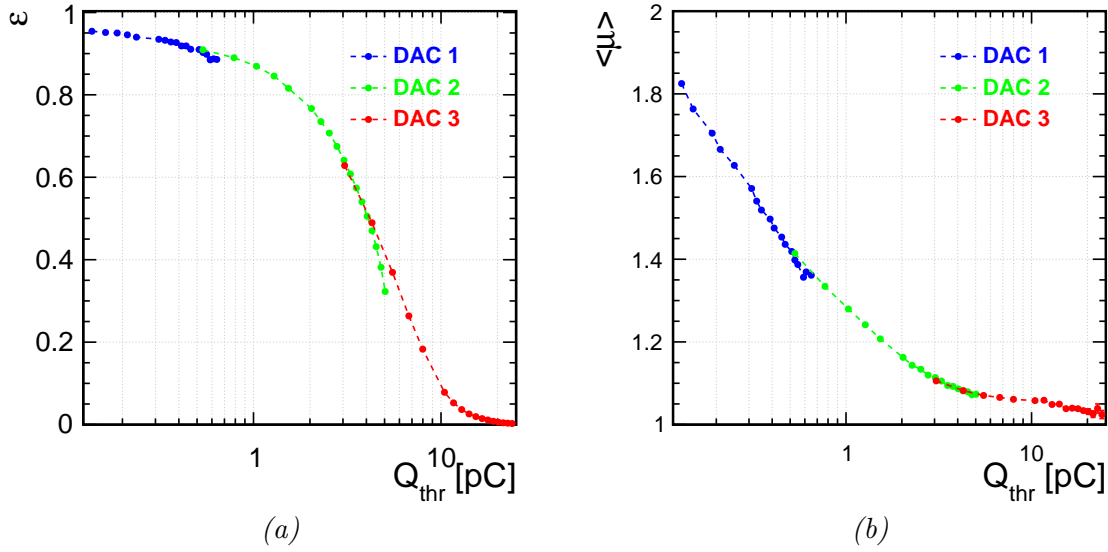


FIGURE 5.13: Measured efficiency (a) and multiplicity (b) versus threshold. Each colour correspond to the 3 SDHCAL HADROC thresholds (the first in blue, second in green and the thirist in red)

The unmatched curve corresponding to the first and second scanned thresholds visible in the Figure 5.13a around $Q_{thr} \sim 6$ pC probably due to a small non-linearity for high DAQ values.

Charge spectrum extraction

In the case of the digital readout, the charge spectrum is not measured directly, but can be determined by measuring the detection efficiency at different charge thresholds. This spectrum can be modelled by the Polya function (Equation 5.17). The parameters extracted by fitting with this function, allow to the tune an accurate Monte Carlo simulation and model at the best the charge fluctuation of the GRPC.

If one calls Q_{thr} the pad threshold and $p(Q_{ind})$ the normalised induced charge distribution, the detection efficiency can be written as

$$\varepsilon = \int_{Q_{thr}}^{\infty} p(Q_{ind}) dQ_{ind} \quad (5.32)$$

which is actually the fraction of the avalanches that contains a number of electrons inducing a charge larger than the threshold. Using the Polya parametrisation $p(Q_{ind}, \bar{Q}_{ind}, \theta)$ for the charge distribution (cf Section 5.2), Equation 5.33 becomes

$$\varepsilon(Q_{thr}; \bar{Q}_{ind}, \theta) = \left(\frac{(\theta + 1)}{\bar{n}(s)\Gamma(\theta + 1)} \right) \int_{Q_{thr}}^{\infty} \left(\frac{Q_{ind}(1 + \theta)}{\bar{Q}_{ind}} \right)^{\theta} \exp\left(-\frac{Q_{ind}(1 + \theta)}{\bar{Q}_{ind}}\right) dQ_{ind} \quad (5.33)$$

The efficiency as function of the threshold Q_{thr} can then be expressed by:

$$\varepsilon(Q_{thr}) = \varepsilon_0 - c \int_0^{Q_{thr}} p(Q_{ind}; \theta, \bar{Q}_{ind}) dQ_{ind} \quad (5.34)$$

where ε_0 is the efficiency of the detector at $Q_{thr} = 0$ and c a normalisation constant. A value of $\varepsilon < 0$ reflects the limited efficiency of the sensor due to the ionisation statistic (cf. Section 5.3.5) and possible dead channels. Fitting Equation 6.1 applied on the full range scan, the values of the Polya

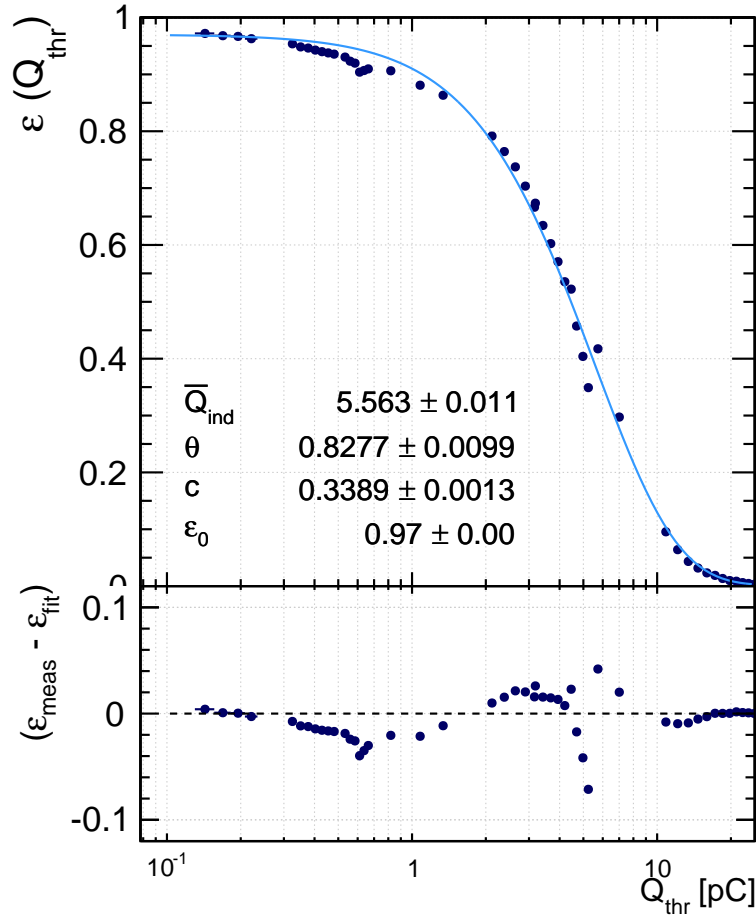


FIGURE 5.14: The GRPC efficiency versus threshold. The blue line represent the best fit using the Equation 6.1.

parameters are extracted. An agreement within 10% between the measured and the fitted efficiency versus threshold is observed. This results validate, a posteriori, the choice of a Polya parametrisation for the induced charge for GRPC. The mean induced charge \bar{Q}_{ind} is 5.56 pC, with $\theta = 0.82$. The shape of the Polya distribution can then be visualised for the extracted parameters as shown in the Figure 5.15⁸.

Scan cross the pad

By reconstructing the position of tracks in each layer, the relative position (x_r, y_r) in the touched readout pad can be determined rather precisely (typically ~ 1 mm). Thus the induced charge shared

⁸The extracted Polya parameters will be used as input for simulation of the SDHCAL response discussed in the Chapter 6

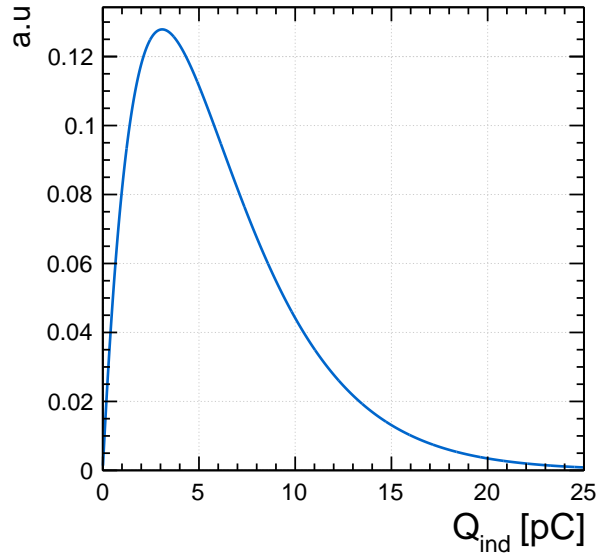


FIGURE 5.15: The shape of the extracted Polya function modelling the avalanche response.

between two, three or four pads can be estimated from data. The efficiency as well as the multiplicity as function of the track position in pad are shown in Figures 5.16a and 5.16b.

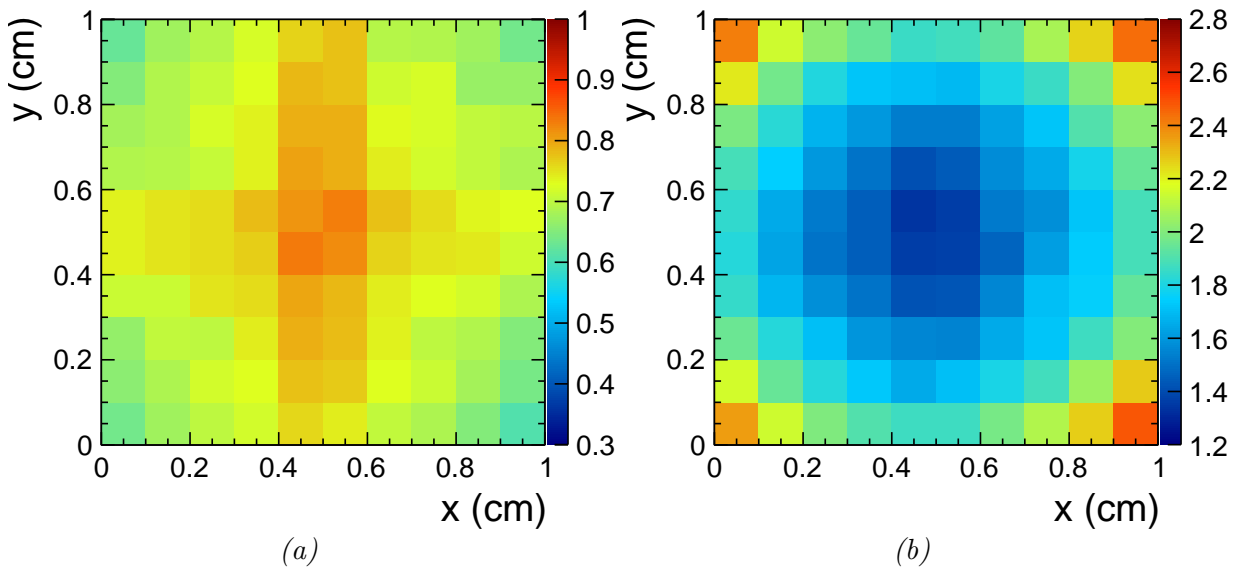


FIGURE 5.16: The average efficiency (a) and the average multiplicity (b) for the lowest threshold as function of the relative position of the reconstructed muon track in readout pad.

An ionisation located in the gas gap produces a charge q which induces a surface charge density $\sigma(x, y)$ in the readout pads. The charge of such distribution is then divided between all the nearest pads. The

charge induced in each readout pad can be formalised by an integration within the pad boundaries,

$$Q_{pad}(x, y) = \int_{-w/2}^{+w/2} \int_{-w/2}^{+w/2} \sigma(x, y) \, dx dy \quad (5.35)$$

where w is the pad size. The threshold is applied in each readout pad, if $Q_{pad}(x, y)$ is above the threshold the pad is considered fired. The multiplicity is then mean number of pads having a charge above the threshold, excluding the zero case⁹.

5.3.5 Chambers uniformity study

The efficiency and multiplicity has been measured in each ASIC's square composed by 8×8 pads. This choice is a compromise between granularity and the statistical significance for the geometrical response of each chamber. The Figure 5.17 shows the efficiency and multiplicity maps for few representative active layers (see Appendix A for the complete list of maps).

The chambers show globally a good uniformity in the efficiency measurement. However, a few chambers display some inefficient regions as shown, for example, in the chamber 16 (Figures 5.17) which has a very low efficiency in the central region of the chamber as well as a low multiplicity.

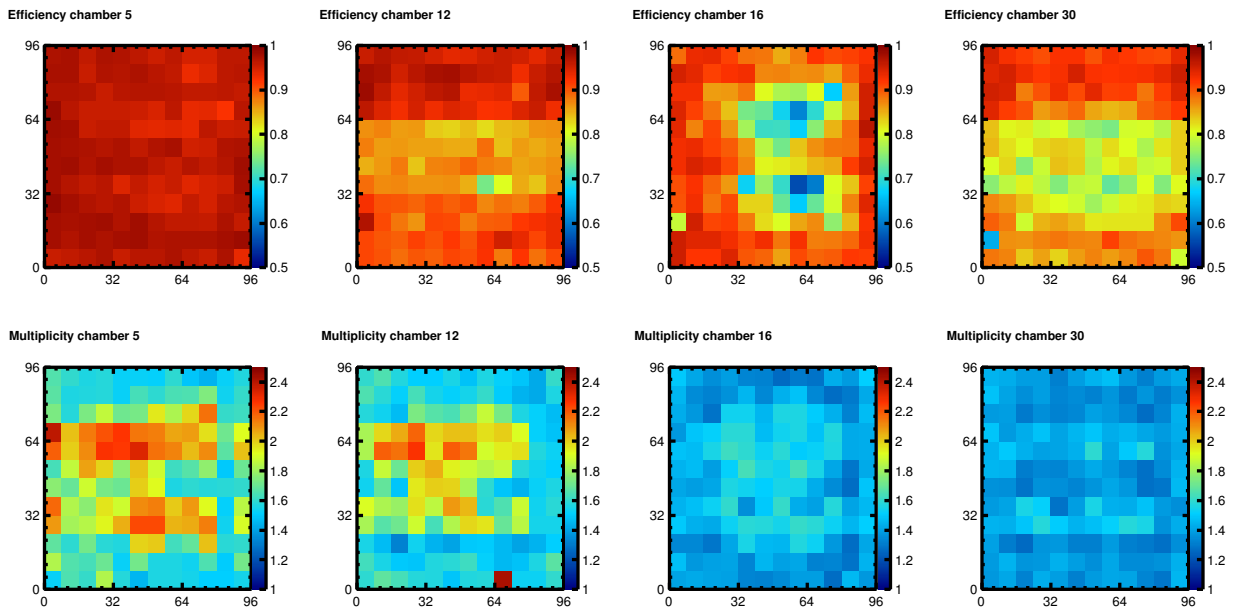


FIGURE 5.17: A representative selection of 4 SDHCAL chambers, showing the efficiency (top) and the multiplicity (bottom) maps.

Another effect noticed is the presence of dead (i.e. masked during the data acquisition) or low responding ASICs. A difference between the response of DIF is sometime observed (i.e. chamber 12 in Figure 5.17). This effects are essentially due to the electronics, and the fact that before the beam test no gain calibration was done.

⁹In the Chapter 6 a model to reproduce the charge sharing and hence the multiplicity is presented.

The multiplicity shows also an effect on the boundary of two ASUs. The Figure 5.17 reports examples of multiplicity maps of few chambers. The effect is almost visible in all the chambers showing an increasing of multiplicity of about $\sim 50\%$ to the central area (the ASUs edges are at $y = 32$ and $y = 64$).

The distributions of the efficiency and the multiplicity by ASICs are shown in the Figures 5.18a and 5.18b respectively. Two contribution in both efficiency and multiplicity distributions can be seen; a peak in which most of the statistic are concentrated (0.95 and 1.6 for efficiency and multiplicity respectively), and a more diffuse contribution. This second contribution originate from ASICs an efficiency below 0.91 and independently a multiplicity above 1.8. These two additional contributions have no geometrical correlation, as shown in Figure 5.18c, where the population of ASICs with an efficiency below 0.91 has a multiplicity centered on ~ 1.6 .

The multiplicity increasing on the boundaries of two joined ASUs is responsible of the observed tail at high multiplicities. On the other side, the difference on efficiency response for the ASU is responsible for presence of the observed bump in efficiency.

5.4 Conclusion

In this chapter, the response of the SDHCAL sensors to minimum ionising particles is shown. The efficiency and multiplicity were measured using the tracking capability of the high granularity of the SDHCAL prototype. These quantities are characteristics of finely segmented gaseous sensors, and allow the measurement of their local response. The angular dependencies of efficiency and multiplicity were also measured, which allows to an estimation of the flexibility of the geometry of the ILC calorimeter design. The measurement of the efficiency over the threshold permitted the determination of the induced charge spectrum in the GRPC and extract the key parameters needed to tune an accurate detector simulation.

The results presented in this chapter are based only in the digital (semi-digital) response of the GRPCs. Analogue measurement of the induced charge response could provide an experimental validation of the method described in Section 5.3.4.

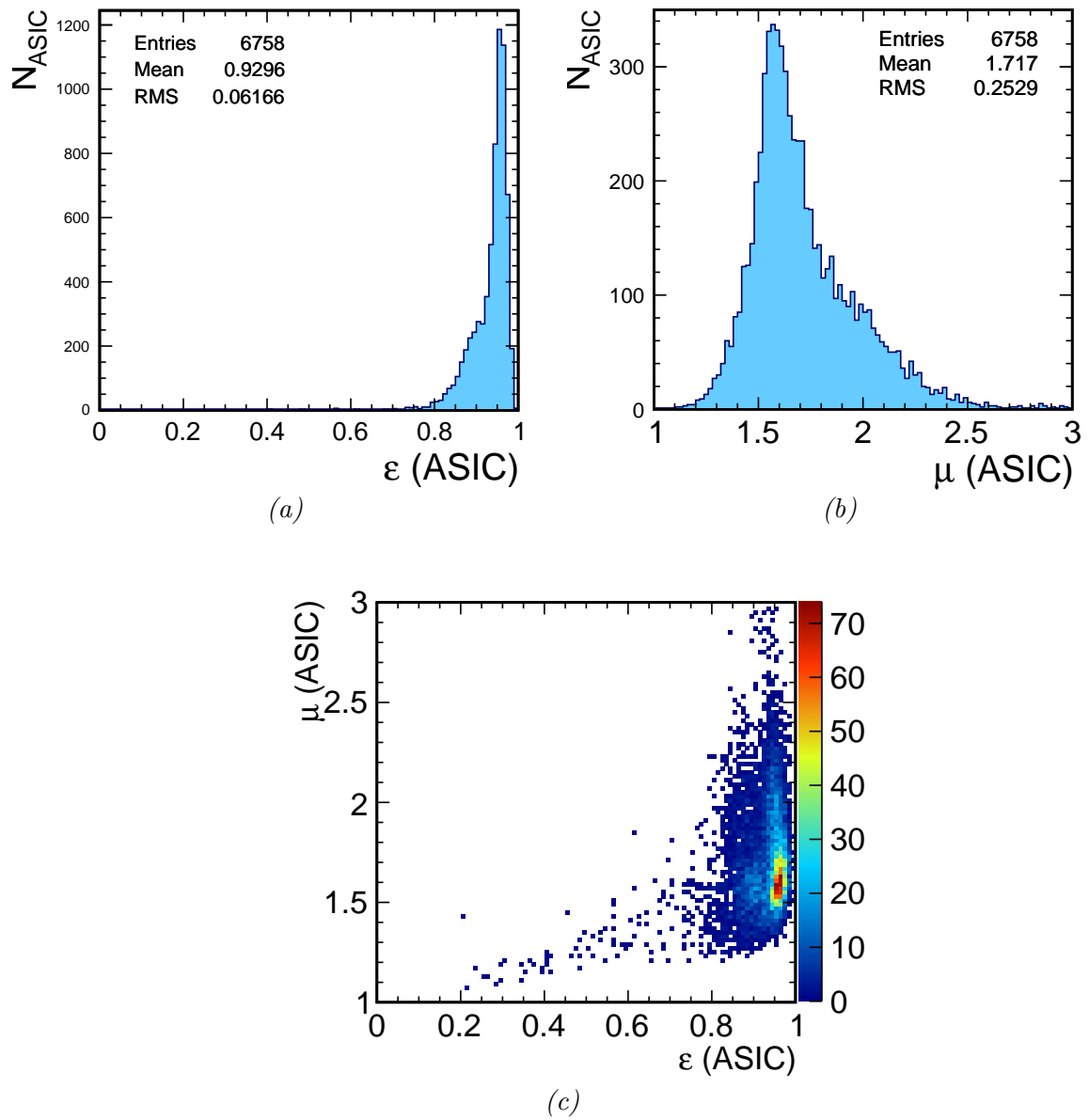


FIGURE 5.18: The summary of the efficiencies(a) and multiplicities(b) as well as their correlation (c) measured in each ASIC's area unit.

Chapter 6

Digitisation procedure for highly granular gaseous detector

“En Algérie il était pris dans cette alternative : ou devenir instituteur ,ce qui signifiait l’aisance pour toute la famille , ou redevenir berger”

— Mouloud Feraoun, Fils Du Pauvre.

6.1	Description of the used gaseous detectors	104
6.1.1	Data sample	105
6.2	The determination of induced Charge spectrum	105
6.2.1	Charge sharing	106
6.3	Digitisation procedure	106
6.3.1	Small-cell approach	107
6.4	Results and discussion	108
6.5	Conclusion	110

Introduction

As discussed the previous chapter (5), the response to minimum ionising particles (MIP) can be characterised by two quantities: the efficiency (the probability to fire at least one pad) and the pad multiplicity (the number of fired pads in each sensor). The multiplicity arises from the induced charge sharing between several pads (marginally by electronic cross talk $\sim 0.3\%$ measured in [64]), and might constitutes an important systematic bias in such calorimeters. Especially, in the case of high energy due to the high density of secondary particles. A basic simulation of the particle shower (hadronic or electromagnetic) using **GEANT4** [95] must be supplemented by a realistic sensor response. An additional module, called “digitisation”, should be added to take into account the physical response of the detector.

The digitisation requires several inputs which are derived from induced charge spectrum distribution and the electronic avalanche size. The measurement of these quantities can be achieved by using reconstructed muon tracks produced by accelerator beam or from cosmic rays.

In this chapter, after a short reminder of the gaseous amplification principle, a digitisation method based on small-cell approach is proposed. A comparison between data and digitised MC-data for two detectors, GRPC and MicroMegas will be then shown and commented upon.

6.1 Description of the used gaseous detectors

Gaseous detectors follow almost the same working principle. A charged particle passing through the sensor ionises the gas creating primary electrons. These electrons drift in the gas gap under an electric field (polarisation field) producing a cascade of secondary ionizations, thus a multiplication (amplification) of charge carriers is observed (Figure. 6.1). The movement of both electrons and ions leads to an induced charge in the readout pads (see Chapter 5).

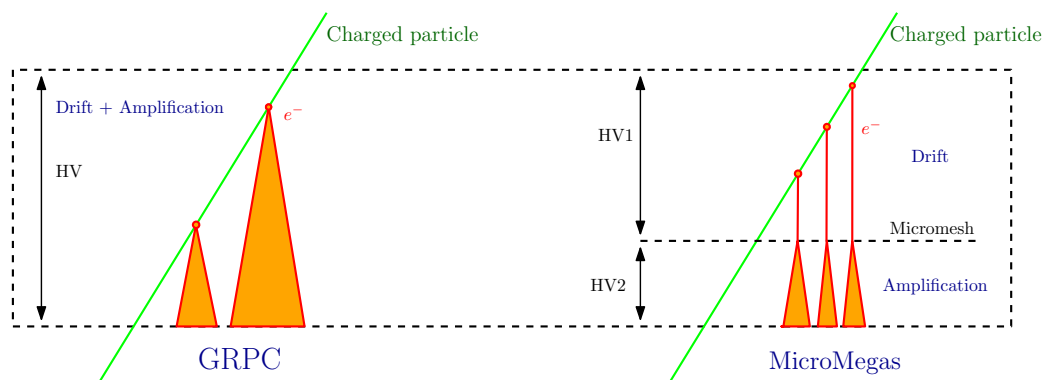


FIGURE 6.1: Schematic of the working principle in the GRPC (left) and MicroMegas (right).

Two kinds of sensor have been used here for the digitisation study, GRPC and MicroMegas. GRPCs consist of two parallel plate electrodes, a positively-charged anode and a negatively-charged cathode polarised by tension of 6.9 – 7kV, both made of a very high resistivity glass material (typically $\sim 10^{12} \Omega\text{cm}$ for glass) and separated by a thin gas volume [64, 96]. The signal is read by pads of $1 \times 1 \text{ cm}^2$ size. A large area of GRPCs (1 m^2) with 1.2 mm gas gap filled by a typical gas mixture of 93% TFE (C_2F_4), 5% CO_2 and 2% SF_6 operated in avalanche mode provides above 98% of efficiency with pad multiplicity of about ~ 1.7 for 0.14 pC threshold [64]. Two operating modes can be distinguished in GRPC sensors, the avalanche and *streamer* modes. In the avalanche mode, the primary ionisation leaves a trail of free charge carriers which trigger an avalanche of charges in the electric field (Townsend avalanche). If the size of the avalanche or the polarisation field is high enough, a streamer is created. A streamer is the state where photons contribute to the spread of the free charge carriers, a conducting plasma filament can be created between the two electrodes at later stage. Only the avalanche mode is considered as operating mode in GRPC for this study.

The MicroMegas chambers consist of an anode PCB segmented into $1 \times 1 \text{ cm}^2$ pads, the mesh is polarised by a tension of 500 V [97]. It uses a gas mixture of 80% Ar and 20% CO_2 . The amplification

and drift gaps are 128 μm and 3 mm respectively. The chambers were tested on in beam condition, as presented in [48], and show an efficiency up to 98%.

The main differences between GRPC and MicroMegas, stem from the drift and multiplication process. Indeed, in MicroMegas, the drift space is separated from the multiplication area by a polarised mesh. While in the GRPC, the charge carriers drift and multiplication happen in the same gap, they occur in 2 spaces separated by a polarised mesh in MicroMegas (Figure. 6.1). The small multiplication gap of MicroMegas leads also to a better spatial resolution, which implies a better pad multiplicity.

6.1.1 Data sample

For GRPC the results presented in this chapter are based on the data recorded during the beam test campaigns of the SDHCAL[98][99] prototype at the SPS CERN facilities in August-September 2012. The experimental setup is described in Chapter 4.

For MicroMegas, the data were taken during the test beam of 2009 in the CERN/PS/T10 zone as described in [97]. Four prototypes of $6 \times 16 \text{ cm}^2$ in addition to one four time larger ($12 \times 32 \text{ cm}^2$) active layer were used.

6.2 The determination of induced Charge spectrum

As mentioned above, the GRPC's were operated in the avalanche mode. Many papers describe the process of avalanche growth and the fluctuation of the induced charge [75, 100]. Most of those agree with the description of the induced charge spectrum. We chose this description to make comparison with the test beam data.

For the determination of the charge spectrum the same method discussed in the Section 5.3.4 is followed. The efficiency is measured for both MicroMegas and GRPC and fitted by the following function,

$$\varepsilon(Q_{thr}) = \varepsilon_0 - \int_0^{Q_{thr}} p(Q_{ind}; \theta, \bar{Q}_{ind}) dQ_{ind} \quad (6.1)$$

where ε_0 is the efficiency of the detector at $Q_{thr} = 0$ and $p(Q_{ind}; \theta, \bar{Q}_{ind})$ is the Polya function defined in Equation 5.18.

The efficiency versus threshold of GRPC measured in 2012 SPS beam test at CERN is shown in Figure 6.2a was already discussed in the Section 5.3.4.

Concerning MicroMegas, as reported in [48], the charge spectrum is Landau distributed. However, the Polya parametrisation fits the experimental results with an accuracy of better than 3% (see Figure 6.2b). Thus Polya PDF is used as the charge distribution function in MicroMegas. The mean induced charge in MicroMegas is 39.2 fC, the width is $\theta = 0.8 \text{ pC}$.

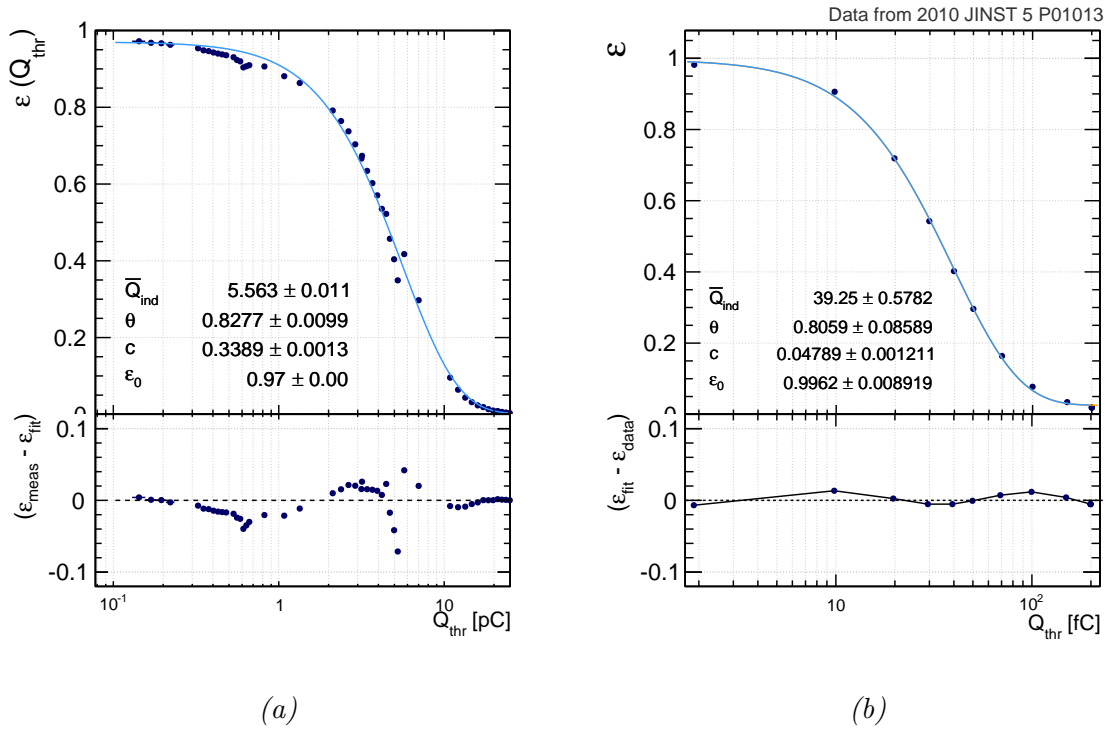


FIGURE 6.2: The GRPC (a) and MicroMegas (b) efficiency versus threshold. The Polya PDF functions are obtained using equation 3.2. The difference between the data points and the best fit curve in (a) at the value $Q_{thr} = 0.6$ pC and $Q_{thr} = 4 - 5$ pC is due to the use of 3 different thresholds regime imperfectly matched.

6.2.1 Charge sharing

The measured average multiplicity of muons, for the GRPC chambers, varies significantly with the position of the reconstructed track in a pad, as can be seen in Figure 6.3a. Multiple pads can be fired if the track position is close to the boundary.

The size of the avalanche can be deduced from the multiplicity distribution: a Gaussian fit ¹ on the multiplicity at the center (where $0.4 < y < 0.6$ cm) of the boundary (Figure. 6.3b) of two adjacent pads shows that the typical size of the charge image is of the order of ~ 1.4 mm (comparable to gas thickness). Thus setting the hit size at 1 mm at simulation level is sufficient to reproduce the multiplicity.

6.3 Digitisation procedure

The digitisation consists as mentioned previously in reproducing the pad response to given energy deposit (GEANT4 cells). The induced charge has to be determined for each pad independently taking into account the charge sharing between neighbour pads. Starting from the GEANT4 simulation of

¹We use the modified Gauss fit function defined by: $\mu(x|0.4 < y < 0.6 \text{ cm}) = \mu_0 + \frac{\alpha}{\sigma\sqrt{2\pi}} \exp -\frac{1}{2} \left(\frac{x-x_0}{\sigma} \right)^2$ where x_0 , σ and α are the mean, the standard deviation and the normalisation of the Gauss function.

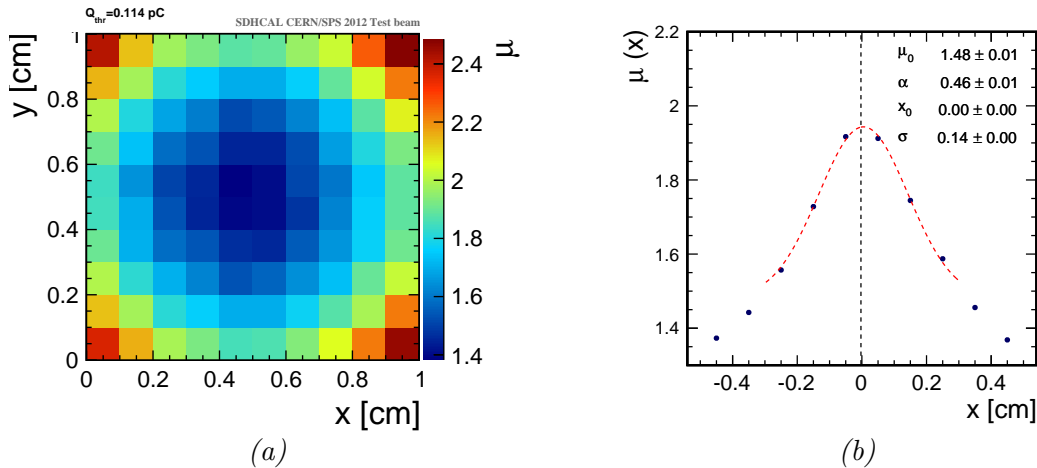


FIGURE 6.3: (a) The multiplicity as a function of the relative MIP position in the pad in GRPC chambers (CERN test beam). (b) The multiplicity as function of the relative MIP x position at the boundary of two pads, where $0.4 < y < 0.6$ cm. The red and black lines represent the best Gauss fit and the pads boundary respectively.

incoming particle, which provides the position of each interaction in the detector, the procedure can be summarised in a few steps:

- for each simulated hit, the value of induced charge is drawn randomly following the induced charge spectrum PDF;
- the charge is distributed to pads following the position of the **GEANT4** hit. The fraction of charge attributed to a pad depends on the detector and the pad size;
- the induced charge above a certain threshold determined for given pad is considered “fired”.

Digitisation procedure can be classified in different methods depending on how the charge splitting over the pads is done.

6.3.1 Small-cell approach

In the approach proposed here, the segmentation of sensitive layer is set at 1 mm, a **GEANT4** hit is regarded as one MIP hit. The chance for having multiple particle hits in the same 1 mm^2 area is then ignored. The digitisation steps are applied to these **GEANT4** hits. The fraction of the charge being shared by multiple neighbour pads are calculated from the charge spatial distribution. The surface charge density shape is approximated by a simple 2D Gaussian function. The standard deviation (σ) of such function is tuned to reproduce the multiplicity and efficiency of each detector. It is summarised into a $N \times N$ sharing fraction table to save computing time. The $N \times N$ weight sharing matrix is determined by an integration of the induced charge density of the avalanche in each cell of $1 \times 1 \text{ mm}^2$. The weights are then normalised to the total integral in $N \times N \text{ mm}^2$. The induced charge in each $1 \times 1 \text{ cm}^2$ pad is the sum of weights distributed in $N \times N \text{ mm}^2$ sharing matrix around the simulated hit within pad boundaries. When the induced charge in the digitised pad is above a certain threshold, the pad is considered fired. This procedure is summarised by a schematic view in Figure 6.4.

For the GRPC the value of σ is set to $\sim 1\text{mm}$ (typical lateral induced charge size) and the spatial distribution is carried by $5 \times 5 \text{ mm}^2$ weight matrix.

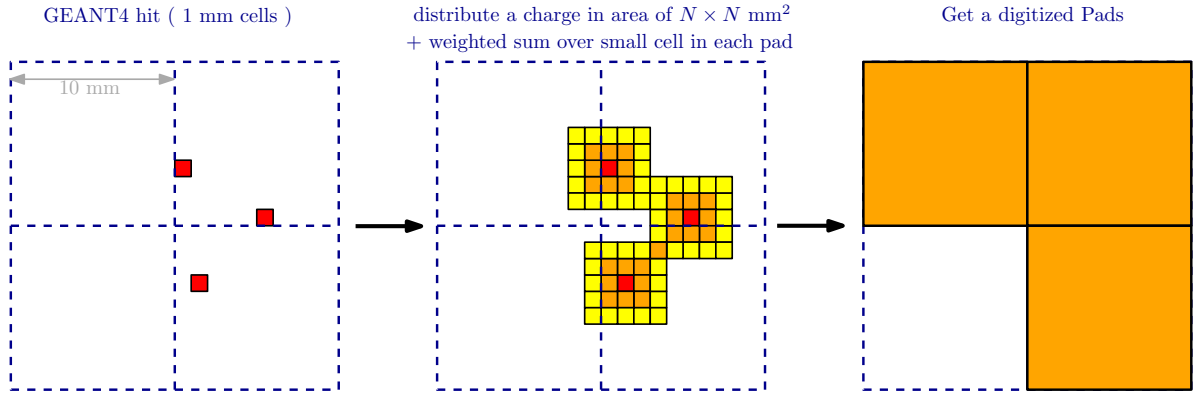


FIGURE 6.4: Schematic description of the working principle of the digitizer. A matrix of $5 \times 5 \text{ mm}$ of cell with corresponding weight is created around the simulated cell (GEANT4 hit). A weighted sum is calculated for each pad (bounded by the blue lines). The digitized pads are the ones which reach the threshold.

The spatial distribution of the charge image is parametrised as 3×3 matrix for MicroMegas. The centre element takes 95% of relative weight. Indeed, the MicroMegas have relatively smaller multiplicity since the amplification region of MicroMegas is much thinner, and directly connected to the readout pads, resulting in a more concentrated charge lateral image.

6.4 Results and discussion

The validation of the digitisation procedure proposed here is tested on MicroMegas and GRPC data. As mentioned above the digitisation is the ability to reproduce the pad multiplicity at different threshold values. The scan done in the MicroMegas test beam presented in [97] is well reproduced (Figure 6.5a). The pad multiplicity takes the value 1.07 at 1 fC threshold, and rapidly decreases to a level of 1.03 at high values. An increasing of about 1% of the multiplicity is observed around 100 fC creating a small bump. According to [97], the bump is induced by knock-on electrons (δ -rays). Indeed, induced charges above 30 fC are mainly originated from events with high energy deposit. These likely produce δ -rays leading to some ionisation on the neighbouring cells and hence a higher multiplicity.

For a charged particle with $\beta \sim 1$, the probability to have a knock-on electron with energy above 1 keV in 1mm of Ar gas is about 2% [101]. This is modelled in the digitiser by amplifying the induced charge of the neighbour cells for 2% of cases randomly. The induced charge in the neighbour cell is then the sum of the initial induced charge ($Q_{neighbor}$) and the total average of the induced charge in the sensor (\bar{Q}_{ind}) with a standard deviation² of σ_δ : $Q'_{neighbour} = Q_{neighbour} + (\bar{Q}_{ind} \pm \sigma_\delta)$. The result shown in Figure 6.5a is obtained for $\sigma_\delta \sim 2.2$. The deviation at high threshold is probably due to the low statistic in this region.

The same measurement was also made for GRPC sensors, where the multiplicity was determined for each threshold value in the range [0.1, 25] pC using 30 GeV muons. The pad multiplicity takes the value of 1.82 at 0.13pC and drops drastically to 1.05 at $Q_{thr} \sim 4 \text{ pC}$ before reaching a plateau in

²The induced charge of the δ -rays is assumed to be Gauss distributed

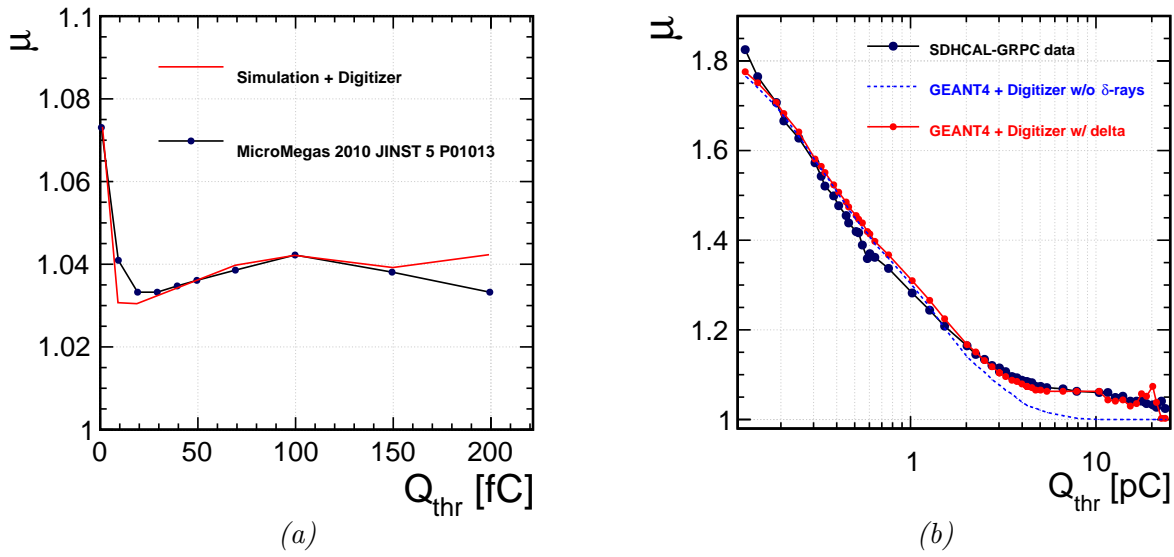


FIGURE 6.5: Multiplicity of MicroMegas (a) and GRPC (b) versus threshold. The red and the black lines represent the simulation (using GEANT4 within the digitiser) and sensor data. The dashed blue line in (b) represents the use of the digitiser without including the δ -rays effect.

between 4 pC – 11 pC and decreases again to 1. The plateau is probably due to the presence of the δ -rays. Following the same approach as MicroMegas the δ -rays effect can be modeled by inducing the same amount of \bar{Q}_{ind} for GRPC in a neighbor cell with $\sigma_\delta \sim 5$, since this value gives the best agreement with the data.

An efficiency scan over the threshold is also done as shown in the Figure 6.6. The efficiency is reproduced for threshold values above 1 pC. A disagreement is however seen for low threshold values where a difference of 3% is observed. This is essentially due to the presence of the dead channels and dead chips³ and also to the non uniformity of the response over chambers (see Appendix A).

Samples of pions using GPRC calorimeter prototype are also considered. Simulated samples are produced with the same particle type in the energy range of 10 GeV up to 100 GeV according to the test beam data. The digitiser reproduces the pion response (number of calorimeter hits) in the calorimeter as shown in Figure 6.7 for three different threshold values (0.114 pC ,5 pC, 15 pC). For the highest threshold, the data have a large dispersion relative to the predicted value by the digitiser. This behaviour is believed to be due to the statistical fluctuations between the 48 chambers at high threshold. The performances achieved here are sufficient for MC-data comparison of complete shower in the detectors.

The measurement of the pion response was only done for the GRPC data where the experimental setup allows to measure the response of hadron showers [99], unlike MicroMegas which have been not tested as calorimeter.

³A chip groups 64 channels

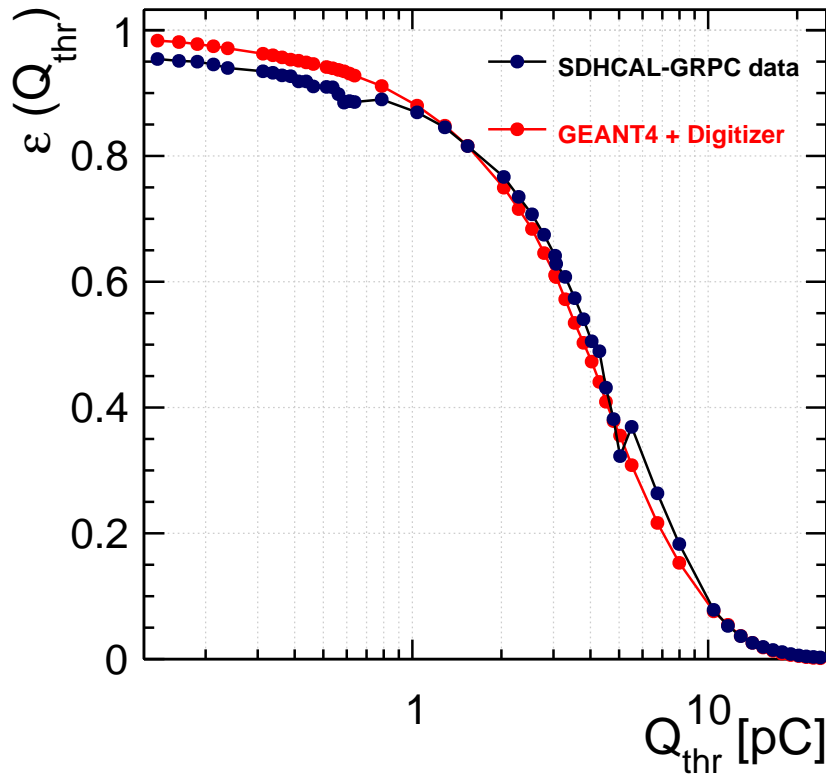


FIGURE 6.6: Evolution of efficiency of GRPC versus threshold. The red and the black lines represent the simulation (using `GEANT4` within the digitiser) and sensor data.

6.5 Conclusion

The digitisation – or the simulation of sensors and electronic associated to a readout pad – is an indispensable and complementary part of generic simulation, such as `GEANT4`. We developed a general gaseous detector digitiser which can reproduce the efficiency and multiplicity response to a minimum ionising particle (MIP), two key response parameters for gaseous calorimeter with a digital readout, using a very fine sensor segmentation.

Polya function is used to model the induced charge spectrum using only two parameters. It describes, with good agreement, the evolution of the efficiency versus the threshold, for both thin GRPC and MicroMegas detectors.

The finite spatial distribution of the induced charge by a MIP track results in the firing of neighbouring pads. The expected number of fired pads highly depends on the relative position within crossed pad. Using a pad sub-segmentation of 1 mm, and sharing the charge with the proper distribution in conjunction with the charge spectrum, the digitiser reproduces adequately the efficiency and multiplicity on MIPs (muons) and pions data.

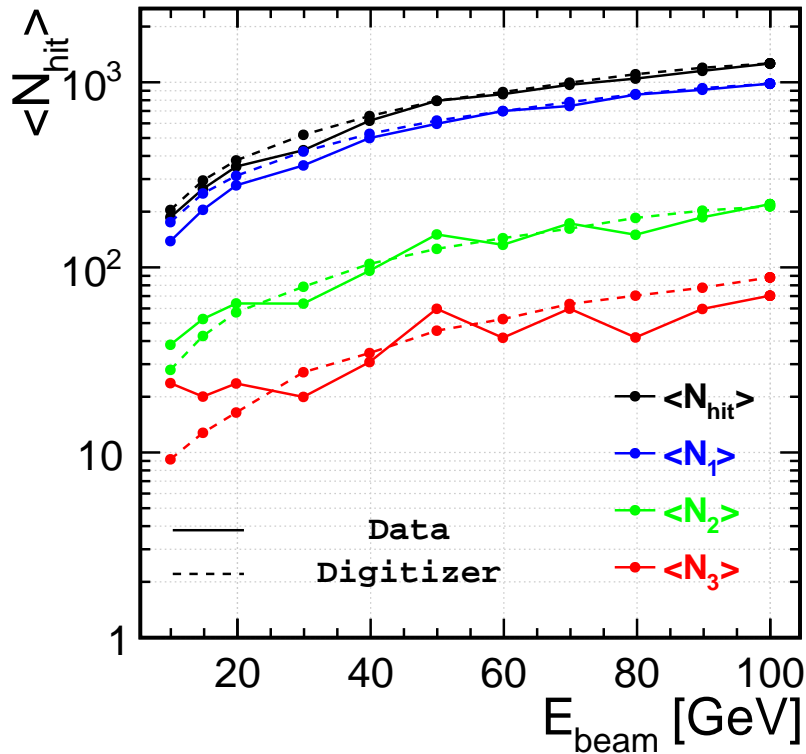


FIGURE 6.7: Number of hits versus pion beam energy for SDHCAL prototype. The blue, green and red curves represent the number of hit reaching only the corresponding threshold values 0.114pC, 5pC, 15pC, respectively. The black curves are the sum of all hits. The data correspond to the solid line, the simulation to the dashed one.

The results shown in this chapter are the first test of the proposed digitisation procedure. Further improvements are underway, especially to reproduce with more accuracy the efficiency at low threshold by including the non-uniformity of the detector and the effect of the dead channels.

Chapter 7

Energy reconstruction in SDHCAL prototype

“An experiment is a question which science poses to Nature, and a measurement is the recording of Nature’s answer”

—Max Planck, The Meaning and Limits of Exact Science.

7.1 Particle identification	114
7.1.1 Principal component analysis	114
7.1.2 Fractal dimension	115
7.1.3 Hit density	117
7.1.4 First interaction plate	118
7.1.5 Additional variables	119
7.2 Event selection	119
7.2.1 Beam muon and cosmic rejection	119
7.2.2 Electron rejection	120
7.2.3 Leakage reduction	122
7.3 Reconstructed energy and intrinsic energy resolution	122
7.3.1 Pure digital mode	124
7.3.2 Semi-digital mode	124
7.3.3 Semi-digital mode versus pure-digital mode	128
7.4 Uniformity correction using minimum ionising particle	129
7.4.1 Basic hadronic showers selection	131
7.4.2 First test	132
7.4.3 Energy reconstruction and resolution	134

After the local characterisation of the calorimeter in term of the detection efficiency and the pad multiplicity the energy global performance for the measurement of the hadronic showers is explored. The SDHCAL prototype was exposed to beams (electrons, pions, muons) of various energies ranging from 5 to 80 GeV, in different beam-test campaigns as described in the Chapter 4. A large amount of showers (electron and pions showers) was then collected (1 billions events).

The analysis described in the following chapter focuses on the energy reconstruction and the energy resolution of the SDHCAL prototype. A meticulous event selection using only the information provided by the calorimeter's data is applied. Innovating techniques in the calorimetric-based particle identification reachable thanks to the high granularity are described and used (see Section 7.1). Then, different parametrisations of the reconstructed energy are tested, in both digital and semi-digital modes. Further, the resolution of the SDHCAL calorimeter is discussed.

Finally, a method for the correction of the response of the SDHCAL calorimeter is explored. It uses the efficiency and multiplicity map measured in the previous chapter (cf Chapter 5) to correct the non-uniformity of the detector and thus reduce the dispersion.

7.1 Particle identification

To study the hadronic showers and reconstruct their energy, a data-based selection using the topological properties of each event in the calorimeter is applied to single out the pions. They are computed using all the spatial information provided by an event. This section enumerates few characterisation procedures used by the SDHCAL group for the particle identification.

7.1.1 Principal component analysis

The Principal Component Analysis (PCA)[102] is a popular data-analysis and dimension-reduction procedure with numerous application in different fields. It has been used for example in the analysis of the extensive air shower[103], electron/jet discrimination in the ATLAS calorimeter [104] and the classification of the galaxies. It uses an orthogonal linear transformation to convert some set of information variables into a linearly uncorrelated ones called principal components. The number of principal components is generally less than or equal to the number of the original variables, thus the origin of the term of dimension-reduction.

In the case of the SDHCAL prototype's data, the observed variables are the hits coordinates $\mathbf{r}_i = (x_i, y_i, z_i)$ (and the reached thresholds). Let consider a set of hit positions taking a form of column vector \mathbf{u} of N_{hit} dimension

$$\mathbf{u} = \begin{bmatrix} r_0 \\ r_1 \\ \vdots \\ r_N \end{bmatrix}. \quad (7.1)$$

The principal components method consists in applying a linear transformation to the original position variables. This transformation is described by an orthogonal matrix and is equivalent to a rotation transformation of the original positions space into a new set of coordinates vector, which permits to identify the principal axis of the hits distribution.

By defining the centre of gravity of the hit set which corresponds to the mean value of the hits set in the 3 directions,

$$\langle \mathbf{u} \rangle = \frac{1}{N} \sum_{i=1}^{N_{hit}} \mathbf{r}_i, \quad (7.2)$$

the covariance matrix can then be written as:

$$\mathbf{C} = \langle \mathbf{v}\mathbf{v}^T \rangle, \quad (7.3)$$

where $\mathbf{v} = u - \langle u \rangle$. The matrix \mathbf{C} is real, positive definite, symmetric and with strictly positive eigenvalues.

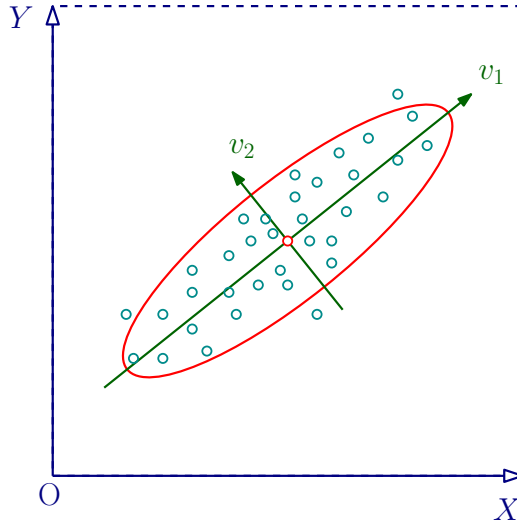


FIGURE 7.1: Example of principal component axes (v_1, v_2) for a given set of points. The ellipse represents the limit of one standard deviation in the (v_1, v_2) frame.

The principal eigenvectors $\{\mathbf{v}_1, \mathbf{v}_2, \mathbf{v}_3\}$ with the corresponding eigenvalues $\{\lambda_1, \lambda_2, \lambda_3\}$ of the matrix \mathbf{C} are then calculated. The eigenvalues are sorted from the smallest to the largest value ($\lambda_1 < \lambda_2 < \lambda_3$). The highest value λ_3 corresponds to standard deviation of the hit distribution in the main axis direction \mathbf{v}_3 . Thus the transverse ratio can be defined by

$$\rho_{\perp} = (\lambda_1 \oplus \lambda_2) / \lambda_3 \quad (7.4)$$

This variable constitutes a powerful discriminant for muon rejection. Since a muon (from cosmic rays and from beam) has a minimal interaction with the detector it leaves a track of couple of hits in each plate. The transverse ratio is expected to be negligible comparing to the one of the hadronic showers.

7.1.2 Fractal dimension

The imaging capability of the highly granular SDHCAL allows the exploration of the fractal nature of the particle showers. Fractals is the name given by Benoit Mandelbrot[105] to self similar objects; objects having a similar structure at different scales. These objects are characterised by a fractional dimension known as fractal dimension.

The fractal dimension summarises detailed information of the spacial configuration of the shower, and is found to be characteristic of the type of the interaction and highly sensitive to the nature of the incident particle [106].

One of the most known method to estimate the fractal dimension is the *box-counting* method; it is therefore the one used in this chapter. In this approach, the effective readout cell size is varied by

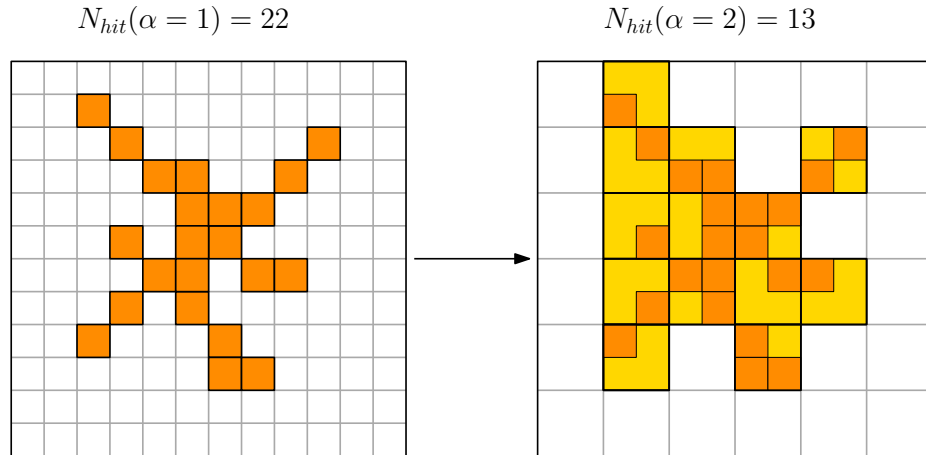


FIGURE 7.2: Example of longitudinal cell grouping in given layer. The number of hits at the ultimate cell size is 22 in this example. In the next scale the number becomes 13.

grouping blocks of α cells, where α defining the scale at which the shower is analysed. If N_α is the number of hits at the scale α , the ratio of the number of hits at the scale β can be written as,

$$R_{\alpha,\beta} = N_\beta/N_\alpha \quad (7.5)$$

Choosing $\beta = 1$ as the reference scale, corresponding to the original size of the readout pads, α is then larger than β ; α has been chosen to take all the integers values $\{1..10\}$.

As shown in the Figure 7.3 the ratio $R_{\alpha,\beta}$ follows roughly a power law with the scale α , for both electromagnetic and hadronic showers. The shower fractal dimension is then defined as

$$D_\beta = \left\langle \frac{\ln(R_{\alpha,\beta})}{\ln(\alpha)} \right\rangle + 1 \quad (7.6)$$

The first term represent the average slope of the power dependence over the variation range, while the second term represents the longitudinal degree of freedom since the effective cell size varies only within detector layers. Each type of particle has the corresponding fractal dimension depending the nature of its interaction with matter. For compact showers, such as the electromagnetic showers, the substructure will stay partly unresolved, and the dimension will be close to 2. In the case of muons, they induce only a non-showering tracks in the calorimeter, which can be regarded as an extreme case of a particle shower, their fractal dimension is then close to 1. Hadronic showers are a mix of compact shower and long travelling particles (in a distance of $\sim \lambda_I$). They will display an intermediate values as shown in Figure 7.4.

A 3D fractal dimension (noted D_{3D}) can also be calculated with a proper longitudinal scale. This allows to integrate the information related to the shower growth.

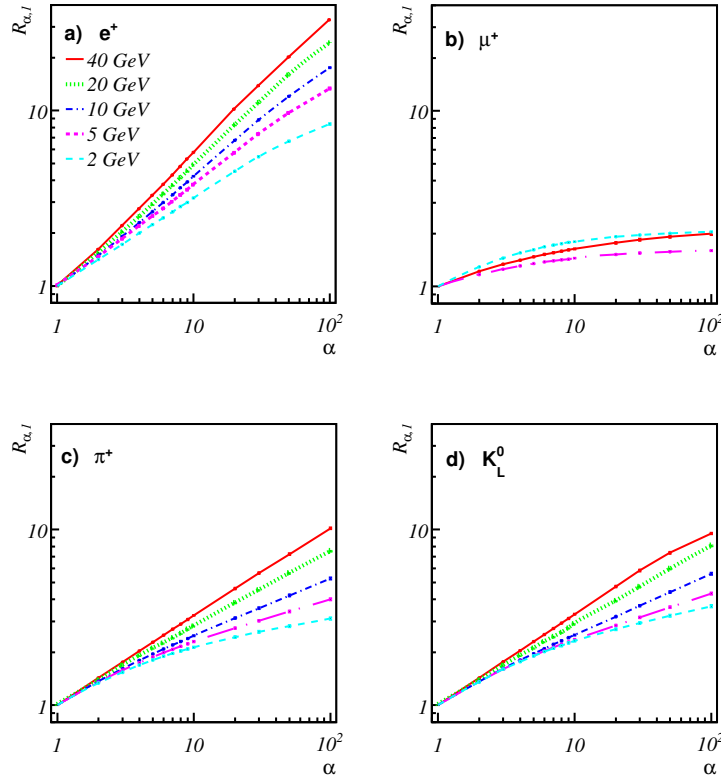


FIGURE 7.3: Dependence of the ratio $R_{\alpha,\beta}$ as function of the scale α for different samples of (a) electron e^+ , (b) muon μ^+ , (c) pion π^+ and (d) K_L^0 . From [106]

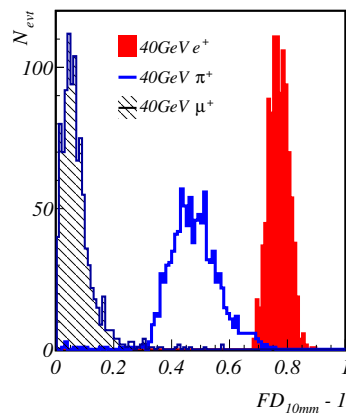


FIGURE 7.4: Distribution of fractal dimension. The different colours correspond to the different type of particles.

7.1.3 Hit density

Another way to discriminate between the electromagnetic and hadronic showers, is the density of the shower. This is achieved by counting for any given hit, the number of first (or second) surrounding neighbours $\delta_{i,j,k}^a$, where a is either 1 for the first neighbours and 2 for first and second neighbours, will

be in the range $[0 - 8]$ ($[0 - 26]$ for the second neighbours). The mean value over all hits present in a given shower (or cluster) provides a discriminant variable:

$$\Delta_a = \frac{1}{N_{hit}} \sum_{(i,j,k)} \delta_{i,j,k}^a \quad (7.7)$$

The hit density is very similar to the fractal dimension since both estimate the intrinsic density of the shower. In the case of MIPs the mean hit density corresponds to the measured multiplicity (~ 3) discussed in the previous chapters (cf. Chapter 5. For electromagnetic showers, the density is expected to be high due to the high multiplicity of tracks within the core showers. Each track hit is expected to have more neighbours. However, in the hadronic shower the induced tracks are more isolated, and the hits density is expected to be close to the MIPs one (Figure 7.5a).

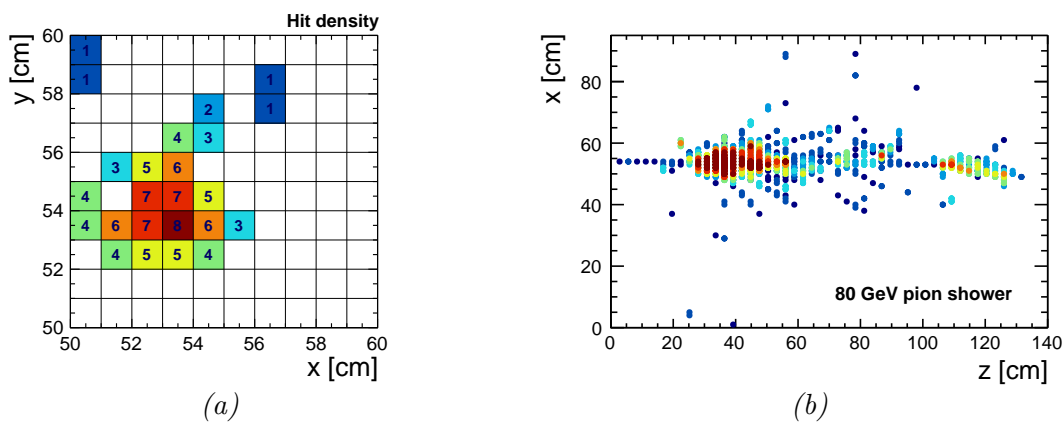


FIGURE 7.5: (a) example of the hit density calculated in each hit in a given layer for pion shower. The numbers represent the multiplicity of the neighbouring fired cells. (b) Hit density calculated for 80 GeV pion shower.

Several experiments, particularly other CALICE prototypes such as the DHCAL, uses this variables to identify the different interacting particles [107].

7.1.4 First interaction plate

For hadronic showers originating from pions or neutral hadron, the hadron traverse a certain distance equivalent to one interaction length before to starts showering. The layer in which the hadron (or electron) initiates a shower is called first interaction plate (or first interaction layer).

Applying a the PCA method in each plate, the recognition of the first interaction plate should satisfy the conditions $\lambda_{1,p} \oplus \lambda_{2,p} > 1.5$ and $N_{hit}(z = p) > 5$. A simpler method consists in counting the number of hits in each plate, the first interaction plate is then defined as the first plate (starting from the front layer) in which the number of hits exceeds 5 and the number of hit in the next one is greater or equal to 5. This method will be used later in the Section 7.3.

7.1.5 Additional variables

Beside the variables described previously, the following quantities are calculated in each single event in the calorimeter.

Centre of gravity

The centre of gravity in each direction (x, y, z) weighted by the hit density (defined previously) is defined as follow

$$\mathbf{G} = \frac{1}{N_{hit}} \sum_{(i,j,k)}^{N_{hit}} \delta_{i,j,k} \mathbf{r}_{i,j,k} \quad (7.8)$$

where the sum is over all the hits indexed by (i, j, k) . The difference with respect the centre of gravity defined in Subsection 7.1.1 is the weighting by hits density which insure the have a centre of the gravity closer to the shower's core.

The number of fired layers

The number of fired layers consists in the simple numeration of the layers containing at least one hit. This variable plays a role in the cosmic muons and electron rejection. Indeed, in the case of the cosmic rays, because of their particular angle, the crossed layers is expected to be less then the available layers, while the beam muons are more penetrating. However, this variable alone does not provide a powerful rejection of cosmic muons, it must be combined with other criteria. This is not the case of the electrons, where the induced electromagnetic showers, which are expected to be denser and less penetrating than hadron ones, the number of fired layers is expected to be less than half of the number of layers available in the calorimeter.

Shower transverse radius

The shower radius is defined by

$$R = \frac{1}{N_{nhit}} \left(\sum_{i=0}^{N_{hit}} (x_i - G_x)^2 + (y_i - G_y)^2 \right)^{1/2} \quad (7.9)$$

where $G_{x,y}$ are the transverse components of centre of gravity defined previously. This definition is equivalent to the one of transverse ratio defined in the Subsection 7.1.1, and used mainly for the beam muon rejection.

7.2 Event selection

7.2.1 Beam muon and cosmic rejection

The passage of muon in the calorimeters leaves a track in the calorimeter. Its specific topology is relatively easy to identify. The transverse ratio, ρ_{\perp} , defined in Equation A.1 constitutes a powerful

discriminant variable as shown in Figure 7.6, in which the ρ_{\perp} distribution for the reconstructed events (both muon and showers) for 7.5 GeV run and for 60 GeV run is shown. No pre-selection is applied in the shown distribution except the removal of the coherent noise (see Chapter 4).

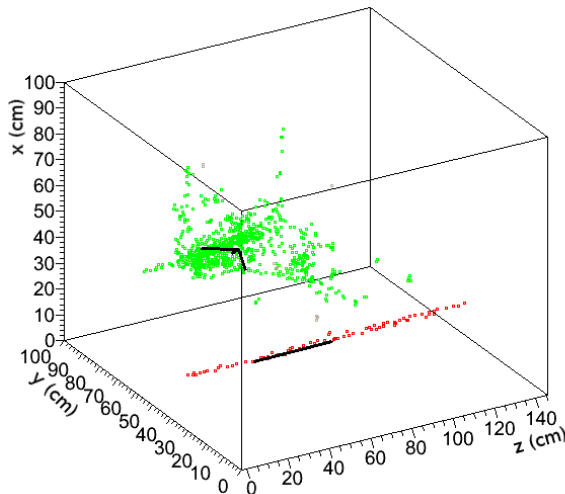


FIGURE 7.6: Example of the PCA-muon rejection.

The muons contribution is peaked in the low value at the ρ_{\perp} . A cut of $\rho_{\perp} \geq 0.1$ leads for 98% of muon rejection.

7.2.2 Electron rejection

As described in Section 4.3, the use of 4 mm thickness lead absorber reduces drastically the electrons contamination for beams above 20 GeV. The contamination increases below this energy, and becomes significant under 10 GeV. Comic and beam muons are the main contamination in the pions runs. The selection of pure hadronic events originated from the pion interactions passes through the calculation of various variables.

To reconstruct the energy of hadronic showers and measure their energy resolution, the contamination by electrons in the pions sample has to be extremely reduced. The two topological variable V_1 and V_2 are used. The first is defined as,

$$V_1 = \frac{1}{N_{hit}} \sum_i^{N_{layer}} N_{5 \times 5}^i \quad (7.10)$$

where $N_{5 \times 5}^i$ is the number of hits in 5×5 pads around the shower barycenter in given layer and N_{hit} the total number of hits. This variable estimates the core shower density, it is expected to be close to one in the case of pure electromagnetic interactions. The second variable is defined by

$$V_2 = D_f^{3D} / \ln(N_{hit}) \quad (7.11)$$

where D_f^{3D} is the fractal dimension in the 3D space as defined in the Section 7.1.2.

The discrimination power of these variables, is illustrated on a scatter plot made for sample of pions (Figure 7.7a) and a sample of electrons (Figure 7.7b) with same energy of (60 GeV). The samples are

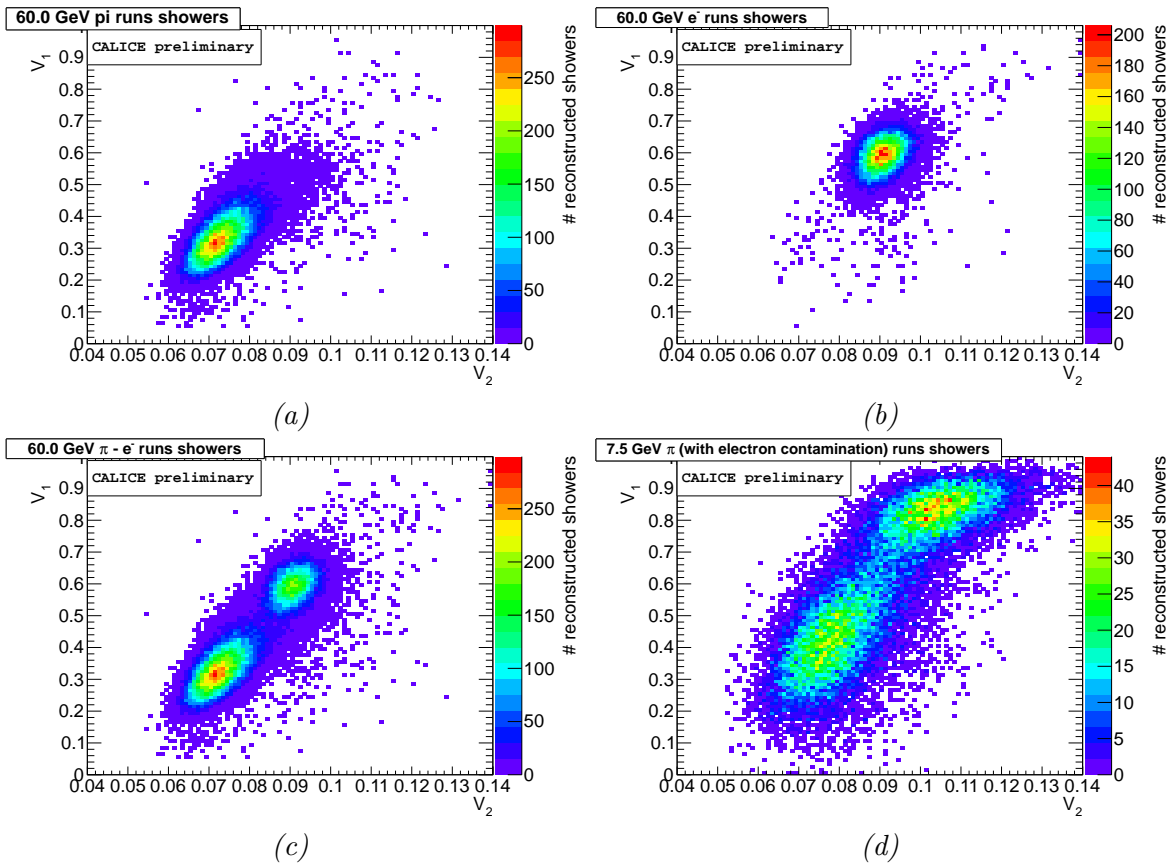


FIGURE 7.7: Correlation between V_1 and V_2 for 60 GeV pions (a), and 60 GeV electrons (b). In (c) the distributions in (a) and (b) are combined. The (d) the scatter plot (V_1 vs V_2) of 7.5 GeV pion run.

combined in Figure 7.7c which shows a clear separation. The same separation is observed for pion runs with a large electron contamination at 7.5 GeV as seen in Figure 7.7d.

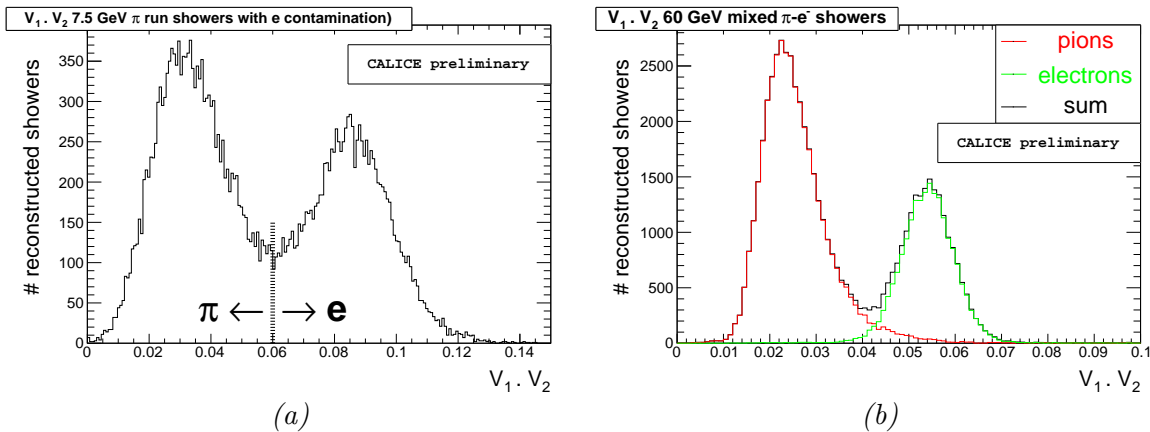


FIGURE 7.8: The electron discriminator variable $V_1 \cdot V_2$ for the 7.5 GeV pion run (a) and for 60 GeV electron and pion runs (b).

To reach a better electromagnetic and hadronic shower separation, the two variable, V_1 and V_2 are combined. As shown in Figure 7.8b, the product of the variable ($V_1 \cdot V_2$) allows for clear separation between electron and pions showers having the same energy. However, a dependence of ($V_1 \cdot V_2$) is seen as function of the energy, thus different cut values are applied for different beam energies as shown in Table 7.1.

E_{beam}	cut($V_1 \cdot V_2$)
5	0.065
[7.5, 15]	0.06
[20, 25]	0.55
[30, 40]	0.05
[50, 60]	0.045
[70, 80]	0.04

TABLE 7.1: Summary of the optimal cut on $V_1 \cdot V_2$ at different energies.

The electron contamination using $V_1 \cdot V_2$ variable is of about of few percent. The rejection improves with the energy allowing almost no pions shower lost (for energies above 10 GeV).

7.2.3 Leakage reduction

To ensure a good measurement of the hadronic showers energy and good estimation of the energy resolution, a selection of well contained shower is required. Indeed, showers interacting later in the calorimeter do not deposit or their total energy in the calorimeter, a fraction of energy is lost by particle leakage. The first interacting plate is required to be in the first 15 layers to reduce the late interacting hadrons. In addition, the last shower plate with hits should be before the 42nd plate, or the ratio of the number of hits in the last seven plates to the number of hits in the 30 first ones should less then 0.15. These last two conditions favour the selection of the fully contained showers in the SDHCAL prototype.

7.3 Reconstructed energy and intrinsic energy resolution

The hadronic showers originated by pions allow the study of the energy response of such particles. As mentioned in the Chapter 3 the linearity of the energy response and the resolution are the most important quality criteria of standard hadronic calorimeter. A method to reconstruct the measured energy is presented in the following section. The data collected by the SDHCAL prototype in all the periods are combined by energies.

At the first level, the estimation of the energy deposited by the hadronic shower in the (semi)-digital calorimeters is the number of hits. The distributions of number of hits at each energy are plotted and fitted. Examples of number of hits distribution are shown in Figure 7.9 for 20 GeV and 60 GeV. As discussed in the Chapter 3 the distribution of number of hits should Gauss distributed in the case of digital calorimeters, because of the suppression of the Landau fluctuation. However, the distributions shown in Figure 7.9 have an asymmetric shape and present a tail at low N_{hit} , specially for a relatively

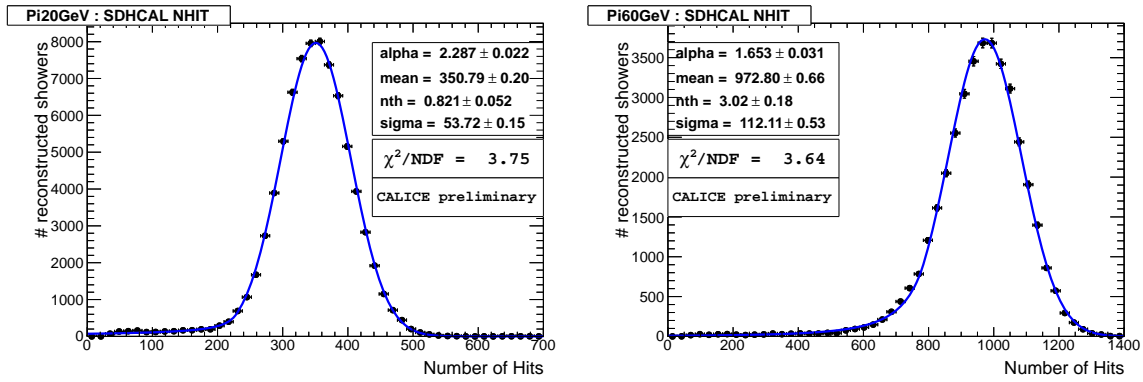


FIGURE 7.9: Total number of hits for pions showers of 20 GeV and 60 GeV.

high energies. This behaviour is a combination of two effects, the geometrical saturation which affects the digital calorimeters at high energy, and shower leakage. The effect of the latter can be reduced as explain in Section 7.2.3.

To reduce the effect of the tail in the estimation of the mean number of hits, \bar{N}_{hit} , two fit ware tried: A Gaussian fit applied in range limited to two standard deviations around the mean value, or Crystal-Ball function (see Appendix A).

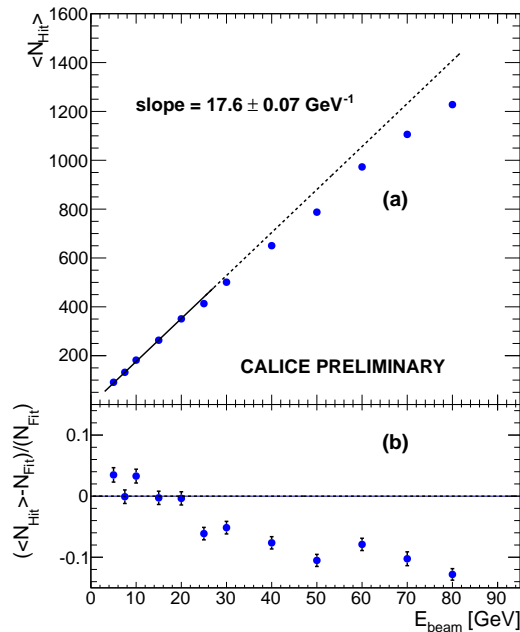


FIGURE 7.10: Mean number of hits as function of beam energy for the reconstructed pion showers. The line indicate a linear fit made with the first six points.

The mean number of hits is determined using Crystal-Ball function. Figure 7.10 shows the evolution of this parameters as function of the beam energy. From this figure we can already conclude that for pions with the energy over 40 GeV the energy estimation using number of hits becomes insufficient. Indeed, at high energy the finite size of the cells limits the showers track counting which induce a saturation effect.

7.3.1 Pure digital mode

The observed deviation of the mean number of hits for energies above 30 GeV suggests the use a no linear function for the reconstructed energy. In order to improve the estimation of the reconstructed energy, a quadratic function of N_{hit} is then chosen

$$E_{reco} = (a + bN_{hit}) N_{hit} \quad (7.12)$$

The parameters a and b are derived from the data by minimising a χ^2 defined by

$$\chi^2 = \sum_{i \in \{events\}} \left(\frac{E_{beam}^i - E_{reco}^i}{E_{beam}^i} \right)^2 \quad (7.13)$$

The distributions of the reconstructed energy are fitted using the same techniques employed previously for the total number of hits (Figure 7.11).

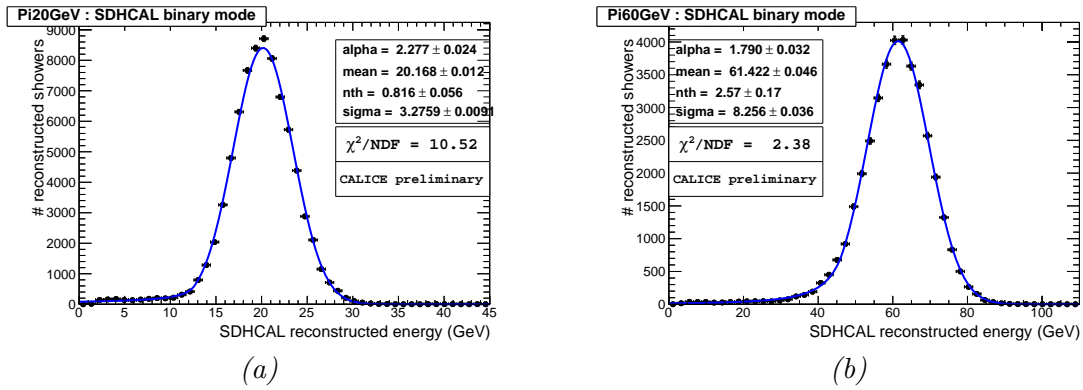


FIGURE 7.11: Reconstructed energy of 20 GeV pions (a) and of 60 GeV pions (b) showers using only the total number of hits (binary mode). The distributions are fitted with Crystal-Ball function.

This parametrisation restores the linearity, as can be seen in Figure 7.12. The energy resolution is defined as $\sigma(E_{reco})/E_{reco}$ where $\sigma(E_{reco})$ is the standard deviation extracted the Crystal-Ball fit; it is shown on Figure 7.13 as function of the beam energy. The quadratic model of the energy reconstruction restores the linearity up to 80 GeV but the saturation effect still remains and impacts the tail of the energy resolution at energies over 50 GeV.

7.3.2 Semi-digital mode

The semi-digital mode is characterised by the presence of three thresholds corresponding to three levels of deposited energy which may help to better estimate the total number of tracks produced in a hadronic shower. In fact, pads covered by two particles in the same time windows (200 ns in our case), and separated by a distance larger then the electronic avalanche (roughly 1 – 2 mm) will have their induced charge added. The MIP charge spectrum (Chapter 5) being broad, the precise measurement of the charge cannot indicate the exact number of charged particles crossing the pad. However it can help to indicate whether this number is low or high. A first validation of this concept is the observation of the hadronic and electromagnetic shower cores, where more particle are produced. A higher density of hits with crossed second and third threshold as shown in Figure 7.14 is observed.

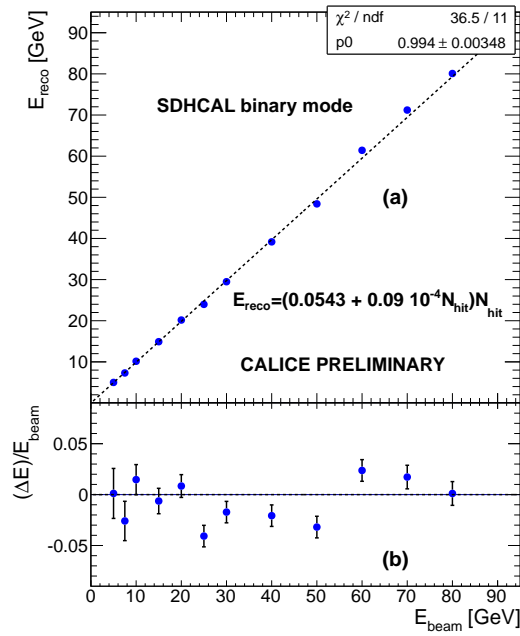


FIGURE 7.12: Mean reconstructed energy for pions as function of the beam energy in the pure digital mode.

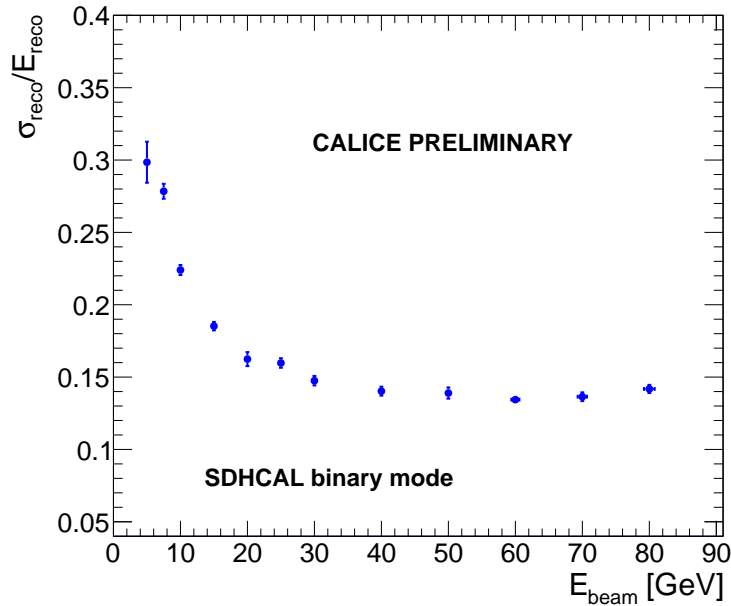


FIGURE 7.13: The pion shower resolution, $\sigma(E_{reco})/E_{reco}$, as function of the beam energy.

The information provided by the threshold suggests to improve the energy measurement by expressing the energy of the showers as a weighted sum of N_1 , N_2 and N_3 . N_1 is the number of hits for which only the first threshold is crossed, N_2 the number of hits which cross the only first and second thresholds and N_3 is the number of hits crossing all the thresholds. The average values of N_1 , N_2 and N_3 are shown in the Figure 7.15 of the selected hadronic showers.

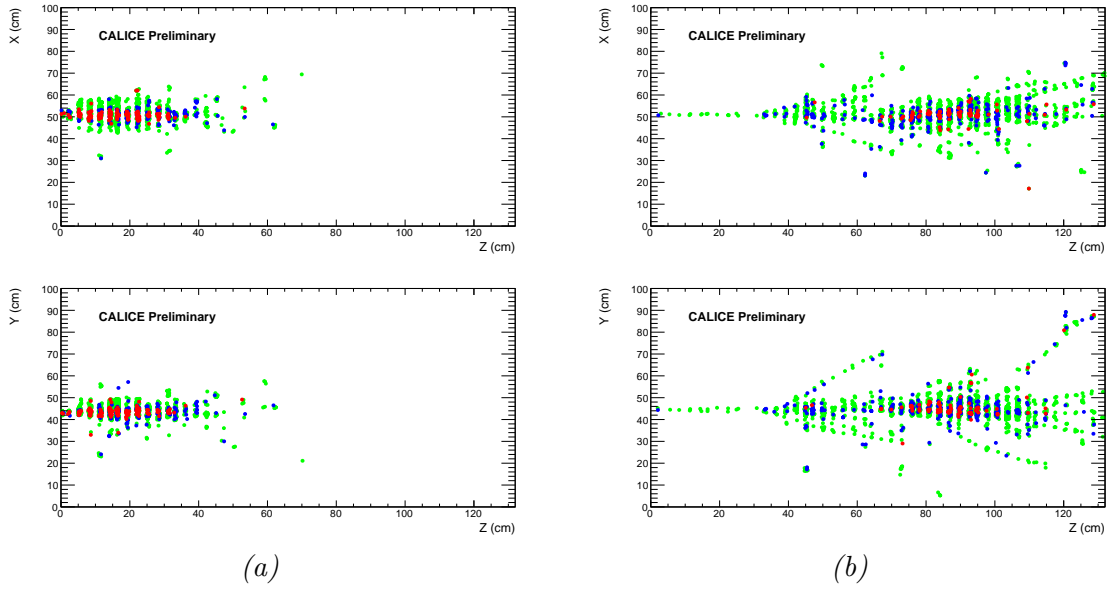


FIGURE 7.14: A 70 GeV electron (a) and a 80 GeV pion (b) event displays. The colours (green, blue, red) correspond to the different thresholds (either 1,2,3)

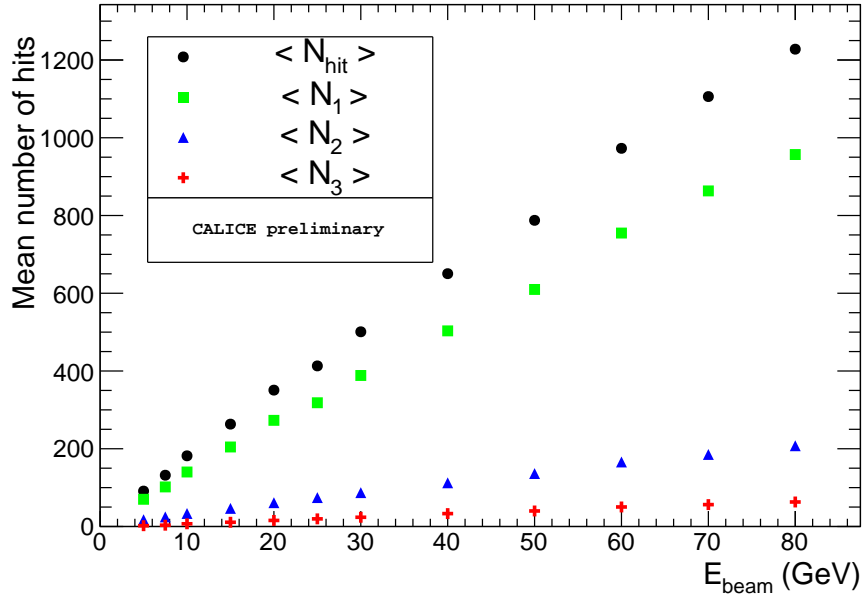


FIGURE 7.15: Average number of hits in the hadronic shower sample corresponding to the first, second and third threshold.

The reconstructed energy can be defined as a simple linear combination of the number of hits at each threshold

$$E_{reco} = \alpha N_1 + \beta N_2 \gamma N_3 \quad (7.14)$$

The complexity of the hadronic shower structure and its evolution with energy excludes the use of constant value of α , β and γ in the full energy range. A quadratic parametrisation of these three quantities as function of the total number of hits ($N_{hit} = N_1 + N_2 + N_3$) is proposed. This leads

for reconstructed energy with 6 parameters. For their determination a χ^2 minimisation is used as expressed in Equation 9.7. The evolution of the quadratic parameters α , β and γ as function of the total number of hits, after the minimisation, are shown in Figure 7.16.

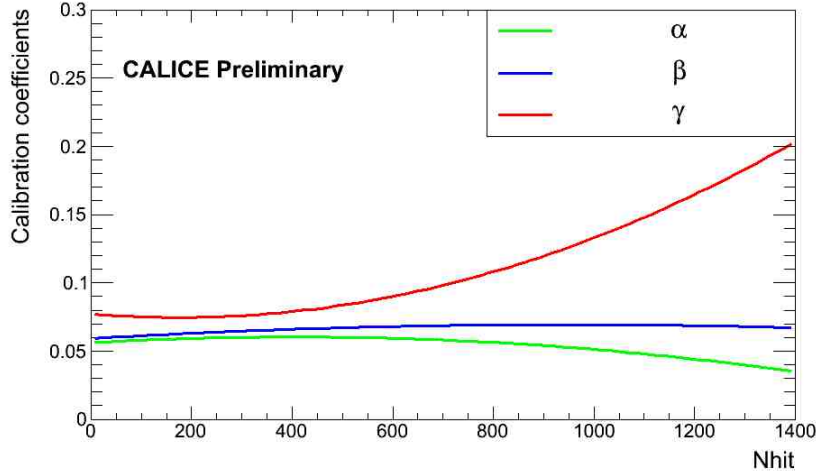


FIGURE 7.16: Evolution of the coefficient α (green), β (blue) and γ (red) as function of the total number of hits.

The parametrisation of the reconstructed energy is not unique, other parametrisations could be more adequate.

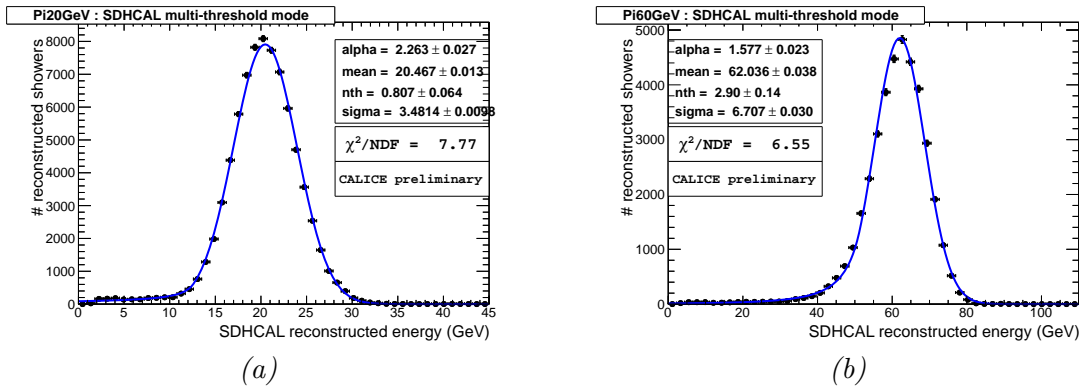


FIGURE 7.17: Reconstructed energy of pion showers ((a) 20 GeV and (b) 60 GeV) using information from three thresholds. The distribution are fitted with a Crystal-Ball function

The reconstructed energy distributions at each beam energy point are then fitted using the Crystal-Ball function as shown in Figure 7.17. As expected, the chosen parametrisation of the reconstructed energy of hadron showers restores the linearity over the full range with an accuracy of 5%. Additionally, the use of the information provided by the presence of three thresholds improves the hadron shower energy resolution at energies above 30 GeV (Figure 7.18). This was predicted by preliminary studies using a Monte Carlo simulation in [108].

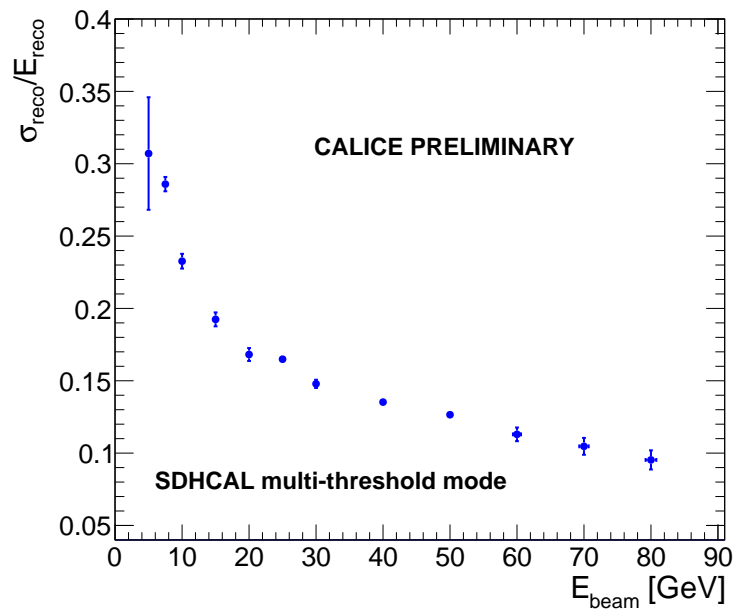


FIGURE 7.18: Resolution $\sigma(E)/E$ of the reconstructed energy as function of beam energy in multi-threshold mode.

7.3.3 Semi-digital mode versus pure-digital mode

The energy reconstruction method using quadratic functions of the total number of hits restores the linearity over a large energy range for both binary and multi-threshold modes. The binary and multi-threshold resolutions are close for energies under 30 GeV. Over that point, the resolution of the multi-threshold mode improves. The direct comparison can be seen in Figure 7.19.

Further comparisons for the reconstructed energy distribution, in both modes, are shown in Figure 7.20 for 80 GeV, 70 GeV and 20 GeV pions. The difference between the two modes is more important at 80 GeV and 70 GeV, while at low energy (20 GeV) the distributions are very similar.

The linearity achieved with the binary mode seems to be better at very low energies (5, 7.5 and 10 GeV), this is probably related to the fact that the multi-threshold mode parametrisation has been tuned for higher energies (> 15 GeV).

The possible contamination of pion sample with electrons at low energy may worsen the energy resolution. This contamination must be highly reduced for a correct estimation of the resolution¹.

The improvement of the energy resolution at high energy, means that the use of the threshold seems to provide additional information to correct the saturation effect which start to show up at energies over 30 GeV.

¹The use of the Cherenkov detector could improve the pion sample purity.

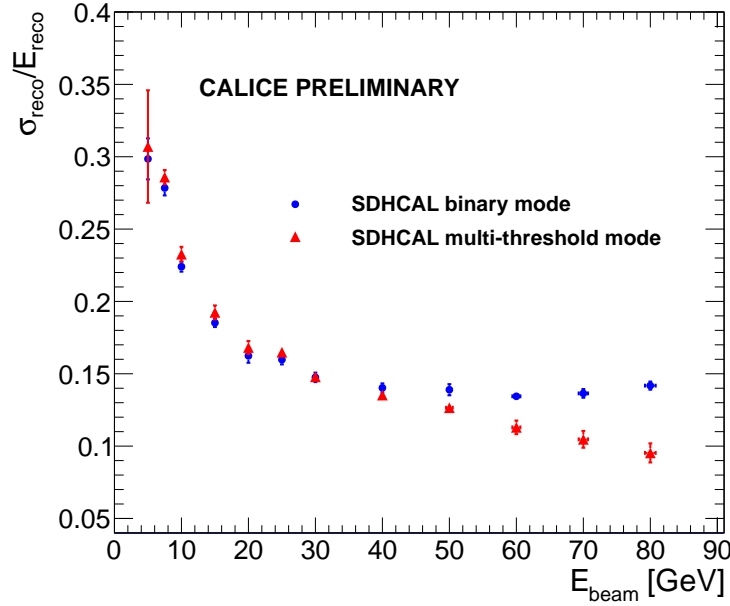


FIGURE 7.19: Resolution $\sigma(E)/E$ of the reconstructed energy as function of beam energy with digital (blue circles) and multi-threshold modes (red circles). In both modes, the energy is reconstructed using quadratic functions of the total number of hits.

7.4 Uniformity correction using minimum ionising particle

In the Chapter 5 the response to muon in term of efficiency and pad multiplicity by ASIC units was shown, as well as the fluctuation of the efficiency and the pad multiplicity as function of the relative position in the GRPC chambers is measured. Since the efficiency and multiplicity represent the main systematic effects in high granular gaseous calorimeter, their fluctuation introduce a bias on the numeration of the number of hits and thus on the estimation of the energy of the incoming particle.

An idea consists to use the MIP recorded during the pions runs to estimate the efficiency and multiplicity of the different ASIC units at each chamber and then introduces a correction factor on the number of hits in each ASIC area unit. The correction factor of an ASIC indexed by i, j, k is given by

$$c_{i,j,k} = \frac{1}{\mu_{i,j,k} \cdot \varepsilon_{i,j,k}} \quad (7.15)$$

where $\mu_{i,j,k}$ and $\varepsilon_{i,j,k}$ are the mean pad multiplicity and the efficiency in the ASIC area unit. The raw response of the calorimeter (R_{raw}) consists on the sample enumeration of the number of hits in a particle shower (see Section 7.3). The corrected response using the MIP can be defined as

$$R_{\text{cor}} = \sum_k^{N_{\text{layer}}} \frac{1}{\langle c \rangle_k} \sum_{(i,j)}^{N_{\text{ASIC}}} N_{i,j,k} \cdot c_{i,j,k} \quad (7.16)$$

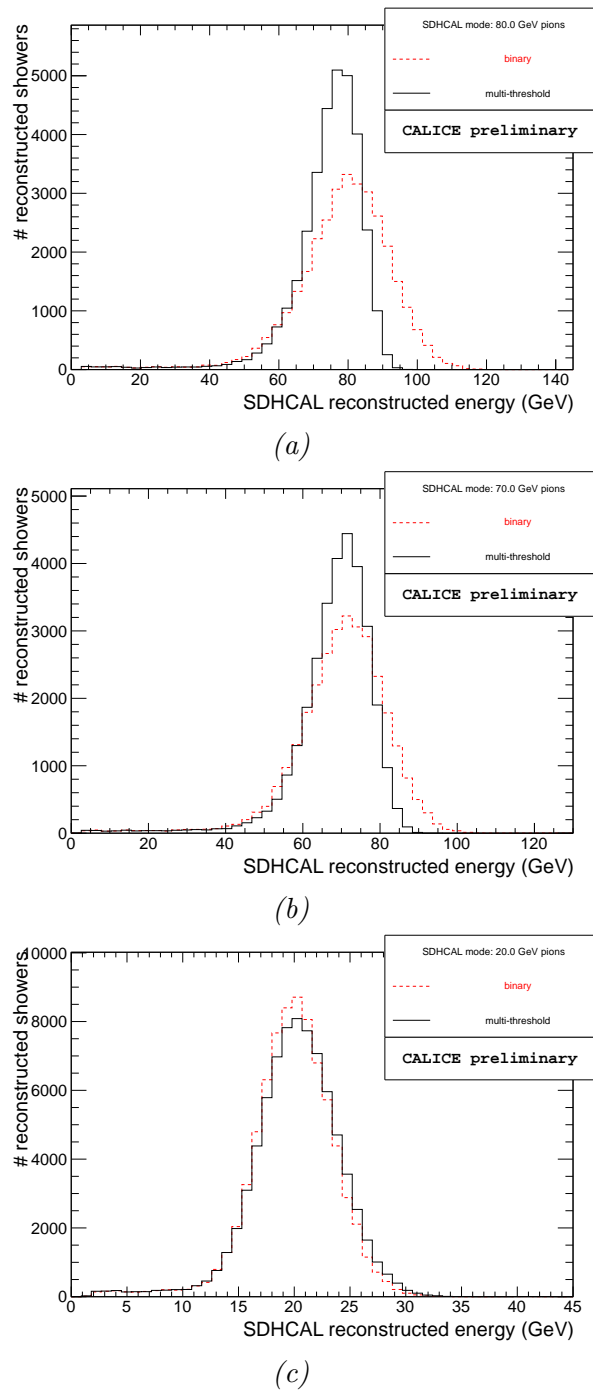


FIGURE 7.20: Distribution of the reconstructed energy with the binary mode (dashed red line), and with the multi-threshold mode (solid black line) for pions of 80 GeV (a), 70 GeV (b) and 20 GeV (c).

where $N_{i,j,k}$ is the number of hits in the ASIC indexed by (i, j, k) , the $\langle c \rangle_k$ is the average correction factor in the chamber k . The ASIC's correction factor distribution for the full detector and for a given pions run is shown in Figure 7.21. The distribution is centered in 1 with a standard deviation of 0.17 introducing a deviation of about 17% on the number of hits in ASIC unit independently from the energy of the incident particle.

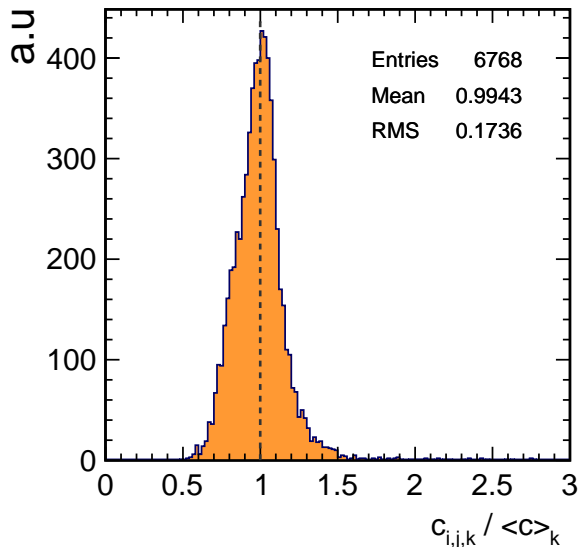


FIGURE 7.21: ASIC's correction factor distribution.

This correction may reduce the constant term in the energy resolution of the calorimeter. This is what we have to demonstrate further.

7.4.1 Basic hadronic showers selection

For this analysis we use another set of selection variables with respect to the previous analysis. First beam and cosmic muons are rejected by asking to have an interaction layer (see Section 7.1). Since the muons (either cosmic or beam muons) are not supposed to initiate an interaction shower, this condition insures a good rejection. However, few muons may interact in the calorimeter producing a small electromagnetic showers, thus events having a radius $R < 3.5$ are rejected.

For the electron rejection, the hit density and fractal dimension are exploited. For more discrimination power the following variable is introduced

$$D = \Delta_1 \oplus \Delta_2 \quad (7.17)$$

where Δ_a is the mean hit density as defined in Equation 7.7. The scatter plots of this variable and the $\ln(D_{3D})$ (where D_{3D} is the 3D fractal dimension defined in Section 7.1.2) show the presence of two populations. The upper one corresponds to the hadronic showers while the lower one to the electromagnetic showers. Thus, the linear cut defined by

$$D > 2.4 + 3 \cdot \ln(D_{3D}) \quad (7.18)$$

is then chosen.

Finally, only events with centre of gravity $G_z < 100$ cm are kept. This favours the fully contained showers, and reduces the leakage. The Figure 7.23 shows the distribution of number of hits before and after the full selection at 60 GeV pion run.

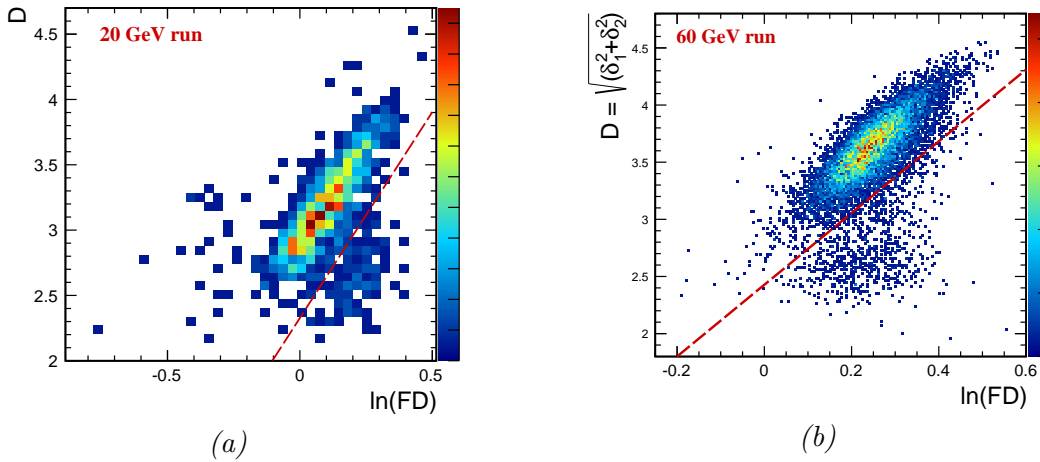


FIGURE 7.22: Correlation between D and $\ln(D_{3D})$ for 20 GeV (a) and 60 GeV (b) pions runs. The dashed red lines represents the chosen linear cut to reduce the electrons contamination.

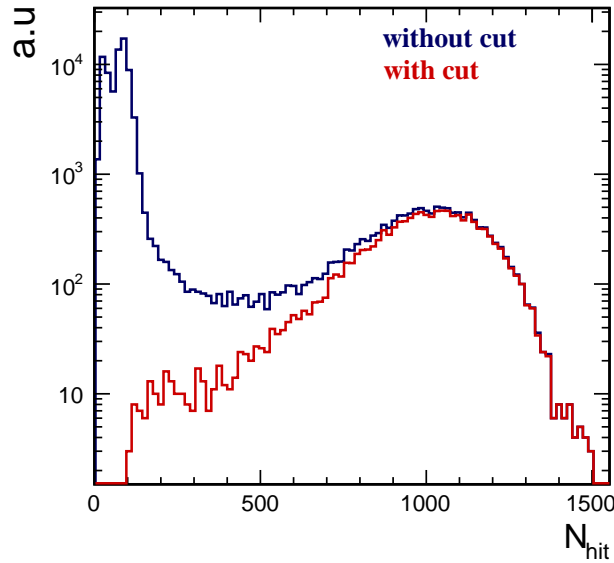


FIGURE 7.23: The distribution of number of hit for 60 GeV pion run before (blue line) and after (red line) the selection.

7.4.2 First test

During the beam test in May 2012 at SPS-H2 line, the position of the detector has changed to shoot the detector in four position as shown in the beam profile (Figure 7.24). This allows the study of the response in different regions in the calorimeter. The Figure 7.25a shows the distribution of the number of hits.

The distribution of the raw response R_{raw} (Figure 7.25a), after applying the correction method described previously, is shown in Figure 7.25b. No visible difference can be noticed. After the calculation of the statistical mean of each spot distribution, the relative deviation of the averages improves a bit using the correction as reported in Table 7.2. A relative deviation in the raw response is of about

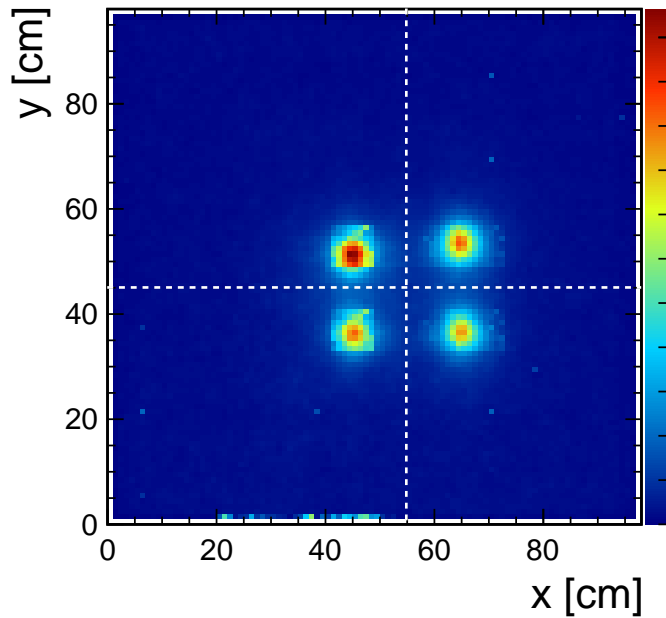


FIGURE 7.24: Beam profile of 50 GeV pion run recorded in May 2012. Four spot can be seen corresponding the four beam position during the run.

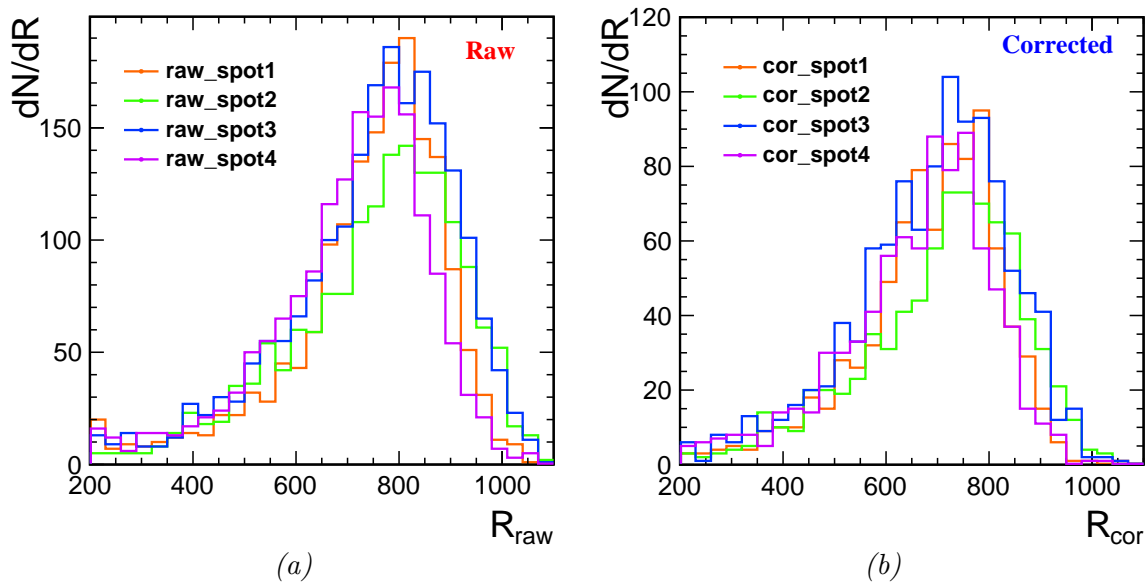


FIGURE 7.25: Distribution of number of hits for four different spots, before and after correction.

2.6% against 2.4% after the correction². Even the correction method do not shows a significant improvement in the case of the four spots data, the result is however encouraging and the impact on the energy resolution at different energies should be visible.

²Note that the correction method does not include a correction of the eventual dead channels or dead ASIC. This may explain the relatively poor improvement in this case.

spot	$\langle R_{raw} \rangle$	$\langle R_{corrected} \rangle$
1	738.7	684.2
2	754.6	707.6
3	747.5	689.8
4	703.2	660.6
$\Delta R/R$	2.6%	2.4%

TABLE 7.2: Average number of hits before and after the correction.

7.4.3 Energy reconstruction and resolution

The energy reconstruction follows the same strategy as described in the Section 7.3. For the current study only the binary mode is considered.

The same parameterization for the reconstructed energy in the binary mode is used. It can be expressed by

$$E_{reco} = (a + bR) R \quad (7.19)$$

where R designates the calorimeter response. R can be either the total number of hits before correction or after correction. A minimisation of the χ^2 is applied to extract the parameters a and b . A Crystal-Ball fit is then applied on the distributions of the reconstructed energy, using the raw and corrected calorimetric response, allowing the measurement of the mean response and the energy resolution as function of the beam energy. The Figure 7.26 summarises the results using both raw and corrected calorimeter response.

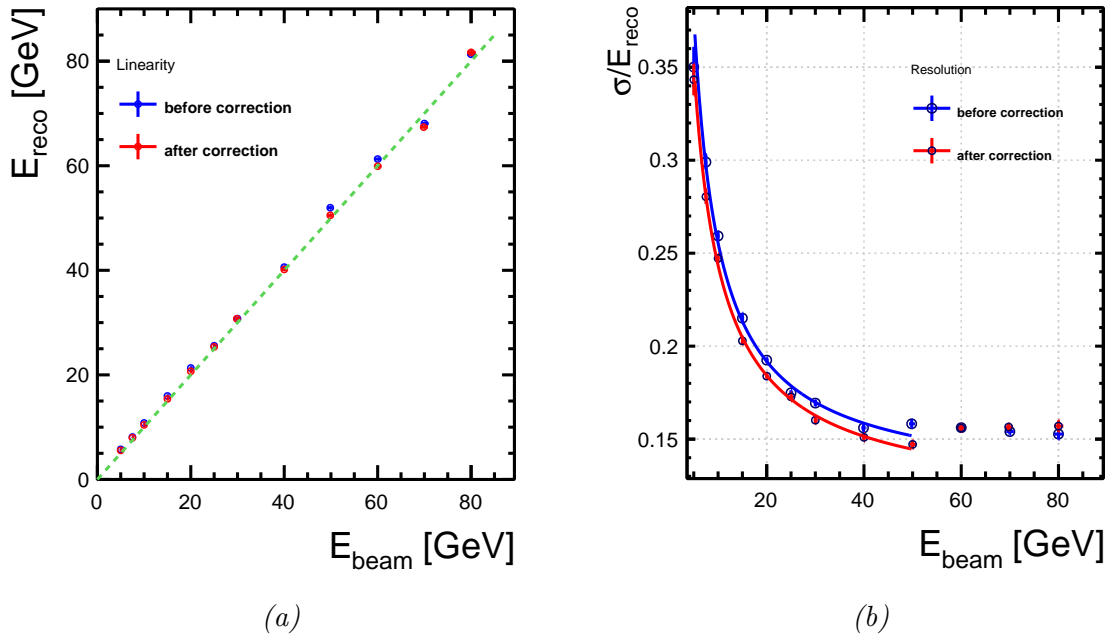


FIGURE 7.26: The mean reconstructed energy (a) and the resolution $\sigma(E)/E$ (b) for pion as function of the beam energy for raw (blue) and corrected (red) response.

The linearity is respected in full energy range. Small deviation between raw and corrected data can be observed at 50 GeV and 60 GeV. In term of resolution the correction method proposed here improves by about 6% the energy resolution for beam energies under 50 GeV.

Chapter 8

Study of High Rate GRPC for LHC Detectors Upgrade

“To succeed, planning alone is insufficient. One must improvise as well.”

— Isaac Asimov, Foundation.

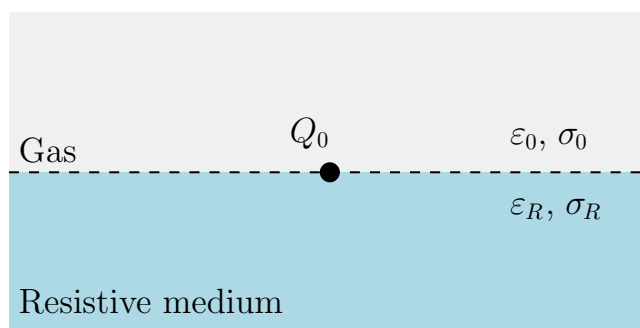
8.1	Experimental setup at DESY test beam	139
8.2	Results and discussion	140
8.3	Conclusion	142

Introduction

The limitation of the detection rate of standard Bakelite Resistive Plate Chambers (RPC) used as muon detectors in the LHC experiments has prevented the use of such detectors in very forward regions (pseudo-rapidity $|\eta| \geq 1.6$) where particle rate exceeds 1 kHz/cm^2 in both CMS[68] and ATLAS[67] detectors.

One alternative to these detectors are RPC's made with low resistivity glass plates ($10^{10} \text{ } \Omega \cdot \text{cm}$). A beam test at DESY has shown that such detectors can operate at few thousand Hz/cm^2 with high efficiency ($> 90\%$). This work has been already reported in [109] and is summarised in this chapter.

RPC's, as described previously, are powerful detectors used in many high energy physics experiments. Their good time resolution and efficiency, in addition to their simplicity and low cost make them excellent candidates for very large area detectors. The high resistivity of glass plates helps to prevent discharge damage in these detectors, but this feature represents a weakness when it comes to their use in high rate environments: the detection efficiency then depends on the operated detection frequency. Both electrons and ions produced during the avalanche growing process have to be recombined when they reach the electrodes surfaces. Under the quasi-static Maxwell's equation in the Laplace domain,

FIGURE 8.1: Point charge Q_0 on the boundary of the gas medium and the glass electrode.

Resistive medium	Resistivity ρ [$\Omega \cdot \text{cm}$]	relative permittivity ε_r	time constant τ [ms]
Float glass	$\sim 10^{12}$	~ 7	708
Bakelite	$\sim 10^{10-12}$	~ 6	6.2 – 620
Doped glass	$\sim 10^{10}$	~ 10	9.7

TABLE 8.1: A characteristics of few used resistive mediums.

the frequency dependence of glass permittivity ε and resistivity ρ can be found [78]. A charge Q_0 at the interface of the resistive plate electrodes surface and the gas (see Figure 8.1), decomposes following an exponential law,

$$Q(t) = Q_0 e^{-t/\tau} \quad (8.1)$$

The time constant τ characterising the recombination of the charge Q_0 can be expressed by the following relation;

$$\tau = \frac{\varepsilon_R + \varepsilon_0}{\sigma_R + \sigma_0} = \rho_R \varepsilon_0 (\varepsilon_r + 1) \quad (8.2)$$

where ρ_R is the volume resistivity of the glass which can be expressed by $\rho_R = 1/\sigma_R$. The gas conductivity is supposed to be negligible here: $\sigma_0 = 0$. ε_0 is the dielectric constant of vacuum and $\varepsilon_R = \varepsilon_r \varepsilon_0$ is the permittivity of the resistive material¹.

A typical glass resistive plate chamber with a volume resistivity of $\rho \sim 10^{12} \Omega \cdot \text{cm}$ leads to an relaxation time of $\tau \sim 1$ s. Table 8.1 summaries the characteristics of the few resistive medium usually used in the HEP experiments. The charges in the resistive medium of the electrodes change the electric field in the gas gap and drop locally its intensity around the initial avalanche. The sensor is then blinded at that position for a time of the order of the relaxation time τ .

The GRPC detector is based on the ionisation produced by charged particles in gas gap. A gas mixture of 93% TFE(C_2F_4), 5% CO_2 and 2% SF_6 is contained in a 1.2 mm gap between 2 glass plates. A high voltage between 6.5 kV and 8 kV was applied on the glass through a resistive coating, assuring the charge multiplication of initial ionisation in avalanche mode with a typical gain of 10^7 .

The new aspect of this detector is the low resistivity of the doped silicate glass ($\sim 10^{10} \Omega \cdot \text{cm}$, compared to the $10^{12} \Omega \cdot \text{cm}$ typical of float glass), provided by *Tsinghua University* following a new process [110]. This leads for an relaxation time of about ~ 10 ms.

The glass plate thickness is 1.1 mm for the cathode and 0.7 mm for the anode. The resistive coating is colloidal graphite of $1 \text{ M}\Omega/\square$ resistivity. The gas was uniformly distributed in the chamber using the

¹Thus ε_r is the relative permittivity of the resistive medium.

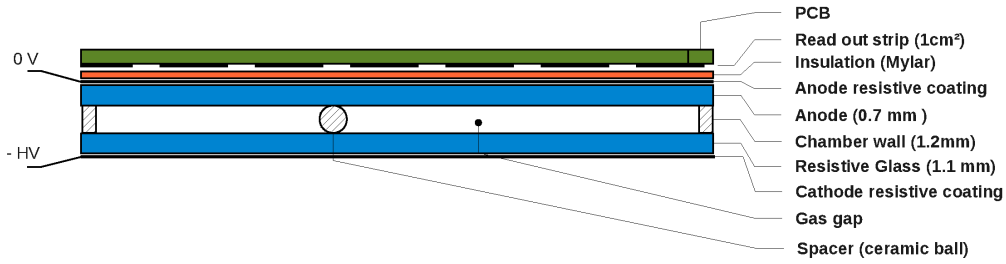


FIGURE 8.2: Schematic drawing of GRPC with electrodes made of silicate glass.



FIGURE 8.3: (a) photo of 30 cm \times 30 cm GRPC with semi-conductive glass. (b) readout pad with size of 1 \times 1 cm²

channelling-based system. Ceramic balls with 1.2 mm diameter were used as spacers. The total GRPC thickness was 3 mm. The signal was collected by 1 \times 1 cm² copper pads (see Figure 8.3b) connected to a semi-digital readout system with 3 thresholds, identical to the one equipping the GRPC chambers used in the SDHCAL prototype developed within the CALICE collaboration [96][98].

8.1 Experimental setup at DESY test beam

The DESY II synchrotron provides an intense and continuous electron beam. It is mainly used as the injector DORIS and PETRA

A bremsstrahlung beam is generated by carbon fiber put in the circulating beam of the electron/positron synchrotron. The photon are converted to electron-positron pairs with metal wire. The momentum of the electrons reaching the experimental area scales between 1 and 5 GeV/c. The particle rate depends on the beam energy, with a maximum of 35 kHz. A collimator situated at the end of the beam line is used performed leading for beam size of few cm².

Two scintillator detectors were placed upstream of the detector. Their role is to measure the beam rate. A schematic layout of a test-beam line is shown in Figure 8.4.

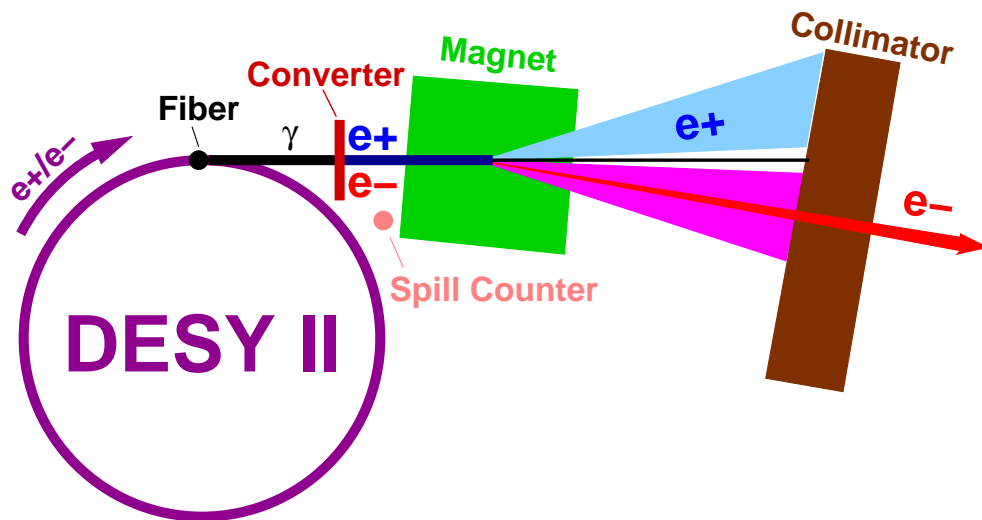
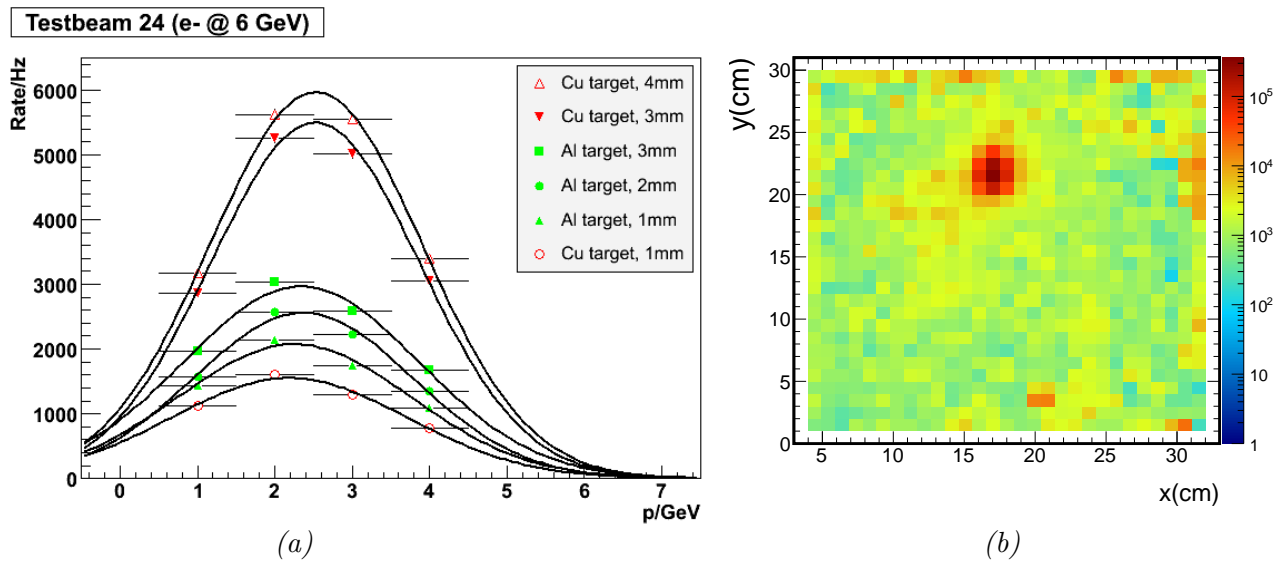


FIGURE 8.4: Schematic layout of a test-beam line at DESY[111]

FIGURE 8.5: e^- Beam rate (Hz) in function of its energy (a) for different targets. The maximum beam rate reached is about ~ 6 KHz using a 4 mm copper target. Beam profile in the chambers with e^- at 2 GeV (b).

Four $30 \times 30 \text{ cm}^2$ area RPCs were built following the design shown in Figure 8.3a and disposed in an experimental setup as shown in the Figure 8.6 and were tested at DESY in January 2012. One additional GRPC made with standard glass was added to the setup.

8.2 Results and discussion

Detector Performances

The local efficiency and multiplicity were measured by using 3 chambers to reconstruct particle tracks and determining the expected hit position in the 4th. The multiplicity μ is defined as the number



FIGURE 8.6: Experimental setup

of fired pads within 3 cm of the expected position. The efficiency ϵ is the fraction of tracks with $\mu \geq 1$. The efficiency (Figure 8.7a) and multiplicity (Figure 8.7b) were measured as function of the polarisation high voltage. The same threshold was used for all voltages. The threshold value is fixed at 50 fC and 7.2 kV was chosen as the working point, giving $(\mu, \epsilon) = (1.4, 95\%)$.

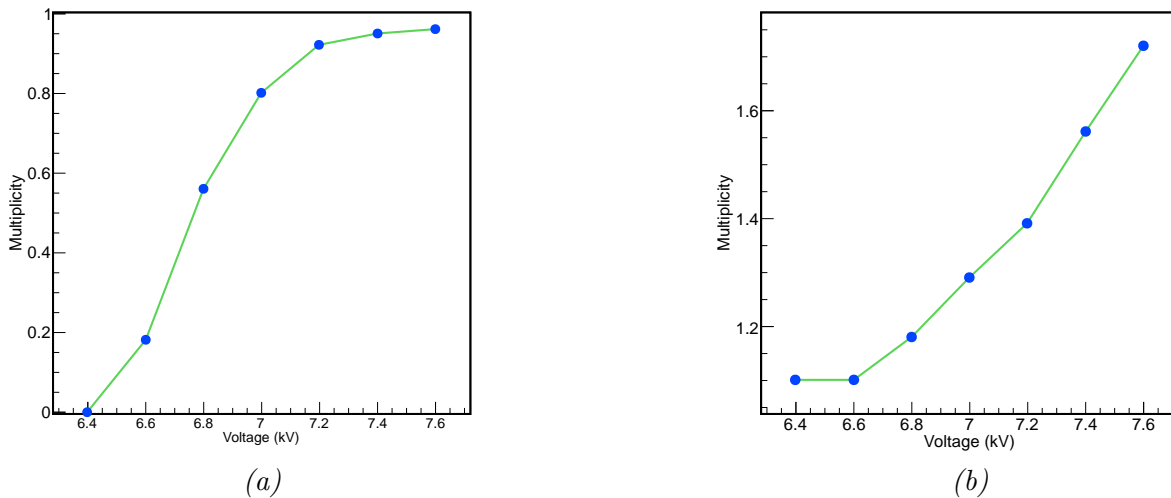


FIGURE 8.7: (a) Efficiency vs high voltage scan. (b) Multiplicity vs high voltage scan

Running at high rate beam

The scintillator detectors were used to determine the total particle flux, which was then divided by the beam RMS area ($\approx 4 \text{ cm}^2$) to obtain the rate by unit area. The measured (μ, ϵ) for different beam rates are plotted in Figure 8.8.

The chamber with standard float glass (GRPC 1) becomes inefficient at rate exceeding one hundred Hz/cm^2 (above 1 kHz the efficiency is below 15%) while the semi-conductive chambers (GRPC 2-5) maintain a high efficiency $\sim 90\%$ until at least 9 kHz/cm^2 .

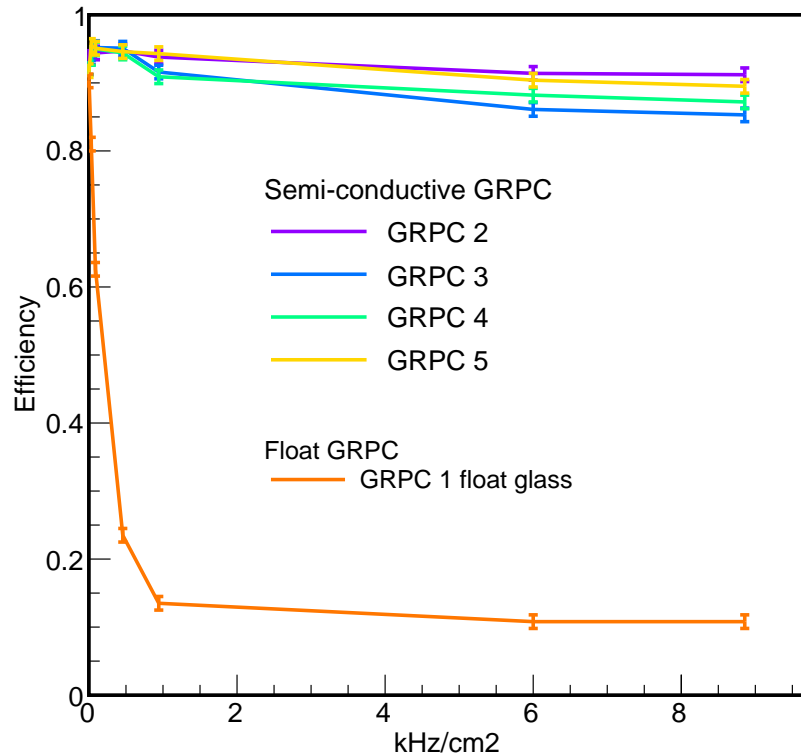


FIGURE 8.8: Efficiency as function the beam rate for different RPC. The orange line corresponds to the GRPC with float glass. The semi-conductive chambers are represented with different colours.

8.3 Conclusion

Glass Resistive Plate Chambers equipped with doped glass were tested at DESY facilities in high rate electron beam, producing very encouraging results; it has been shown that the main weakness of standard GRPCs, namely the drop of efficiency at high rate, is clearly overcome, with deficiencies remaining at around 90% at rate of 9 kHz/cm^2 . This feature, combined with GRPC capability to provide precise time measurement, makes them an excellent candidate for the future LHC muons detector upgrades.

Part III

Higgs analysis

Chapter 9

Tagging the Higgs boson using $Z \rightarrow q\bar{q}$ at 250 GeV ILC

“I never expected this to happen in my lifetime and shall be asking my family to put some champagne in the fridge.”

—Peter Higgs, on CERN when Higgs boson was discovered.

9.1	Introduction	146
9.2	Phenomenological aspects	147
9.2.1	Signal production processes	147
9.2.2	Background processes	148
9.3	Simulation Tools	150
9.3.1	Signal and background processes weighting	150
9.3.2	Simulation of the detector response for particle flow analysis	151
9.4	Analysis Tools	152
9.4.1	Event shape variables	152
9.4.2	Multivariate analysis	153
9.5	Jet reconstruction	156
9.5.1	QCD phenomena and jet formation	156
9.5.2	Jet clustering algorithms principle	156
9.5.3	Jet energy smearing	158
9.5.4	Z jets identification and optimisation of the jet finder	159
9.6	Fast and full simulations	161
9.7	Visible Higgs boson event selection	163
9.7.1	Rejection of $q\bar{q}(\gamma)$ events	163
9.7.2	WW/ZZ vetoes	163
9.7.3	Boosted decision tree construction	167
9.7.4	Testing the model independence	173
9.8	Total Higgs-strahlung cross section and determination of g_{ZZH} coupling strength	175
9.9	Conclusion	177

9.1 Introduction

The measurement of the Higgs boson properties at the future e^+e^- collider ILC can be achieved via the known higgs-strahlung process (Figure 9.1). The $e^+e^- \rightarrow ZH$ represents the largest production cross section for a center-of-mass (c.o.m.) energy of $\sqrt{s} = 250$ GeV assuming a Higgs mass of 125 GeV (Figure 9.2).

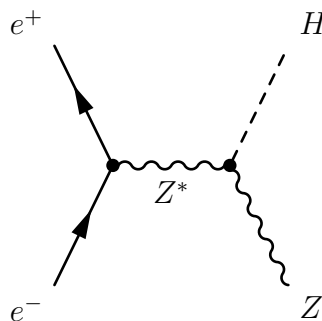


FIGURE 9.1: Leading order Feynman diagram of the Higgs boson production via Higgs-strahlung process.

This chapter presents the study of the Higgs boson recoil mass and Higgsstrahlung cross section measurement in the ILC environment, using first a fast simulation smearing of the jet's energy and momentum, then using a full simulation of the ILD concept. The analysis is performed at $\sqrt{s} = 250$ GeV with $M_H = 125$ GeV, assuming an integrated luminosity of $\mathcal{L} = 500 \text{ fb}^{-1}$ corresponding to 4 years of data taking. The Monte-Carlo (MC) production is based on the ILC's beam parameters, which includes the beamstrahlung effect and the initial state radiations (ISR).

The well defined centre-of-mass energy of collision allows to perform analyses independent from the Higgs boson decay products. Indeed, the identification of the ZH signature can be made by tagging the Z boson, and selecting the proper recoil mass against its decay products. This approach allows to measure the Higgs branching ratios and Higgs production cross section independently from the Higgs decay modes, including invisible Higgs ones, such as $H \rightarrow ZZ \rightarrow \nu\bar{\nu}\nu\bar{\nu}$.

Previous studies [112] have addressed the case where the Z boson decays to $\mu^+\mu^-$ and e^+e^- pairs. For these leptonic channels, the energy and the momentum can be precisely measured with a high performance tracking detector such as the ones proposed for the ILC detectors (SiD and ILD [113]) aiming at momentum resolution of about $\sigma_{(1/p_t)} \sim 2 \times 10^{-5} \text{ GeV}^{-1}$. A precision of about 2.6% on the ZH cross section can be achieved at ILC [112].

However, analyses considering only the leptonic channels, are limited by the statistical precision due to the small branching ratio of $Z \rightarrow \mu^+\mu^-$ and $Z \rightarrow e^+e^-$ process ($\sim 3.3\%$). Thus the idea is to extend this analysis to hadronic decay mode of the Z boson¹, $Z \rightarrow q\bar{q}$, which represent a large branching ratio of about $\sim 70\%$. The challenge is greater since it depends on the jet clustering algorithm which may introduce confusion in the recombination process for hadronic decays of the Higgs boson (and $H \rightarrow \tau\tau$). Thus different reconstruction efficiencies are expected for each decay mode of the Higgs boson.

¹The Z boson decaying into pair of *tau* leptons, which can fake the hadronic decay, is not considered in this study.

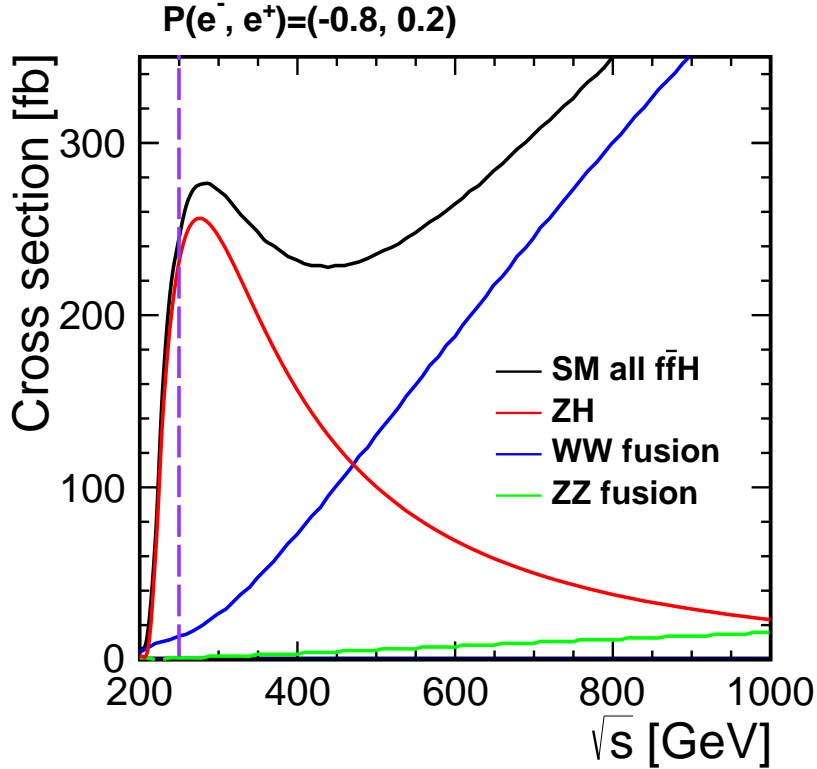


FIGURE 9.2: Higgs boson production cross section as function of the e^+e^- center of mass energy. The purple dashed line represents the ILC operating at a center-of-mass energy of $\sqrt{s} = 250$ GeV

The following study is based on a fast simulation. A smearing of the four momentum of the stable particles takes care of the expected performance of the ILD detector. The jets are then reconstructed using standard e^+e^- jet clustering. The Z boson jet pair is selected by having a mass consistent with a Z boson. In order to reduce the background contamination, an event selection based on a Boosted Decision Tree (BDT) [114] is exploited.

9.2 Phenomenological aspects

9.2.1 Signal production processes

The production of the Higgs boson in e^+e^- collisions at 250 GeV goes, in the standard model of particle physics, mainly through the higgsstrahlung process, in which a Higgs boson is radiated by the Z boson. The leading order cross section is

$$\sigma(e^+e^- \rightarrow HZ) = \frac{G_F^2 M_Z^4}{96\pi s} [\nu_e^2 + a_e^2] \lambda^{1/2} \frac{\lambda + 12M_Z^2/s}{[1 - M_Z^2/s]} \quad (9.1)$$

$$\text{with } \nu_e = -1 + \sin^4 \theta_W \quad a_e = -1$$

λ is equal to $[1 - (M_H + M_Z)^2/s][1 - (M_H - M_Z)^2/s]$ and represents the phase space term of the two-body process. This term is null at threshold ($\sqrt{s} = M_H + M_Z$) defining a kinematic limit. However, the Z boson can be produced off shell, leading to a production of a Higgs boson with mass a bit greater than the kinematic limit $M_H^{\text{limit}} = \sqrt{s} - M_Z$.

The higgsstrahlung is not the only process leading to the production of a Higgs boson, WW and ZZ fusion production modes can also be considered. The Feynman diagrams for these processes are shown in Figure 9.3 and Figure 9.4 respectively. The obtained final states are $e^+e^- \rightarrow H\nu\nu$ and $e^+e^- \rightarrow He^+e^-$. The cross section of these processes is quite small compared to the Higgsstrahlung one for $\sqrt{s} = 250$ GeV and increases with centre of mass energy and becomes the dominant production process for $\sqrt{s} > 500$ GeV for WW fusion ($\sqrt{s} > 1$ TeV for ZZ fusion). The consideration of the WW and ZZ production processes is only usefully for the colliding energy over 350 GeV where the contribution to the total cross section exceeds 25%. Thus for a centre of mass energy of 250 GeV these processes are neglected.

9.2.2 Background processes

9.2.2.1 W^\pm pairs production

The background W^+W^- is produced, at leading order, according to the two diagrams presented in Figure 9.3. The first mode occurs via a Z boson or a photon (γ) in the s -channel, the second occurs via the exchange of a neutrino in the t -channel. Following the decay of each W boson in either quark

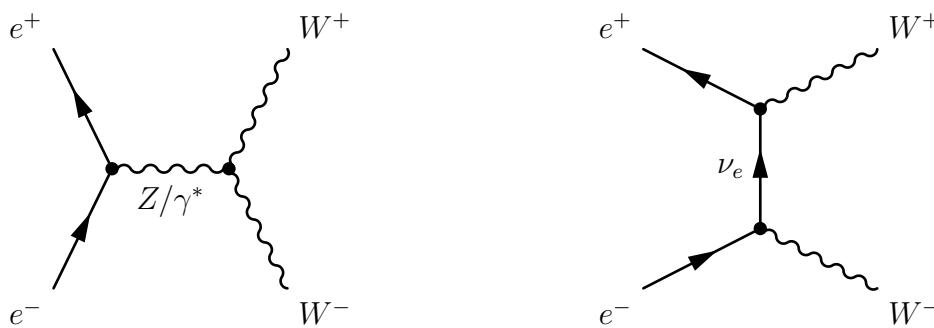


FIGURE 9.3: Leading order diagrams $e^+e^- \rightarrow WW$ production.

pair or lepton pair, the final states can be summarised in three categories:

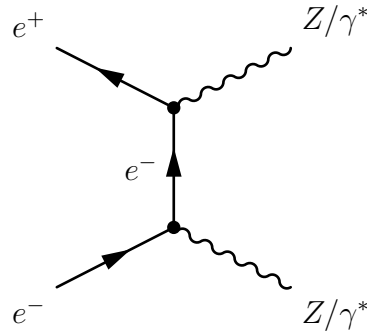
- hadronic mode in which each W boson decays in $q\bar{q}$ pairs (leading to four jets);
- leptonic mode in which each W boson decays in a pair of leptons (including neutrinos);
- semi-leptonic mode where one W boson decays into $q\bar{q}$ pair while the other decays into two leptons.

The fraction of these final states are indicated in Table 9.1. This process constitutes a common background in the analyses of the multi-jets final state and constitutes an irreducible background.

9.2.2.2 Z pairs production

Under the term Z -pair (or ZZ) the different final states ZZ , $Z\gamma^*$ and $\gamma^*\gamma^*$ are included. They are produced via an exchange of an electron in the t -channel as shown in Figure 9.4. The production of a

mode	final state	fraction
Hadronic	$q\bar{q}q\bar{q}$	45.6%
Semi-leptonic	$q\bar{q}l\bar{\nu}$	43.9%
leptonic	$l\bar{l}l\nu$	10.5%

TABLE 9.1: Final states fractions of the $e^+e^- \rightarrow W^+W^-$ process.FIGURE 9.4: Leading order diagrams $e^+e^- \rightarrow ZZ$ production.

Z pair on shell is possible if the centre mass energy is equal to the double of the Z mass. The different decay modes as well as their branching ratios are shown in Table 9.2. Like in the W pair processes this

final state	fraction
Hadronic	$q\bar{q}q\bar{q}$ 49%
Semi-leptonic	$q\bar{q}\nu\bar{\nu}$ 28%
	$q\bar{q}l\bar{l}$ 14%
leptonic	$l\bar{l}\nu\bar{\nu}$ 4%
	$\nu\bar{\nu}\nu\bar{\nu}$ 4%
	$l\bar{l}l\bar{l}$ 1%

TABLE 9.2: Final states fraction of the $e^+e^- \rightarrow ZZ$ process.

background is also common in the multi-jets analyses. In addition, the ZZ process is an irreducible background since in the analysis presented here where the tagging of the Higgs boson is only done by the reconstruction of the Z boson decay mode.

9.2.2.3 Production $q\bar{q}$ pairs

The production of a quark pair occurs via a Z boson or a photon as shown in the diagram in Figure 9.5. The Z boson can be on shell, via the emission of an initial state photon (ISR). The privileged energy for the emitted photon is given by $E_\gamma = \frac{s-M_Z^2}{2\sqrt{s}}$. The photon is emitted more less collinear to the beam axis. If the angle is small enough it will not be detected, such events are then characterised by missing momentum in the O_z direction. Otherwise, it will be detected in the forward calorimeters (ex. LumiCAL).

The background $e^+e^- \rightarrow q\bar{q}$ leads in principle to a 2-jets final state. However a quark with enough energy can emit a gluon leading to the formation of an additional jet. In an analysis which requires

at least two jets in the final state, the $q\bar{q}$ is clearly an important background thanks to its final state topologies and its large cross section.

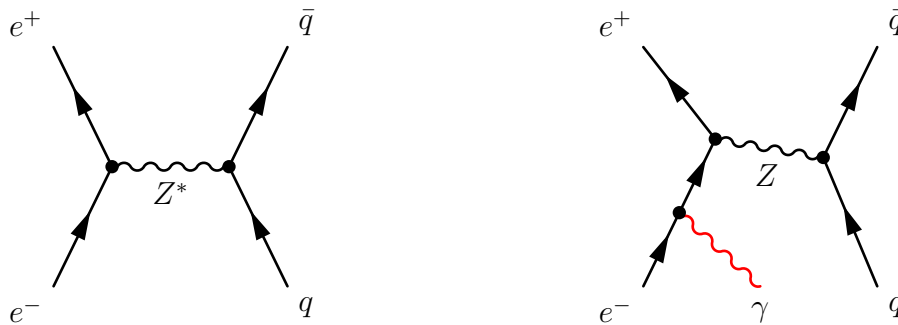


FIGURE 9.5: Leading order Feynman diagram for $e^+e^- \rightarrow q\bar{q}$.

9.3 Simulation Tools

Both signal and background Monte Carlo (MC) samples analysed in this chapter are generated by the ILC group [115] using the version 1.95 of the event generator WHIZARD[116, 117]. The beamstrahlung spectrum calculated with GUINEA-PIG[44] and the Initial (ISR) and final (FSR) State Radiations are included in the event generation.

The full detector simulation is performed in GEANT4[118]. The ILC detector is simulated within MOKKA[119]² which is an interface between GEANT4 and the detector parameters stored in a data base. In the current study the detector model ILD_o2_v06 is used. It includes the SDHCAL option of the hadron calorimeter and SiW-ECAL option as electromagnetic calorimeter.

The reconstruction of the events and the event analysis is performed in the MARLIN[120, 121] framework. The packages MARLINReco [121, 122] and PandoraPFA[36] take care of the charged particle tracking and the Particle Flow reconstruction in ILC detector.

9.3.1 Signal and background processes weighting

The total expected statistics depends on the beam polarisation. The Monte Carlo events are generated for 100% polarised beams. Events from different polarisations need to be mixed in order to obtain a realistic case of partial polarisations P_{e^+} and P_{e^-} of the beams. The number of events generated with a given polarisation $e_L^-e_R^+$ or $e_R^-e_L^+$ is given by

$$N_{true}^{(LR,RL)} = \sigma_{(LR,RL)} \cdot \mathcal{L} \quad (9.2)$$

where $\sigma_{(LR,RL)}$ is the cross section of the considered process, \mathcal{L} is the desired luminosity³. The number of generated events, N_{gen} , is usually less than the true number of events at the luminosity \mathcal{L} . Thus,

²Modellierung mit Objekten eines Kompakten Kalorimeters

³The LL and RR polarisations are not mentioned, since these polarisation are suppressed in the ZH and WW/ZZ processes.

the weight, w , should be applied to normalise the number of generated events to the true one. The weight is calculated as

$$w_{(LR,RL)} = \frac{\sigma_{(LR,RL)} \cdot \mathcal{L}}{N_{gen}} \quad (9.3)$$

This number is calculated for each MC sample used in the current study in Table 9.3. Another weight $w(LR, RL)$, has also to be applied to the MC sample to take into account the polarisation $P(e^+, e^-)$ of the beams. It is derived from the properties of the polarisation:

$$\begin{cases} P_R + P_L = 1 \\ P_R - P_L = P \end{cases} \quad (9.4)$$

where P represents the beam polarisation and $P_R(P_L)$ is the percentage of right-handed (left-handed) events. For example, a 60% positron polarisation is obtained mixing 80% events with right-handed positron beam with 20% events with left-handed positron beam. Similarly, a -80% electron polarisation equals to 10% right-handed and 90% left-handed electron beam. To get for example the weight for a process with the polarisation “ LR ”, the two previous requests are combined to get $w_{LR}(+60\%, -80\%) = 80\% \cdot 10\% = 0.08$. Thus, a general formula emerges from this example,

$$\begin{aligned} w_{LR} &= \left(\frac{1+P(e^-)}{2}\right) \left(\frac{1-P(e^+)}{2}\right) \\ w_{RL} &= \left(\frac{1-P(e^-)}{2}\right) \left(\frac{1+P(e^+)}{2}\right) \end{aligned} \quad (9.5)$$

This will be used further for the study of the impact of the different polarisations on the analysis.

polarisation	process	σ [fb]	N_{events}	weight ($L = 500 \text{ fb}^{-1}$)
$e_L^- e_R^+$	$ZH \rightarrow q\bar{q} + X$	346.013	437368	0.395563
	$WW \rightarrow q\bar{q}q\bar{q}$	14874.3	1074111	6.92401
	$WW \rightarrow q\bar{q}l\nu$	18781	1753663	5.35479
	$ZZ \rightarrow q\bar{q}q\bar{q}$	1402.06	1004632	0.697798
	$ZZ \rightarrow q\bar{q}l^+l^-$	1422.14	1299591	0.547149
	$Z/\gamma \rightarrow q\bar{q}$	129149	1629438	39.6299
$e_R^- e_L^+$	$ZH \rightarrow q\bar{q} + X$	221.952	267357	0.415085
	$WW \rightarrow q\bar{q}q\bar{q}$	136.357	136325	0.500117
	$WW \rightarrow q\bar{q}l\nu$	172.733	158021	0.546551
	$ZZ \rightarrow q\bar{q}q\bar{q}$	604.971	603931	0.500861
	$ZZ \rightarrow q\bar{q}l^+l^-$	713.526	637256	0.559843
	$Z \rightarrow q\bar{q}$	71272.8	1676503	21.2564

TABLE 9.3: Processes and their respective cross sections and statistics in two polarisation modes ($e_R^- e_L^+$ and $e_L^- e_R^+$) at 250 GeV centre of mass.

9.3.2 Simulation of the detector response for particle flow analysis

The use of Particle Flow Algorithm means the reconstruction of all the visible particles combining the information of all sub-detectors. The charged particles will be measured in the tracker, ignoring their calorimeter deposit, while neutral particles (photons, neutral hadrons) are measured by the

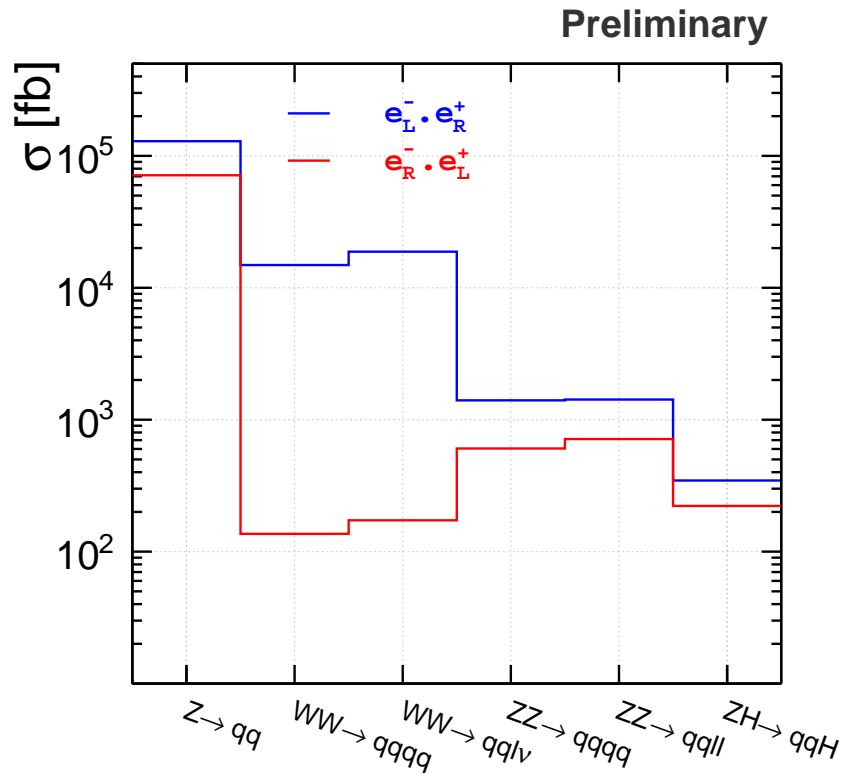


FIGURE 9.6: Cross sections of different processes at centre of mass of 250 GeV

calorimeters⁴. Each reconstructed particle is considered as Particle Flow Object (PFO). Only PFO with $|\cos\theta| < 0.998$ and $p_t > 0.5$ GeV are kept to mimic the acceptance of the ILC detector.

9.4 Analysis Tools

9.4.1 Event shape variables

The global structure of the hadronic events can be best characterised using event shape variables. The variables studied here are the thrust (T), the jet resolution parameters and sphericity. These variables are mainly used in the pre-selection in order to reduce the contribution of the background process $Z \rightarrow q\bar{q}$.

Thrust

The global event shape variable thrust, T [123, 124] is defined as

$$T = \frac{\sum_i |\mathbf{p}_i \cdot \mathbf{n}|}{\sum_I |\mathbf{p}_i|} \quad (9.6)$$

⁴The neutrinos are ignored.

where \mathbf{p}_i is the momentum vector of particle i . The thrust axis, \mathbf{n}_T , is the unit vector which maximises the above expression. The values of the thrust vary from 0.5 for spherical to 1.0 for narrow 2-jets events. This variable will be used in order to reduce the $Z \rightarrow q\bar{q}$ contribution.

The major thrust[125] T_{major} can be determined by maximising the previous expression in plane perpendicular to the thrust axis, \mathbf{n}_T . The resulting direction is called the major $\mathbf{n}_{\text{major}}$. The minor axis, $\mathbf{n}_{\text{minor}} = \mathbf{n}_{\text{major}} \times \mathbf{n}_T$, is defined to give an orthogonal system. Minor (T_{minor}) is normalized sum of momenta projection onto $\mathbf{n}_{\text{minor}}$.

Jet resolution parameters

The jet resolution parameters as defined in Section 9.5 are the transition values, $y^{n \rightarrow n+1}$, at which the classification of event changes from n jets to $(n + 1)$ jets.

Sphericity

The sphericity, S , is defined using the eigenvalues of the sphericity tensor [126],

$$s^{ij} = \frac{\sum_a p_a^i \cdot p_a^j}{\sum_a p_a^2} \quad i, j = 1, 2, 3 \quad (9.7)$$

where p_a^i is the i^{th} component of the momentum vector \mathbf{p}_a . From the eigenvalues of s^{ij} , $Q_1 \leq Q_2 \leq Q_3$, the sphericity is defined as

$$S = \frac{3}{2} (Q_1 + Q_3) \quad (9.8)$$

The hadronic decays in the $Z \rightarrow q\bar{q}$ process have a relatively small sphericity, in which the jets are generally very narrow.

9.4.2 Multivariate analysis

Multivariate analysis methods (MVA) are methods based on machine learning techniques and used to extract maximum of information from a given data set. In high energy physics, MVA classify events as background or signal-like by providing MVA by two training samples, one containing all the known properties about the signal and the other all known properties about the background. These samples are generally taken from simulation. Then, the MVA tries to find all possible correlations useful for the classification, even unknown non-linear correlations. This is therefore superior to simple cut-based approaches.

Several multivariate methods were developed with different properties but obeying to the same concept mentioned above. They are currently widely used in different aspects of HEP analysis. The most known methods are likelihood estimators, Fisher discriminants, artificial neural network and boosted decision trees.

The analysis presented in this chapter uses boosted decision trees described in further detail in the following.

9.4.2.1 Boosted decision trees

The method of Boosted Decision Tree (BDT)[127] is one of the machine learning technique used in high energy physics[23, 128]. It is a composition of a set of trees, each having a structure as seen in Figure 9.7a. It starts from an initial “node” (or root node). Each node can be recursively split into two daughters of branches, until some stopping condition is reached. The process leading to a full tree is called growing or training or learning.

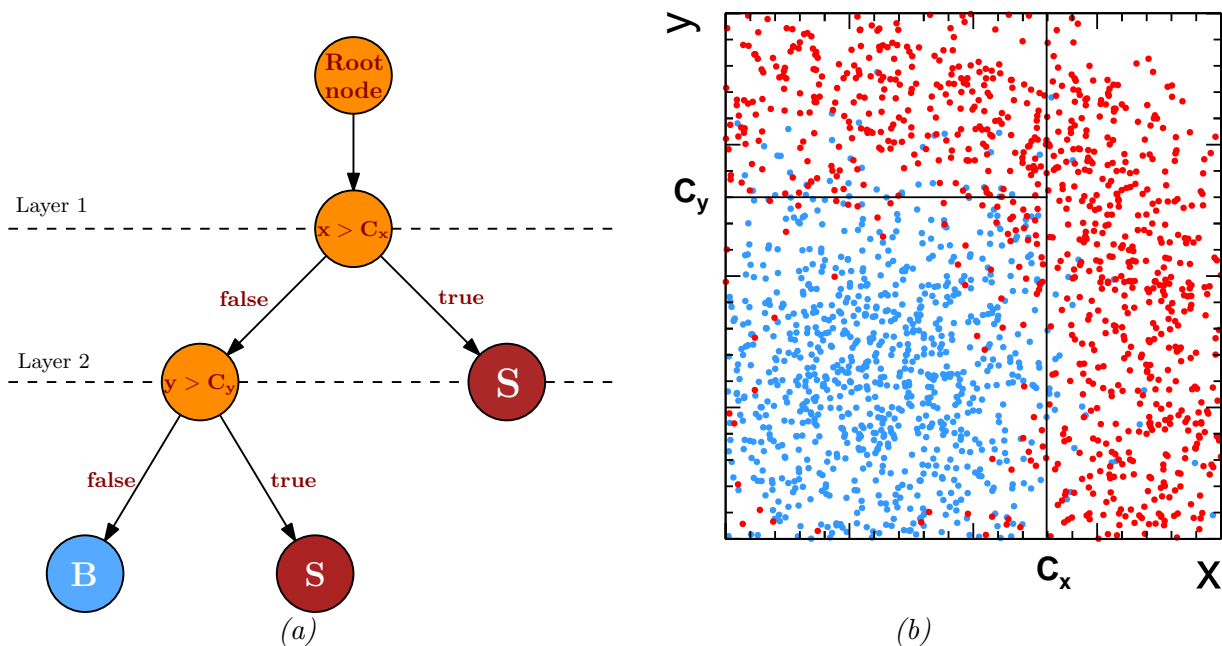


FIGURE 9.7: (a) Graphical representation of decision tree example with a depth of two layers: Starting from the *Root node*, a cut is performed on the variable x maximising the signal significance and the events are split into other nodes.

An example of a decision tree is shown in Figure 9.7a representing a case of two observables x and y in which signal and background are distributed as shown in Figure 9.7b. Such a case cannot be solved with a simple rectangular cuts without losing a significant amount of signal. The use of the decision tree classifies a given event into signal or background and with better efficiency than cut-based approaches. For this purpose the tree needs to build up, or grow. As most of the MVA technique, this is done with the training data: data sample in which the distinction between the signal and the background is already known. The tree grows then node-by-node. At each node creation step, the best cut for the discrimination signal/background is chosen under a certain criterion. The splitting of the node is achieved by creating a certain number of cut values for each observable and then choosing the cut with the lowest impurity.

Let consider the purity of the sample in a branch by

$$p = \frac{\sum_s w_s}{\sum_s w_s + \sum_b w_b} \quad (9.9)$$

where \sum_s and \sum_b are the weighted sums of signal and background events respectively. Note that $p(1-p)$ is equal to 0 in the sample is pure signal or pure background. The signal and background mixing in a given node can be defined in order to characterize the performance of a variable or a cut criteria at that node. This is commonly achieved by using *Gini index* [129] defined as

$$\text{Gini} = \sum_i w_i p(1-p) \quad (9.10)$$

The training procedure selects the best cut value that maximises the gain in the Gini index between parent node and daughter nodes:

$$G = \text{Gini}_{\text{parent}} - (\text{Gini}_1^{\text{daughter}} + \text{Gini}_2^{\text{daughter}}) \quad (9.11)$$

The splitting stops if either the number of events at the node is lower than a given threshold or the maximum number of allowed nodes is reached ⁵.

Decision trees are known to be particularly sensitive to statistical fluctuation. Small changes in the input variable may lead to very different trees, hence different performances. Decision trees which give instead poor performance even after their training are called *weak learners*.

The solution proposed to overcome these problems is the use of the *Boosting* algorithm, a successful way of improving the classifier performance. The idea behind boosting consists in increasing (boosting) the weight, w_i , of misclassified events on the final leaves ⁶. A new tree is built using the new weights, again misclassified events have their weights boosted and the procedure is repeated (typically between 100 and 500 times). In each iteration a certain score α , also called *boost weight*, is given to the tree.

In the so-called *AdaBoost*[130, 131] (adaptive boost) methods the weight takes the form

$$w_m = (1 - f_{err})/f_{err} \quad (9.12)$$

where f_{err} is the misclassification rate in the final nodes of the previous tree. The score for a given tree T_m becomes $\alpha_m = \ln(w_m)$

After having optimised and scored M trees on training sample, the BDT response is a weighted average of the score over the individual trees,

$$T(x) = \sum_{m=1}^M \alpha_m T_m(x) \quad (9.13)$$

$T_m(x)$ takes either the values 1 or -1 . If an event tends to be signal or background respectively 1 or -1 . The final classifier is an average of all the classifiers obtained with the different weights.

9.4.2.2 Toolkit for multivariate analysis (TMVA)

The Toolkit for Multivariate Analysis (TMVA) [114] is a data analysis package which can operate as part of ROOT[94] framework. It provides various of supervised learning techniques used for the event

⁵There are three major measures of node impurity used in practice: mis-classification error, the Gini index and the cross-entropy.

⁶The weight here quantifies the event misclassification.

classification. The software consists of object-oriented implementation in C++ of number of multivariate methods and provides training testing and performance evaluation algorithms and visualisation scripts.

Several multivariate algorithm are embedded in TMVA. The most known being Fisher, Likelihood, Boosted decision tree and Neural networks. The analysis presented in this thesis uses the *TMVA* package.

9.5 Jet reconstruction

9.5.1 QCD phenomena and jet formation

The quarks and anti-quarks produced in the hadronic decay of Z boson $Z \rightarrow q\bar{q}$ are never observed as free particles due to the colour confinement. They give rise to jets of particles observed in the detector. When the $q\bar{q}$ pair is produced at high energy, the fragmentation into high energy partons (gluon and $q\bar{q}$ pairs) is described by the *perturbative* QCD. At lower energy scales, soft gluon radiation – known as the *non-perturbative* QCD phase – is less well described, and has to be modelled using several phenomenological models. In the last phase, the partons produced form stable final state particles: hadron, lepton and photons that can be detected in the detector. This fragmentation process is depicted in Figure 9.8.

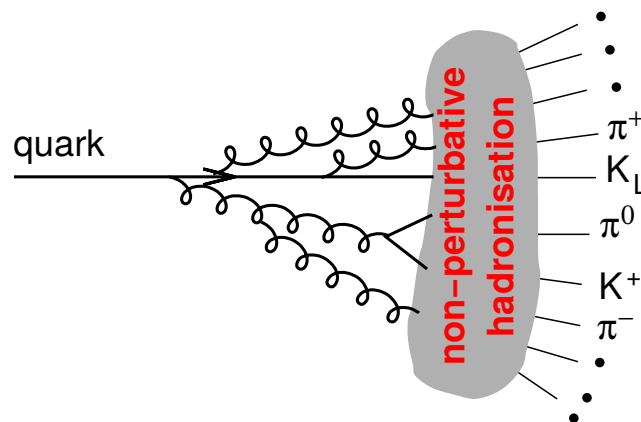


FIGURE 9.8: Schematic representation of hadronization or jet production from a quark.

9.5.2 Jet clustering algorithms principle

The primary quarks or gluons produced during a certain process are identified as a group of particles in the detector as described in the previous section. The measurement of the properties of the primary quark or gluon passes through the correct assignment of the remaining particles in the final state to the quark's (gluon's) jet. To obtain the best estimation of the energy and the momentum of each parton the common way is to cluster all the particles originating from the same parton fragmentation.

Most of the clustering algorithms can be characterised by the following points:

- **a distance** (test variable) $y_{i,j}$ between two objects i and j . This measure is used to decide which particle pair should be combined first;
- **a maximum distance** y_{cut} or **resolution parameter** defining the maximum distance from which two particles can be considered separated⁷;
- **a recombination scheme** describing how to construct the 4-momentum of the object that is formed when two particles get combined.

Most of the jet algorithms follow similar principle: they iteratively combine final state, n , particles (particle flow objects in our case) to form final state jets.

For each pair of these final state particles (objects) (i, j) , the algorithm's distance is calculated. Then, the algorithm combines the objects starting from the pair with smallest value for y_{ij} which is replaced by a *pseudo-jet* with 4-momentum $p_{i,j}^\mu$ using a predefined combination scheme. In the next iteration, again all pair distances on $(n - 1)$ remaining objects are calculated. The procedure is repeated until all pairs of particles reach $y_{ij} > y_{cut}$. Clusters of particles that remain at this stage are called jets. For the given value of y_{cut} the event is characterised by the number of reconstructed jets.

For many applications it is essential to obtain the *transition values* $y^{n \rightarrow n+1}$: the transition value at which the event classification changes from n -jets to $(n + 1)$ -jets by reducing the y_{cut} value. The final jet configuration is identical for all values of y_{cut} between two subsequent transition values. Using the transition values one can select a value for y_{cut} such that the event is resolved into the required number of jets. Hence the event can be *forced* into a desired number of jets⁸.

One of the first jet algorithm that follows the previous recursive procedure is the one developed by the JADE[133] collaboration in order to study the jet production in the e^+e^- collision at PETRA. This algorithm permitted to measure the coupling constant α_s of the strong interaction and to test various QCD models of parton showering. This algorithm is characterised by the distance

$$y_{ij} = \frac{2E_i E_j}{E_{vis}^2} (1 - \cos\theta_{ij}) \quad (9.14)$$

The E_i and E_j denote the energy of the particle i and j and θ_{ij} is their opening angle. The y_{ij} is normalised by the visible energy E_{vis} , sum of the energy of all visible particles in the event. The recombination scheme mentioned previously consists on in adding the 4-momenta via a variety of schemes during the combination of the particles:

$$\begin{aligned} \text{E-scheme:} & \quad E_{ij} = E_i + E_j & \text{and} & \quad \mathbf{p}_{ij} = \mathbf{p}_i + \mathbf{p}_j \\ \text{E}_0\text{-scheme:} & \quad E_{ij} = E_i + E_j & \text{and} & \quad \mathbf{p}_{ij} = (\mathbf{p}_i + \mathbf{p}_j) \cdot E_{ij}/|\mathbf{p}_i + \mathbf{p}_j| \\ \text{P-scheme:} & \quad E_{ij} = |\mathbf{p}_{ij}| & \text{and} & \quad \mathbf{p}_{ij} = \mathbf{p}_i + \mathbf{p}_j \end{aligned}$$

The JADE algorithm is not adequate for the study of the multiple soft gluon radiation by the initial quarks. Two gluons emitted in the different directions having a relatively small energy will be associated by the JADE algorithm due the term $E_i E_j$ for the Equation 9.14. The algorithm tends to create jets formed by soft gluons. This makes JADE sensitive to high order perturbative correction of soft gluons.

⁷When this distance is reached by the algorithm the clustering ends.

⁸In the determination of the W boson characteristic in the hadronic decays of W^+W^- pairs at the LEP2[132], the event have to be clustered to four jets.

Durham clustering algorithm

The Durham algorithm[134] (or k_{\perp} -algorithm) is derived from the JADE algorithm by replacing the test variable with

$$y_{ij} = \frac{2 \min\{E_i^2, E_j^2\}}{E_{vis}^2} (1 - \cos\theta_{ij}) \quad (9.15)$$

Using this new expression, a soft gluon is associated to another soft gluon if their opening angle is lower than the opening angle with high energy parton. Thus the formation of jets from soft gluons encountered in JADE is overcome.

Another advantage of Durham algorithm is the fact that the hadronisation of the parton final states can be shown to have, on average, little influence on the jet-rates. This can be evaluated at generator level by studying the difference between parton and hadron level. The difference vary significantly between clustering procedures and is shown to be smallest for Durham algorithm [135]. However, there is no best jet clustering algorithm, every algorithm has specific qualities and problems, but in the multi-jet events at LEP2 the Durham clustering algorithm is generally accepted as one of the best in recounting the energy flow of the original partons and is therefore used for the analysis presented in this thesis.

The algorithms described above have been implemented in a framework called **FastJet-v3.0.6**[136, 137]. It offers many tools and various jet algorithms dedicated to hadron and e^+e^- colliders.

9.5.3 Jet energy smearing

To simulate the effect of the detector response as well as the confusion in the reconstruction of the particles, the energy and the momentum of the particles have to be smeared to the expected jet energy resolution. Let us consider that the jet energy resolution reachable by a detector (like ILD) can be expressed by

$$\left(\frac{\sigma(E_j)}{E_j}\right) = \alpha \quad (9.16)$$

where E_j is the jet energy. Other parametrisations can be applied such as $(\sigma(E_j)/E_j) = \alpha/\sqrt{E_j}$ where the jet resolution improves at high energy which is not the case because of the confusion in the particle reconstruction⁹.

The smearing is done by generating a random number following a Gauss distribution centred in 0 and with a standard deviation of $\sigma(E_j) = \alpha \cdot E_j$. To avoid negative jet masses, the jet's momentum has to satisfy the quadrature condition $\mathbf{p}_j^2 = E_j^2 - m_j^2$. On the basis of this condition, the momentum is smeared by Gaussian function of standard deviation of

$$\sigma(\mathbf{p}_j) = \left(\frac{E_j}{\mathbf{p}_j}\right) \sigma(E_j) = \left(\frac{E_j^2}{\mathbf{p}_j}\right) \alpha \quad (9.17)$$

In this parametrisation, the jet energy resolution is constant with the jet energy.

The choice of the parameters α is made later using the reconstruction of the events in full ILD detector simulation (see Section 9.6).

⁹High energy jets are more boosted and the particles are more collinear and collimated.

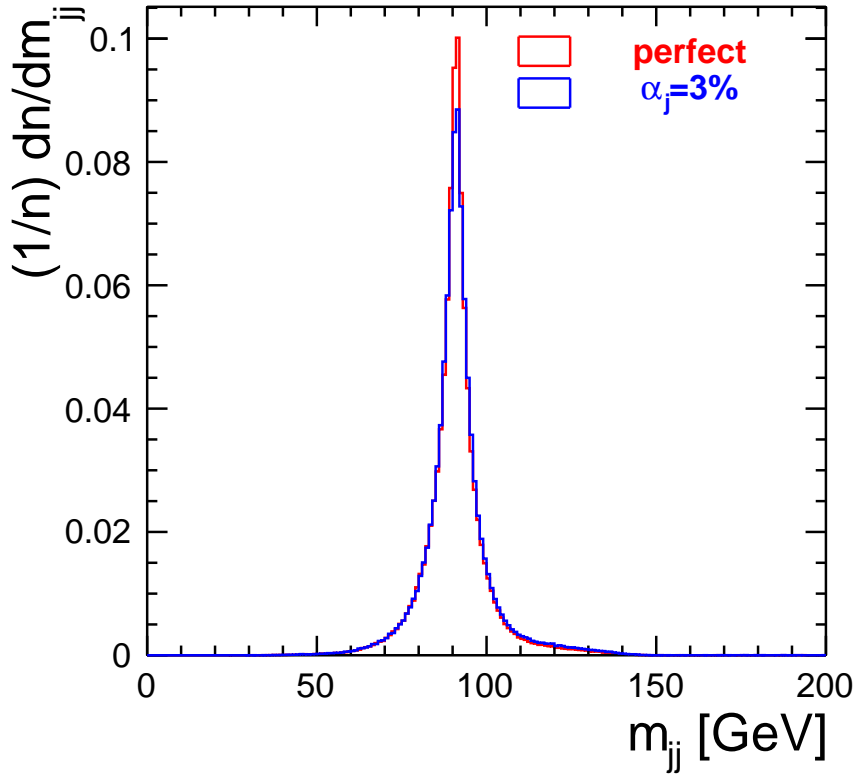


FIGURE 9.9: The invariant mass of di-jet system of the process $Z \rightarrow q\bar{q}$, before (red) and after smearing with $\alpha = 3\%$.

9.5.4 Z jets identification and optimisation of the jet finder

The task of the Z boson jet identification is the tagging of the jets produced in the decay of the Z boson. In the first step, the jet clustering is performed using the Durham algorithm (described previously) using a fixed y_{cut} . Not forcing the final state to a predefined number of jets does not constraint the Higgs decay mode. Indeed, the $ZH \rightarrow q\bar{q} + X$ has various final state topologies as shown in Figure 9.12.

Unlike for $Z \rightarrow \mu^+\mu^-(e^+e^-)$ channels, in the hadronic channel $Z \rightarrow q\bar{q}$ the jet finding blurs the separation between the Higgs and Z boson decay products (see Figure 9.10). The separation between the Higgs and Z boson decays is not obvious. This leads to different selection efficiencies for different Higgs decay modes. The hadronic channel can never be truly model independent as the $Z \rightarrow \mu^+\mu^-(e^+e^-)$ channels.

In the ZH events, where the Z boson decays hadronically, many topologies can be identified depending on the Higgs boson decay modes. The events cannot be forced in predefined number of jets in order to provide an unbiased Higgs boson selection. The events are then resolved in an arbitrary number of exclusive jets using Durham with fixed y_{cut} . The resolved jets are combined in all possible pairs¹⁰. The identification of the Z boson jets is then done using the invariant mass criterion; the jet pair with

¹⁰Note that the number of the possible combinations is given by $C_2^{N_{jets}} = N_{jets}!/2 \cdot (N_{jets} - 2)!$

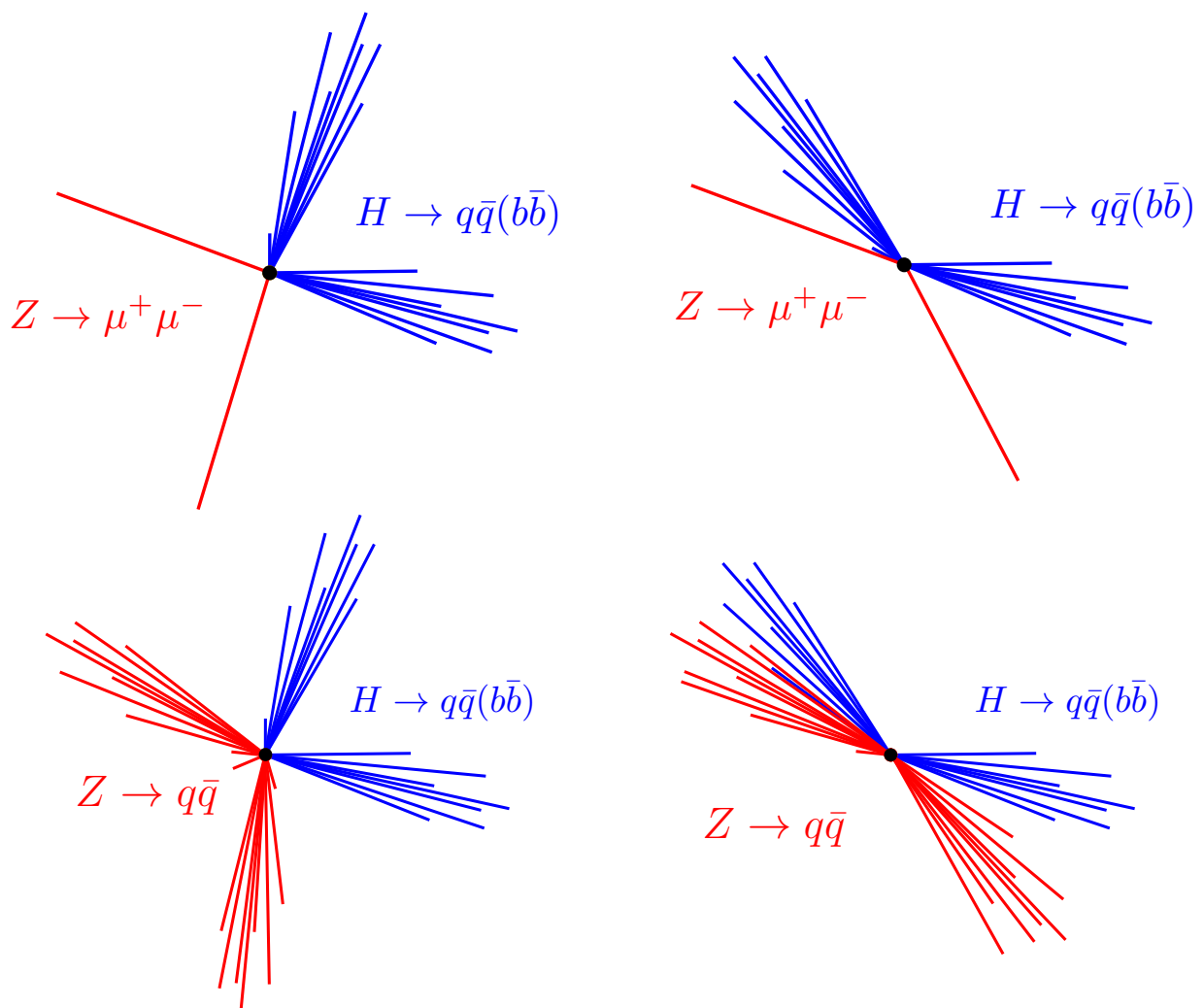


FIGURE 9.10: For the channel $ZH \rightarrow \mu^+\mu^- + X$, the identification muons from the Z boson are obvious (on top). For the hadronic channel, the Z boson jets finding blurs the separation between Z and H bosons (on bottom).

invariant mass closest to the true Z boson mass is selected. The Figure 9.11 represents the selected Z boson jet candidates sorted out from all possible combinations.

In order to find an optimal y_{cut} for the reconstruction of the signal, the selected di-jet mass is fitted by a *Voigtian*; a convolution of a Breit-Wigner and Gaussian probability density functions, where the Breit-Wigner function describes the Z boson resonance and the Gaussian the effect of the jet resolution and the jet clustering.

The evolution of χ^2 as well as the number of resolved jets as function of y_{cut} is then drawn in Figure 9.13a and Figure 9.13b respectively. The χ^2 shows a minimum around $y_{cut} = 0.006$ which corresponds to an average number of jets of ~ 4 . This can be noticed in Figure 9.13c where the number of jet distribution for $y_{cut} = 0.006$ is peaked at 4 as expected, since for a Higgs boson for $m_H = 125$ GeV the most probable decay mode is the $H \rightarrow b\bar{b}$ leading to 4-jets in the ZH final state.

During the combination the algorithm is required to take only the jets with high track multiplicity: $N_{track} \geq 5$.

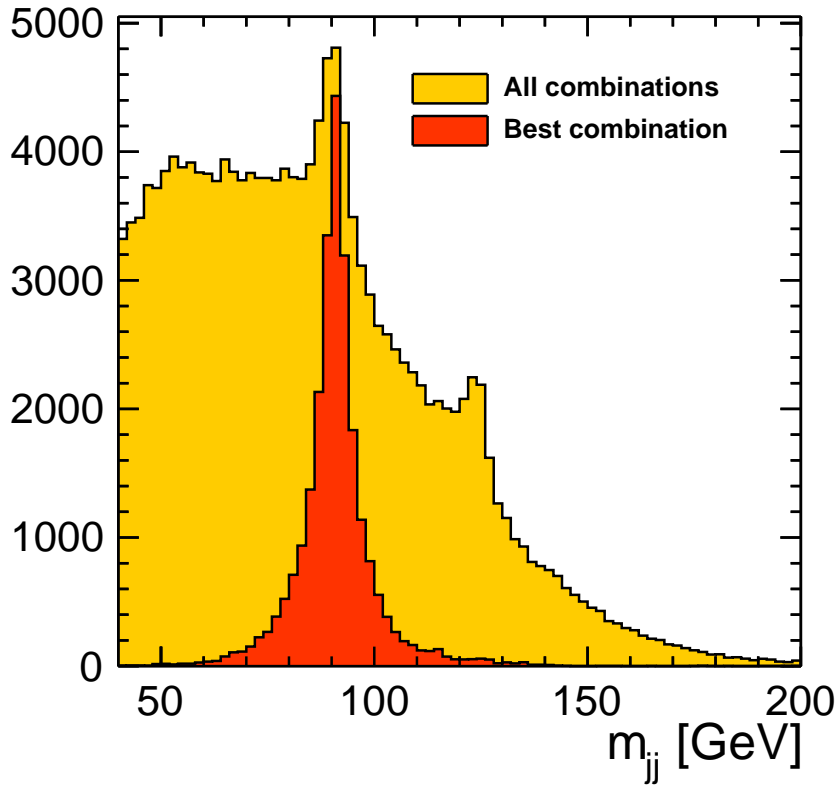


FIGURE 9.11: Distribution of invariant mass of all the di-jet combinations (in yellow) and the selected Z boson di-jet candidates (in red). The second peak in the yellow distribution represents the invariant mass of the Higgs boson products.

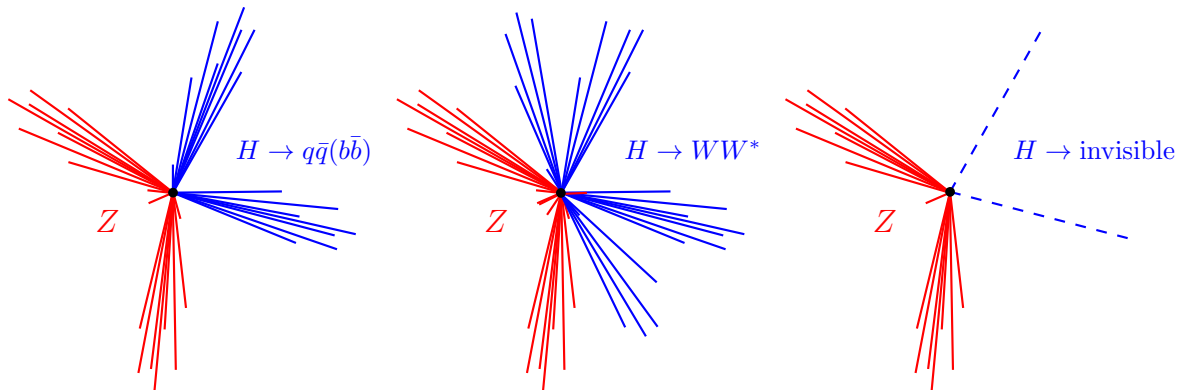


FIGURE 9.12: Example of various topologies that the $ZH \rightarrow q\bar{q} + X$ channel offers.

9.6 Fast and full simulations

The fast simulation is performed smearing the jet energy as described in the Section 9.5.3. The estimate of the smearing parameter α is obtained by simulating the $ZH \rightarrow q\bar{q} + X$ events in full ILD

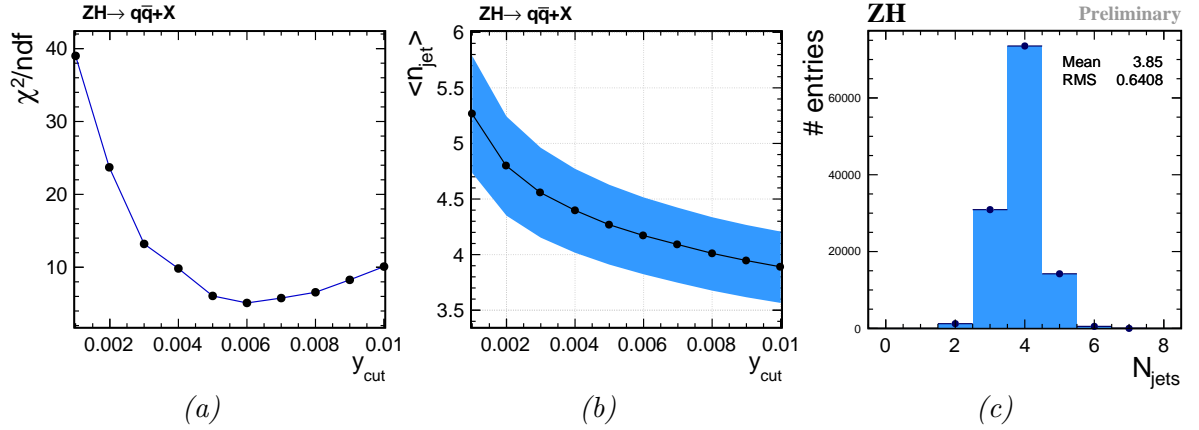


FIGURE 9.13: The evolution of the reduced χ^2 (a) and number of resolved jet (b) as function of y_{cut} parameter. (c) Distribution of the resolved number of jets for the optimal $y_{\text{cut}} = 0.006$.

configuration. The reconstructed Z mass and the recoil mass are compared to between full and fast simulations.

After the full simulation using Mokka, the reconstruction is performed by the PandoraPFA algorithm which returns a collection of Particle Flow Objects (PFO). The jet clustering is then applied and the best di-jet pairs are sorted out as described in the previous section.

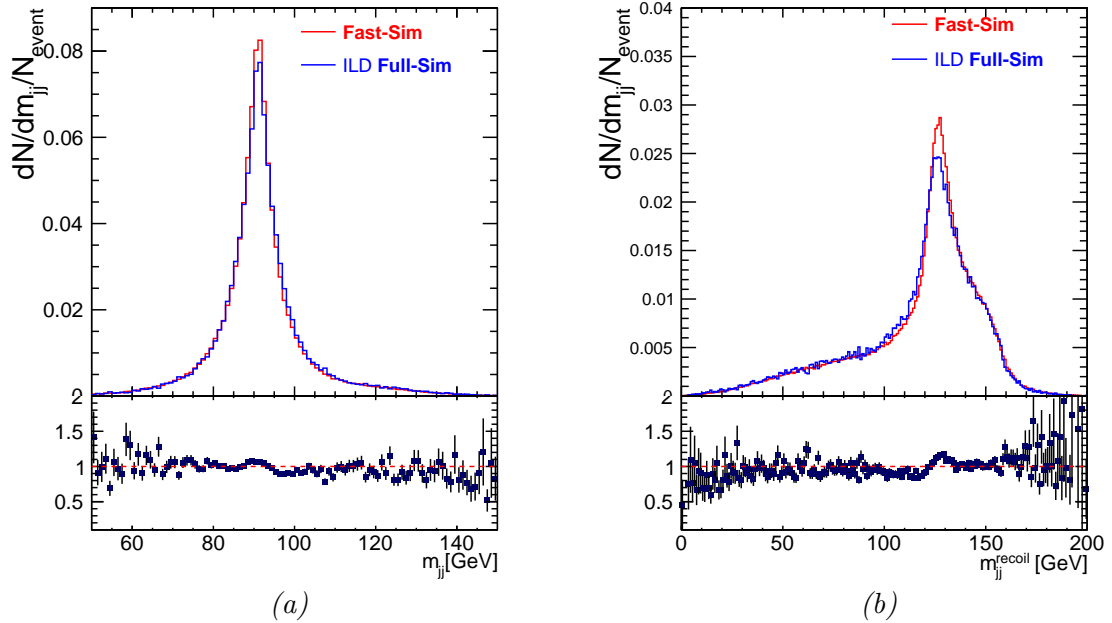


FIGURE 9.14: Reconstructed Z boson mass(a) in $ZH \rightarrow q\bar{q} + X$ events and recoiling mass (b) for fast and full ILD detector simulation. The fast simulation is done smearing the jet energy with $\alpha = 3\%$. The ratio between the two distributions (full and fast simulations) is represented on the bottom of the figures.

The Figure 9.14 shows the selected di-jets invariant mass and the corresponding recoil mass after the ZH reconstruction for full and fast simulations. The fast simulation is done smearing the resolved jet's energy with $\alpha = 3\%$. The full and fast simulations show an agreement better than 10%.

The large number of events and the time required for the full-simulation and the reconstruction constrains the use of the full-simulation. Thus, only the signal events are fully simulated. The background processes are kept in fast-simulation.

9.7 Visible Higgs boson event selection

As shown in the Figure 9.12, the Higgs boson can either decay invisibly or visibly. The signatures are slightly different. Thus the event sample has to be divided into these two categories for the analysis. This section focuses on the visible decay case.

Before to engage in the analysis, and determine the $ZH \rightarrow q\bar{q} + X$ cross section, the main backgrounds have to be reduced. For this, a veto on the WW and ZZ is applied reducing their contribution. Then a cut-based or MVA-based analysis is applied to reduce further the background contribution and then extract the hadronic ZH cross section.

9.7.1 Rejection of $q\bar{q}(\gamma)$ events

The process $Z \rightarrow q\bar{q}(\gamma)$ generate the main background for various analyses in the ILC environment thanks to its high production cross section. In this process high energy photons can be emitted¹¹ and almost collinear to the beam axis. This events are mostly rejected by forcing them into 2-jet topology. The invariant mass of the system, $m_{jj}^{\text{event} \rightarrow q\bar{q}(\gamma)}$, is then calculated and expected to be close to the Z boson mass in the case of unmeasured ISR photon, and close to \sqrt{s} in the case of an ISR photon in the detector region. The Figure 9.15 shows the distribution of $m_{jj}^{\text{event} \rightarrow q\bar{q}(\gamma)}$ for the signal and $q\bar{q}(\gamma)$ background. The events are then asked to satisfy the $m_{jj}^{\text{event} \rightarrow q\bar{q}(\gamma)} > 100$ GeV.

For further rejection of $q\bar{q}(\gamma)$, a cut on the ratio between the energy of the selected Z boson di-jet, E_{jj} , (see Section 9.5.4) and the visible energy in the event, E_{vis} is applied. The Figure 9.16 shows the distribution of this quantity for signal and $q\bar{q}$ process.

Another selection can be applied in order to reduce such background by tagging the most energetic and isolated photons. Event containing photons with an energy over 50 GeV are then dropped. This selection is equivalent the one described below, thus in this analysis the first approach was adopted.

9.7.2 WW/ZZ vetoes

The rejection of the WW/ZZ is performed using specific vetoes. First these backgrounds are classified by their final states; hadronic or semi-leptonic. The Table 9.4 lists the different topologies of the WW/ZZ backgrounds. In order to veto these processes, the events are forced to 3-jets and 4-jets configurations using the jet clustering.

¹¹ The ISR is emitted with most probable energy is $E_{\text{ISR}} = \frac{\sqrt{s}}{2} - \frac{M_Z^2}{2\sqrt{s}}$ ($E_{\text{ISR}} \sim 108$ GeV)

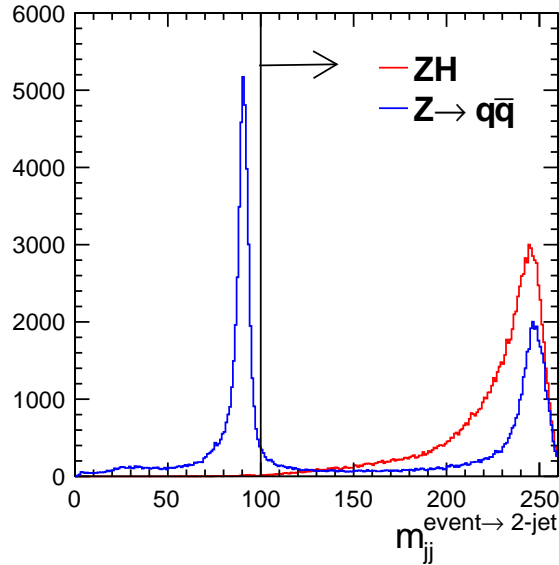


FIGURE 9.15: Invariant mass of the two jets when the event is forced into 2-jet topology for the signal and $Z \rightarrow q\bar{q}(\gamma)$ processes. The cut value is set to $m_{jj}^{\text{event} \rightarrow 2\text{-jet}} > 100$

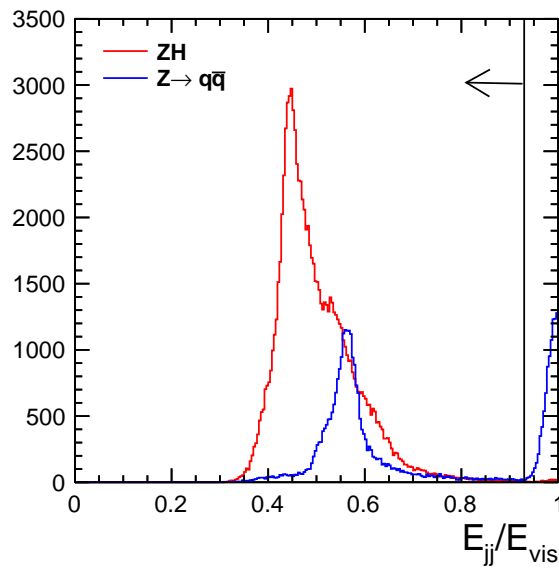


FIGURE 9.16: Ratio E_{jj}/E_{vis} for the signal $ZH \rightarrow q\bar{q} + X$ and $q\bar{q}(\gamma)$ background (after applying the cut shown in Figure 9.15). The energy of the selected di-jet should be less than 93% of the visible event energy.

WW/ZZ $\rightarrow q\bar{q}q\bar{q}$ vetoes

Forcing the event into 4-jets using Durham jet clustering, the jet configuration which minimises

$$\chi_{ZZ}^2 = (m_{12} - m_Z)^2 + (m_{34} - m_Z)^2; \quad (9.18)$$

Process	final state	jet topology
$WW \rightarrow q\bar{q}q\bar{q}$	4 quarks	4 jets
$ZZ \rightarrow q\bar{q}q\bar{q}$	4 quarks	4 jets
$WW \rightarrow q\bar{q}ll$	2 quarks + 2 leptons	4 jets
$ZZ \rightarrow q\bar{q}l\nu$	2 quarks + 1 lepton	3 jets

TABLE 9.4: The final states of the ZZ/WW processes.

is selected ¹². This helps to identify the $ZZ \rightarrow q\bar{q}q\bar{q}$ and $ZZ \rightarrow q\bar{q}ll$. For the signal, the first di-jet mass is expected to be peaked on the Z -boson mass while the second is expected to be peaked on the Higgs-boson mass. A cut on the reconstructed di-jet masses is then applied to reduce ZZ contribution as shown in Figure 9.17.

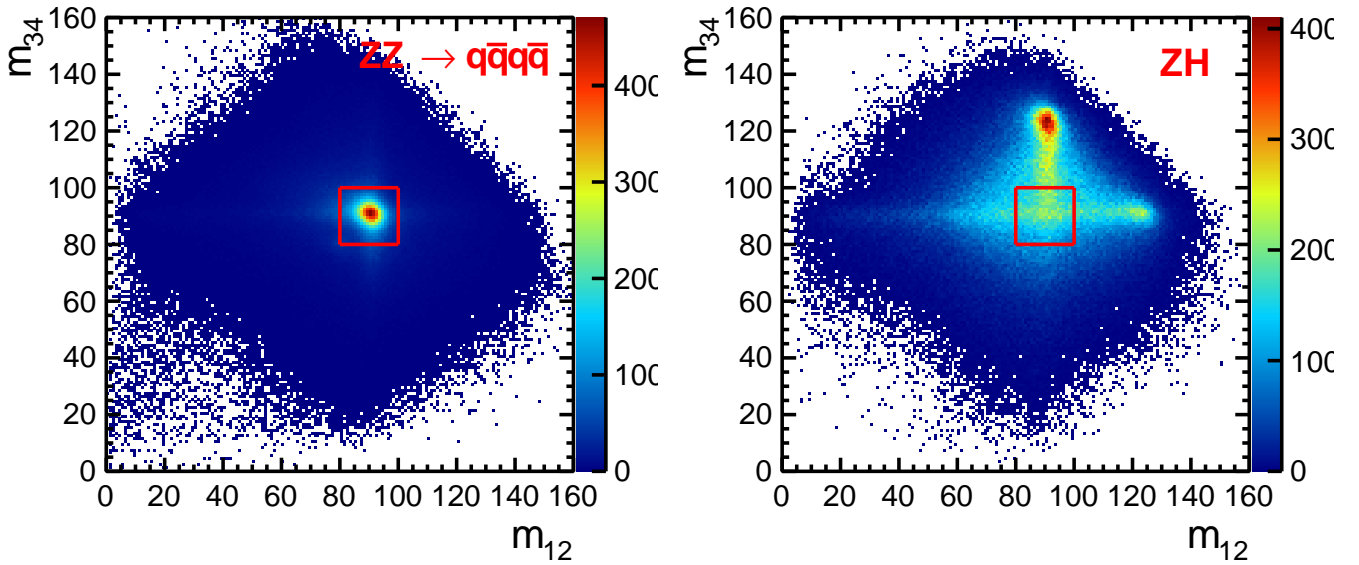


FIGURE 9.17: The di-jet masses reconstruction for $ZZ \rightarrow q\bar{q}q\bar{q}(q\bar{q}ll)$ and $ZH \rightarrow q\bar{q} + X$ processes. The red box represents the excluded area.

As $ZZ \rightarrow q\bar{q}q\bar{q}(q\bar{q}ll)$, the $WW \rightarrow q\bar{q}q\bar{q}$ is reconstructed by forcing the events into 4-jets configuration and selecting a jet combination which minimises,

$$\chi_{WW}^2 = (m_{12} - m_W)^2 + (m_{34} - m_W)^2; \quad (9.19)$$

The reconstructed di-jet masses are then expected to be peaked at the W -boson mass. A cut on the reconstructed di-jet masses is then applied to reduce $WW \rightarrow q\bar{q}q\bar{q}$ contribution as shown in Figure 9.18.

¹²In the four jets final states the possible configurations for a set of jets labelled $\{1, 2, 3, 4\}$ are $\{12, 34\}$, $\{14, 23\}$ and $\{13, 24\}$

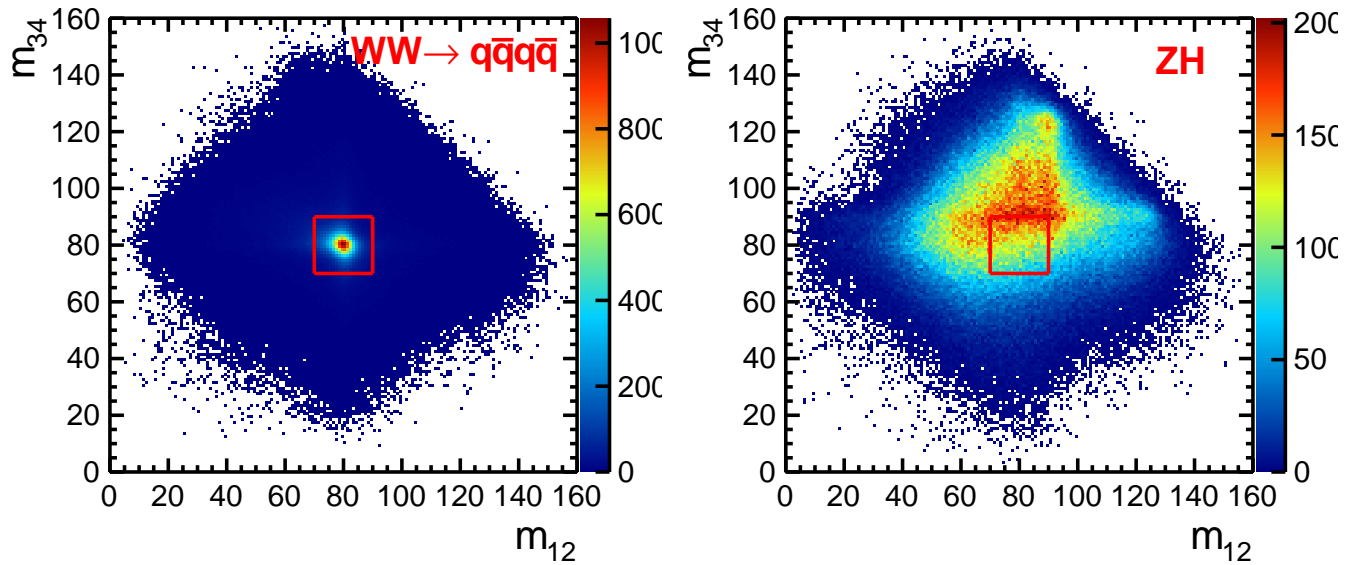


FIGURE 9.18: The di-jet masses reconstruction for $WW \rightarrow q\bar{q}q\bar{q}$ and $ZH \rightarrow q\bar{q}+X$ processes. The red box represents the excluded area.

$WW \rightarrow q\bar{q}l\nu$ vetoes

The semi-leptonic $WW \rightarrow q\bar{q}l\nu$ as shown in Table 9.4 has a 3-jet topology. Thus the events are forced into 3-jets final stat configuration. The jet pair closest to the W -boson mass is selected. The selected mass as well as the recoil mass are expected to be peaked at the W -boson mass. A cut is applied on these quantities as shown in Figure 9.19.

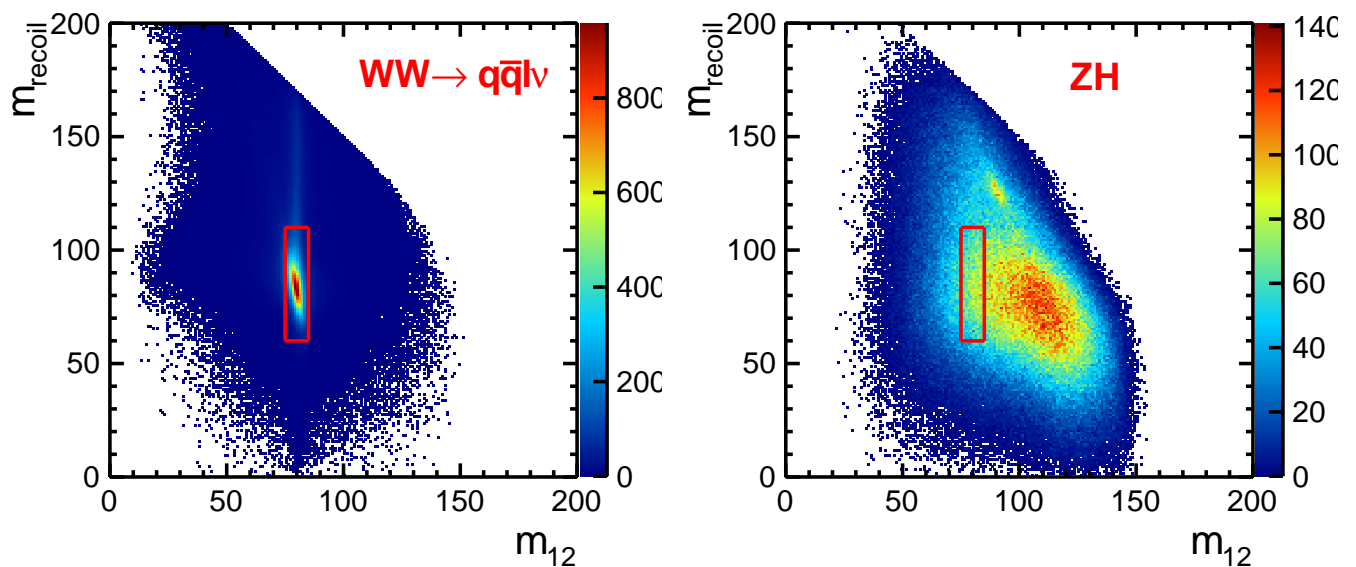


FIGURE 9.19: The $WW \rightarrow q\bar{q}l\nu$ veto. The red box represents the veto area.

9.7.3 Boosted decision tree construction

The recoil analysis is based on the identification of the di-jet system as produced by the decay of the Z boson. It is thus necessary to distinguish the processes which lead, at least, to two jets in the final state from those produced in the Higgsstrahlung process.

For the higgs-strahlung process the invariant mass of the di-jet system, M_{12} , should be peaked at the Z boson mass while the invariant mass of the recoiling system, m_{recoil} is expected to yield the Higgs boson mass ($M_H = 125$ GeV). It is unlikely that the background processes fulfil both conditions at once. This can be seen in the Figure 9.20a and Figure 9.20b. These distributions suggest to restrict the analysis to the following mass ranges:

- $50 < m_{12} < 110$
- $100 < m_{recoil} < 200$

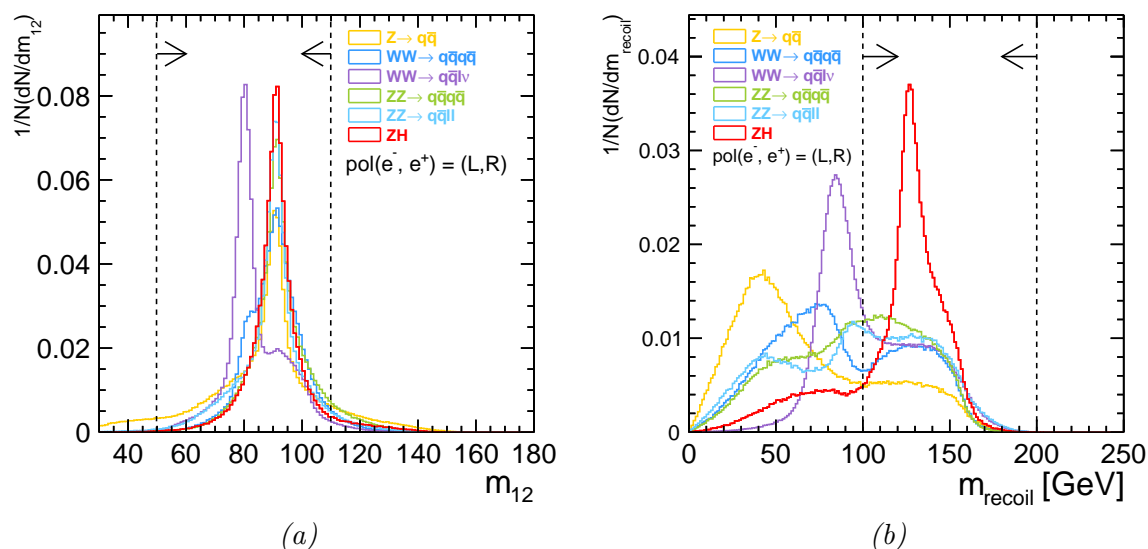


FIGURE 9.20: Normalized signal and background distributions of the invariant mass of the di-jet system m_{12} (a) and of the recoil mass m_{recoil} (b) for $q\bar{q}X$ channel.

In order to reject further the background contributions, six variables from those defined previously are combined in boosted decision tree. The exact list of parameters used for the training of the BDT are reported in the Appendix B.

The model independence context of the following analysis, imposes to use variables introducing a minimum bias on the Higgs boson selection however its decay mode. Thus kinematic variables of the Z boson system are mainly used for the BDT training. The recoil mass of the di-jet system is not used in the training.

- m_{jj} : the invariant mass of the selected di-jet system resolved using Durham algorithm in fixed y_{cut} mode;
- $|\cos\theta_Z|$: production angle of the Z boson di-jet system. For the signal process the Z boson is almost angle independent while for most of the background processes it peaked in the forward-backward regions as shown in the Figure 9.21

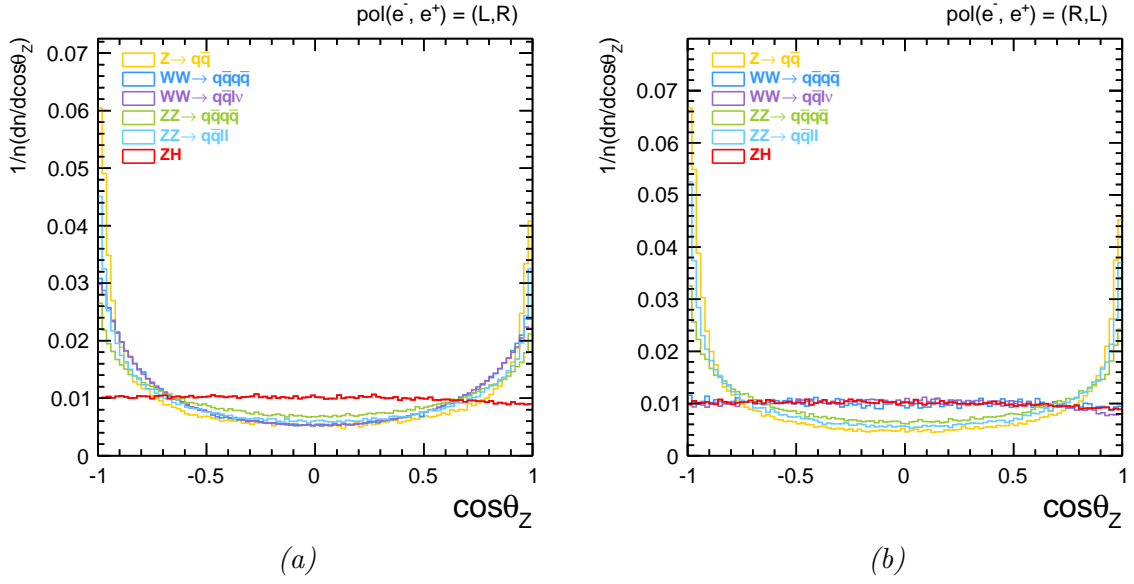


FIGURE 9.21: The production angle of the di-jet system for two different polarisations. The red distribution represents the signal while other colours represent the main backgrounds. Note that these distributions are done after the WW/ZZ vetoes and $q\bar{q}$ rejection.

- $\Delta\theta_{12}$: the opening angle of the di-jet system also called *acollinearity* (Figure 9.22). For the $q\bar{q}$ process, already strongly suppressed by the $q\bar{q}(\gamma)$ veto (see Section 9.7.1), $\Delta\theta_{12}$ is expected to be peaked at the angle π since the di-jet has a back-to-back configuration.

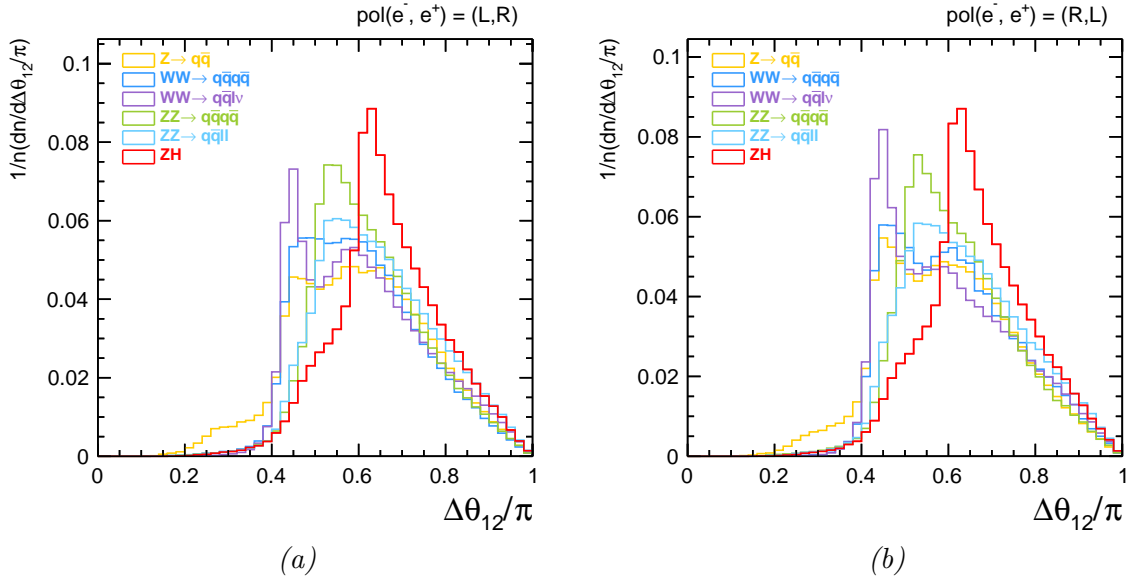


FIGURE 9.22: Distribution of the acollinearity (di-jet opening angle) for the signal (red) and main backgrounds (other colours) and for the different beam polarisations. Note that these distributions are done after the WW/ZZ vetoes and $q\bar{q}$ rejection.

- $\Delta\phi_{12}$: also called *acoplanarity* represents the distance in azimuth angle defined as $\Delta\phi_{12} = |\phi_1 - \phi_2|$, where the $\phi_{1,2}$ is the azimuth angle of the individual jet in the di-jet system (see

Figures 9.23). Note that this variable is similar to the acollinearity, but is essentially insensitive to the initial state radiations.

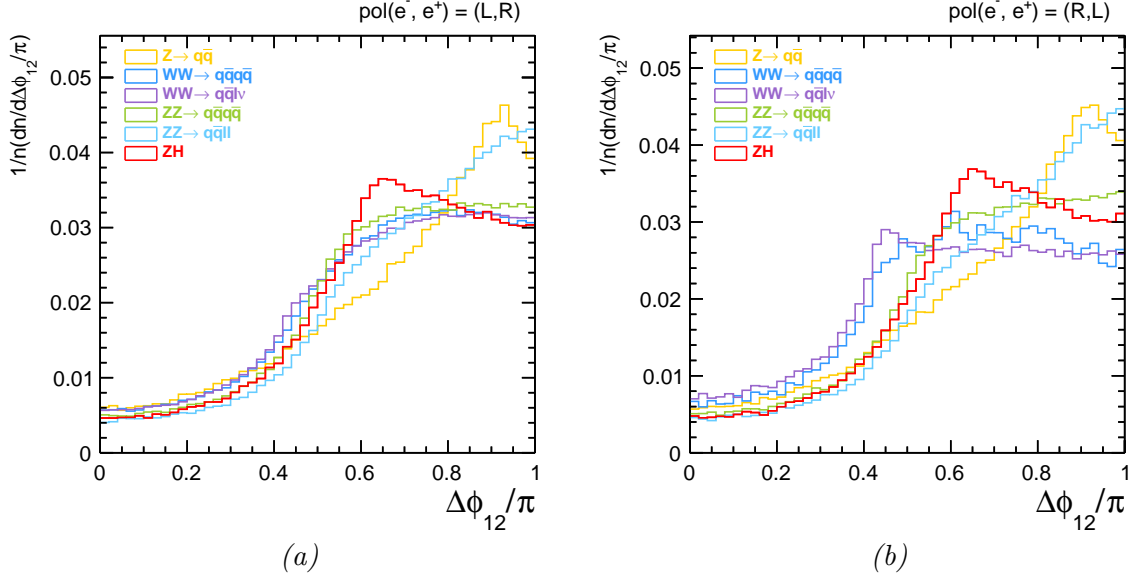


FIGURE 9.23: Distribution of the acoplanarity for the signal (red) and main backgrounds (other colours) and for the different beam polarisations. Note that these distributions are done after the WW/ZZ vetoes and $q\bar{q}$ rejection.

- $|\Delta E_{12}|$: The energy difference of the two selected jets (see Figure 9.24). In the ZZ process the Z bosons are expected to be produced with a larger boost which may introduce a larger jet energy spread compared to the signal process.

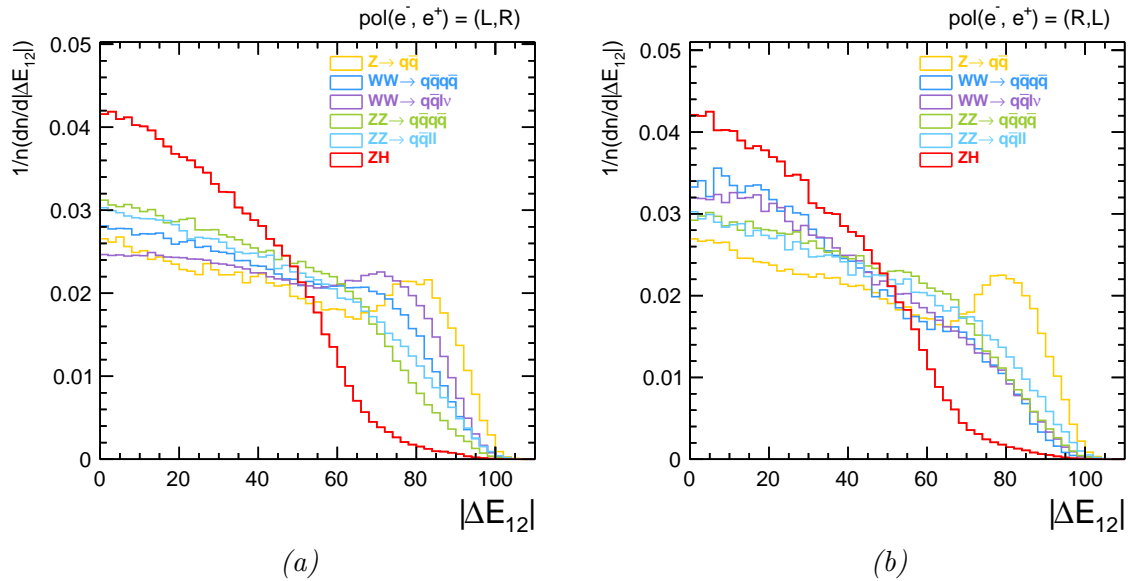


FIGURE 9.24: The absolute energy difference between the two selected jets for both polarisation ((e_L^-, e_R^+) and (e_R^-, e_L^+))

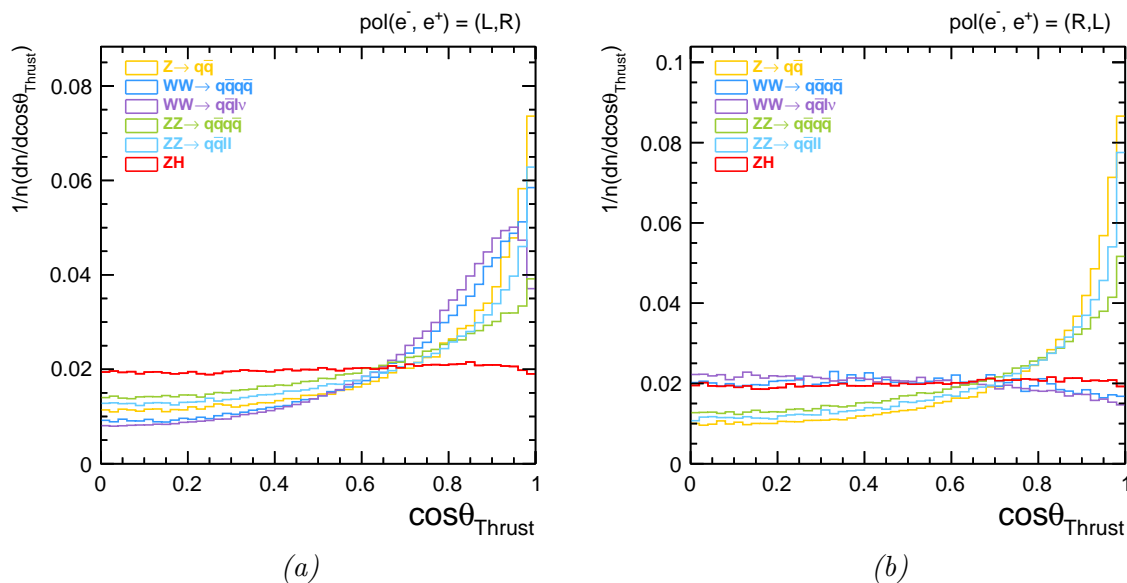


FIGURE 9.25: The thrust angle for two different polarisations. The red distribution represents the signal while other colours represent the main backgrounds. Note that these distributions are done after the WW/ZZ vetoes and $q\bar{q}$ rejection.

- $\cos \theta_{\text{Thrust}}$: the polar angle of the thrust axis (see Figure 9.25).
- $-\log(\mathbf{y}_{23})$, $-\log(\mathbf{y}_{34})$: Durham jet resolution parameters.

The last two variables are introduced to increase the discrimination power of the BDT forest. The bias introduced by a cut on this two quantities for different visible Higgs decay modes is minimal since all the decay modes have the same shape as shown in the Figure 9.26 except for the invisible decay mode of the Higgs which has a specific topology.

The boosted decision tree training leads to a response variable ranging in $[-1, 1]$. The signal is expected to be peaked in 1 while the background in -1 . The distribution of this variable is shown in Figure 9.27.

Since in the ILC the polarisation of the colliding beam can be polarised (see Chapter 2) the generated sample which have been generated with 100% polarised beams are combined following the method described in Section 9.3.1. The polarisation reachable with the ILC machine[60] at $\sqrt{s} = 250$ GeV early stage is 80% for electron and 30% for positrons. Two configurations can be then $P(e^-, e^+) = (-80\%, +30\%)$ and $P(e^-, e^+) = (+80\%, -30\%)$. The BDT_{score} distributions for the true polarisations are shown in Figure 9.28.

Most of the recoil mass values of the Higgs-strahlung events are located inside the recoil mass range $[100, 200]$ GeV. Denoting the number of accepted signal process events by N_S and the number of accepted background events by N_B , the standard deviation of the total number of accepted events is given by $\sqrt{N_S + N_B}$, which is true considering that a Gaussian law is appropriate for $(N_S + N_B)$ distribution. Thus the statistical *significance* can be defined as the ratio

$$\mathcal{S}(c) = \left(\frac{N_S(c)}{\sqrt{N_S(c) + N_B(c)}} \right)_{BDT_{\text{score}} \geq c} \quad (9.20)$$

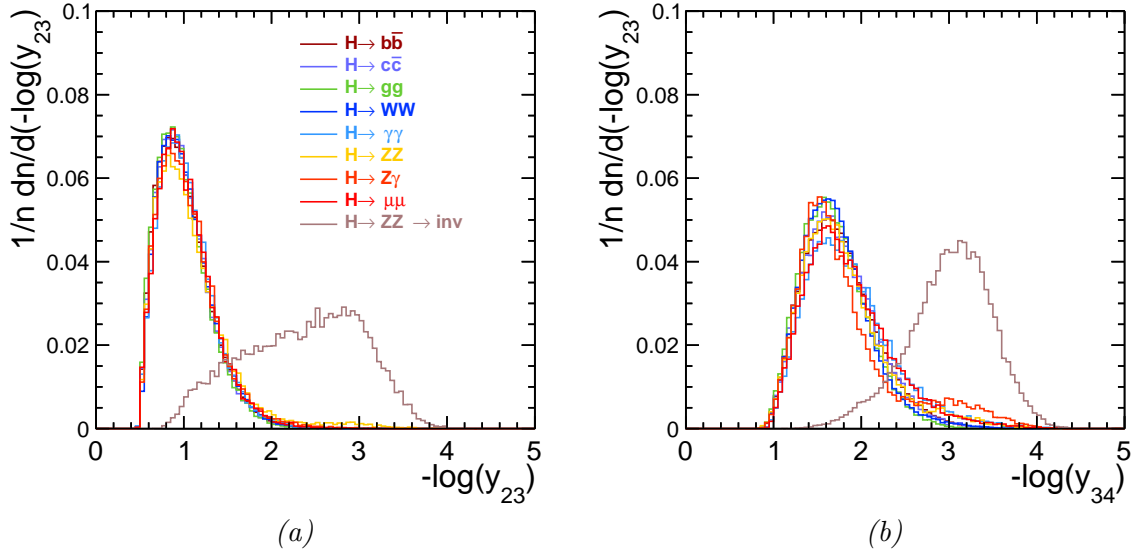


FIGURE 9.26: Distribution for different Higgs boson decay modes of $-\log y_{23}$ (a) and $-\log y_{34}$ (b). The brown distribution represents the invisible Higgs.

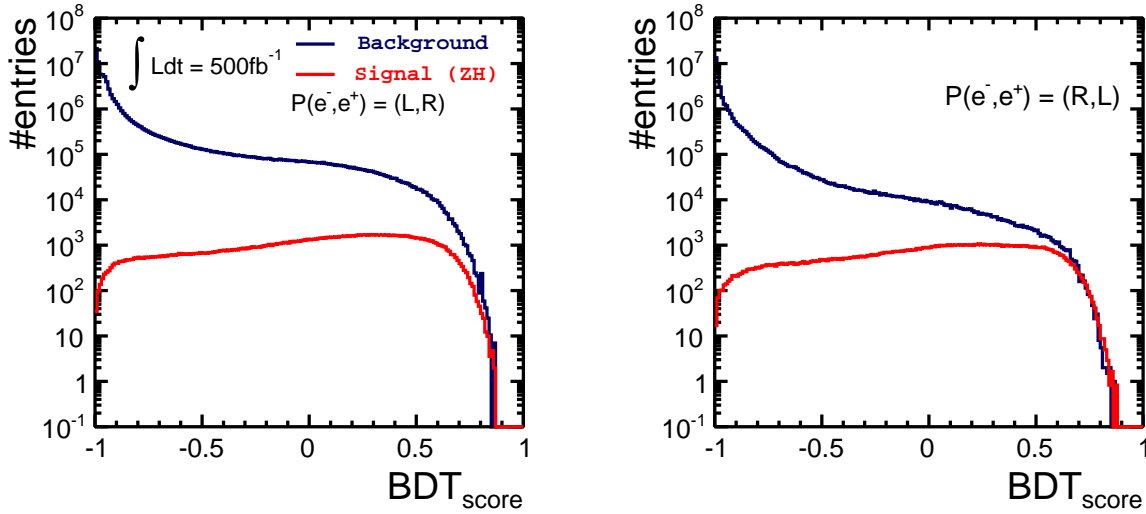


FIGURE 9.27: Response of the boosted decision tree classifier for the signal and the combined backgrounds for the two polarisation: (e_L^-, e_R^+) (left) and (e_R^-, e_L^+) (right).

$\mathcal{S}(c)$ depends on the cut that is applied to the BDT score (denoted here by c). Maximising \mathcal{S} with respect to this cut optimises the cut for accepting more signal events while reducing the contamination of background.

The evolution of the significance as function of the BDT_{score} cut is shown in Figure 9.29 for both beam polarisations. From these plots the values of the BDT cut can be obtained: $BDT_{score} > 0.1$ for the polarisation $P(e^-, e^+) = (-80\%, +30\%)$ and $BDT_{score} > 0$ for the polarisation $P(e^-, e^+) =$

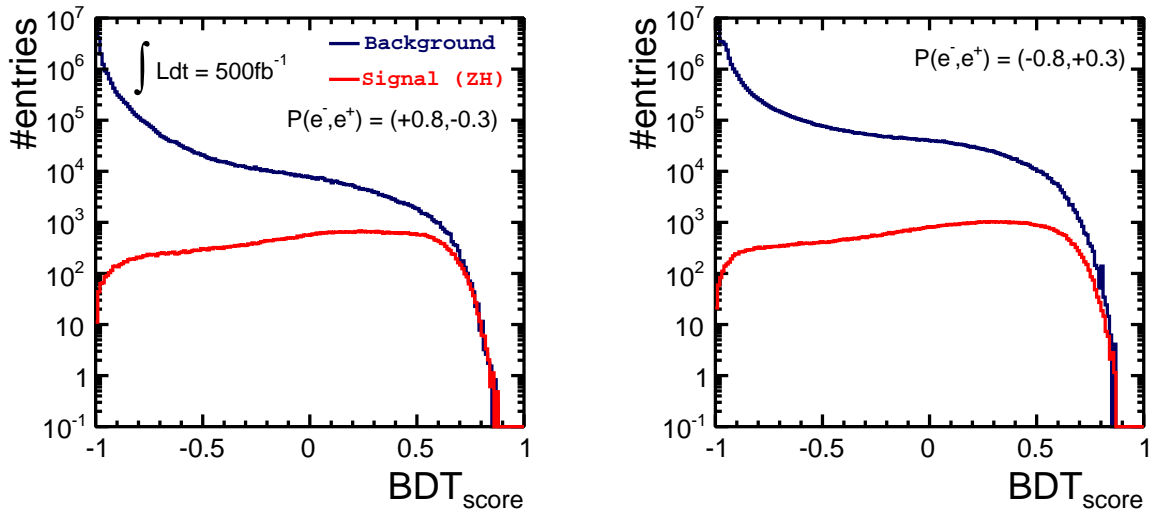


FIGURE 9.28: Response of the boosted decision tree classifier for the signal and the combined backgrounds for the two polarisations: (+80%, -30%) (left) and (-80%, +30%) (right).

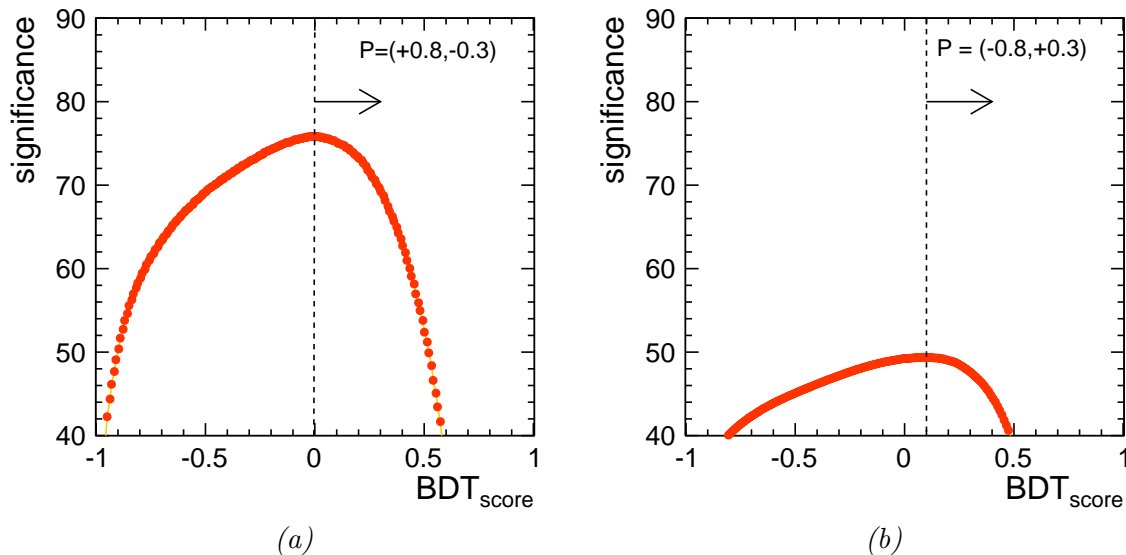


FIGURE 9.29: Evolution of the statistical significance as function of the $BDT_{score}cut$ for the two beam-polarisations ((-80%, +30%), (+80%, -30%)).

(+80%, -30%). The recoil mass distributions after the selection for each polarisation are shown in Figure 9.30a and Figure 9.30b.

This results suggest a preference for running in the configuration $P(e^-, e^+) = (+80\%, -30\%)$.

Table 9.5 and Table 9.6 summarise the selection efficiencies of the signal and background processes after all the analysis stages. Each beam polarisation is represented separately in different tables. More than 30% of the signal is kept after the selection while only less than 7% background remains.

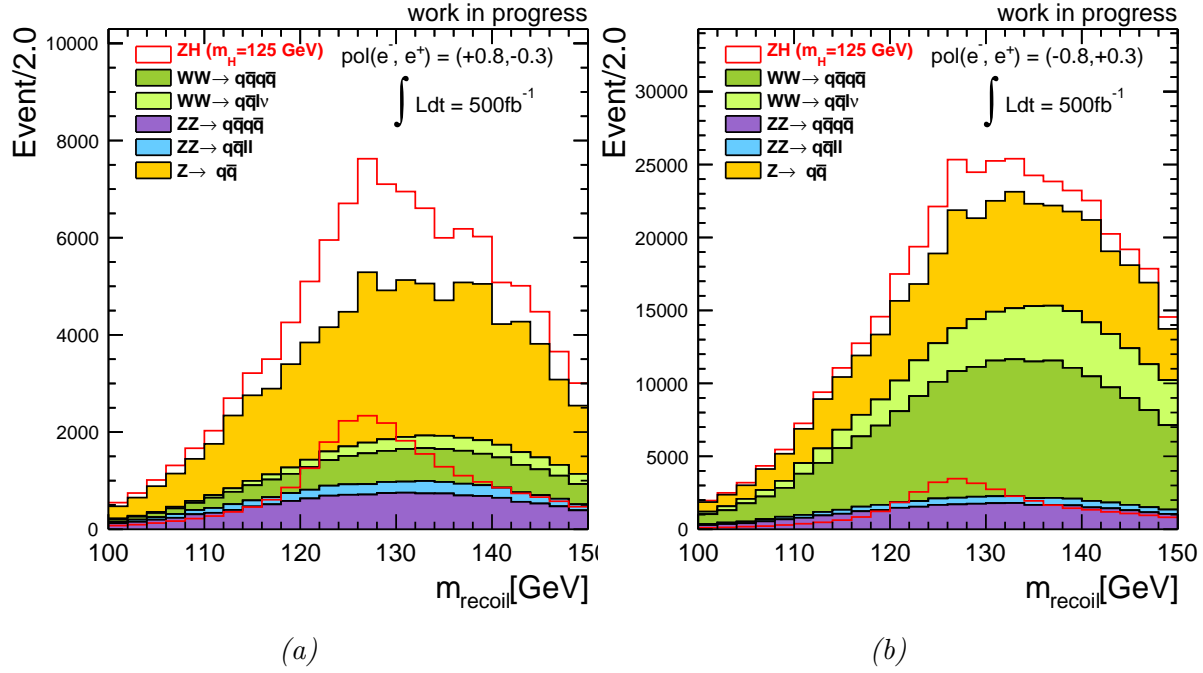


FIGURE 9.30: Distribution of the recoil mass after the selection chain for the polarisations $((-80\%, +30\%)$ and $(+80\%, -30\%)$.

Process ($BDT_{score} > 0$)	N_{tot}^{LR}	N_{tot}^{RL}	N_{sel}^{LR}	N_{sel}^{RL}	N_{tot}	N_{sel}	ε_{sel}
Process $P(e^-, e^+) = (+0.8, -0.3)$							
$Z \rightarrow q\bar{q}$	1747094	1841069	7048	5322	1138174	3360.05	0.003
$WW \rightarrow q\bar{q}q\bar{q}$	1074479	136357	46188	8119	117376	6366.2	0.054
$WW \rightarrow q\bar{q}l\nu$	1919148	172733	28688	3617	168219	3120.02	0.019
$ZZ \rightarrow q\bar{q}q\bar{q}$	1005427	604971	89266	47195	389098	30733.4	0.079
$ZZ \rightarrow q\bar{q}ll$	1422143	713526	35303	15837	467188	10500.2	0.022
ZH	439607	268672	160461	99494	172559	63820.1	0.370

TABLE 9.5: Summary of the selection statistics and efficiencies for the different processes (signal and backgrounds) for the beam polarisation $P(e^-, e^+) = (+0.8, -0.3)$.

The beam polarisation $P(e^-, e^+) = (+0.8, -0.3)$ shows larger signal efficiency for large significance as expected from the Figure 9.30a. This is essentially due to the fact that this beam polarisation favours the σ_{RL} cross section which shows a reduction larger by two orders of magnitude comparing to σ_{LR} as shown in Figure 9.6.

9.7.4 Testing the model independence

The model independence on the Higgs boson research in the channel $q\bar{q}X$ requires to have the same selection efficiency for the different Higgs decay modes. Thus Higgs boson samples of 10000 events have been generated for each relevant decay mode.

The generated samples are passed through the same analysis chain and the same selections. The efficiencies for each decay mode are shown in Figure 9.31 for each beam polarisation.

Process ($BDT_{score} > 0.1$)	N_{tot}^{LR}	N_{tot}^{RL}	N_{sel}^{LR}	N_{sel}^{RL}	N_{tot}	N_{sel}	ε_{sel}
Process $P(e^-, e^+) = (-0.8, +0.3)$							
$Z \rightarrow q\bar{q}$	1747094	1841069	5393	3930	1086488	3292.46	0.003
$WW \rightarrow q\bar{q}q\bar{q}$	1074479	136357	36668	6571	633343	21680.8	0.034
$WW \rightarrow q\bar{q}l\nu$	1919148	172733	19772	2398	1128747	11650.6	0.010
$ZZ \rightarrow q\bar{q}q\bar{q}$	1005427	604971	73568	38275	609349	44376.9	0.073
$ZZ \rightarrow q\bar{q}ll$	1422143	713526	27863	12122	856927	16724.1	0.020
ZH	439607	268672	142641	87321	266574	86501.2	0.324

TABLE 9.6: Summary of the selection statistics and efficiencies for the different processes (signal and backgrounds) for the beam polarisation $P(e^-, e^+) = (-0.8, +0.3)$.

To takes into account the beam polarization the efficiency for each beam polarisation is given by

$$\begin{aligned} \varepsilon &= \frac{N_{sel}}{N_{tot}} \\ &= \frac{w_{LR} \cdot N_{sel}^{LR} + w_{RL} \cdot N_{sel}^{RL}}{w_{LR} \cdot N_{tot}^{LR} + w_{RL} \cdot N_{tot}^{RL}} \end{aligned} \quad (9.21)$$

where w_{LR}, w_{RL} are defined in Equation 9.5, N_{sel} the number of selected events and N_{tot} the total number of events. The Gaussian propagation error is used to estimate the statistical uncertainties of obtained efficiency. Considering that the number of selected events, N_{sel} is binomially distributed with N_{tot} trials and single success probability ε . Thus the standard deviation is simply written by

$$(\delta\varepsilon(H \rightarrow X_i))^2 = \frac{\varepsilon(1 - \varepsilon)}{BR(H \rightarrow X_i)N_{tot}}, \quad (9.22)$$

where N_{tot} the total number of events of the ZH process and $BR(H \rightarrow X_i)$ is the theoretical branching ratio of the Higgs boson decay ¹³.

The Figure 9.31 shows the signal selection efficiency for several Higgs decay channels, for both considered beam polarisations. Within the precision of this study, there are slight differences of the signal selection efficiency over the Higgs decay modes. This analysis followed in this chapter is sensible to the channels having an invisible decay. This is translated by a large fraction of the missing momentum. In the Higgs decays into Z boson pair, in 4% of cases the pair decays into neutrinos, $ZZ \rightarrow \nu\bar{\nu}\nu\bar{\nu}$. Other 4% of the Z pair goes into $ll\nu\nu$ with non-negligible fraction of missing momentum. Thus $H \rightarrow ZZ$ decay channel is expected to most sensitive to the previous selection, as can be seen in Figure 9.31. This effect is also visible on $H \rightarrow WW$.

By contrast, the Higgs boson decaying into two fermions ($H \rightarrow b\bar{b}, gg, c\bar{c}, \tau\tau, \mu\mu$) shows an efficiency slightly higher. This due to the tendency of selection to favours the 4-objects topology in the final state where the Z boson jets are easy to identify.

The results is that the selection efficiency depends on the Higgs decay with difference of a few percents. The mean signal selection efficiency as obtained in table is a weighted average over the single selection efficiencies with branching fraction as weight. An estimation of the dispersion can be given by determining the variance of the efficiencies values around the mean. A relative dispersion is found to be of order of 5-6% for both beam polarisations. This will be introduced as systematic uncertainty on the measurement of the cross section (see next section).

¹³Notes that the division by the branching fraction of the Higgs boson is added to account the importance of each channel.

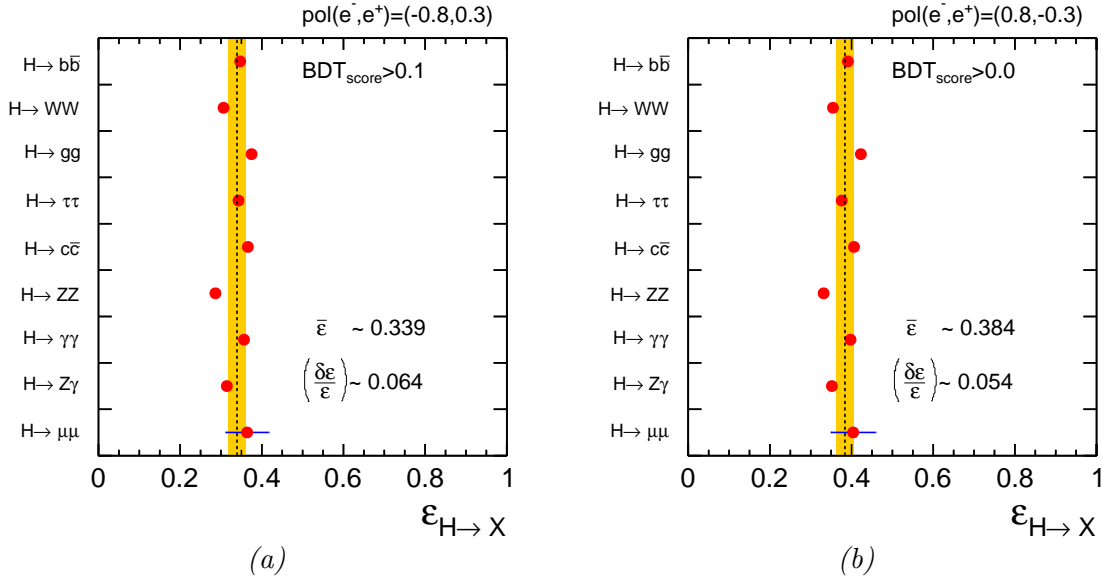


FIGURE 9.31: Selection efficiencies for different decay modes of the SM Higgs boson, for the polarisation $(-0.8, +0.3)$ in (a) and $(+0.8, -0.3)$ in (b).

Beam polarisation	$\bar{\epsilon}$	$\delta\epsilon/\epsilon$
$P(e^-, e^+) = (-0.8, +0.3)$	0.339 ± 0.022	0.064
$P(e^-, e^+) = (+0.8, -0.3)$	0.384 ± 0.021	0.054

TABLE 9.7: summary of the selection efficiencies for the two chosen beam polarisations, as well as the relative deviation of different Higgs decay modes efficiency.

The Table 9.7 summarises the selection efficiencies for both beam polarisations, $(-0.8, +0.3)$ and $(+0.8, -0.3)$ for a mass recoil in the range $100 < m_{recoil} < 150$ GeV. It suggests that the model independence measurement of the Higgs boson properties is possible in the limits of 5%.

9.8 Total Higgs-strahlung cross section and determination of g_{ZZH} coupling strength

In the previous section the criteria to select the signal events and the suppression of the background from various processes have been applied. The remaining spectrum is a superposition of the signal and background events (see Figure 9.30). In the following, the total Higgs-strahlung cross section σ_{ZH} as well as the related statistical uncertainty are extracted.

The cross section of the Higgs-Strahlung process is estimated using

$$\sigma_{ZH}(Z \rightarrow q\bar{q}) = \frac{N_{\text{tot}} - N_{\text{b}}}{\epsilon \cdot \mathcal{L}} \quad (9.23)$$

where N_{tot} is the total number of candidate events after the selection, N_{b} is the number of background events, ϵ is the signal selection efficiency and \mathcal{L} is the integrated luminosity of the machine. The

corresponding uncertainty is obtained by propagating the error over all the terms of the cross section. The relative uncertainty can then be written as

$$\left(\frac{\Delta\sigma_{ZH}}{\sigma_{ZH}}\right) = \left(\frac{\Delta\sigma_{ZH}}{\sigma_{ZH}}\right)_{\text{stat}} \oplus \left\{ \left(\frac{\Delta\epsilon}{\epsilon}\right) \oplus \left(\frac{\Delta\mathcal{L}}{\mathcal{L}}\right) \right\}_{\text{sys}} \quad (9.24)$$

The first term represents the statistical uncertainty on the cross section measurement. It directly related to the significance of the signal previously defined. Assuming a statistical fluctuation this term can be expressed by,

$$\left(\frac{\Delta\sigma_{ZH}}{\sigma_{ZH}}\right)_{\text{stat}} = \frac{\sqrt{N_{\text{tot}}}}{N_{\text{tot}} - N_b} = \mathcal{S}^{-1}. \quad (9.25)$$

The other terms represent the systematic uncertainty related to the selection efficiency and the luminosity. The ILC is expected to measure the luminosity with a precision better than 0.1%, the luminosity term in Equation 9.25 can then be neglected. The remaining term, $(\delta\epsilon/\epsilon)$, have non-negligible impact on the measurement of the cross section measurement. This term has been determined in the previous section.

polarisation	$\sigma_{ZH}(Z \rightarrow q\bar{q})$
$P(e^-, e^+) = (-0.8, +0.3)$	$210.51 \text{ fb} \pm (3.89)_{\text{stat}}$
$P(e^-, e^+) = (+0.8, -0.3)$	$141.90 \text{ fb} \pm (2.00)_{\text{stat}}$

TABLE 9.8: Estimation of cross section $\sigma_{ZH}(Z \rightarrow q\bar{q})$ for two different beam polarisations.

On the basis of recoil mass spectrum shown in Figure 9.30, the simplest way to estimate the cross section is to count the total number of events N_{tot} , in the range $100 < m_{\text{rmrecoil}} < 150 \text{ GeV}$ and subtract the background. The results can be seen in Table 9.8.

The branching fraction of the Z boson are well known, the total Higgs-Strahlung cross section can then be determined by ¹⁴

$$\sigma_{ZH} = \frac{\sigma_{ZH}(Z \rightarrow q\bar{q})}{\text{BR}(Z \rightarrow q\bar{q})} \quad (9.26)$$

The values of $\text{BR}(Z \rightarrow q\bar{q})$ is well measured by LEP experiments, it takes the value of 69.91%. The estimation of the total cross section are reported on the Table 9.9. These measurements, as expected,

Beam polarisation	$\sigma_{ZH} = \sigma_{ZH}(Z \rightarrow q\bar{q})/\text{BR}(Z \rightarrow q\bar{q})$	σ_{ZH}^{SM}
$P(e^-, e^+) = (-0.8, +0.3)$	$301.11 \text{ fb} \pm (3.89)_{\text{stat}}$	300.66 fb
$P(e^-, e^+) = (+0.8, -0.3)$	$202.98 \text{ fb} \pm (2.00)_{\text{stat}}$	203.05 fb

TABLE 9.9: Estimation of total cross section σ_{ZH} for two different beam polarisations.

are compatible with the theoretical values.

The Higgs-Strahlung process offers also the possibility to measure the coupling constant, g_{HZZ} at the vertex HZZ . Indeed, the cross section is directly related to the Higgs coupling to the vector boson Z , g_{HZZ} . From the Equation A.1 one can write:

$$\sigma_{ZH} = g_{HZZ}^2 \cdot F(s; M_H, M_Z) \quad (9.27)$$

¹⁴The error on the branching fraction of the $Z \rightarrow \text{hadrons}$ is of about 0.06%, which is negligible here.

where $F(s; M_H, M_Z)$ is an arbitrary function depending on the centre-of-mass energy and the Z and Higgs boson masses. The Higgs-Strahlung cross section is proportional to g_{HZZ}^2 . The statistical uncertainty of g_{HZZ} is then:

$$\left(\frac{\delta g_{HZZ}}{g_{HZZ}}\right) = \frac{1}{2} \left(\frac{\delta \sigma_{ZH}}{\sigma_{ZH}}\right) \quad (9.28)$$

The statistical uncertainties g_{HZZ} and σ are reported on the Table 9.10. A precision of less than 1% of the coupling strength g_{HZZ} is reached.

Beam polarisation	$\left(\frac{\delta \sigma_{ZH}}{\sigma_{ZH}}\right)$	$\left(\frac{\delta g_{HZZ}}{g_{HZZ}}\right)$
$P(e^-, e^+) = (-0.8, +0.3)$	1.85%	0.92%
$P(e^-, e^+) = (+0.8, -0.3)$	1.41%	0.70%

TABLE 9.10: The relatives statistical uncertainties on the measurement of σ_{ZH} and g_{HZZ} for the two beam polarisations.

9.9 Conclusion

The analysis presented in this chapter is based on simulated e^+e^- collisions in a linear collider at a centre-of-mass energy of 250 GeV and integrated luminosity of 500 fb^{-1} . A precision better than 2% on the cross section of the Higgsstrahlung process σ_{ZH} with a hadronically decaying Z, can be reached in the recoil mass window of $100 < m_H < 150 \text{ GeV}$. The correspondence $\sigma_{ZH} \propto g_{HZZ}^2$ offers then the possibility to extract the coupling strength at the HZZ vertex with a precision better than 1%.

The beam polarisation appears to be crucial for rejecting WW background, which improves by factor 1.65 the signal significance for the beam polarisation $P(e^-, e^+) = (+0.8, -0.3)$.

The selection shows very similar efficiencies for various Higgs decay modes with a dispersion of 5 – 6%. Therefore the Higgsstrahlung tagging analysis displays a small bias, allowing a quasi model-independent measurement of σ_{ZH} . However, the analysis is sensitive to invisible $H \rightarrow ZZ$ and $H \rightarrow WW$ decay modes (with 2 or 4 neutrinos in the final state). This effect can be corrected by estimating the contribution of these processes with dedicated analyses.

A future study could improve the jet reconstruction algorithm and the tagging of the Z boson jets, which may improve the model independence of the analysis. Other studies could push further the analysis, by measuring the Higgs significance as function of the jet energy resolution.

General conclusion

“The Answer to the Great Question... Of Life, the Universe and Everything... Is... Forty-two,” said Deep Thought, with infinite majesty and calm.”

— Douglas Adams, *The Hitchhiker’s Guide to the Galaxy*

The precision goal on ILC physics requires the optimisation of a detector for particle flow. The reconstruction of each single particle in an event puts a stringent requirements on the calorimeter system. Unprecedented high granularity is mandatory for lateral and longitudinal segmentation for both electromagnetic and hadronic calorimeters.

The semi-digital gaseous detector as one of technology for a hadronic calorimeter options is outlined in this thesis. A prototype has been achieved and successfully operated. It consists of sampling structure alternating stainless steel and finely segmented GRPC, as needed for the particle flow algorithm, with an embedded electronic readout. It has been demonstrated that the cost-effective GRPCs can operate with high efficiency and uniform response on large area.

A generic algorithm for physical event reconstruction based on the time clustering method was presented in Chapter 4. This allowed the measurement of the intrinsic noise of the calorimeter, which was found to be of order of 0.35 hit/200 ns. This confirmed that the GRPC chambers are almost noise-free. The coherent noise was also studied; these events with an occurrence of $1/10^6$ are easily identified and removed for the further analyses.

In Chapter 5 the response of the SDHCAL prototype to minimum ionising particles was exposed. These particles were used to extract the intrinsic performance of the sensors, such as the detection efficiency and pad multiplicity. An efficiency over 95% was found with an average pad multiplicity of 1.7 for all the sampling GRPC chamber. The measured efficiency for different values of threshold permitted to extract the induced charge spectrum. With properly reconstructed muons, the induced charge image on the readout pads could be deduced. These information were then used to tune a digitisation module, simulating the sensor and associated electronic responses, as depicted in Chapter 6 to the 5% level.

The prototype raw response to pions was also studied in Chapter 7. Methods to linearise and calibrate the calorimeter response were developed. They demonstrated a 3-4% relative linearity when applied to the raw data. The relative resolution associated to the linearised energy response was estimated in both binary and the multi-threshold modes, yielding to $\sim 15\%$ resolution in the binary mode over 40 GeV and down to 10% in the multi-threshold mode (at 80 GeV). The multi-threshold capability of the SDHCAL prototype at high energy (> 40 GeV) improves clearly the energy resolution. This

improvement reaches 30% at 80 GeV. It is probably related to a better treatment of the saturation effect thanks to the additional information provided by the second and the third thresholds. An in-situ calibration of the sensors response, efficiency and multiplicity, was performed using minimum ionising particles. An improvement of order of 6% has been reached in the binary mode.

Finally a side study of a new kind of GRPC was performed: GRPC equipped with doped glass were tested at DESY facilities in high rate beam conditions. It has been shown that the main weakness of standard GRPC, namely the insensitivity of high rate beam, is clearly overcome. The efficiency of the new chambers remains at around 90% at rate of 9 kHz/cm². This detector has been proposed for the future LHC muons detector upgrades.

The tagging of the Higgs production via Higgsstrahlung process (ZH) using the hadronic decay of Z boson was described in Chapter 9. This has been done with 125 GeV Higgs mass at a centre of mass energy collision of 250 GeV with an integrated luminosity of 500fb⁻¹. A precision better than 2% was then reached on the measurement of the ZH cross section, which corresponds to 1% precision on the measurement of the coupling strength g_{HZZ} at the HZZ vertex.

Beam polarisation was found to be important for the sensitivity of the analysis. An improvement of factor a 1.65 could be reached. The model independence has been checked showing very similar efficiencies as function of the decaying mode of the SM Higgs boson with a dispersion lower than 6%. This may introduce a bias. It can be seen that the lower efficiencies are linked to the presence of neutrinos in the final state. This might be overcome by designing specific analyses. This method could also permit a model independent measurement of the branching ratios of the Higgs boson. The results then can be combined with lepton channels for a better precision.

Appendix A

SDHCAL technical details

A.1 Crystal-Ball function

The Crystal-Ball function consists of a Gaussian core and a power-law tail below a certain threshold. It was first used first by the Crystal Ball Collaboration, is one of the probability density function commonly used to model various lossy process in high energy physics. The Crystal-Ball function is given by:

$$f(x; \alpha, n, \bar{x}, \sigma) = N \cdot \begin{cases} \exp\left\{-\frac{(x-\bar{x})^2}{2\sigma^2}\right\}, & \text{for } \frac{x-\bar{x}}{\sigma} > -\alpha \\ A \cdot (B - \frac{x-\bar{x}}{\sigma})^n, & \text{for } \frac{x-\bar{x}}{\sigma} \leq -\alpha \end{cases} \quad \text{where } \begin{cases} A &= \left(\frac{n}{|\alpha|}\right) \cdot \exp\left(-\frac{|\alpha|^2}{2}\right) \\ B &= \frac{n}{|\alpha|} - |\alpha| \end{cases} \quad (\text{A.1})$$

N is a normalisation factor and α , n , \bar{x} and σ are parameters which are determined from data. Figure A.1 shows an example of the Crystal-Ball function shape.

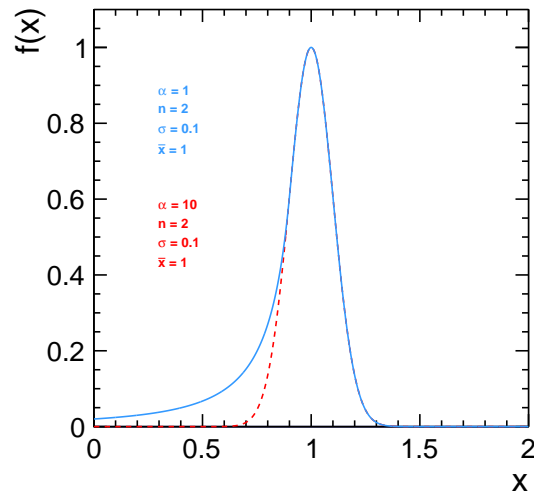


FIGURE A.1: Example of Crystal-Ball function with two different value of α .

A.2 SDHCAL efficiency and multiplicity maps

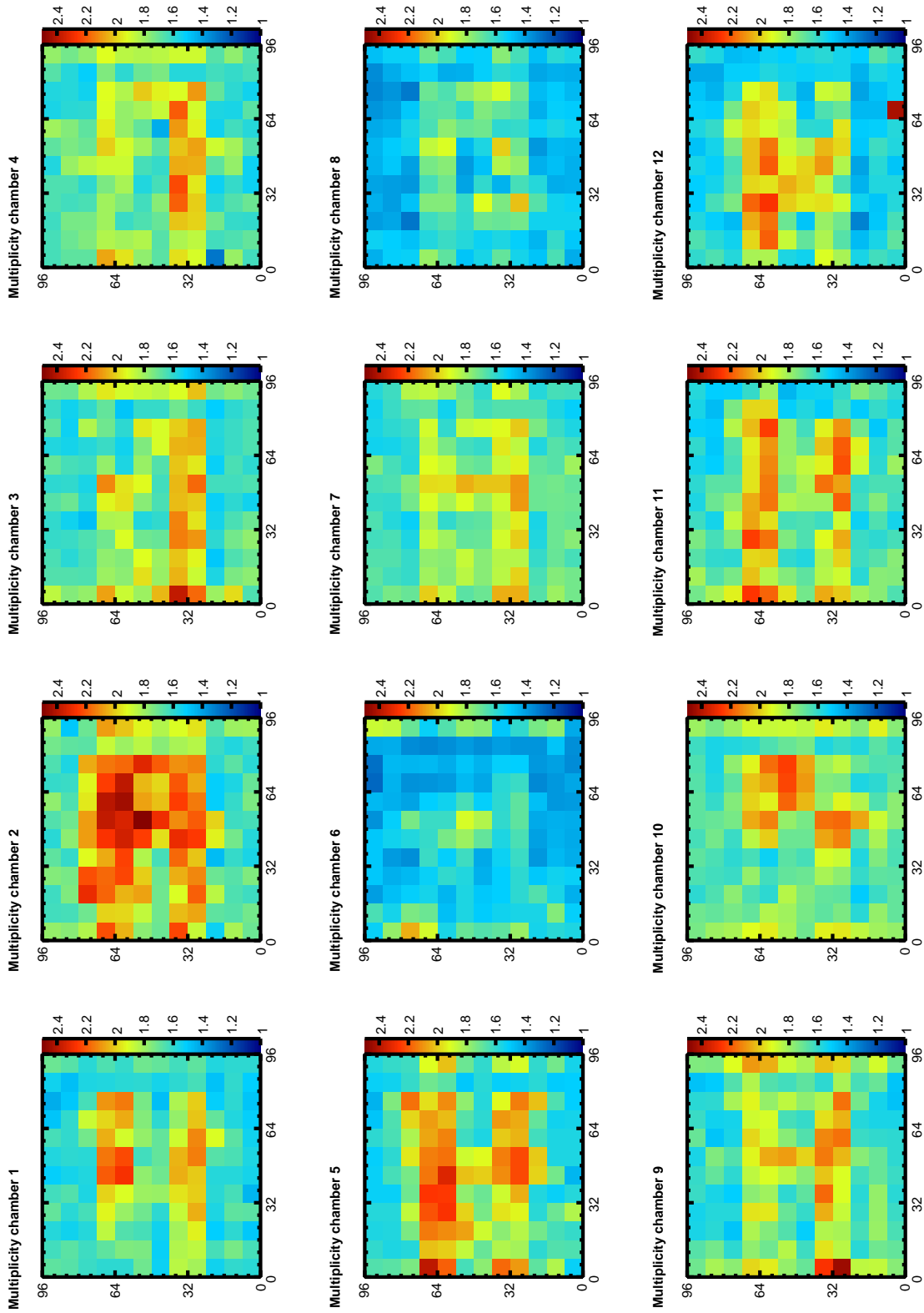


FIGURE A.2: Multiplicity maps of the SDHCAL chambers.

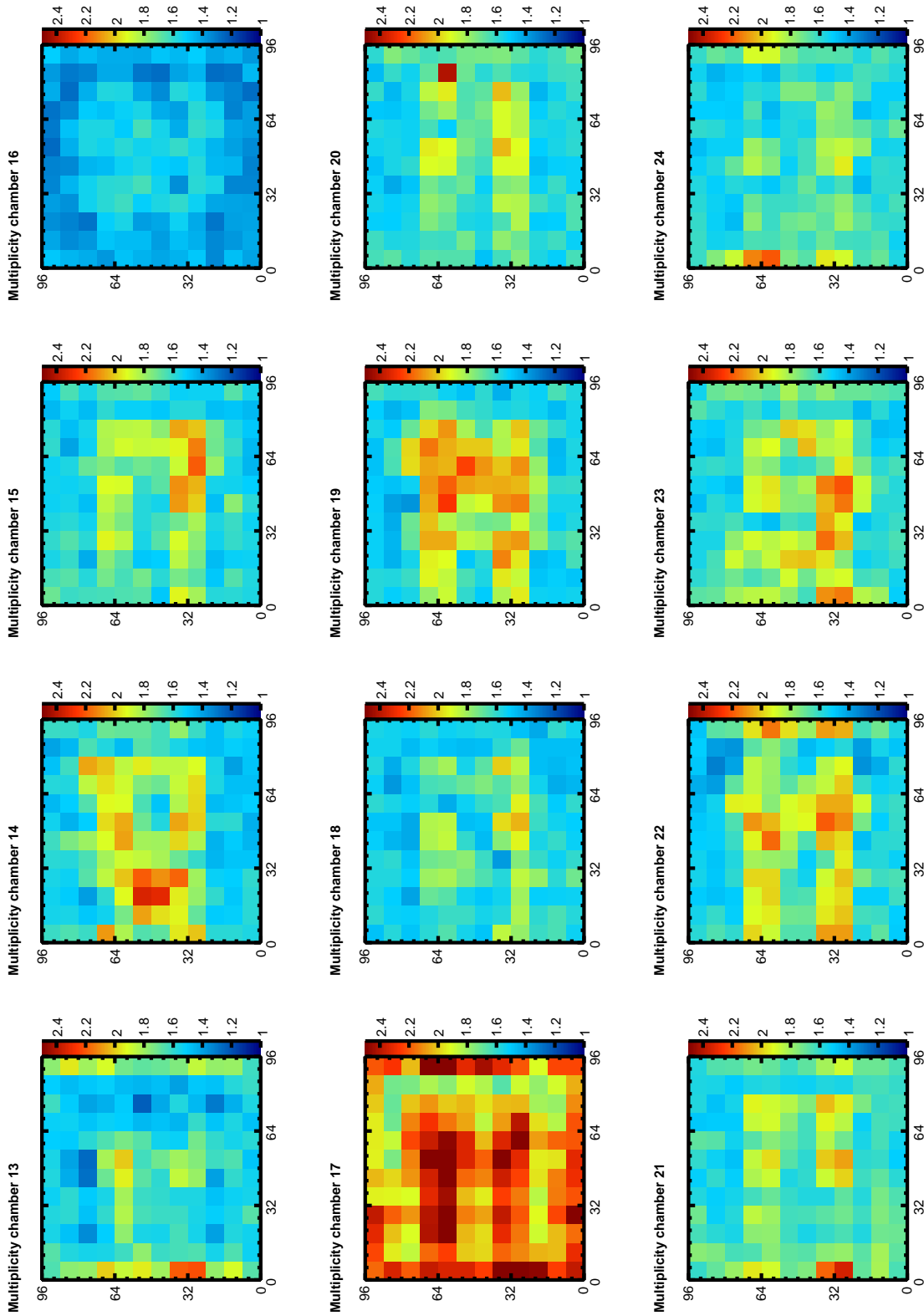


FIGURE A.3: Multiplicity maps of the SDHCAL chambers.

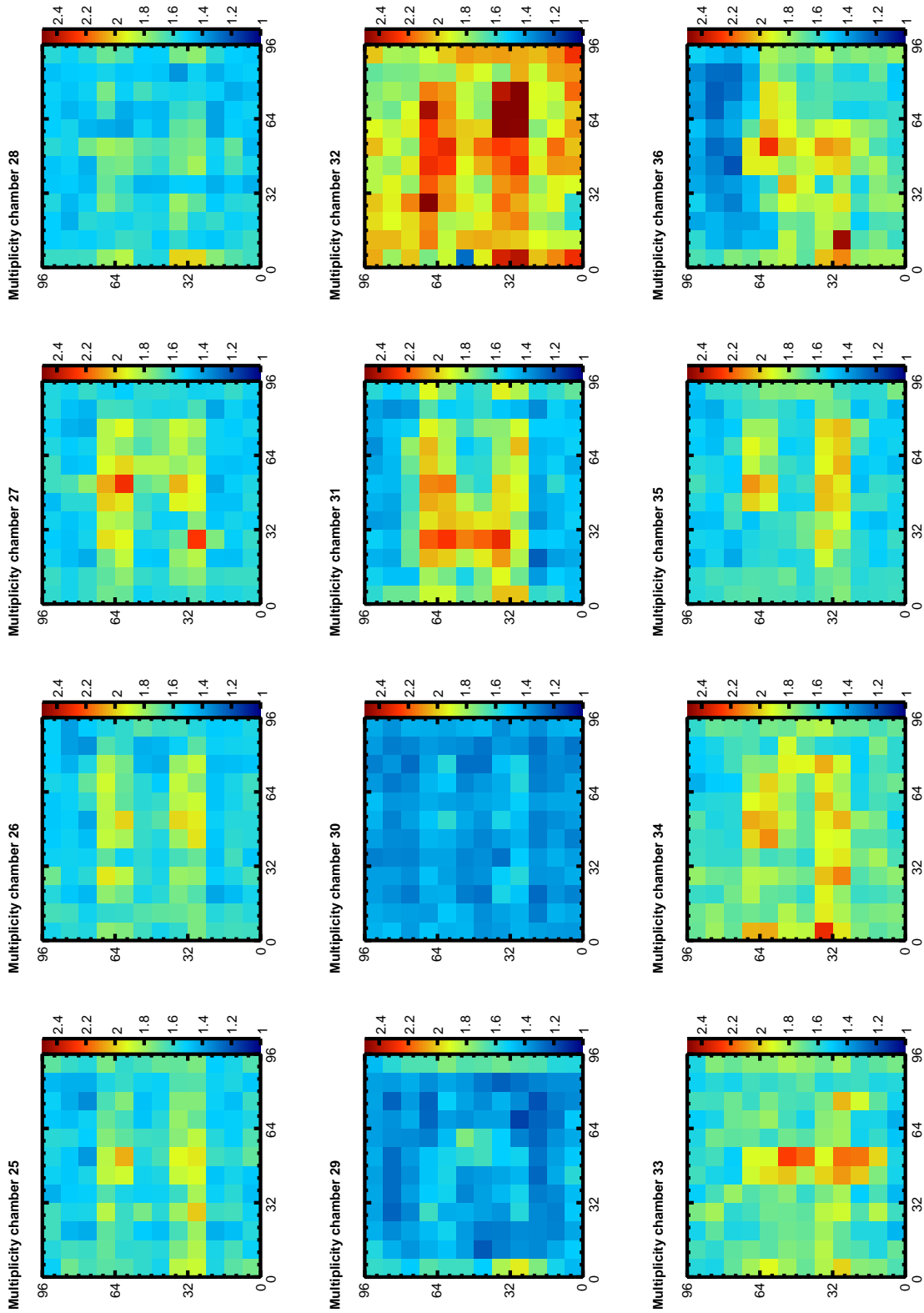


FIGURE A.4: Multiplicity maps of the SDHCAL chambers.

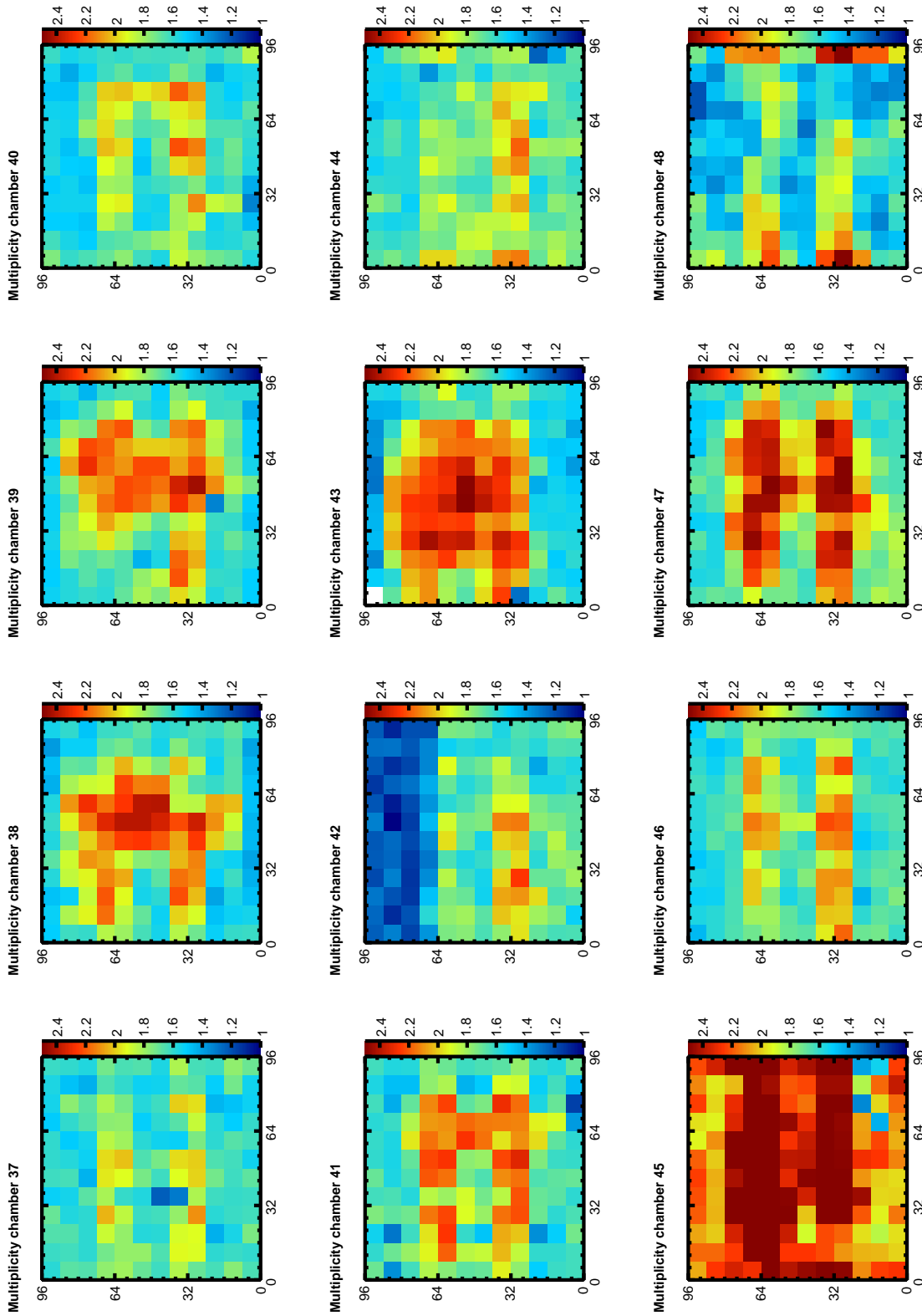


FIGURE A.5: Multiplicity maps of the SDHCAL chambers.

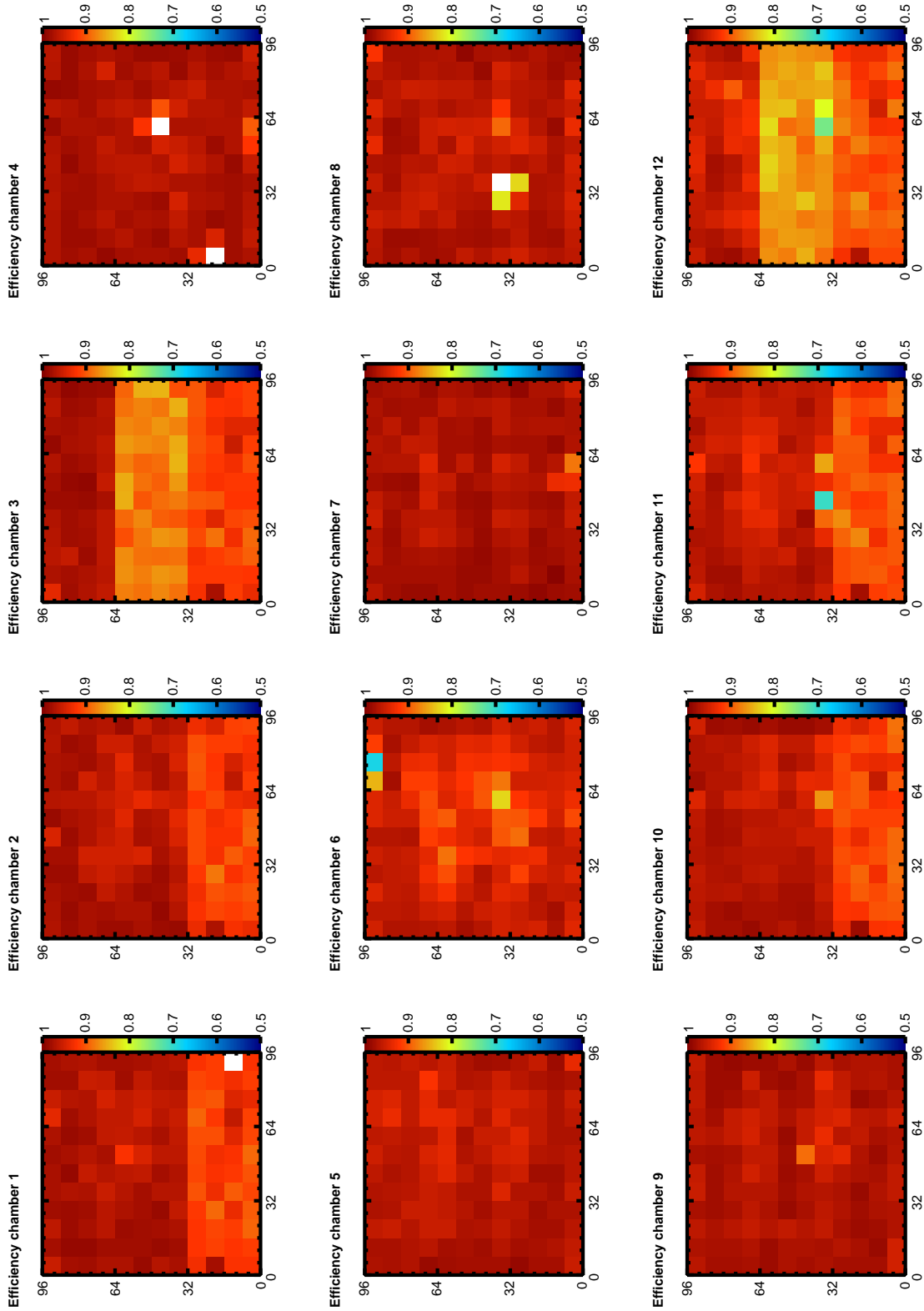


FIGURE A.6: Efficiency maps of the SDHCAL chambers.

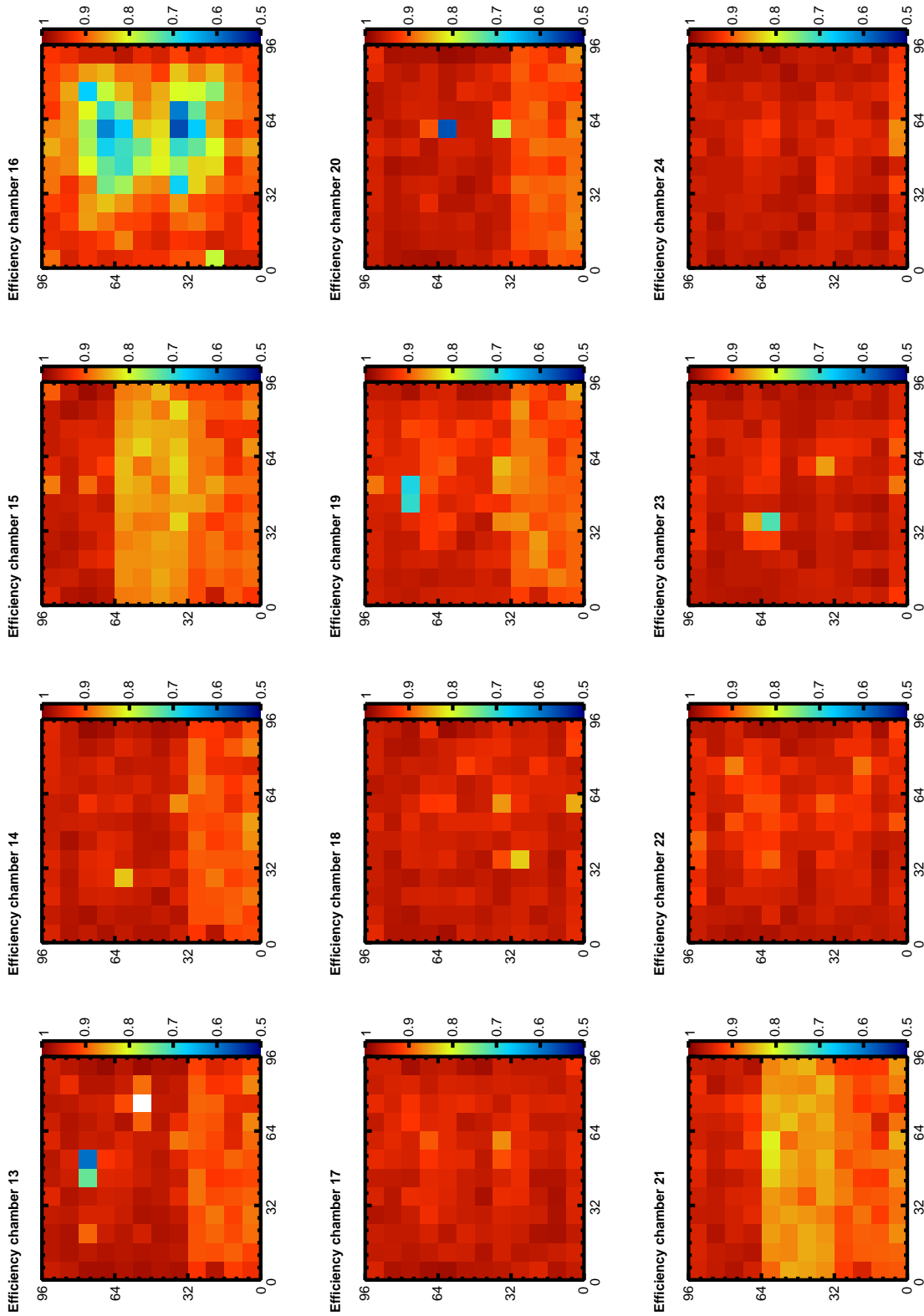


FIGURE A.7: Efficiency maps of the SDHCAL chambers.

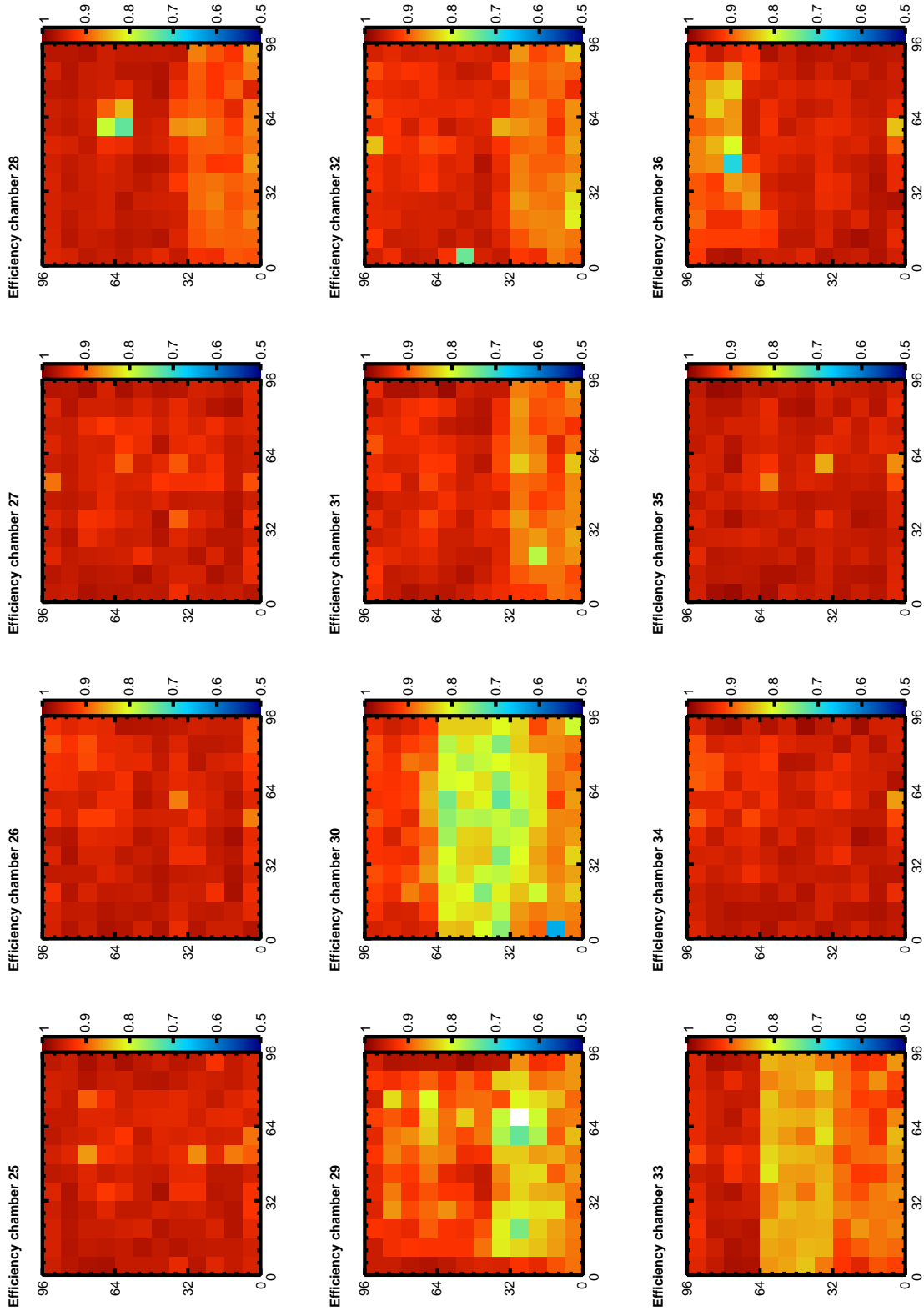


FIGURE A.8: Efficiency maps of the SDHCAL chambers.

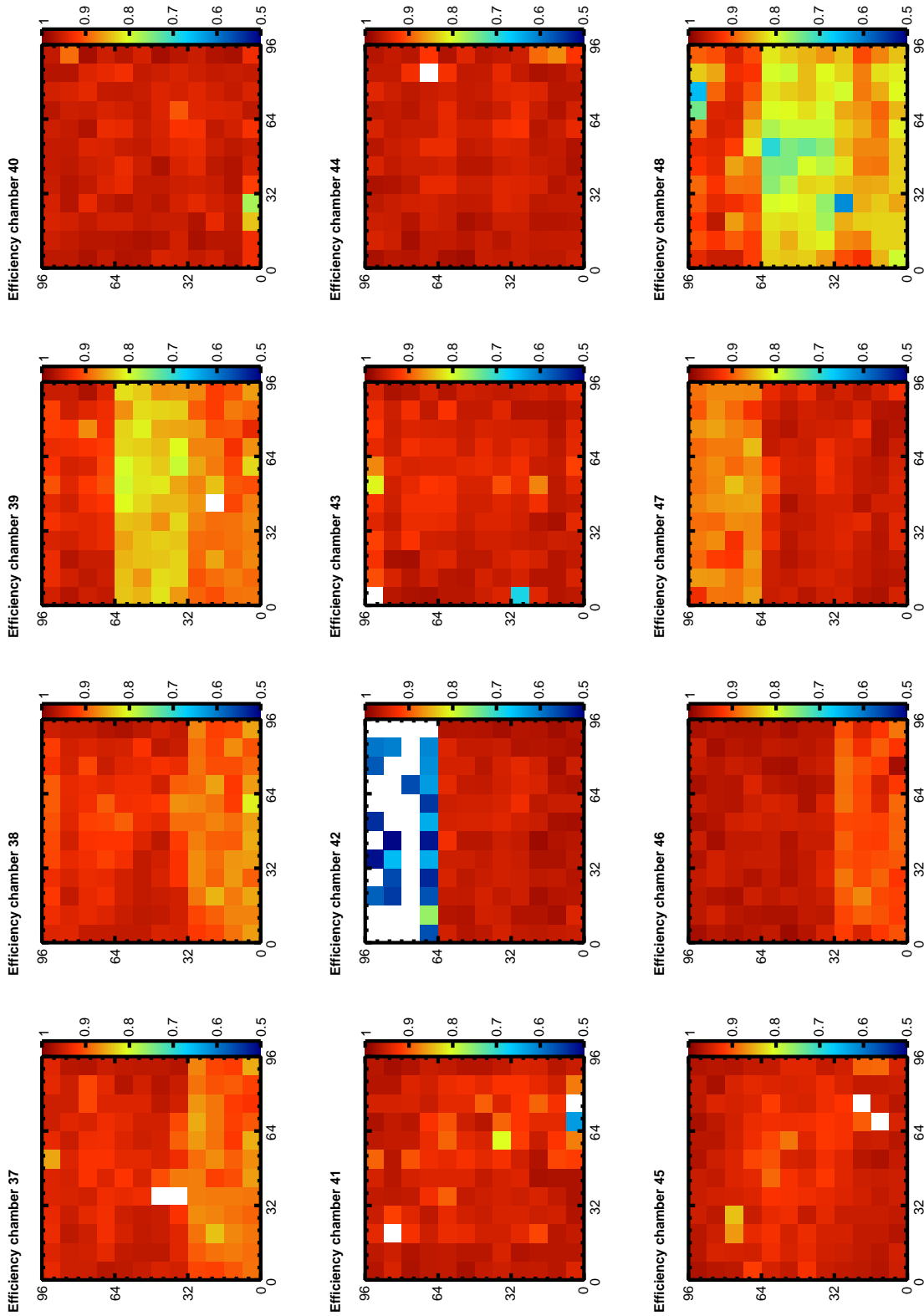


FIGURE A.9: Efficiency maps of the SDHCAL chambers.

A.3 Observed resolution

The following table lists the resolution observed as plotted in Figure 7.13 and Figure 7.18.

Energy (GeV)	binary mode	multi-threshold mode
5	0.298 ± 0.014	0.31 ± 0.04
7.5	0.278 ± 0.005	0.286 ± 0.005
10	0.224 ± 0.003	0.233 ± 0.005
15	0.185 ± 0.003	0.192 ± 0.004
20	0.162 ± 0.005	0.168 ± 0.002
25	0.160 ± 0.003	0.165 ± 0.003
30	0.148 ± 0.003	0.149 ± 0.002
40	0.140 ± 0.003	0.135 ± 0.002
50	0.139 ± 0.004	0.127 ± 0.005
60	0.134 ± 0.001	0.113 ± 0.006
70	0.136 ± 0.003	0.105 ± 0.007
80	0.142 ± 0.003	0.095 ± 0.004

TABLE A.1: Summary of the observed SDHCAL resolution in the binary and muti-threshold modes.

Appendix B

Boosted decision tree training details

B.1 Training parameters

The list of parameters and their corresponding values that were used for the training of the boosted decision trees with the TMVA package for the hadronic tagging of the Higgs boson are listed in the Table B.1

TMVA parameters	Value	Description
<code>NTrees</code>	1000	Number of tree in the forest
<code>BoostType</code>	<code>GradBoost</code>	Type of boosting
<code>MaxDepth</code>	2	Max depth of the decision tree allowed
<code>Shrinkage</code>	0.10	Learning rate for <code>GradBoost</code> algorithm
<code>nCut</code>	20	Number of grid points in variable range used in finding optimal cut in node splitting

TABLE B.1: List of the TMVA setting used to grow the BDT

B.2 Correlation Matrices

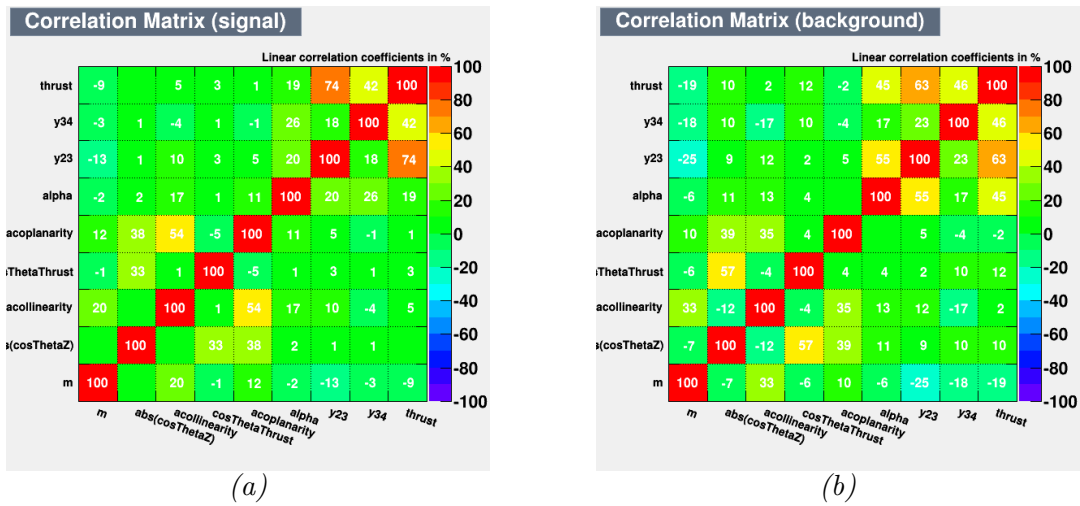


FIGURE B.1: Correlation matrix of the input variables for the signal (a) and background (b).

Bibliography

- [1] S. L. Glashow, *Partial-symmetries of weak interactions*, *Nuclear Physics* **22** (1961), no. 4 579 – 588.
- [2] A. Salam, *Gauge Unification of Fundamental Forces*, *Rev.Mod.Phys.* **52** (1980) 525–538.
- [3] S. Weinberg, *A model of leptons*, *Phys. Rev. Lett.* **19** (Nov, 1967) 1264–1266.
- [4] G. t Hooft and M. Veltman, *Regularization and renormalization of gauge fields*, *Nuclear Physics B* **44** (1972), no. 1 189–213.
- [5] F. Hasert, S. Kabe, W. Krenz, J. V. Krogh, D. Lanske, J. Morfin, K. Schultze, H. Weerts, G. Bertrand-Coremans, J. Sacton, W. V. Doninck, P. Vilain, U. Camerini, D. Cundy, R. Baldi, I. Danilchenko, W. Fry, D. Haidt, S. Natali, P. Musset, B. Osculati, R. Palmer, J. Pattison, D. Perkins, A. Pullia, A. Rousset, W. Venus, H. Wachsmuth, V. Brisson, B. Degrange, M. Haguenaue, L. Kluberg, U. Nguyen-Khac, P. Petiau, E. Belotti, S. Bonetti, D. Cavalli, C. Conta, E. Fiorini, M. Rollier, B. Aubert, D. Blum, L. Chounet, P. Heusse, A. Lagarrigue, A. Lutz, A. Orkin-Lecourtois, J. Vialle, F. Bullock, M. Esten, T. Jones, J. McKenzie, A. Michette, G. Myatt, and W. Scott, *Observation of neutrino-like interactions without muon or electron in the gargamelle neutrino experiment*, *Physics Letters B* **46** (1973), no. 1 138 – 140.
- [6] U. Amaldi, A. Böhm, L. Durkin, P. Langacker, A. K. Mann, W. J. Marciano, A. Sirlin, and H. Williams, *Comprehensive analysis of data pertaining to the weak neutral current and the intermediate-vector-boson masses*, *Physical Review D* **36** (1987), no. 5 1385.
- [7] H. Fritzsch, M. Gell-Mann, and H. Leutwyler, *Advantages of the color octet gluon picture*, *Physics Letters B* **47** (1973), no. 4 365–368.
- [8] CMS Collaboration, *Observation of a new boson at a mass of 125 gev with the CMS experiment at the LHC*, *Physics Letters B* **716** (2012), no. 1 30 – 61.
- [9] ATLAS Collaboration, *Observation of a new particle in the search for the standard model higgs boson with the ATLAS detector at the LHC*, *Physics Letters B* **716** (2012), no. 1 1 – 29.
- [10] A. Djouadi, *The anatomy of electroweak symmetry breaking tome ii: The higgs bosons in the minimal supersymmetric model*, *Physics reports* **459** (2008), no. 1 1–241.
- [11] M. E. Peskin and D. V. Schroeder, *An introduction to quantum field theory*. Westview, 1995.
- [12] G. L. Kane, *Modern elementary particle physics*. Addison-Wesley, 1987.
- [13] J. F. Gunion, S. Dawson, G. L. Kane, and H. E. Haber, *The Higgs hunter’s guide*. Westview, 1990.

- [14] R. Feynman, *Gell-mannm*, *Phys. Rev* **109** (1958) 193.
- [15] F. Englert and R. Brout, *Broken symmetry and the mass of gauge vector mesons*, *Phys. Rev. Lett.* **13** (Aug, 1964) 321–323.
- [16] P. W. Higgs, *Broken symmetries and the masses of gauge bosons*, *Phys. Rev. Lett.* **13** (Oct, 1964) 508–509.
- [17] J. Goldstone, A. Salam, and S. Weinberg, *Broken symmetries*, *Phys. Rev.* **127** (Aug, 1962) 965–970.
- [18] M. S. Chanowitz, *Strong $W W$ scattering at the end of the 90's: Theory and experimental prospects*, [hep-ph/9812215](#).
- [19] M. Lüscher and P. Weisz, *Scaling laws and triviality bounds in the lattice ϕ^4 theory (iii). n -component model*, *Nuclear Physics B* **318** (1989), no. 3 705 – 741.
- [20] T. Hambye and K. Riesselmann, *Sm higgs mass bounds from theory*, *arXiv preprint hep-ph/9708416* (1997).
- [21] **LEP Working Group for Higgs boson searches, ALEPH Collaboration, DELPHI Collaboration, L3 Collaboration, OPAL Collaboration** Collaboration, R. Barate et al., *Search for the standard model Higgs boson at LEP*, *Phys.Lett.* **B565** (2003) 61–75, [[hep-ex/0306033](#)].
- [22] The ALEPH, DELPHI, L3, OPAL, SLD Collaborations, the LEP Electroweak Working Group, the SLD Electroweak and Heavy Flavour Groups, *Precision Electroweak Measurements on the Z Resonance*, *Phys. Rept.* **427** (2006) 257, [[hep-ex/0509008](#)].
- [23] **CDF Collaboration** Collaboration, T. Aaltonen et al., *Observation of Single Top Quark Production and Measurement of $-V_{tb}$ — with CDF*, *Phys.Rev.* **D82** (2010) 112005, [[arXiv:1004.1181](#)].
- [24] **CMS Collaboration** Collaboration, S. Chatrchyan et al., *Evidence for the direct decay of the 125 GeV Higgs boson to fermions*, *Nature Phys.* **10** (2014) [[arXiv:1401.6527](#)].
- [25] T. C. Collaboration, *Evidence for the direct decay of the 125 gev higgs boson to fermions*, *Nat Phys* **10** (Aug, 2014) 557–560. Letter.
- [26] ATLAS Collaboration, *Evidence for the spin-0 nature of the higgs boson using {ATLAS} data*, *Physics Letters B* **726** (2013), no. 1-3 120 – 144.
- [27] **CMS Collaboration** Collaboration, C. Collaboration, *Study of the mass and spin-parity of the higgs boson candidate via its decays to z boson pairs*, *Phys. Rev. Lett.* **110** (Feb, 2013) 081803.
- [28] C. Adolphsen, M. Barone, B. Barish, K. Buesser, P. Burrows, et al., *The International Linear Collider Technical Design Report - Volume 3.II: Accelerator Baseline Design*, [arXiv:1306.6328](#).
- [29] N. Phinney, N. Toge, and N. Walker, *ILC Reference Design Report Volume 3 - Accelerator*, [arXiv:0712.2361](#).
- [30] B. Aurand, I. Bailey, C. Bartels, A. Brachmann, J. Clarke, et al., *Beam Polarization at the ILC: The Physics Impact and the Accelerator Solutions*, [arXiv:0903.2959](#).

- [31] H. Baer, T. Barklow, K. Fujii, Y. Gao, A. Hoang, et al., *The International Linear Collider Technical Design Report - Volume 2: Physics*, [arXiv:1306.6352](#).
- [32] **CMS Collaboration** Collaboration, C. Collaboration, *Properties of the observed Higgs-like resonance using the diphoton channel*, .
- [33] M. Klute, R. Lafaye, T. Plehn, M. Rauch, and D. Zerwas, *Measuring Higgs Couplings at a Linear Collider*, *Europhys.Lett.* **101** (2013) 51001, [[arXiv:1301.1322](#)].
- [34] **ATLAS Collaboration, CMS Collaboration** Collaboration, S. Blyweert, *Top-quark mass measurements at the LHC*, [arXiv:1205.2175](#).
- [35] K. Seidel, F. Simon, and M. Tesar, *Prospects for the Measurement of the Top Mass in a Threshold Scan at CLIC and ILC*, .
- [36] M. Thomson, *Particle flow calorimetry and the pandorapfa algorithm*, *Nuclear Instruments and Methods in Physics Research Section A: Accelerators, Spectrometers, Detectors and Associated Equipment* **611** (2009), no. 1 25–40.
- [37] T. Behnke, J. E. Brau, P. N. Burrows, J. Fuster, M. Peskin, et al., *The International Linear Collider Technical Design Report - Volume 4: Detectors*, [arXiv:1306.6329](#).
- [38] A. Hoummada, C. Adloff, Y. Karyotakis, J. Repond, J. Yu, G. Eigen, C. Hawkes, Y. Mikami, O. Miller, N. Watson, et al., *Response of the calice si-w electromagnetic calorimeter physics prototype to electrons*, .
- [39] CALICE collaboration web site, . <https://twiki.cern.ch/twiki/bin/view/CALICE/>.
- [40] J. B. et al., *Particle data group*, *Phys. Rev.* (2012 and 2013 partial update for the 2014 edition), no. D86 010001.
- [41] U. Amaldi, *Fluctuations in calorimetry measurements*, *Physica Scripta* **23** (1981), no. 4A 409.
- [42] E. Longo and I. Sestili, *Monte carlo calculation of photon-initiated electromagnetic showers in lead glass*, *Nuclear Instruments and Methods* **128** (1975), no. 2 283 – 307.
- [43] W. R. Nelson, H. Hirayama, and D. W. Rogers, *The egs4 code system slac-265 stanford linear accelerator center*, 1985.
- [44] “Atomic and Nuclear Properties of Materials.”
<http://pdg.lbl.gov/2013/AtomicNuclearProperties/index.html>.
- [45] M. Holder, J. Knobloch, J. May, H. Paar, P. Palazzi, D. Schlatter, J. Steinberger, H. Suter, H. Wahl, E. Williams, F. Eisele, C. Geweniger, K. Kleinknecht, G. Spahn, H.-J. Willutzki, W. Dorth, F. Dydak, T. Flottmann, V. Hepp, K. Tittel, J. Wotschack, P. Bloch, B. Devaux, M. Grimm, J. Maillard, B. Peyaud, J. Rander, A. Savoy-Navarro, R. Turlay, and F. Navarra, *Performance of a magnetized total absorption calorimeter between 15 gev and 140 gev*, *Nuclear Instruments and Methods* **151** (1978), no. 1–2 69 – 80.
- [46] C. Leroy and P.-G. Rancoita, *Physics of cascading shower generation and propagation in matter: principles of high-energy, ultrahigh-energy and compensating calorimetry*, *Reports on Progress in Physics* **63** (2000), no. 4 505.
- [47] T. Gabriel, D. Groom, P. Job, N. Mokhov, and G. Stevenson, *Energy dependence of hadronic activity*, *Nuclear Instruments and Methods in Physics Research Section A: Accelerators, Spectrometers, Detectors and Associated Equipment* **338** (1994), no. 2–3 336 – 347.

- [48] C. A. et al., *Beam test of a small MICROMEGAS DHCAL prototype*, *Journal of Instrumentation* **5** (2010), no. 01 P01013.
- [49] T. Behnke, S. Bertolucci, R. Heuer, and R. Settles, *Tesla: The superconducting electron positron linear collider with an integrated x-ray laser laboratory. technical design report. pt. 4: A detector for tesla*, tech. rep., DESY-01-011, 2001.
- [50] V. Ammosov, V. Gapienko, A. Ivanilov, A. Semak, Y. Sviridov, E. Usenko, V. G. Zaetz, and F. Sefkow, *RPC as a detector for high granularity digital hadron calorimetry*, Tech. Rep. DESY-04-057. DESY-2004-057, DESY, Hamburg, Mar, 2004.
- [51] J. Yu, E. Baldelomar, K. Park, S. Park, M. Sosebee, N. Tran, and A. White, *Application of large scale gem for digital hadron calorimetry*, *Physics Procedia* **37** (2012) 393–401.
- [52] V. Morgunov and A. Raspereza, *Novel 3d clustering algorithm and two particle separation with tile hcal*, *arXiv preprint physics/0412108* (2004).
- [53] J.-C. Brient and H. Videau, *The Calorimetry at the future e+ e- linear collider*, *eConf C010630* (2001) E3047, [[hep-ex/0202004](http://arxiv.org/abs/hep-ex/0202004)].
- [54] I. Laktineh, *Construction of a technological semi-digital hadronic calorimeter using grpc*, in *Journal of Physics: Conference Series*, vol. 293, p. 012077, IOP Publishing, 2011.
- [55] M. Bedjidian, J.-P. Ianigro, R. Kieffer, I. Laktineh, N. Lumb, and S. Vanzetto, *Glass resistive plate chambers for a semi-digital {HCAL}*, *Nuclear Instruments and Methods in Physics Research Section A: Accelerators, Spectrometers, Detectors and Associated Equipment* **623** (2010), no. 1 120 – 122. 1st International Conference on Technology and Instrumentation in Particle Physics.
- [56] C. de La Taille et al., *Performance of 2nd generation calice/eudet asics*, in *Journal of Physics: Conference Series*, vol. 293, p. 012016, IOP Publishing, 2011.
- [57] M. Bedjidian, K. Belkadhi, V. Boudry, C. Combaret, D. Decotigny, E. C. Gil, C. de La Taille, R. Dellanegra, V. Gapienko, G. Grenier, et al., *Performance of glass resistive plate chambers for a high-granularity semi-digital calorimeter*, *Journal of Instrumentation* **6** (2011), no. 02 P02001.
- [58] OMEGA: *Microelectronics for particle physics*, . <http://omega.in2p3.fr/>.
- [59] Altera, *Cyclone III FPGA Family*, . www.altera.com/devices/fpga/cyclone3/cy3-index.jsp.
- [60] C. Adolphsen, M. Barone, B. Barish, K. Buesser, P. Burrows, et al., *The International Linear Collider Technical Design Report - Volume 3.II: Accelerator Baseline Design*, [arXiv:1306.6328](https://arxiv.org/abs/1306.6328).
- [61] L. Caponetto, C. Combaret, C. de La Taille, F. Dulucq, R. Kieffer, I. Laktineh, N. Lumb, L. Mirabito, and N. Seguin-Moreau, *First test of a power-pulsed electronics system on a grpc detector in a 3-tesla magnetic field*, *Journal of Instrumentation* **7** (2012), no. 04 P04009.
- [62] *SWIG simplified wrapper and interface generator*, . www.swig.org.
- [63] *Future Technology Devices International*, . <http://www.ftdichip.com/>.

- [64] M. Bedjidian, K. Belkadhi, V. Boudry, C. Combaret, D. Decotigny, et al., *Performance of Glass Resistive Plate Chambers for a high granularity semi-digital calorimeter*, *JINST* **6** (2011) P02001, [[arXiv:1011.5969](https://arxiv.org/abs/1011.5969)].
- [65] S. Aplin, J. Engels, F. Gaede, N. A. Graf, T. Johnson, et al., *LCIO: A Persistency Framework and Event Data Model for HEP*, .
- [66] R. Santonico and R. Cardarelli, *Development of resistive plate counters*, *Nuclear Instruments and Methods in Physics Research* **187** (1981), no. 2003 377 – 380.
- [67] Atlas Collaboration and others, *Atlas muon spectrometer technical design report*, *CERN/LHCC* **97** (1997) 22.
- [68] M. Abbrescia, A. Colaleo, G. Iaselli, F. Loddo, M. Maggi, B. Marangelli, S. Natali, S. Nuzzo, G. Pugliese, A. Ranieri, F. Romano, S. Altieri, G. Belli, G. Bruno, R. Guida, S. Ratti, C. Riccardi, P. Torre, and P. Vitulo, *The {RPC} system for the {CMS} experiment at the {LHC}*, *Nuclear Instruments and Methods in Physics Research Section A: Accelerators, Spectrometers, Detectors and Associated Equipment* **508** (2003), no. 1-2 137 – 141. Proceedings of the Sixth International Workshop on Resistive Plate Chambers and Related Detectors.
- [69] A. Zallo, *The babar {RPC} system*, *Nuclear Instruments and Methods in Physics Research Section A: Accelerators, Spectrometers, Detectors and Associated Equipment* **456** (2000), no. 1-2 117 – 120. Proceedings of the 5th Int. Workshop on Resistive Plate Chambers and Related Detectors.
- [70] A. Abashian, K. Abe, K. Abe, S. Azuchi, P. Behera, S. Chidzik, S. Chinomi, K. Gotow, F. Haitani, H. Hanada, K. Hanagaki, Y. Hoshi, Y. Igarashi, Y. Inoue, N. Kawamura, K. Korotushenko, D. Marlow, N. Morgan, T. Nagamine, M. Nakajima, T. Nakajima, E. Nakano, S. Narita, K. Neichi, L. Piilonen, E. Prebys, H. Sakai, W. Sands, S. Schrenk, T. Takahashi, T. Takayama, Y. Teramoto, M. Ueki, M. Yamaga, A. Yamaguchi, and H. Yuta, *The k_{\perp}/μ detector subsystem for the belle experiment at the kek b-factory*, *Nuclear Instruments and Methods in Physics Research Section A: Accelerators, Spectrometers, Detectors and Associated Equipment* **449** (2000), no. 1-2 112 – 124.
- [71] R. Acquafredda and al, *The opera experiment in the cern to gran sasso neutrino beam*, *Journal of Instrumentation* **4** (2009), no. 04 P04018.
- [72] J. Va'vra, *Summary of session 6: Aging effects in RPC detectors*, *Nucl.Instrum.Meth.* **A515** (2003) 354–357.
- [73] R. Kieffer, *Caractérisation d'un calorimètre hadronique semi-digital pour le futur collisionneur ILC*. PhD thesis, Université Claude Bernard-Lyon I, 2011.
- [74] W. Riegler, C. Lippmann, and R. Veenhof, *Detector physics and simulation of resistive plate chambers*, *Nuclear Instruments and Methods in Physics Research Section A: Accelerators, Spectrometers, Detectors and Associated Equipment* **500** (2003), no. 1-3 144 – 162. {NIMA} Vol 500.
- [75] H. Genz, *Single electron detection in proportional gas counters*, *Nuclear Instruments and Methods* **112** (1973), no. 1 - 2 83 – 90.
- [76] C. Lippmann and W. Riegler, *Space charge effects in resistive plate chambers*, *Nuclear Instruments and Methods in Physics Research Section A: Accelerators, Spectrometers, Detectors and Associated Equipment* **517** (2004), no. 1-3 54 – 76.

- [77] W. Blum, W. Riegler, and L. Rolandi, *Particle detection with drift chambers*. Springer, 2008.
- [78] W. Riegler, *Induced signals in resistive plate chambers*, *Nucl.Instrum.Meth.* **A491** (2002) 258–271.
- [79] I. Smirnov, *Heed, program to compute energy loss of fast particles in gases*, *CERN Program Library Writeup W* **5060**.
- [80] S. Biagi, *Magboltz: Transport of electrons in gas mixtures*, *CERN program library* (2009).
- [81] V. Palladino and B. Sadoulet, *Application of classical theory of electrons in gases to drift proportional chambers*, *Nuclear Instruments and Methods* **128** (1975), no. 2 323–335.
- [82] M. E. Rose and S. A. Korff, *An investigation of the properties of proportional counters. i*, *Phys. Rev.* **59** (Jun, 1941) 850–859.
- [83] H. Raether, *Electron avalanches and breakdown in gases*, *Butterworths* (1964).
- [84] R. A. Wijzman, *Breakdown probability of a low pressure gas discharge*, *Phys. Rev.* **75** (Mar, 1949) 833–838.
- [85] W. Legler, *Z. physik 140 (1955) 221*, *Ann. Physik Lpz* **18** (1956), no. 5.
- [86] A. H. Cookson, B. W. Ward, and T. J. Lewis, *Townsend’s first ionization coefficient for methane and nitrogen*, *British Journal of Applied Physics* **17** (1966), no. 7 891.
- [87] S. Curran, J. Angus, and A. Cockroft, *Ii. investigation of soft radiations by proportional counters*, *Philosophical Magazine* **40** (1949), no. 300 36–52.
- [88] J. Byrne, *Statistics of electron avalanches in the proportional counter*, *Nuclear Instruments and Methods* **74** (1969), no. 2 291–296.
- [89] A. Lansiant and J.-P. Morucci, *Amplification gazeuse dans un compteur proportionnel*, *Journal de Physique Appliquée* **23** (1962), no. S6 102–104.
- [90] P. Fonte, R. Ferreira-Marques, V. Peskov, and A. Policarpo, *Single-electron pulse-height spectra in thin-gap parallel-plate chambers*, *Nuclear Instruments and Methods in Physics Research Section A: Accelerators, Spectrometers, Detectors and Associated Equipment* **433** (1999), no. 1 513–517.
- [91] W. Shockley, *Currents to Conductors Induced by a Moving Point Charge*, *Journal of Applied Physics* **9** (Oct., 1938) 635–636.
- [92] S. Ramo, *Currents induced by electron motion*, *Proc. Ire* **27** (1939), no. 9 584.
- [93] F. James and M. Winkler, *MINUIT User’s Guide*, .
<http://inspirehep.net/record/1258345>.
- [94] R. Brun and F. Rademakers, *Root - an object oriented data analysis framework*, in *Proceedings AIHENP’96 Workshop, Lausanne, Sep. 1996*, *Nucl. Inst. & Meth. in Phys. Res. A* **389** (N. I. . M. in Phys. Res. A, ed.), no. 389, pp. 81–86, 1997.
- [95] S. A. et al., *Geant4 simulation toolkit*, *Nuclear Instruments and Methods in Physics Research Section A: Accelerators, Spectrometers, Detectors and Associated Equipment* **506** (2003), no. 3 250 – 303.

- [96] R. Kieffer, I. B. Laktineh, N. Lumb, M. Bedjidian, M. Donckt, R. Han, and L. Mirabito, *Development of new kind of grpc for a semi-digital hadronic calorimeter*, in *Nuclear Science Symposium Conference Record (NSS/MIC), 2010 IEEE*, pp. 1468–1471, 2010.
- [97] C. A. et al., *Micromegas chambers for hadronic calorimetry at a future linear collider*, *Journal of Instrumentation* **4** (2009), no. 11 P11023.
- [98] I. Laktineh, *Development of a semi-digital hadronic calorimeter using GRPC*, *Nucl.Instrum.Meth.* **A623** (2010) 231–233.
- [99] Y. Haddad, *First Results of the SDHCAL technological prototype*, *Proceedings of the CHEF2013 Conference - Eds. J.-C. Brient, R. Salerno, and Y. Sirois* (2013) 1–488, [[arXiv:1401.5825](https://arxiv.org/abs/1401.5825)].
- [100] C. Lu, *Induced Signal in RPC*, *eConf* **C0604032** (2006) 0201.
- [101] H. Bichsel, *A method to improve tracking and particle identification in tpcs and silicon detectors*, *Nuclear Instruments and Methods in Physics Research Section A: Accelerators, Spectrometers, Detectors and Associated Equipment* **562** (2006), no. 1 154–197.
- [102] K. Pearson, *On lines and planes of closest fit to systems of points in space*, *Philosophical Magazine* **2** (11) (1901) 559–572.
- [103] E. Faleiro, J. M. G. Gomez, L. Munoz, A. Relano, and J. Retamosa, *Principal components analysis of extensive air showers applied to the identification of cosmic tev gamma-rays*, *The Astrophysical Journal Supplement Series* **155** (2004), no. 1 167.
- [104] M. R. Vassali and J. M. Seixas, *Principal component analysis for neural electron/jet discrimination in highly segmented calorimeters*, *AIP Conference Proceedings* **583** (2001), no. 1 89–91.
- [105] B. B. Mandelbrot, *Fractals: form, chance and dimension*. Freeman, San Francisco, CA, 1977. Modified trans. of : *Les objets fractals*. Paris, Flammarion, 1975.
- [106] M. Ruan, D. Jeans, V. Boudry, J.-C. Brient, and H. Videau, *Fractal dimension of particle showers measured in a highly granular calorimeter*, *Phys. Rev. Lett.* **112** (Jan, 2014) 012001.
- [107] B. Bilki, *CALICE Digital Hadron Calorimeter: Calibration and Response to Hadrons*, [arXiv:1404.0041](https://arxiv.org/abs/1404.0041).
- [108] S. Mannai, “Energy reconstruction in grpc semi-digital hcal.” Talk given at CALICE collaboration meeting, Lyon, France.
- [109] Y. Haddad, G. Grenier, I. Laktineh, N. Lumb, and S. Cauwenbergh, *High Rate Resistive Plate Chamber for LHC detector upgrades*, *Nucl.Instrum.Meth.* **A718** (2013) 424–426, [[arXiv:1211.5698](https://arxiv.org/abs/1211.5698)].
- [110] Y. Wang, J. Wang, Q. Yan, Y. Li, and J. Cheng, *Study on the performance of high rating mrpc*, in *Nuclear Science Symposium Conference Record, 2008. NSS '08. IEEE*, pp. 913–916, Oct, 2008.
- [111] DESY test beam facility webpage, .
<https://aida.web.cern.ch/aida/activities/access/DESY/>.

- [112] **ILD Design Study Group** Collaboration, H. Li et al., *HZ Recoil Mass and Cross Section Analysis in ILD*, [arXiv:1202.1439](https://arxiv.org/abs/1202.1439).
- [113] T. Behnke, J. E. Brau, P. N. Burrows, J. Fuster, M. Peskin, et al., *The International Linear Collider Technical Design Report - Volume 4: Detectors*, [arXiv:1306.6329](https://arxiv.org/abs/1306.6329).
- [114] **TMVA Core Developer Team** Collaboration, J. Therhaag, *TMVA: Toolkit for multivariate data analysis*, *AIP Conf.Proc.* **1504** (2009) 1013–1016.
- [115] “ILC centrally produced monte carlo generator samples.”
- [116] W. Kilian, T. Ohl, and J. Reuter, *WHIZARD: Simulating Multi-Particle Processes at LHC and ILC*, *Eur.Phys.J.* **C71** (2011) 1742, [[arXiv:0708.4233](https://arxiv.org/abs/0708.4233)].
- [117] W. Kilian, T. Ohl, and J. Reuter, *O’mega: An optimizing matrix element generator*, tech. rep., LCTOOL-2001-040-rev, [arXiv: hep-ph/0102195](https://arxiv.org/abs/hep-ph/0102195)-rev, 2001.
- [118] S. Agostinelli, J. Allison, K. a. Amako, J. Apostolakis, H. Araujo, P. Arce, M. Asai, D. Axen, S. Banerjee, G. Barrand, et al., *Geant4—a simulation toolkit*, *Nuclear instruments and methods in physics research section A: Accelerators, Spectrometers, Detectors and Associated Equipment* **506** (2003), no. 3 250–303.
- [119] “MOKKA web page.” <http://polzope.in2p3.fr:8081/MOKKA>.
- [120] F. Gaede, *Marlin and lccd—software tools for the {ILC}*, *Nuclear Instruments and Methods in Physics Research Section A: Accelerators, Spectrometers, Detectors and Associated Equipment* **559** (2006), no. 1 177 – 180. Proceedings of the X International Workshop on Advanced Computing and Analysis Techniques in Physics Research {ACAT} 05 X International Workshop on Advanced Computing and Analysis Techniques.
- [121] O. Wendt, *Marlin and marlinreco*, *Proc. of LCWS06, Bangalore* (2006).
- [122] O. Wendt, F. Gaede, and T. Krämer, *Event reconstruction with marlinreco at the international linear collider*, *Pramana* **69** (2007), no. 6 1109–1114.
- [123] S. Brandt, C. Peyrou, R. Sosnowski, and A. Wroblewski, *The Principal axis of jets. An Attempt to analyze high-energy collisions as two-body processes*, *Phys.Lett.* **12** (1964) 57–61.
- [124] E. Farhi, *Quantum chromodynamics test for jets*, *Physical Review Letters* **39** (1977), no. 25 1587.
- [125] D. P. Barber, U. Becker, H. Benda, A. Boehm, J. G. Branson, J. Bron, D. Buikman, J. Burger, C. C. Chang, H. S. Chen, M. Chen, C. P. Cheng, Y. S. Chu, R. Clare, P. Duinker, G. Y. Fang, H. Fesefeldt, D. Fong, M. Fukushima, J. C. Guo, A. Hariri, G. Herten, M. C. Ho, H. K. Hsu, T. T. Hsu, R. W. Kadel, W. Krenz, J. Li, Q. Z. Li, M. Lu, D. Luckey, D. A. Ma, C. M. Ma, G. G. G. Massaro, T. Matsuda, H. Newman, J. Paradiso, F. P. Poschmann, J. P. Revol, M. Rohde, H. Rykaczewski, K. Sinram, H. W. Tang, L. G. Tang, S. C. C. Ting, K. L. Tung, F. Vannucci, X. R. Wang, P. S. Wei, M. White, G. H. Wu, T. W. Wu, J. P. Xi, P. C. Yang, X. H. Yu, N. L. Zhang, and R. Y. Zhu, *Discovery of three-jet events and a test of quantum chromodynamics at petra*, *Phys. Rev. Lett.* **43** (Sep, 1979) 830–833.
- [126] J. D. Bjorken and S. J. Brodsky, *Statistical model for electron-positron annihilation into hadrons*, *Phys. Rev. D* **1** (Mar, 1970) 1416–1420.

- [127] B. P. Roe, H.-J. Yang, J. Zhu, Y. Liu, I. Stancu, and G. McGregor, *Boosted decision trees as an alternative to artificial neural networks for particle identification*, *Nuclear Instruments and Methods in Physics Research Section A: Accelerators, Spectrometers, Detectors and Associated Equipment* **543** (2005), no. 2 577–584.
- [128] **D0 Collaboration** Collaboration, V. Abazov et al., *Evidence for production of single top quarks and first direct measurement of $-\text{V}tb-$* , *Phys.Rev.Lett.* **98** (2007) 181802, [[hep-ex/0612052](#)].
- [129] C. Gini, *Variabilità e mutabilità*, Reprinted in *Memorie di metodologica statistica (Ed. Pizetti E, Salvemini, T)*. Rome: Libreria Eredi Virgilio Veschi **1** (1912).
- [130] Y. Freund, *Boosting a weak learning algorithm by majority*, *Information and computation* **121** (1995), no. 2 256–285.
- [131] Y. Freund, R. E. Schapire, et al., *Experiments with a new boosting algorithm*, in *ICML*, vol. 96, pp. 148–156, 1996.
- [132] **OPAL Collaboration** Collaboration, G. Abbiendi et al., *W^+W^- production and triple gauge boson couplings at LEP energies up to 183-GeV*, *Eur.Phys.J.* **C8** (1999) 191–215, [[hep-ex/9811028](#)].
- [133] **JADE Collaboration** Collaboration, W. Bartel et al., *Experimental Studies on Multi-Jet Production in e^+e^- Annihilation at PETRA Energies*, *Z.Phys.* **C33** (1986) 23.
- [134] S. Catani, Y. L. Dokshitzer, M. Olsson, G. Turnock, and B. Webber, *New clustering algorithm for multi - jet cross-sections in e^+e^- annihilation*, *Phys.Lett.* **B269** (1991) 432–438.
- [135] S. Moretti, L. Lönnblad, and T. Sjöstrand, *New and old jet clustering algorithms for electron-positron events*, *Journal of High Energy Physics* **1998** (1998), no. 08 001.
- [136] M. Cacciari, G. P. Salam, and G. Soyez, *FastJet User Manual*, *Eur.Phys.J.* **C72** (2012) 1896, [[arXiv:1111.6097](#)].
- [137] M. Cacciari and G. P. Salam, *Dispelling the N^3 myth for the k_t jet-finder*, *Phys.Lett.* **B641** (2006) 57–61, [[hep-ph/0512210](#)].